ALMA MATER STUDIORUM · UNIVERSITÀ DI BOLOGNA

Dottorato di ricerca in Fisica
XXXV ciclo

Settore concorsuale: 02/D1
Settore scientifico-disciplinare: FIS/07

Diffusive models and chaos indicators for non-linear betatron motion in circular hadron accelerators

Presentata da:
Carlo Emilio Montanari

Coordinatore Dottorato: **prof. Michele Cicoli**	Supervisore: **prof. Armando Bazzani**
	Co-supervisore: **dott. Massimo Giovannozzi**

Esame finale anno 2023

What Mother Nature does is rigorous until proven otherwise; what humans and science do is flawed until proven otherwise.

N. N. Taleb, *Antifragile: Things That Gain from Disorder*.

Abstract

Understanding the complex dynamics of beam-halo formation and evolution in circular particle accelerators is crucial for the design of current and future rings, particularly those utilizing superconducting magnets such as the CERN Large Hadron Collider (LHC), its luminosity upgrade HL-LHC, and the proposed Future Circular Hadron Collider (FCC-hh). A recent diffusive framework, which describes the evolution of the beam distribution by means of a Fokker-Planck equation, with diffusion coefficient derived from the Nekhoroshev theorem, has been proposed to describe the long-term behaviour of beam dynamics and particle losses. In this thesis, we discuss the theoretical foundations of this framework, and propose the implementation of an original measurement protocol based on collimator scans in view of measuring the Nekhoroshev-like diffusive coefficient by means of beam loss data. The available LHC collimator scan data, unfortunately collected without the proposed measurement protocol, have been successfully analysed using the proposed framework. This approach is also applied to datasets from detailed measurements of the impact on the beam losses of so-called long-range beam-beam compensators also at the LHC. Furthermore, dynamic indicators have been studied as a tool for exploring the phase-space properties of realistic accelerator lattices in single-particle tracking simulations. By first examining the classification performance of known and new indicators in detecting the chaotic character of initial conditions for a modulated Hénon map and then applying this knowledge to study the properties of realistic accelerator lattices, we tried to identify a connection between the presence of chaotic regions in the phase space and Nekhoroshev-like diffusive behaviour, providing new tools to the accelerator physics community.

Contents

Introduction

The development and use of particle accelerators have been of paramount importance in making significant discoveries in fundamental particle physics. These large-scale devices, such as the Large Hadron Collider [1] at CERN, require extensive collaboration and expertise in various fields of physics and engineering. The success of these experiments is highly dependent on delivering high-quality beams at the collision points. This is where the field of accelerator physics comes into play, with a focus on understanding and improving the many aspects of particle motion inside the accelerator, overcoming the multiple challenges that arise from the complex nature of the dynamics of a high-energy particle beam in the accelerator's environment. The complexity of these challenges increases along with the requirements and goals for future accelerator machines, such as the planned LHC luminosity upgrade, HL-LHC [2, 3].

The physics concepts describing the dynamics of charged particles in circular accelerators are based on some building blocks, as the motion of particles in a circular storage ring or collider can be reduced to that of a charged relativistic particle under the influence of an electromagnetic field. As such, the dynamics of particles within accelerators falls within the realm of classical mechanics and can be understood and described in terms of Hamiltonian formulations of the dynamics and, in the context of single-particle tracking, through the use of symplectic maps.

However, in classical mechanics, when non-linear effects are introduced we observe the emergence of phenomena linked with concepts such as deterministic chaos, and resonances, which makes the overall system becoming extremely complex, with numerous problems that are still open, especially when it comes to determining the long-term evolution of these non-linear Hamiltonian systems. Research in these areas, which lie at the intersection of mathematics and physics, is ongoing and constantly evolving.

For modern circular particle accelerators, one open problem is understanding the complex dynamics of beam-halo formation and evolution, which is essential for optimal design and operation of a storage ring or collider. This is particularly important for colliders that use superconducting magnets, such as the LHC, its luminosity upgrade HL-LHC, and the proposed FCC-hh [4], as even tiny beam losses have a direct and major impact on accelerator performance.

The dynamics of the beam-halo is affected by a variety of factors, including unavoidable non-linear field errors in superconducting magnets, and ripples in their power converters. This in general can be precisely described using a

Hamiltonian approach, from which equations of motion can be derived. However, when time-dependent effects are present, a significant change in the nature of beam dynamics occurs. For example, modulations in the characteristic frequencies of the Hamiltonian system can result in extended weakly-chaotic layers in phase space [5]. In these regions, the orbit diffusion can be modelled as a stochastic process. The complexity increases when the periodic modulations themselves appear to be stochastic in nature, as they could involve the entire accessible phase space.

A recent framework has been proposed [6, 7], which describes the long-term behaviour of beam dynamics and particle losses in circular accelerators using a diffusive model. This framework uses a Fokker-Planck equation to describe the evolution of the beam distribution, with the diffusion coefficient being a key quantity for describing the beam dynamics. The use of diffusive models for transverse dynamics of charged particles in accelerator physics is not new, with a significant amount of literature available on the subject (see for example Refs. [8–20] and references therein). However, the model developed in this framework has a unique feature, which is the assumption that the functional form of the diffusion coefficient is derived from the optimal estimate of the perturbation series provided by the Nekhoroshev theorem [21–23].

The merit of having such a global diffusive framework is the possibility of extrapolating the long-term losses, the evolution of the beam emittance, and the evolution of the beam-tail population by using indirect measurements such as the beam loss signal. An increased understanding of each of these quantities would significantly help to improve the designs of current and future accelerator rings. Moreover, the knowledge of valid scaling laws for long-term extrapolation can also provide a great advantage in the context of numerical simulations and particle tracking, as realistic particle tracking simulations over the order of magnitude of a few hours of real beam time are currently not feasible.

In this thesis, we begin by providing a complete review of the diffusive framework. Then, the first original contribution is the derivation of an original measurement protocol, which is optimized for probing a Nekhoroshev-like diffusive coefficient from beam loss data. This protocol makes use of collimator scans, a technique that has been used extensively in the LHC to inspect both the beam tail population and to measure a diffusion coefficient, although a different diffusive framework was used for the latter.

The available LHC collimator scan data, which were gathered during a dedicated LHC Run 2 collimator scan measurement campaign, have been analysed in detail to extract information on the diffusive dynamics and to assess the validity of the proposed Fokker-Planck model with Nekhoroshev-like diffusion coefficient. The results of this analysis are presented and discussed in detail, since the data were taken with the aim of measuring a local diffusion coefficient, without making assumptions on the functional form of the global diffusion coefficient.

Then another original application of the diffusive framework is presented in the analysis of the loss signal measured during the testing and the application of beam-beam wire compensators on the LHC Beam 2 during a dedicated Run 2 measurement campaign. Wire compensators are a novel device that aims to counteract beam-beam effects in LHC, which are responsible for beam losses and beam-quality degradation. Analysis of the loss signal via our diffusive model aims to provide information on the long-term effects of wire compensators on both beam losses and emittance.

Finally, we investigated the use of dynamic indicators as a tool for studying the phase space properties of realistic accelerator lattices in single-particle tracking simulations. Dynamic indicators are mathematical tools that inspect the linear response of a dynamical system to small perturbations in either its initial conditions or along the orbit. They are used to probe the chaotic character of an orbit and to inspect the geometry of regular orbits.

Many typologies of dynamic indicators exist and are widely used mainly in celestial mechanics, which shares some of its Hamiltonian formulations with accelerator physics. Some of these indicators are also used in accelerator physics, such as the Fast Lyapunov Indicator [24, 25], and the Frequency Map Analysis [26, 27], while more recent ones, such as the Reversibility Error Method (REM) [28, 29] and the Generalized Alignment Index (GALI) [30, 31] are still not widely used in the field.

With the intent of also providing new valid tools to the accelerator physics community, we first inspect the classification performance of these indicators in detecting the chaotic character of orbits on a simple accelerator-like non-linear model, the modulated Hénon map. Next, we apply the knowledge achieved to study the phase-space properties of realistic accelerator lattices, with the main goal of identifying a connection between the presence of extended chaotic regions in the phase space and Nekhoroshev-like diffusive behaviour.

Structure of the work

The thesis is divided into three parts. In Part I, we provide a complete review of the diffusive framework, as well as the fundamental elements of classical mechanics, and accelerator physics, which are required for the rest of this thesis: in Chapter 1, we recall the fundamentals of Hamiltonian mechanics, along with the notions necessary to understand the Nekhoroshev theorem; in Chapter 2, we present the elements of stochastically perturbed Hamiltonian systems which ultimately lead to the formulation of the diffusive model under study;

finally, in Chapter 3, we focus on the elements of accelerator physics that are required to understand the context of this thesis.

In Part II, we begin with the original contributions of this thesis: in Chapter 4, we present the implementation of an optimized measurement protocol to detect a Nekhoroshev-like diffusive coefficient from beam loss data by collimator scans; in Chapter 5, we study the available LHC collimator scan data; finally, in Chapter 6, we present the analysis of the loss signal measured during the testing and application of beam-beam wire compensators at the LHC.

In Part III, we focus on the field of single-particle tracking simulations and the usage of a wide set of dynamic indicators: in Chapter 7, we present a comparative study based on the dynamics generated by the Hénon map, in which we determine the best performing indicators for an accelerator-like model with time-dependent modulation of linear frequencies. Finally, in Chapter 8, the results of the study are applied to an HL-LHC lattice, and we investigate the properties of the dynamics generated by the magnetic lattice by means of selected dynamic indicators.

Part I

Theoretical foundations

1 | Hamiltonian dynamics

In this chapter, we present a brief review of the fundamental concepts of Hamiltonian mechanics that are used throughout this thesis. Starting from the coordinate transformations, we then focus on the fundamental concepts of perturbation theory, such as the averaging principle.

Next, we present the KAM and Nekhoroshev theorems, two fundamental results of perturbation theory, which constitute the foundation of this thesis. These two theorems give important insights into the behaviour of an otherwise integrable Hamiltonian system under small perturbations, which is exactly the case in the study of the dynamics of a charged particle in the magnetic field of a circular accelerator.

Finally, we introduce the concept of a symplectic map, which is a mathematical object that at the heart of multiple applications in the field of accelerator physics such as the one-turn map, and we see how these two theorems can be applied to the study of symplectic maps.

1.1 | Generalities

We start by recalling some of the fundamental concepts of Hamiltonian dynamics. This will also define the core elements of nomenclature and notation that will be used throughout this thesis. This theoretical recall mainly follows Ref. [32].

Let $(\mathbf{q}(t), \mathbf{p}(t))$ be a set of coordinates in a $2n$ dimensional phase space, and let $\mathcal{H}(\mathbf{q}, \mathbf{p}, \ t)$ be a differentiable real function, a dynamical system is said to be *Hamiltonian* if the following equations hold:

$$\dot{q}_i = \frac{\partial \mathcal{H}}{\partial p_i} , \qquad \dot{p}_i = -\frac{\partial \mathcal{H}}{\partial q_i} i = 1, .., n. \tag{1.1}$$

These equations are called *Hamilton* or *canonical* equations with $\mathcal{H}$ being the *Hamiltonian* of the system under study. They are related to a geometrical Least Action Principle via the differential 1-form in the extended $2n+1$-dimensional phase space

$$\omega = p_i \mathrm{d}q_i - \mathcal{H} \mathrm{d}t \, . \tag{1.2}$$

In fact, if one considers the differential of the 1-form

$$\mathrm{d}\omega = \mathrm{d}p_i \wedge \mathrm{d}q_i - \frac{\partial \mathcal{H}}{\partial q_i} \mathrm{d}q_i \wedge \mathrm{d}t - \frac{\partial \mathcal{H}}{\partial p_i} \mathrm{d}p_i \wedge \mathrm{d}t \tag{1.3}$$

one defines the vortex lines as the curves in the extended phase space whose tangent is parallel to the null eigenvector of the 2-form $d\omega$. Then it is possible to prove that the vortex lines 1-form have a one-to-one projection on the time axis that corresponds to the orbits $\mathbf{q}(t)$, $\mathbf{p}(t)$ that solve the Hamilton equations,

1.1.1 | Canonical transformations

The advantage of having a Hamiltonian formulation of a system is the freedom to make a convenient coordinate choice in the phase space. For example, positions and momenta are independent and can be exchanged in role or mixed to achieve optimal formulations, which might highlight specific properties and invariants in the system, while the Hamiltonian equation maintains its form. Such changes in coordinates have, however, to maintain the canonical of the Hamiltonian equation defined in Eq. (3.9), also referred to as *symplectic conditions*.

Let us consider a Hamiltonian $\mathscr{H}(\mathbf{p}, \mathbf{q}, t)$, for which we wish to apply a coordinate transformation $(p_i, q_i) \longrightarrow (P_i, Q_i)$. To maintain the Hamiltonian properties, we then look for a new Hamiltonian $\mathscr{K}(\mathbf{P}, \mathbf{Q}, t)$ for which

$$\dot{P}_i = -\frac{\partial \mathscr{K}}{\partial Q_i}\,, \qquad \dot{Q}_i = \frac{\partial \mathscr{K}}{\partial P_i}\,. \tag{1.4}$$

Both Hamiltonian formulations need to leave invariant the structure of the differential form (1.3) to maintain the canonical form of the equation of motion:

$$d(p_i dq_i - \mathscr{H} dt) = d(P_i dQ_i - \mathscr{K} dt)\ , \tag{1.5}$$

which implies that the differential

$$dF = p_i dq_i - P_i dQ_i + (\mathscr{K} - \mathscr{H})dt\,, \tag{1.6}$$

must be exact. This provides the Hamiltonian transformation laws

$$p_i = \frac{\partial F}{\partial q_i}\,, \qquad P_i = -\frac{\partial F}{\partial Q_i}\,, \qquad \mathscr{K} = \mathscr{H} + \frac{\partial F}{\partial t}\,. \tag{1.7}$$

Note that the Hamiltonian function changes if the transformations are time-dependent. The function $F(\mathbf{q}, \mathbf{Q}, t)$ is called the *generating function* of the coordinate transformation.

In the Hamiltonian formulation, it is also possible to assign the role of time to another coordinate. We will see in Chapter 3 how this possibility enables the Courant-Snyder coordinate system, used in accelerator physics.

When a coordinate is used to parameterize the orbit, we see that the momentum conjugate to that coordinate, with a minus sign, becomes the new Hamiltonian function.

As an example, let us assign the role of time to the kth space coordinate q_k. Let us indicate the kth pair of coordinates as $p_k = \tilde{p}$, $q_k = \tilde{q}$. From this we can choose the formally equivalent form

$$p_i \mathrm{d}q_i - \mathscr{H}\mathrm{d}t = \sum_{i \neq k} p_i \mathrm{d}q_i + (-\mathscr{H})\mathrm{d}t + (-\tilde{p})\mathrm{d}\tilde{q}\,, \tag{1.8}$$

which highlights the new coordinate roles, as now it is possible to express the motion as a function of $\tilde{q}$, whilst $-\tilde{p}$ plays the role of the Hamiltonian. In this new form, the equivalent equations of motion become

$$\begin{aligned} \frac{\mathrm{d}p_i}{\mathrm{d}\tilde{q}} &= -\frac{\partial \tilde{p}}{\partial q_i}\,, & \frac{\mathrm{d}q_i}{\mathrm{d}\tilde{q}} &= \frac{\partial \tilde{p}}{\partial p_i} & (i \neq k)\,, \\ \frac{\mathrm{d}\mathscr{H}}{\mathrm{d}\tilde{q}} &= -\frac{\partial \tilde{p}}{\partial t}\,, & \frac{\mathrm{d}t}{\mathrm{d}\tilde{q}} &= \frac{\partial \tilde{p}}{\partial \mathscr{H}}\,. \end{aligned} \tag{1.9}$$

Finally, the phase flow of a Hamiltonian system is itself a group of canonical transformations as a consequence of the geometrical nature of the variational principle associated with the canonical equations. This property justifies the construction of *symplectic integrators*, i.e. algorithms for the numerical integration of Hamilton equations that preserve the Hamiltonian structure of the system.

1.1.2 | Action-angle variables

We consider a n degree-of-freedom integrable Hamiltonian system, which will have a $2n$ dimensional phase space with a symplectic manifold described by the phase variables (q_i, p_i), where n integrals of motion J_i in involution are known (i.e. if one considers J_i as Hamiltonian functions, the corresponding phase flows that solve the canonical equations, commute).

The Liouville theorem states that, if the surfaces M_k defined by $J_i = k_i$ are compact, then they are diffeomorphic to n tori $\mathbb{T}^n$, and it is possible to perform a canonical change of variables to the action-angle coordinates (ϕ_i, I_i) such that the action $I_i(\mathbf{J})$ are first integrals of motion and the angles ϕ_i evolve according to

$$\dot{\phi}_i = \omega_i(I_1 \ldots, I_n)\,, \tag{1.10}$$

where ω_i defines the *frequencies* of the motion.

This implies that if we set as Hamiltonian one of the integrals of the motion, for example $\mathcal{H} = J_1(\mathbf{I}$, we see that the new equations of motion read

$$\dot{I}_i = 0 , \qquad \dot{\phi}_i = \omega_i(I_1 \ \ldots , \ I_n) , \tag{1.11}$$

The actions I_i can be explicitly calculated. Let us start with the one-dimensional case, where the only integral of motion is the Hamiltonian $\mathcal{H}$ itself, and its conserved value h is the energy, and the set M_k reduces to M_h.

We can then define a canonical transformation starting from the generating function $S(\mathbf{I}, \mathbf{q})$, which yields

$$\mathbf{p} = \frac{\partial S}{\partial \mathbf{q}} , \qquad \boldsymbol{\phi} = \frac{\partial S}{\partial \mathbf{I}} , \qquad \mathcal{H}\left(\mathbf{p} = \frac{\partial S}{\partial \mathbf{q}}, \mathbf{q}\right) = h(\mathbf{I}) . \tag{1.12}$$

The invariant torus are the level closed curves identified by the value of the Hamiltonian $\mathcal{H} = h$ that depends on the action $\mathcal{H} = \mathcal{H}(I)$. On the energy level curves, the differential of the generating function dS reduces

$$\mathrm{d}S = \frac{\partial S}{\partial q}\, \mathrm{d}q = p \, \mathrm{d}q , \tag{1.13}$$

which implies

$$S(q, I) = \int_{M_h}^{q} p \, \mathrm{d}q , \tag{1.14}$$

The 1−form $p \, \mathrm{d}q$ is closed and therefore locally exact on invariant surfaces M_h. But if one performs a cycle with a level curve M_h, the S value changes according to

$$\Delta S(I) = \oint_{M_{h(I)}} \mathbf{p} \, \mathrm{d}\mathbf{q} . \tag{1.15}$$

Due to Stokes' theorem, this last integral corresponds to the area inside the curve. To define an angular variable ϕ by the second equation of (1.12), we require that

$$\oint_{M_{h(\mathbf{J})}} \mathrm{d}\boldsymbol{\phi} = 2\pi , \tag{1.16}$$

Then the periodicity of ϕ on the torus implies

$$\oint_{M_{h(I)}} \mathrm{d}\left(\frac{\partial S}{\partial I}\right) = \frac{\partial \Delta S(I)}{\partial I} = 2\pi , \tag{1.17}$$

from which we finally get the expression for the canonical action variable I

$$I = \frac{1}{2\pi} \oint_{M_h} p \, \mathrm{d}q \, . \tag{1.18}$$

On the other hand, differentiating (1.14) in $\mathbf{I}$ we obtain the following, from the definition of ϕ

$$\phi = \frac{1}{2\pi} \frac{\partial}{\partial I} \int p \, \mathrm{d}q \, . \tag{1.19}$$

Generalization to systems with many degrees of freedom requires one to prove that the differential form $\mathbf{pdq}$ is closed on the invariant surfaces and the construction n basic cycles $\gamma_1, \ldots, \gamma_n$ ID on the tori M_{k_i}. Then the variation of the angular variable ϕ_i, integrated along the cycle γ_j, is equal to $2\pi\delta_{ij}$, where δ_{ij} is the Kronecker symbol.

In such a scenario, the actions variables $\mathbf{I}_i$ then read as

$$\mathbf{I}_i(k_1, \ldots, k_n) = \frac{1}{2\pi} \int_{\gamma_i} \mathbf{p}_j \, \mathrm{d}\mathbf{q}_j \, . \tag{1.20}$$

It can be shown that these integrals are independent of the choice of γ_i. [32]

1.2 | Perturbation theory for Hamiltonian systems

Many physical systems can be modelled and described in terms of an ideal integrable Hamiltonian affected by small non-integrable perturbations. A common example is the problem of the motion of planets around the Sun, which can be treated as a perturbation of an ideal motion of non-interacting planets around a fixed attracting centre. Another relevant example, as we shall see in the next chapter, is how the motion of a charged particle inside a circular accelerator can be described as the perturbation of an otherwise ideal harmonic oscillator-like betatron motion around a reference orbit.

Understanding how these perturbations affect the properties of a Hamiltonian system is one of the main problems in dynamical systems, which was called by Poincaré *"fundamental problem of dynamics"*. Multiple approaches to this problem have been explored and grouped under the general topic of *perturbation theory*.

If the evolution timescale of the perturbation is much smaller than the timescale of the unperturbed system, a standard approach that is often proposed in perturbation theory is to *average* over time the perturbations, under the idea that dynamics can be separated into a slow-fast variables evolution.

This method is called *averaging principle*. We highlight this specific choice of words, as Arnold reminds us, it is “not a theorem, but a physical proposition, that is, a vaguely stated and, strictly speaking, false assertion”. However, “Such assertions often happen to be fruitful sources for mathematical theorems” [32].

Let us consider an integrable Hamiltonian system $\mathscr{H}_0$ with n degrees of freedom. This defines a foliation of a domain of its phase space into invariant tori, which defines the action-angle variables $\mathbf{I} = (I_1, \ldots, I_n)$, $\boldsymbol{\phi} = (\phi_1, \ldots, \phi_n)$.

The Hamiltonian $\mathscr{H}_0$ depends only on the action variables $\mathscr{H}_0 = \mathscr{H}_0(\mathbf{I})$. The equations of motion in the unperturbed case have the standard form:

$$\dot{\mathbf{I}} = 0\,, \qquad \dot{\boldsymbol{\phi}} = \frac{\partial \mathscr{H}_0}{\partial \mathbf{I}} = \boldsymbol{\omega}(I_1, \ldots, I_n)\,, \tag{1.21}$$

where $\boldsymbol{\omega}$ are the frequencies of motion. Let us now add a small Hamiltonian perturbation to $\mathscr{H}_0$, i.e. we consider $\mathscr{H}_1(\mathbf{I}, \boldsymbol{\phi}, \epsilon)$ of period 2π, with ϵ being a small parameter that represents the magnitude of the perturbation. The resulting perturbed Hamiltonian reads:

$$\mathscr{H} = \mathscr{H}_0 + \epsilon \mathscr{H}_1\,. \tag{1.22}$$

If $\mathscr{H}_0$ is integrable, we can write the equations of motion in terms of the action angle variables (I_j, ϕ_j):

$$\dot{I}_j = -\epsilon \frac{\partial \mathscr{H}_1}{\partial \phi_j}\,, \qquad \dot{\phi}_j = \omega_j + \epsilon \frac{\partial \mathscr{H}_1}{\partial I_j}\,. \tag{1.23}$$

The same notation can be used if the perturbation is also periodic in time with frequency ω_p, as one can extend the phase space to introduce one new degree of freedom: the angle $\psi = \omega_p t$ and the conjugated momentum I_ψ.

If we apply the concept of averaging principle to the perturbed Hamiltonian system, considering the angle fast variables and the action slow variables, we transform the perturbed system into a simpler one, where the fast periodic oscillations are averaged out. These oscillations are eventually treated as an extra drift element in the original unperturbed solution. We then define a new averaged Hamiltonian $\langle \mathscr{H} \rangle$ which reads

$$\langle \mathscr{H} \rangle (\mathbf{I}) = \mathscr{H}_0(\mathbf{I}) + \epsilon \left\langle \mathscr{H}_1(\mathbf{I}, \boldsymbol{\phi}) \right\rangle\,, \tag{1.24}$$

where we are considering the standard definition of integral average

$$\langle f \rangle = \frac{1}{(2\pi)^n} \oint_{\mathbb{T}^n} \mathrm{d}^n \boldsymbol{\phi}\, f(\mathbf{I}, \boldsymbol{\phi})\,. \tag{1.25}$$

To be able to correctly apply the averaging principle, it is fundamental that all the Fourier components of the perturbation have a fast variation. This condition requires that the frequencies ω_j are not under any resonant conditions.

That is, there must be no vector of frequencies $\omega_{1,\ldots,r}$ $(r \leq n)$ such that there exists a vector $k_j \in \mathbb{Z}^r$ for which $\sum k_j\omega_j \approx 0$.

When a non-resonant condition holds, it is possible to prove that the action variables I_j, can change by a quantity $\mathcal{O}(\epsilon)$ after a time interval $\mathcal{O}(\epsilon)$, When a resonant condition is satisfied, it is not possible to perform this kind of averaging since we have a slow dynamics also in the angular dependence, that may introduce significant effects of the perturbation on the action dynamics. This can be seen in a simple example $r = 2$, i.e. where, in an $n-$dimensional system, which has an $n-$size vector of frequencies $\boldsymbol{\omega}$, we consider ω_1 and ω_2 to be in resonant condition with integer numbers k_1 and k_2. If we consider the following linear symplectic transformation

$$\theta_1 = k_1\phi_1 + k_2\phi_2\,, \qquad \theta_j = \phi_j,\ \text{for } 3 \leq j \leq n\,, \tag{1.26}$$

which also implies the linear transformation of the momenta I_j into $\tilde{I}_j$ due to the symplectic conditions. We obtain the result that the new equation of motion for θ_1 is

$$\dot{\theta}_1 = k_1\omega_1 + k_2\omega_2 + \epsilon\frac{\partial\mathcal{H}_1}{\partial\tilde{I}_1} \approx \epsilon\frac{\partial\mathcal{H}_1}{\partial\tilde{I}_1} = \mathcal{O}(\epsilon)\,. \tag{1.27}$$

As θ_1 evolves as a slow variable, it does not meet the conditions to be averaged. All the other $n-2$ angles θ_j, however, do, as they exhibit an evolution $\mathcal{O}(1)$. This canonical transformation can be extended, and the resulting system will be a system with r slow evolving angles and $n-r$ fast angles.

1.3 | Kolmogorov-Arnold-Moser (KAM) theory

As stated in the previous section, the averaging principle is not a mathematically proven theorem that can be applied to every physical system. However, for the case of Hamiltonian systems, there are rigorous results that offer better insight into the effects of perturbations. One of the most important results is the theorem of Kolmogorov [33] for *non-degenerate* Hamiltonian systems, rigorously proven by Moser [34], then extended by Arnold [35] for *isoenergetically non-degenerate* ones, which proves the existence of invariant tori for a perturbed Hamiltonian system.

Let us consider a perturbed Hamiltonian system in the form of

$$\mathcal{H}(\mathbf{I}, \boldsymbol{\phi}, \epsilon) = \mathcal{H}_0(\mathbf{I}) + \epsilon\mathcal{H}_1(\mathbf{I}, \boldsymbol{\phi}, \epsilon)\,. \tag{1.28}$$

When considering the unperturbed Hamiltonian $\mathcal{H}_0$, we have that its phase space is foliated into invariant tori $\mathbf{I} = const.$ The tori with non-resonant frequencies have trajectories that fill them everywhere densely. On the contrary, the tori with resonant frequencies will be foliated into invariant tori of lower dimension.

The unperturbed system $\mathscr{H}_0$ is classified as *non-degenerate* if its frequencies are functionally independent, namely, if

$$\det\left(\frac{\partial\omega}{\partial\mathbf{I}}\right) = \det\left(\frac{\partial^2\mathscr{H}_0}{\partial\mathbf{I}^2}\right) \neq 0\,. \tag{1.29}$$

In such a nondegenerate system, the non-resonant tori form a set in the phase space of full measure. The resonant tori, instead, form a set of measure zero, which, however, is still dense in the phase space. Most importantly, we have the following application.

$$\begin{aligned} F : \mathbb{R}^n &\longrightarrow \mathbb{R}^n \\ (\mathbf{I}) &\longrightarrow (\boldsymbol{\omega}) \end{aligned} \tag{1.30}$$

is a diffeomorphism. This means that the invariant tori are equally well described by the action variables I or by their corresponding frequencies ω.

The unperturbed system $\mathscr{H}_0$ is classified as *isoenergetically non-degenerate* if the following condition holds:

$$\det\begin{pmatrix} \frac{\partial\omega}{\partial\mathbf{I}} & \omega_n \\ \omega_n & 0 \end{pmatrix} = \det\begin{pmatrix} \frac{\partial^2\mathscr{H}_0}{\partial\mathbf{I}^2} & \frac{\partial\mathscr{H}_0}{\partial I_n} \\ \frac{\partial\mathscr{H}_0}{\partial I_n} & 0 \end{pmatrix} \neq 0\,, \tag{1.31}$$

i.e., one of the frequencies does not vanish and the ratio of the other frequencies $n-1$ to it is functionally independent of the value of $\mathscr{H}_0$. Likewise to the non-degenerate condition, also this condition guarantees the existence on every energy level surface of a set of densely populated invariant tori, which will have full measure for non-resonant frequencies and zero measure for resonant frequencies. The non-degenerate and the isoenergetically non-degenerate conditions are independent.

Now that we have recalled these definitions, we can state the KAM theorem, which proves the existence of a large measure set of invariant tori for the perturbed $\mathscr{H}$ in the phase space:

Theorem 1 (KAM [33–35]). *If the unperturbed Hamiltonian system $\mathscr{H}_0$ is non-degenerate or isoenergetically non-degenerate, then, in the perturbed Hamiltonian system such as Eq.* (1.28)*, most of the non-resonant invariant tori do not disappear but are only slightly deformed. More specifically, there exist positive constants ϵ_0, a_1, a_2, and a_3, independent of ϵ, such that for any $\epsilon < \epsilon_0$ one can find:*

(a). a near to identity canonical transformation

$$\begin{aligned} \mathscr{C}_\epsilon : V' \times \mathbb{T}^n &\longrightarrow V \times \mathbb{T}^n \\ (\mathbf{I}', \boldsymbol{\phi}') &\longrightarrow (\mathbf{I}, \boldsymbol{\phi}) \end{aligned} \tag{1.32}$$

with $V' \subseteq \mathbb{R}^n$ *open;*

(b). *a set* $V_\epsilon \subseteq V'$*;*

(c). *a smooth function* $h'_\epsilon(\mathbf{I}', \boldsymbol{\phi}')$ *defined on* $V' \times \mathbb{T}^n$*;*

which satisfy

(i). $\mathrm{Vol}(V \backslash V_\epsilon) \leq a_1\sqrt{\epsilon}$*;*

(ii). $\|\mathbf{I} - \mathbf{I}'\| \leq a_2\sqrt{\epsilon}$*,* $\|\boldsymbol{\phi} - \boldsymbol{\phi}'\| \leq a_3\sqrt{\epsilon}$*;*

(iii). *whenever* $\mathbf{I}' \in V_\epsilon$ *the perturbed Hamiltonian field* $\mathcal{H}_\epsilon \circ \mathcal{C}_\epsilon(\mathbf{I}', \boldsymbol{\phi}')$ *admits an invariant torus.*

From this theorem, we can define a set $\mathcal{S}_\epsilon = \mathcal{C}_\epsilon(V_\epsilon \times \mathbb{T}^n) \subseteq V \times \mathbb{T}^n$ of large measure composed of invariant tori. This set is also referred to as the set of *KAM tori*. Within this set, due to *(ii)*, we have that any orbit $(\mathbf{I}(t), \boldsymbol{\phi}(t))$ having initial condition $(\mathbf{I}(0), \boldsymbol{\phi}(0)) \in \mathcal{S}_\epsilon$ satisfies the relation $\forall\ t$

$$\|\mathbf{I}(t) - \mathbf{I}(0)\| \leq 2a_2\sqrt{\epsilon}\,. \tag{1.33}$$

This set of invariant tori $\mathcal{S}_\epsilon$ is constructed as a complement of a neighbourhood of all the non-linear resonances regions in the phase space. Meaning, if we consider any vector $k \in \mathbb{Z}^n$ defining a resonance order, we have a resulting resonant manifold which reads

$$\mathcal{R}_k = \left\{\mathbf{I} \in V \,\middle|\, \sum_i k_i\omega_i(\mathbf{I}) = 0\right\}\,, \tag{1.34}$$

and we exclude a neighbourhood of $\mathcal{R}_k$ following a Diophantine law:

$$\left|\sum_i k_i\omega_i(\mathbf{I})\right| \leq \frac{\gamma_0\sqrt{\epsilon}}{|k|^\tau}\,, \tag{1.35}$$

where $\gamma_0 > 0$ is a suitable positive constant and $\tau > n - 1$. This excluded neighbourhood of resonances is referred to as *Arnol'd web*.

The proof of the KAM theorem is based on the possibility to define a converging procedure for consistently eliminating the fast phases of $\mathcal{H}$ in increasingly high orders in the small parameter. Such procedure has the property of quadratic convergence, as after m successive changes of variables, the phase-dependent discrepancy in the new Hamiltonian is of order ϵ^{2^m}.

At each step, the generating function is constructed on the sum of the Fourier harmonics of $\mathcal{H}_1$ whose order do not exceed an integer N. The integer

N is then chosen so that the absolute value of the remainder $R_{1N} = \mathcal{H}_1 - \mathcal{H}_{1N}$ of the Fourier series does not exceed ϵ. These progressive steps gradually lead to a superconvergence to the non-resonant KAM set.

The KAM theorem has important consequences for the analysis of stability of perturbed Hamiltonian systems. The most immediate one being the existence of large invariant compact regions for Hamiltonian systems, that implies the global stability of the orbits for systems with two degrees of freedom:

Theorem 2. *([33]) In an isoenergetically non-degenerate system with two degrees of freedom, all initial conditions will have their action variables remaining near their initial value.*

This theorem has immediate proof, as such a system has a four-dimensional phase space with three-dimensional energy levels which are highly populated by two-dimensional KAM tori. Since a two-dimensional torus has the topological property to divide a three-dimensional energy level, an orbit starting in a gap between two KAM tori will be forever trapped between those tori. Resulting action variable oscillations will not exceed the order of magnitude of $\sqrt{\epsilon}$, following the estimates given by KAM theorem.

When instead we are considering a system with more than two degrees of freedom, we have that the $n-$dimensional invariant tori do not separate a $(2n-1)$-dimensional energy-level manifold like points on a plane or lines in a space. Consequently, the gaps between tori, related by different resonance spaces, are all connected with each other. Therefore, the KAM Theorem does not prevent an orbit with initial condition near a resonance region to eventually evolve far away from its initial action value.

1.4 | Nekhoroshev theorem

As stated in the previous section, even though the stability set $\mathcal{S}_\epsilon$ has large relative measure, its complement can be open, dense, and if the number of degrees of freedom is larger than two, also connected, enabling the orbits' diffusion in the phase space.

Therefore, the possibility for solutions to wandering the complement of $\mathcal{S}_\epsilon$, such as the so called Arnol'd diffusion, can prevent any result of stability over an infinite time.

For this reason, it becomes difficult (if not impossible) to treat the problem of the orbit stability for infinite time in the case of a perturbed Hamiltonian system. But it is possible to operate with asymptotic estimates, which are limited to very long times[1]. We look for estimates in the following form:

$$\|\mathbf{I}(t) - \mathbf{I}(0)\| \le r(\epsilon) \tag{1.36}$$

which are valid for times $|t| \le T(\epsilon)$ such that $r \to 0$ and $T \to \infty$ in the limit $\epsilon \to 0$.

In the case $\mathcal{H}$ satisfies a technical property called *steepness*[2], a very important result on the estimate of diffusion scale times holds. An analytic function is said to be *steep* if it has no stationary points and its restriction to any plane of any dimension has only isolated stationary points.

Such result is stated by Nekhoroshev in his celebrated theorem, named after him:

Theorem 3 (Nekhoroshev's theorem [21]). *Let us consider a perturbed Hamiltonian system in the form of Eq* (1.28)*. If the unperturbed Hamiltonian $\mathcal{H}_0$ is steep, there exist positive constants ϵ_0, a, b, t_0, r such that for any $\epsilon < \epsilon_0$, and for any motion* $(\mathbf{I}(t), \boldsymbol{\phi}(t))$ *with* $(\mathbf{I}(0), \boldsymbol{\phi}(0)) \in V \times \mathbb{T}^n$ *it is*

$$\|\mathbf{I}(t) - \mathbf{I}(0)\| \le r\epsilon^a \,, \tag{1.37}$$

for any time t satisfying:

$$0 \le t \le t_0 \exp\left(\frac{\epsilon_0}{\epsilon}\right)^b \,, \tag{1.38}$$

where the value of the constants a, b depend on the steepness properties of $\mathcal{H}_0$.

A complete overview of the theorem's proof is presented in [38], the outline of it is that the long-term behaviour of the orbits can be studied removing from $\mathcal{H}$ only a finite number of harmonics in an open subset of the phase space $\epsilon\mathcal{H}_{1k}(\mathbf{I})e^{ik\cdot\boldsymbol{\phi}}$, precisely those with order $|k| = \sum_{i=1}^{n} |k_i|$ up to a given threshold K. The harmonics with $|k| \ge K$ can then be estimated to be exponentially small. As a consequence, if K is suitably large, these terms turn out to be very small, and they can determine large deviations of the actions only after long exponential times.

1.5 | Symplectic maps

A $2n \times 2n$ matrix A is defined as symplectic if it satisfies the equation

$$\mathrm{A}\mathrm{J}\mathrm{A}^t = \mathrm{J} \,, \tag{1.39}$$

---

[1] For example, in the case of hadron colliders orders of magnitudes higher than the usual operation time.

[2] The notion of steepness was introduced by Nekhoroshev in [36]. The definition we report here is a necessary and sufficient condition for steepness [37].

where A^t denotes the transposed matrix and J is a block matrix defined according to

$$J = \begin{pmatrix} 0 & I_n \\ -I_n & 0 \end{pmatrix}, \tag{1.40}$$

where I_n is the $n \times n$ identity matrix.

A map $M : \mathbb{R}^{2n} \to \mathbb{R}^{2n}$ is said to be a *symplectic map* if its Jacobian matrix DM, whose elements $DM_{i,j}$ are given by

$$DM_{i,j}(\mathbf{x}) \equiv \frac{\partial M_i}{\partial x_j}(\mathbf{x}), \tag{1.41}$$

is a symplectic matrix for every $\mathbf{x}$, meaning

$$DM(\mathbf{x}) J DM^t(\mathbf{x}) = J. \tag{1.42}$$

The symplectic condition for a map characterizes the canonical transformations of the phase space and the phase flows of Hamiltonian systems. In the case of a 2-dimensional map it reduces to the area-preserving condition.

An example of symplectic map is defined by the Poincaré map of a Hamiltonian phase flow on a section of the phase space or by the one period evolution map in case of periodic Hamiltonian systems. A simple conceptual scheme of a Poincaré section is shown in Fig. 1.1. For a time-dependent Hamiltonian $\mathcal{H}(\mathbf{x}, t)$, with period T ($\mathcal{H}(\mathbf{x}, t = T) = \mathcal{H}(\mathbf{x}, t = 0)$), one can define a symplectic map M as the one period map which will represent the evolution of an initial condition $\mathbf{x}(0)$ to $\mathbf{x}(T)$.

1.5.1 | Poincaré-Birkhoff theorem

After we have seen the most important theorems on how small perturbations can affect the dynamics of a Hamiltonian system, we are interested to discuss some specific results for the dynamics described by an area-preserving map.

The first important theorem we will present is the Poincaré-Birkhoff theorem [39]. This theorem shows how the interplay between the perturbation and the natural resonances present in the map leads to the creation of new structures in the phase space, also referred to as *resonant islands*.

Let us consider an area-preserving map T_k ($k \in \mathbb{Z}$). If the system described by T_k is integrable, we can define action-angle coordinates ($\boldsymbol{\phi}$, $\mathbf{I}$) where, for every I, an invariant curve Γ_I is defined, along which, at each turn, ϕ increases by an angle $\omega(I)$. The map T_j therefore will read as a *twist map*:

$$\begin{pmatrix} \phi^{(k+1)} \\ I^{(k+1)} \end{pmatrix} = \begin{pmatrix} \phi^{(k)} + \omega_j \left(I^{(k)} \right) \\ I^{(k)} \end{pmatrix}. \tag{1.43}$$

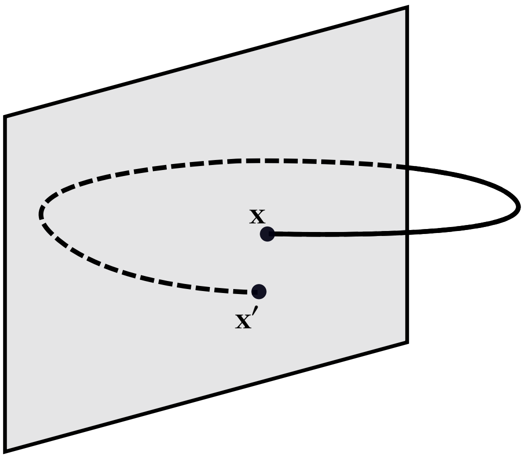

Figure 1.1: Simple sketch of the concept behind a Poincaré section of a symplectic evolution.

Since the frequency is a generic function of the action I, we have that some initial conditions $\mathbf{x}(\phi, I)$ will have a resonant frequency $\omega(I)/(2\pi) \in \mathbb{Q}$, i.e. a frequency $n\omega(I) = 2\pi\ell$. For these resonant frequencies, we have that the $n-$th iteration of the map T^n will map a point into itself, and that the resulting orbit given by $\mathrm{T}^k\mathbf{x}_0$ will be a finite set of n points. For non-resonant frequencies, i.e. $\omega(I)/(2\pi) \in \mathbb{R} \setminus \mathbb{Q}$, the orbit given by $\mathrm{T}^k\mathbf{x}_0$ is dense on the invariant curve Γ_I.

Now let us introduce a perturbation of the map $\mathrm{T}_{k,\epsilon} = \mathrm{T}_k + \epsilon\mathrm{T}_k^{(1)}$, the resulting perturbed map $\mathrm{T}_{j,\epsilon}$ will now read

$$\begin{pmatrix} \phi^{(k+1)} \\ I^{(k+1)} \end{pmatrix} = \begin{pmatrix} \phi^{(k)} + \omega_j \left(I^{(k)}\right) + \epsilon f(I^{(k)}, \phi^{(k)}) \\ I^{(k)} + \epsilon g(I^{(k)}, \phi^{(k)}) \end{pmatrix}, \tag{1.44}$$

with f, g regular on their domains. The Poincaré-Birkhoff theorem states that if and $d\omega/dI \neq 0$, the unperturbed resonant invariant curves Γ_I, with $n\omega(I) = 2\pi\ell$, will be not preserved by the perturbation. However, the perturbed map T_ϵ^n will have a chain of $2n$ fixed points close to Γ_I, half of them are elliptic, and half of them hyperbolic. Near the elliptic fixed point there exist new invariant curves that corresponds to the KAM tori with non-resonant secondary frequencies, whereas the separatrix curves connecting the hyperbolic points creates a chaotic layer.

The sketch of the proof is based on the fact that the derivative of the function $\omega(I)$ is not vanishing. If the invariant curve Γ_I, have a resonant frequency $\omega(I^*)$ of order n, each point of the curve is a fixed point for the map T^n. This implies that there exist also the curves Γ_+, where $I_+ > I^*$, and Γ_-, where $I_- < I^*$,

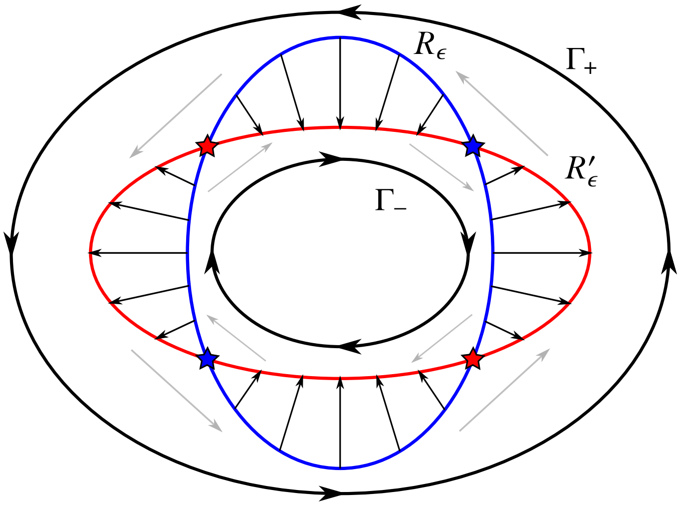

FIGURE 1.2: Schematic picture of the concept behind the Poincaré-Birkhoff theorem proof. The invariant curves Γ_- and Γ_+ are characterized by rotation frequencies different in sign under the perturbed map T^n_ϵ. The curve R_ϵ is made of points with no rotation, and it is mapped into R'_ϵ by the map. As the map is area-preserving, we observe an even number of intersections between R_ϵ and R'_ϵ, which correspond to the fixed points given by the theorem. These fixed points can be distinguished between elliptic and hyperbolic by inspecting the direction of the arrows in the pictures, which ultimately represents the dynamic flow near them. Elliptic points (blue stars) have arrows rotating around them, hyperbolic points (red stars) have arrows pointing away from them.

on which ϕ rotates with opposite direction. We can assume, without loss of generality, that $n\omega(I_-) < n\omega(I^*) < n\omega(I_+)$ and, therefore, $\omega(I_-) < 0$ and $\omega(I_+) > 0$.

This fact holds also for the perturbed map T_ϵ. Due to the regularity of f and g, we know that for each angle ϕ there exists a value of the action I_ϕ, for which T^n_ϵ has zero phase advance. The set of all pairs (ϕ, I_ϕ) describes a closed curve that we name R_ϵ, which will describe a full radial variation under the action of T^n_ϵ. This curve R_ϵ will be close to the unperturbed invariant curve Γ_I. Let us now define as R'_ϵ the resulting curve after having applied T^n_ϵ at each point of R_ϵ, as stated before, the difference will be a variation in radius. As the map is area-preserving, the area enclosed by the evolved curve R'_ϵ cannot be greater or smaller than the area enclosed by the starting curve R_ϵ. Therefore, it is impossible that one of the two curves surrounds the other, and they must intersect in an even number of points, and the points of intersection are fixed points of T^n_ϵ. A schematic picture of this scenario is given in Fig. 1.2.

To determine the nature of these fixed points, that is, to assess whether they are stable elliptic points or unstable hyperbolic points, we have to consider the flow of T^n in the neighbourhood of Γ^+ and Γ^- and look at how it connects to the dynamics of the orbits given by $R_\epsilon \to T^n R_\epsilon$.

If we inspect the arrows represented in Fig. 1.2, we can distinguish two different scenarios at the intersections. When the arrows move around the fixed point, it is an elliptic fixed point. When the arrows move *away* from the fixed point, the dynamic is hyperbolic. It follows that these $2n$ fixed points will be an alternation of n elliptic fixed points of period n, with n hyperbolic fixed points of the same period. This pattern of fixed points gives the origin to the Poincaré-Birkhoff islands.

1.5.2 | KAM and Nekhoroshev theorems for symplectic maps

The Poincaré-Birkhoff theorem suggests that the effect of a small perturbation on an integrable symplectic map preserve the non-resonant invariant curves according to the KAM theorem. A more precise statement is obtained by extending the KAM theorem to symplectic maps.

Likewise, also the results presented in the Nekhoroshev theorem can be extended to symplectic maps. However, for both theorems, the final statements are not necessary identical to the Hamiltonian version (see [40] and references therein).

Theorem 4 (KAM, area-preserving maps). *Let us consider a perturbed symplectic map like the one in Eq.* (1.44)*, where f and g are analytic on their domains, and let $\boldsymbol{\omega}$ be a frequency vector that follows a Diophantine law like the one presented in Eq.* (1.35)*. Then, an invariant orbit with frequency vector $\boldsymbol{\omega}$ in the unperturbed system is mapped into a closed orbit of the perturbed system for ϵ sufficiently small. Moreover, the measure of the closed orbits in a polydisc $\|\mathbf{I}\| \ll R$ approaches the measure of the disc itself as $\epsilon \to 0$.*

The theorem is very similar to Theorem 1: for symplectic maps we have that the KAM theorem guarantees stability of motion only for maps up to 2D, where a 1D invariant curve constitutes a topological barrier to the motion. For higher dimensions, the existence of invariant tori does not constitute such a barrier. For example, in a 4D map, a KAM tori will be a 2D tori (i.e. the direct product of two circles), which does not constitute a topological barrier as its complement is a connected set of dimension two.

A more broad stability result is obtained by generalizing the Nekhoroshev theorem for Hamiltonian flows to symplectic maps [22, 23].

Theorem 5 (Nekhoroshev, symplectic maps). *Let us consider a symplectic map in a phase space of dimension $2n$, with $n \geq 2$, analytic in a polydisc of unit radius, having* *the origin as an elliptic fixed point. If the frequency vector* ω *satisfies the Diophantine condition, then any orbit with initial point in a polydisc of radius* $I/2$ *will remain in a polydisc of radius* I *for a time* $t \leq T$*, with*

$$T = T_0 \exp \left[\left(\frac{I_*}{I} \right)^{1/2\kappa} \right] , \qquad (1.45)$$

with the constants κ*,* T_0*, and* I_* *depending on the Diophantine condition and the Fourier components of the perturbation.*

The estimate (1.45) can be also related to the optimal estimate in the order of the asymptotic perturbative expansion that reduces the perturbed map to an integrable form. In the next chapter, we will also see what is the logical flow which suggests the usage of the form $1/(2\kappa)$ for the exponent within the exponential term.

2 | Stochastic Hamiltonian systems

After having introduced the basic concepts of the theory of stochastic Hamiltonian systems in Chapter 1, we now turn to the study of the diffusive properties of these systems. These properties are related to the introduction of a stochastic perturbation in the Hamiltonian describing the system under consideration. The framework we review here for the application of the averaging principle on stochastic Hamiltonian systems follows the line of work presented in [6, 7, 41].

The chapter is structured as follows. We will first present the fundamental concepts of stochastic processes in Section 2.1, in which we will define the notation used and show some simple models of stochastic-induced diffusion over toroidal surfaces and integrable Hamiltonian systems. Next, we will focus in Section 2.2 on the application of the averaging principle to stochastic Hamiltonian systems, and show how it is possible to reach an expression of the diffusion process in terms of a Fokker-Planck equation. Finally, in Section 2.3, we will show how the diffusion coefficient $D(I)$ has a functional form related to the stability time estimate of the Nekhoroshev theorem.

2.1 | Stochastic perturbations

2.1.1 | Notation for stochastic processes

Let us start by defining the following notation: If $\xi(s)$ is a regular stationary stochastic Gaussian process, we set

$$w(t) = \int_0^t \xi(s)\,\mathrm{d}s\,, \qquad w_1(t) = \int_0^t w(t)\,\mathrm{d}s\,, \tag{2.1}$$

If the realizations $\xi(t)$ are continuous, with a correlation function

$$\langle \xi(t)\xi(t+\tau)\rangle = \Omega(\gamma\tau)\,, \qquad \Omega(\gamma\tau) \simeq \frac{\gamma}{2} e^{-\gamma|\tau|}\,. \tag{2.2}$$

the limit $\gamma \longrightarrow \infty$ is the white noise limit where the process $\xi(t)$ loses its regularity. The correlation (2.2) is generic in many physical systems, since it is satisfied by Markov processes and strongly chaotic systems, and the white noise limit $\gamma \longrightarrow \infty$ allows one to approximate the physical orbits with the solution of a stochastic differential equation even if the white noise is not a regular function. Then $w(t)$ is the Wiener process. We can write $w_1(t)$ in the form

$$w_1(t) = \int_0^t \int_0^s \xi(u)\,\mathrm{d}u\,\mathrm{d}s' = \int_0^t \xi(u) \int_u^s \mathrm{d}s'\,\mathrm{d}u = \int_0^t (s'-u)\xi(u)\,\mathrm{d}u\,. \tag{2.3}$$

This form is convenient if we want to present the processes $w(t)$ and $w_1(s)$ in the standard form

$$\int_0^t K(t,s)\xi(s)\,\mathrm{d}s \tag{2.4}$$

where $K(t,s)$ is called the *kernel* of the noise. We have that $K = 1$ for $w(t)$ and $K = t-s$ for $w_1(t)$. This implies that the variance is $\sigma^2(t) = t$ for Wiener noise $w(t)$ while for its integral $w_1(t)$, we have

$$\sigma^2(t) = \int_0^t (t-u)^2\,\mathrm{d}u = \frac{t^3}{3}\,. \tag{2.5}$$

If instead we are considering a noise characterized by a specific spectrum, also referred to as coloured noise, we can consider its Fourier expansion, which reads

$$\xi(t) = \int_\omega \hat{\xi}(\omega)e^{i\omega t}\,\mathrm{d}\omega \tag{2.6}$$

where here the random variables $\hat{\xi}(\omega)$ are such that

$$\left\langle \hat{\xi}(\omega) \right\rangle = 0 \quad \left\langle \hat{\xi}(\omega)\hat{\xi}'(\omega') \right\rangle = F(\omega)\delta(\omega-\omega') \tag{2.7}$$

where $\hat{\xi}'(\omega')$ comes from the Fourier expansion of $\xi(t+\tau)$ and $F(\omega)$ is called *power spectrum* of the noise. The following relation holds

$$\langle \xi(t+\tau)\xi(t)\rangle = \int_\omega\int_{\omega'} \left\langle \hat{\xi}(\omega)\overline{\hat{\xi}}\,(\omega') \right\rangle e^{i(\omega-\omega')t+i\omega\tau}\,\mathrm{d}\omega\,\mathrm{d}\omega' = \int_\omega F(\omega)e^{i\omega\tau}\,\mathrm{d}\omega\,, \tag{2.8}$$

i.e. the correlation function is the Fourier transform of the power spectrum $F(\omega)$.

2.1.2 | Simple diffusion models

Diffusion over a toroidal surface

We start by investigating the fast diffusion process of a probability distribution on a toroidal surface. We are interested in this process as such a situation occurs in action-angle Hamiltonian systems for the angle variable.

Let us consider a simple example of angular diffusion. Let x be an angular variable defined over the interval $[0,1]$. We consider the stochastic Hamiltonian dynamics

$$\begin{aligned} \dot{\phi} &= \omega + I \quad \mod 1\,, \\ \dot{I} &= \epsilon\xi(t)\,. \end{aligned} \tag{2.9}$$

The distribution function $\rho_T(\hat{x}, t)$ for the angular variables$\hat{\phi}$ can be defined using the solution $\rho(\hat{x}, t)$ with open boundary conditions on $\mathbb{R}$ using

$$\rho_T(x, t) = \sum_{k=-\infty}^{+\infty} \rho(x + k, t) \quad x \in [0, 1]\,, \quad k = 0, \pm 1, \pm 2, \ldots\,. \tag{2.10}$$

In the white noise limit, the solution of (2.9) on $\mathbb{R}$ is given by

$$y = y_0 + \epsilon w(t)\,, \qquad x = x_0 + (\omega + \epsilon y_0)t + \epsilon w_1(t)\,, \tag{2.11}$$

by writing the evolution of the average value of $x(t)$ in the form $\langle x(t) \rangle = x_0 + (\omega + \epsilon y_0)t$, $x(t)$ is a Gaussian process and the probability density in $\mathbb{R}$ reads

$$\rho(x, t) = \frac{\exp\left\{\frac{-(x - \langle x(t) \rangle)^2}{2\sigma^2(t)}\right\}}{\sqrt{2\pi\sigma^2}}\,, \qquad \sigma^2(t) = \epsilon^2 \frac{t^3}{3}\,, \tag{2.12}$$

we can then apply (2.10) and finally obtain

$$\rho_T(x, t) = \sum_{n=-\infty}^{+\infty} \frac{\exp\left\{\frac{-(x - \langle x(t) \rangle + n)^2}{2\sigma^2}\right\}}{\sqrt{2\pi\sigma^2}} \qquad n = 0, \pm 1, \pm 2, \ldots\,. \tag{2.13}$$

If we represent the solution in the form of a Fourier series,

$$\rho_T(x, t) = \sum_{k=-\infty}^{+\infty} f_k(t) e^{2\pi i k x}\,, \tag{2.14}$$

the f_k coefficients are given by

$$f_k = \int_0^1 e^{-2\pi i k x} \rho_T(x, t)\, \mathrm{d}x \tag{2.15}$$

$$= \sum_{n=-\infty}^{+\infty} \frac{1}{\sqrt{2\pi\sigma^2}} \int_0^1 \exp\left\{\frac{-(x - \langle x(t) \rangle + n)^2}{2\sigma^2} - 2\pi i k x\right\} \mathrm{d}x\,. \tag{2.16}$$

By assuming real f_k coefficients, we obtain

$$\rho_T(x, t) = 1 + 2 \sum_{k=1}^{\infty} e^{-2\pi^2\sigma^2 k^2} f_k \cos(2\pi k(x - \langle x(t) \rangle))\,. \tag{2.17}$$

The most important aspect of this example, is how ρ_T relaxes to the uniform distribution $\propto e^{-\sigma^2(t)}$, and the relaxation timescale can be estimated by

$$\sigma^2 \propto \epsilon^2 t^3 \simeq 1\,, \tag{2.18}$$

so that $t \simeq \epsilon^{-2/3}$, while for the Wiener process $y(t)$ the diffusion timescale is $t \simeq \epsilon^{-2}$ since

$$\sigma^2 \propto t\,. \tag{2.19}$$

Application to an integrable Hamiltonian system

We now consider the simplest stochastic perturbed Hamiltonian system and observe how the perturbation causes a fast diffusion on the angular variable. Some of the methods used here will be used similarly for the more generic scenario. Let us consider the following stochastic perturbed Hamiltonian

$$\mathcal{H} = \mathcal{H}_0(I) - \epsilon \phi \xi(t) \,. \tag{2.20}$$

From this Hamiltonian, we have the equations of motion

$$\begin{aligned} I' &= \epsilon \xi \,, \\ \phi' &= \omega(I) \,, \end{aligned} \tag{2.21}$$

from which follows immediately

$$I = I_0 + \epsilon w(t) \,. \tag{2.22}$$

Therefore, the action is a Gaussian process with average value I_0 and variance

$$\sigma_I^2 = \epsilon^2 t \,. \tag{2.23}$$

In a perturbation approach $\epsilon \ll 1$ we study the evolution of the system over time $t \ll \epsilon^{-2}$. Then in the Taylor expansion for ϕ', we obtain

$$\phi' = \omega(I_0) + \omega'(I_0)\epsilon w(t) + \mathcal{O}(\epsilon^2) \,, \tag{2.24}$$

the contribution of the term $\mathcal{O}(\epsilon^2)$ can be neglected at this timescale. A direct integration leads to

$$\phi = \phi_0 + \omega(I_0)t + \epsilon \omega'(I_0) w_1(t) \,, \tag{2.25}$$

so that the relaxation timescale of the angle variable is estimated by

$$\sigma_\phi^2 \propto \epsilon^2 t_\phi^3 \simeq 1 \tag{2.26}$$

i.e. $t_\phi \simeq \epsilon^{-2/3}$. The perturbation approach is justified if one chooses $t \simeq t_\phi$ since $t\epsilon^2 \simeq \epsilon^{4/3} \ll 1$. It follows that the angle variable can be considered a fast variable in the diffusion process, whereas the action is a slow variable.

2.2 | Averaging principle for stochastic Hamiltonians

We now present an extension of the averaging principle to the case of generic stochastic perturbed Hamiltonian system in the action-angle variables in the presence of weak chaotic dynamics in the phase space.

As the perturbation causes the breakdown of the KAM tori in certain regions of the phase-space, we observe an overlapping of a regular dynamics and a random dynamics characterized by a small Lyapunov exponent (i.e. a small chaotic character), depending on the initial condition. We set as working hypotheses that it is possible to achieve a phenomenological description of the dynamics of the system by means of a stochastic perturbed Hamiltonian description in the form of

$$\mathcal{H}_0(I) + \xi(t)\mathcal{H}_1(\phi, I)\,, \tag{2.27}$$

where (ϕ, I) are the action-angle variables and the noise realization also depends on the orbit initial condition. The use of these models is due to their ability to capture the impact of combining an integrable Hamiltonian with a chaotic Hamiltonian environment that causes variations in the phase space. Additionally, they can simulate the effects of weak layers of chaos in the phase space that lead to pseudo-random disruptions in the evolution of the action variables. In order to keep the symplectic nature of the dynamics intact, we take into account regular (i.e., coloured) stationary noise.

Each orbit is the result of a superposition of a regular dynamic and small variations due to random disturbances in the phase space. The perturbation $\mathcal{H}_1(\phi, I)$ represents the intensity of the variations, while the "noise" $\xi(t)$ takes into account the correlation properties of the fluctuations: the noise instances $\xi(t)$ are based on a probability space, which can encompass hidden degrees of freedom and the correlation of the associated stochastic process, linked to the chaotic nature of the dynamics.

In the case of a weak chaotic region, instances depend on the initial condition, and the system (2.27) is an effective representation of the dynamics. Of course, the measure of the chaotic region should be large to avoid the dynamical traps of Hamiltonian systems, which are caused by the stickiness of trajectories to certain specific domains in phase space. In the case of weak chaos, the white noise approximation cannot be applied directly to the process $\xi(t)$, but one can assume that $\|\mathcal{H}_1\| \ll 1$, where $\|\ \|$ is the L^2 norm, so that it is possible to introduce a slow diffusion time $\tau \propto \|\mathcal{H}_1\|^2 t$ for the action variable at which the white noise approximation is valid.

Specifically, the "noise" depends on the angle variables that can be regarded as a fast variable, which are independent on a timescale much shorter than the diffusion timescale. To achieve this, let us consider the slow variables

$$\theta = \phi - \Omega(I)t\,, \tag{2.28}$$

where $\Omega(I) = \partial\mathcal{H}_0/\partial I$, which we use to define the new Hamiltonian

$$\xi(t)\mathcal{H}_1\left(\theta + \Omega(I)t, I\right)\ . \tag{2.29}$$

To reach an approximate solution of the stochastic dynamics of (2.27), we consider the evolution of angle-action variables (θ, I) for a time T, which gives us the following map expression:

$$\begin{aligned}\Delta\theta_j &= \int_0^T \frac{\partial\mathcal{H}_1}{\partial I_j}\left(\theta + \Omega(I)t, I\right)\xi(t)\,\mathrm{d}t - \int_0^T t\frac{\partial\mathcal{H}_1}{\partial\phi_k}\left(\theta + \Omega(I)t, I\right)\frac{\partial\Omega_k}{\partial\partial I_j}\xi(t)\,\mathrm{d}t\\ \Delta I_j &= -\int_0^T \frac{\partial\mathcal{H}_1}{\partial\phi_j}\left(\theta + \Omega(I)t, I\right)\xi(t)\,\mathrm{d}t\end{aligned} \tag{2.30}$$

where $\Delta\theta = \theta(T) - \theta(0)$ and $\Delta I = I(T) - I(0)$.

The time interval T should be long enough to consider the noises $\xi(t)$ and $\xi(t+T)$ independent, but should be short in comparison to the evolution time of the action and the slow phase. We can observe the distinct nature of the fluctuations in the action I and the angle θ due to the presence of the slow evolving term $\propto t\frac{\partial\Omega}{\partial I}$, which results in an increase in sensitivity to the fluctuations of the process $\xi(t)$ during the time interval T. The stationary solution for the angle distribution is a uniform distribution, however, if $\Delta\theta$ is small during a time interval T, the existence of resonances $k\Omega(I) = 0$ does not allow for averaging the angles in the action dynamics.

Let us now estimate the variance of angle variables using the dominant term for an evolution time T_θ under the assumption that the action variables can be considered constant during such a time interval. We obtain the following

$$\begin{aligned}\mathrm{Var}(\Delta\theta)_{ij} \propto \int_0^{T_\phi}\int_0^{T_\phi} \frac{\partial\mathcal{H}_1}{\partial\phi_k}\left(\theta + \Omega(I)t, I\right)\frac{\partial\mathcal{H}_1}{\partial\phi_m}\left(\theta + \Omega(I)s, I\right)\times&\\ \times\frac{\partial\Omega_m}{\partial I_i}\frac{\partial\Omega_k}{\partial I_j}ts\Phi(t-s)\,\mathrm{d}t\,\mathrm{d}s\,,&\end{aligned} \tag{2.31}$$

which leads to the following estimate:

$$\|\mathrm{Var}(\Delta\theta)\| \propto \left\|\left(\frac{\partial\Omega}{\partial I}\right)^2\right\|\left(\|\mathcal{H}_1\|^2\right)\frac{T_\theta^3}{2}\,, \tag{2.32}$$

where T_θ is the relaxation timescale. To get a consistent expression for T_θ, let us consider

$$\mathcal{H}_1(\phi, I) = \epsilon\hat{\mathcal{H}}_1(\phi, I)\,, \tag{2.33}$$

where $\|\hat{\mathcal{H}}_1\| = \mathcal{O}(1)$. The relaxation timescale for the slow angle variables can be approximated as $\epsilon^{-2/3}$. Once this time has passed, it can be assumed that the angles are distributed uniformly. It is important to note that this estimate is based on the assumption that

$$\frac{\partial\Omega}{\partial I} = \mathcal{O}(1)\,, \tag{2.34}$$

so that the evolution of the action dynamics does not alter the distribution of angles; that is, the uniform distribution must remain unchanged as the actions evolve. When considering an almost isochronous system, that is

$$\frac{\partial\Omega}{\partial I} = \mathcal{O}(\epsilon)\,, \tag{2.35}$$

the previous estimate gives a relaxation timescale $T_\phi \simeq \epsilon^{-4/3}$.

Let us now consider for such a system a time interval T for its evolution, such that both the actions and the slow angles evolve; we have the following

$$\begin{aligned}\Delta I_j = &-\int_0^T \frac{\partial\mathcal{H}_1}{\partial\phi_j}\xi(s)\,\mathrm{d}s + \int_0^T\int_0^t \frac{\partial^2\mathcal{H}_1}{\partial I_k\partial\phi_j}\frac{\partial\mathcal{H}_1}{\partial\phi_k}\xi(t)\xi(s)\,\mathrm{d}s\,\mathrm{d}t\\ &-\int_0^T\int_0^t \frac{\partial^2\mathcal{H}_1}{\partial\phi_k\partial\phi_j}\left[\frac{\partial\mathcal{H}_1}{\partial I_k} - \frac{\partial\Omega}{\partial I_k}\frac{\partial\mathcal{H}_1}{\partial\phi_k}t\right]\xi(t)\xi(s)\,\mathrm{d}s\,\mathrm{d}t\,,\end{aligned} \tag{2.36}$$

where we are implying $H_1(\phi+\Omega(I)t, I)$, and we are neglecting terms of order $\mathcal{O}(\epsilon^2)$.

Let us now consider the following notation for the Fourier expansion of $\mathcal{H}_1$:

$$\mathcal{H}_1(\phi+\Omega(I)t, I) = \sum_k h_k(I)\exp\left[ik(\phi+\Omega(I)t)\right]\,. \tag{2.37}$$

We can explicitly compute the variance of the fluctuating terms $D(I,\theta)$ in terms of the Fourier expansion, which then reads

$$\begin{aligned}D(I,\theta) &= \sum_k\int_\omega\int_0^T ik_jh_k(I)\exp(ik(\theta+\Omega(I))s+\omega s)\hat{\xi}(\omega)\,\mathrm{d}s\,\mathrm{d}\omega\\ &= \sum_k ik_jh_k(I)\exp(ik\theta)\int_\omega \frac{\exp(i(k\Omega(I)+\omega)T)-1}{i(k\Omega(I)+\omega)}\hat{\xi}(\omega)\mathrm{d}\omega\,.\end{aligned} \tag{2.38}$$

In this equation, we notice the occurrence of small denominators, which provides a contribution to the fluctuations of order $\mathcal{O}(T)$ when $k\Omega(I)+\omega = 0$. When this is the case, the variance reads

$$\begin{aligned}D(I,\theta) = &\frac{1}{T}\sum_{k,n} k_jn_lh_k(I)\bar{h}_n(I)e^{i(k-n)\theta}\times\\ &\times\int_\omega \frac{\left(e^{i(k\Omega(I)+\omega)T}-1\right)\left(e^{-i(n\Omega(I)+\omega)T}-1\right)}{(k\Omega(I)+\omega)(n\Omega(I)+\omega)}F(\omega)\,\mathrm{d}\omega\,.\end{aligned} \tag{2.39}$$

This integral can then be written in the alternative form

$$D(I,\theta) = \frac{4}{T}\sum_{k,n} k_j n_l h_k(I)\bar{h}_n(I)e^{i(k-n)(\theta+\Omega(I)T)}\times$$
$$\times\int_\omega \frac{\sin\left((k\Omega+\omega)\frac{T}{2}\right)\sin\left((n\Omega+\omega)\frac{T}{2}\right)}{(k\Omega(I)+\omega)(n\Omega(I)+\omega)}F(\omega)\mathrm{d}\omega\,. \tag{2.40}$$

If we then consider the limit $T \gg 1$, if $k = n$, by using the integral

$$\int_{-\infty}^{\infty}\frac{\sin^2(ax)}{x^2}\,\mathrm{d}x = \pi a\,, \tag{2.41}$$

it is possible to prove that the limit

$$\Delta(I) = \lim_{T\to\infty}\frac{4}{T}\int_\omega \frac{\sin^2\left((k\Omega(I)+\omega)\frac{T}{2}\right)}{(k\Omega(I)+\omega)^2}F(\omega)\,\mathrm{d}\omega \tag{2.42}$$

is finite, with the main contribution given by the condition $k\Omega(I) \simeq \omega$. That is, the action values at which the unperturbed frequencies satisfy a resonant condition with a Fourier component in the noise. This implies that, if we consider a noise power spectrum with a peak at ω_*, the variance of the action fluctuations is maximal at $I = I_*$, so that $k\Omega(I_*) = \omega_*$. If $F(\omega) = \text{const}$, that is, the white noise limit, we can prove that

$$D(I) = \sum_{k,n} k_j k_l |h_k(I)|^2 = \epsilon^2\left\langle\frac{\partial\hat{\mathcal{H}}_1}{\partial\phi_j}\frac{\partial\hat{\mathcal{H}}_1}{\partial\phi_l}\right\rangle_\phi\,. \tag{2.43}$$

If instead we consider the case $n \neq k$, we have a fast fluctuating term with zero mean in the integral of Eq. (2.40) when $T \gg 1$. This means that its contribution to the action variance vanishes in the limit $T \to \infty$, unless a resonance condition

$$(k-n)\Omega(I) = 0 \tag{2.44}$$

is satisfied. If that is the case, we have a finite contribution to the integral that reads

$$D(I,\theta) \simeq \sum_{k,n}^{res} k_j n_l h_k(I)\bar{h}_n(I)e^{i(k-n)\theta}\Delta(I)\,, \tag{2.45}$$

where the sum runs on the resonant harmonic that depends on the action values. In this scenario, the variance is influenced by the angles θ, resulting in a uniform distribution in the angle variables that are not invariant for the action fluctuations. However, if the actions can be considered constant for a time interval of the order of $\mathcal{O}(\epsilon^{-2/3})$, it is possible to average the variance $D(I,\theta)$ over the angle variables, as each orbit can cover all angle values at a fixed action before diffusion occurs. In this case, the impact of resonances between the noise spectral components and the perturbation components can be disregarded, and we regain the desired result

$$D_{i,j}(I) = \sum_k k_j k_l |h_k(I)|^2 \Delta(I)\,. \tag{2.46}$$

In fact, if it is assumed that the relaxation time of the angles θ is much shorter than the diffusion time of the action variables, the angles can be considered as fast random variables that define the various noise instances independently of the random perturbation $\xi(t)$, then we can examine the average dynamics of the action with regard to both the random perturbation and the angles θ

$$\begin{aligned} E(\Delta I_j)_\theta &= \frac{1}{2}\frac{\partial}{\partial I_k}\int_0^T\int_0^T \frac{\partial \mathcal{H}_1}{\partial \phi_j}(\theta+\Omega t)\frac{\partial \mathcal{H}_1}{\partial \phi_k}(\theta+\Omega s)\Phi(t-s)\,\mathrm{d}s\,\mathrm{d}t \\ &= \frac{1}{2}\frac{\partial}{\partial I_k}\sum_k k_j k_l |h_k(I)|^2 \int_0^T\int_0^T \exp(ik\Omega(t-s))\Phi(t-s)\mathrm{d}s\,\mathrm{d}t\,, \end{aligned} \tag{2.47}$$

where we have neglected the contribution of the terms with zero mean value with respect to the angle variables.

We remark that if $\Phi(\tau)$ is decaying sufficiently fast for $\tau \to \infty$, we have the limit

$$\lim_{T\to\infty}\frac{1}{2T}\frac{\partial}{\partial I_k}\sum_k k_j k_l |h_k(I)|^2 \int_0^T\int_0^T \exp(ik\Omega(I)(t-s))\Phi(t-s)\,\mathrm{d}s\,\mathrm{d}t\,, \tag{2.48}$$

then, the corresponding variance for the fluctuating terms reads

$$E(\Delta I^2) = \frac{\partial}{\partial I_k}\sum_k k_j k_l |h_k(I)|^2 \int_0^T\int_0^T \exp(ik\Omega(t-s))\Phi(t-s)\mathrm{d}s\,\mathrm{d}t + \mathcal{O}(\epsilon^4)\,, \tag{2.49}$$

which coincides with (2.46) if divided by T.

We now introduce the diffusion timescale $\epsilon^2 T \ll 1$ to apply a diffusion limit as $\epsilon \to 0$ and $T \to \infty$. In the limit of $\epsilon \to 0$, we select a time step $T \gg \gamma^{-1}$, i.e. the correlation timescale of the environment fluctuations, so that the fluctuations of $\Delta\theta$ and ΔI can be considered independent at subsequent time intervals. If we take into account an evolution timescale $T_\theta \simeq \epsilon^{-2/3}$ such that $\gamma^{-1} \ll T \ll \epsilon^{-2/3}$ the action evolution can be described by a diffusion process whose diffusion and drift coefficients are obtained by averaging over the angle variables

$$\Delta I_j = -\sqrt{T_\theta \epsilon^2}\sqrt{D_{j,l}(I)}\hat{\xi}_l + \frac{T_\theta \epsilon^2}{2}\frac{\partial}{\partial I_l}D_{j,l}(I)\,, \tag{2.50}$$

where $D(I)$ is defined by the equation (2.46)and $\hat{\xi}_l$ are independent and identically distributed random variables with zero mean value and unit variance.

If we now define the action diffusion timescale $\tau = \epsilon^2 t$, we can write the estimate

$$T_\theta \epsilon^2 \simeq \epsilon^{4/3} \simeq \Delta\tau \ll 1\,, \tag{2.51}$$

which holds in the limit $\epsilon \to 0$. Then, we can approximate with the relation (2.50) the solution of a stochastic differential equation in the diffusion time

$$\mathrm{d}I_j = \sqrt{D_{j,l}(I)}\,\mathrm{d}w_l(\tau) + \frac{1}{2}\frac{\partial}{\partial I_l}D_{j,l}(I)\,\mathrm{d}\tau\,. \tag{2.52}$$

From this final expression, we have that the evolution of the distribution function $\rho(I,\tau)$ on the diffusion timescale is well approximated by the solution of the Fokker-Planck equation

$$\frac{\partial \rho}{\partial \tau} = -\frac{1}{2}\frac{\partial}{\partial I_j}\left[\frac{\partial}{\partial I_k}D_{j,k}(I)\right]\rho(I,\tau) + \frac{1}{2}\frac{\partial^2}{\partial I_j \partial I_k}D_{j,k}(I)\rho(I,\tau) \tag{2.53}$$

which can be easily rewritten in the form

$$\frac{\partial \rho}{\partial \tau} = \frac{1}{2}\frac{\partial}{\partial I_j}D_{j,k}(I)\frac{\partial}{\partial I_k}\rho(I,\tau)\,, \tag{2.54}$$

which is the desired functional form.

2.3 | Functional form for $D(I)$

We have reached the result that, under certain conditions, the evolution of an action distribution function $\rho_0(I,t)$ can be described by a Fokker-Planck equation of the form

$$\frac{\partial \rho}{\partial \tau} = \frac{1}{2}\frac{\partial}{\partial I_j}D_{j,k}(I)\frac{\partial}{\partial I_k}\rho(I,\tau)\,, \tag{2.55}$$

where the diffusion coefficient $D_{j,k}(I)$ reads

$$D_{j,k}(I) = \left\langle \frac{\partial \hat{\mathcal{H}}_1}{\partial \phi_j}\frac{\partial \hat{\mathcal{H}}_1}{\partial \phi_k} \right\rangle\,. \tag{2.56}$$

In the context of accelerator physics, we have seen how the betatron motion can be described in terms of two action variables (I_x, I_y), which define the two non-linear invariants for the two separate transverse planes. However, if we assume that such a diffusive process takes place mainly along a one-dimensional direction, we can justify a 1D approach and reduce Eq. (2.55) to the one-degree-of-freedom case.

With the generic Hamiltonian notation, the resulting Fokker-Planck equation reads

$$\frac{\partial \rho}{\partial \tau} = \frac{1}{2}\frac{\partial}{\partial I_j} D(I) \frac{\partial}{\partial I_k} \rho(I, \tau)\,, \tag{2.57}$$

with the diffusion coefficient given by

$$D(I) = \frac{1}{\|\mathscr{H}_1\|^2} \left\langle \left(\frac{\partial \hat{\mathscr{H}}_1}{\partial \phi} \right)^2 \right\rangle_\phi \,. \tag{2.58}$$

If we want to work with regular time units t, we can consider this form of Fokker-Plank equation:

$$\frac{\partial \rho}{\partial t} = \frac{\epsilon^2}{2}\frac{\partial}{\partial I_j} D(I) \frac{\partial}{\partial I_k} \rho(I, t)\,, \tag{2.59}$$

where now $\epsilon^2 = \lambda \|\mathscr{H}_1\|^2$ represents the timescale constant of the diffusive process.

Now we are interested in having an effective generic functional form for $D(I)$. To achieve this, we follow the construction presented in [6], and the references therein.

To estimate the norm of $\mathscr{H}_1$, we see that the perturbation theory suggests a possible estimate based on the asymptotic character of the perturbation series. Assuming that there are no low-order resonances in the phase space, we can rely on the progressive expansion of the perturbative series, which gives us the following generic estimate [22]:

$$\|R_n(I)\| \propto (n!)^\kappa \left(\frac{I}{I_*} \right)^{n/2} \,, \tag{2.60}$$

where the factorial term takes into account the number of contributions due to the structure of the functional equations defining the perturbation series, the exponent κ is related to the number of degrees of freedom, and the parameter I_* represents an apparent radius of convergence of the perturbative series and corresponds to the amplitude above which fast escape to infinity occurs.

For each I, we then have an optimal order for the Normal Form remainder defined by the relations

$$n^{\kappa} = \left(\frac{I}{I_*}\right)^{1/2} \quad \Rightarrow \quad n = \left(\frac{I_*}{I}\right)^{1/2\kappa} . \tag{2.61}$$

If we then substitute this relation in the previous equation, we obtain a Nekhoroshev-like estimate that reads

$$\left\|R_{\text{opt}}\left(I\right)\right\| \propto \exp\left[-\kappa\left(\frac{I_*}{I}\right)^{1/2\kappa}\right] . \tag{2.62}$$

This relation shows how the optimal estimate scales as a function of the action I.

From this optimal remainder for the perturbation series, which can also be used as a measure of the long-term stability of the orbits at specific amplitudes, we can finally assume the following estimate for $\mathscr{H}_1$:

$$\|\mathscr{H}_1(\phi, I)\| \simeq \exp\left[-\left(\frac{I_*}{I}\right)^{1/2\kappa}\right] . \tag{2.63}$$

This estimate enables us to define the following functional form for the diffusion coefficient

$$D(I) = c\exp\left[-2\left(\frac{I_*}{I}\right)^{1/2\kappa}\right] , \tag{2.64}$$

where c is a normalization constant evaluated according to

$$c\int_0^{I_{\mathrm{a}}} D(I)\,\mathrm{d}I = 1 , \tag{2.65}$$

so that $D(I)$ is normalized over the boundaries considered for the Fokker-Planck system, as I_{a} represents the absorbing boundary condition, i.e. a over-linerier over which we can consider a particle as "lost". With this notation, the timescale of the process is completely determined by ϵ^2, however, variation of this notation can be freely considered.

Let us now consider this last form of the Fokker-Planck equation, along with an absorbing boundary condition at I_{a}, i.e. the phase-space limit beyond which an initial condition is considered lost. Note that $D(I)$ and ρ have dimensions $[I^2t^{-1}]$ and $[I^{-1}]$, respectively.

In Fig. 2.1 (top and centre), we consider the behaviour of $D(I)$ from Eq. (2.64) for some values of κ and for $\epsilon^2 = 1$. We can distinguish three

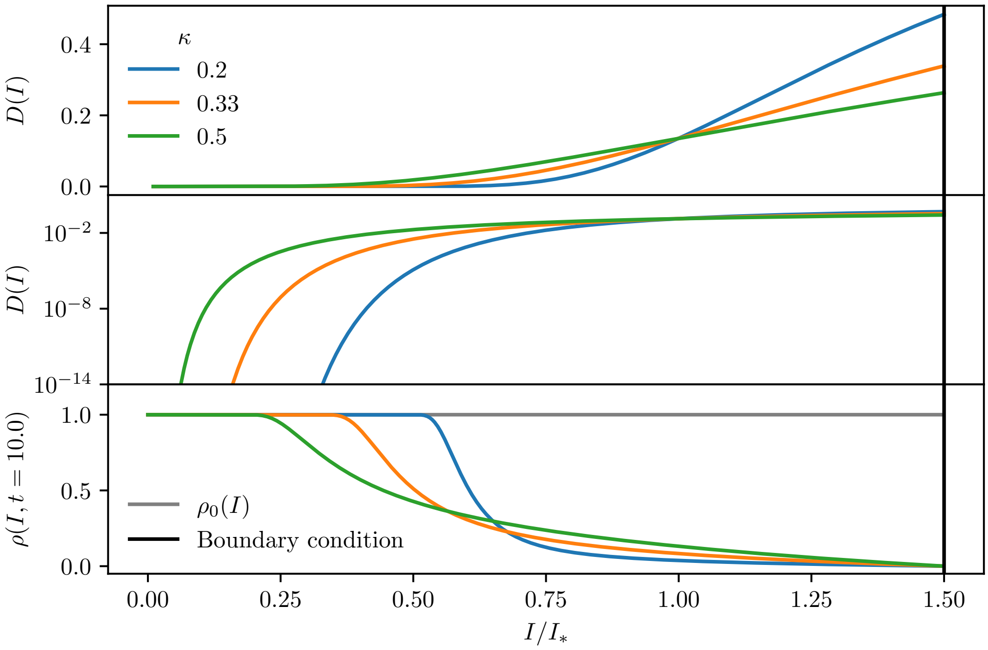

Figure 2.1: Top and centre: plot of $D(I)$ both in linear and logarithmic scale for three values of κ as a function of I/I_*. Bottom: evolution of an uniform distribution (in grey) over the same time interval corresponding to ($t = 10.0$ [a. u.]) for three values of κ. (Simulations parameter: ($I_* = 1.0\ [\sigma^2]$)).

regions for this type of function: (i) a stable core region for $I \ll I_*$, for which $D(I)$ has values decreasing to zero exponentially fast; (ii) a ramp-up region for $I\ .\ I_*$, where $D(I)$ starts to have non-negligible values and changes from an exponential growth to an almost linear one; (iii) a region for $I > I_*$, where $D(I)$ features an almost linear growth (in logarithmic scale a saturation appears). These three regions are more or less distinguishable depending on the value of κ.

In Fig. 2.1 (bottom), we also display the result of the numerical integration of Eq. (2.59) for some values of κ, performed on an initial distribution $\rho_0(I) = 1$ with a Crank-Nicolson scheme [42] (see Appendix 4.A for some details on the integration scheme used in our studies). It is also possible to observe in the shape of the distribution function a stable core region, corresponding to $I/I_* \ll 1$, where $D(I)$ starts having values very close to zero, a fast decrease region, and finally a saturation region, for $I/I_* = 1$ and beyond, where $\rho(I, t)$ assumes small values.

3 | Fundamentals of Accelerator Physics

After the introduction to Hamiltonian mechanics in Chapter 1, and the overview of stochastic Hamiltonian systems presented in Chapter 2, we now turn to the presentation of the fundamental concepts of accelerator physics. In particular, we will introduce the fundamental nomenclature, coordinates, and common approximations and assumptions used in this domain. These concepts will be required to understand the open challenges of non-linear beam dynamics, and how they can be related to known results in the field of stochastic Hamiltonian systems as, as we will see, the field of accelerator physics makes large use of the formalism and results from Hamiltonian mechanics.

It should be noted that the following information is not intended to serve as a comprehensive overview of accelerator physics. For a more detailed introduction to the subject, the reader is directed to Refs. [43, 44], which were consulted in the creation of this chapter. Our focus here is to provide an overview of the specific topics that are propaedeutical for the original contributions of this thesis.

A particle accelerator is a device that uses electromagnetic fields to accelerate a beam of charged particles, allowing for collisions with a target or another particle beam. These machines can be classified as linear or circular depending on their geometry. This study will focus specifically on circular accelerators.

An important consideration when working with circular particle accelerators is the type of particles that are accelerated, since a charged particle moving along a curved trajectory will lose energy due to synchrotron radiation [45]. The amount of energy lost per turn in a circular orbit due to synchrotron radiation follows the law [46]:

$$U_0 = C_\gamma \beta_0^3 \frac{E_0}{\rho}\,, \tag{3.1}$$

where E_0 is the energy of the particle, β_0 the relativistic ratio v/c, ρ the radius of the circular orbit, and $C_\gamma = q^2/3\epsilon_0(mc^2)^4$ a constant [47] dependent on the particle charge q and mass m. Due to the factor m^{-4} in U_0, this energy loss factor becomes negligible for hadron beams, but must be taken into account when working with electron beams in circular accelerators. In this research, we will only examine hadron machines and energy scales at which synchrotron radiation can be neglected.

Additionally, this study will focus on single-particle dynamics, which means that the motion of each individual particle in the beam will be considered independent and the repulsive Coulomb force between charges within the beam will be neglected.

The motion of the particles can be broken down into two components: longitudinal, in the direction of motion along the circumference, and transverse, in the plane normal to the longitudinal motion. These two components are also known, respectively, as synchrotron motion and betatron motion. The focus of this study will be on the transverse motion of the particles, which, as we will see in this chapter, can be described by means of an ideal integrable Hamiltonian system on which we then add non-linear terms and perturbations to describe the actual beam dynamics.

This non-linear Hamiltonian system describing the betatron motion is the point of departure and motivation for the study of the non-linear betatron motion and the application of the framework presented in the previous chapter, which will be the topic of the following parts and the original contribution of this thesis.

The chapter is organized as follows. In Section 3.1, we introduce the Frenet-Serret coordinate system, which is the standard coordinate system used in accelerator physics, and we inspect the Hamiltonian of a charged particle in an electromagnetic field. In Section 3.2, we solve the equations of motion in the transverse plane, considering an ideal scenario with only linear components of the magnetic field. Next, in Section 3.3, we define the invariant of the motion, the emittance, which comes from the definition of the Courant-Snyder ellipse. Then, in Section 3.4, we give a brief overview of the effects that arise in betatron motion when considering non-linear terms in the dynamics. In Section 3.5, we introduce the concept of one-turn map, in which the importance of symplectic maps in the context of accelerator physics is shown. In Section 3.6, we present the concept of dynamic aperture and how a Nekhoroshev scaling law emerges from the study of the non-linear dynamics effects on it. Finally, in Section 3.7, we give a brief overview of the fundamental concepts of longitudinal motion, since the modulation effects given by it on the transverse motion will be of specific interest in the Part III of this thesis, where we will also inspect how modulation effects contribute to the non-linear dynamics of the betatron motion.

3.1 | Particle motion and Frenet-Serret coordinate system

The standard choice of coordinates in accelerator physics, which takes advantage of the toroidal symmetry of the circular accelerator, is the Frenet-

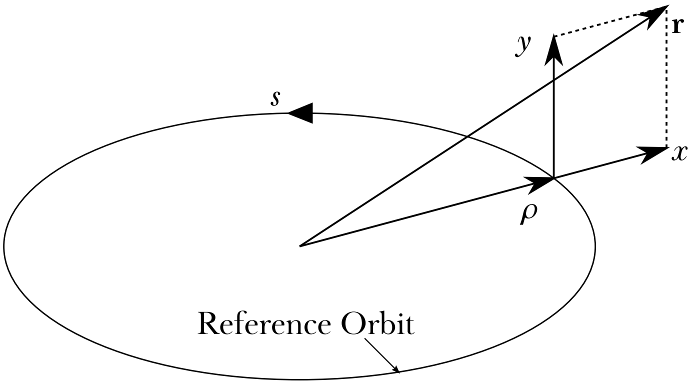

FIGURE 3.1: The Frenet-Serret coordinate system applied to a vector **r** in the starting Cartesian system. The reference orbit represents an ideal trajectory of particles in the accelerator, whose radius of curvature is ρ. The coordinate s is measured along the trajectory, while x and y are orthogonal to it.

Serret coordinate system.

Starting from the Cartesian system (X, Y, Z), centred in the accelerator centre, the Frenet-Serret coordinate system considers as one curvilinear coordinate the path length along the reference orbit s, which describes the ideal longitudinal motion of a particle inside the accelerator, and two Cartesian coordinates x and y for the transverse ones. In Fig. 3.1, we illustrate the coordinate system applied to a vector **r**.

Mapping the Cartesian system to the Frenet-Serret coordinate system reads:

$$X = (x+\rho)\cos\left(\frac{s}{\rho}\right), \qquad Y = y\,, \qquad Z = (x+\rho)\sin\left(\frac{s}{\rho}\right). \tag{3.2}$$

To keep the particles on a reference orbit of radius ρ, a constant magnetic field of intensity B is applied. ρ then is given by the equilibrium between the magnetic force and the centrifugal force. This equilibrium is expressed by the quantity $B\rho$, defined as *beam rigidity*, which corresponds to

$$B\rho = \frac{p}{e} \tag{3.3}$$

where p is the momentum of the particle and e its charge.

Starting from this coordinate system, it is possible to achieve a practical Hamiltonian expression for a particle in an accelerator.

Let us begin from the Hamiltonian of a relativistic charged particle under the effect of an electromagnetic field, which acts on the particle via the Lorentz force. The particles are accelerated, in modulus, by the action of an electric field **E** (or by the corresponding scalar potential Φ), and their trajectories are bent, to keep them in the circular reference orbit, by a magnetic field **B**, which can be expressed via the vector potential **A**, i.e. $\mathbf{B} = \nabla \times \mathbf{A}$.

The Hamiltonian of a relativistic particle under Lorentz force reads

$$\mathcal{H} = e\Phi + \sqrt{m^2c^4 + (c\mathbf{p} - e\mathbf{A})^2}\,. \tag{3.4}$$

We then express the square norm of $(c\mathbf{p} - e\mathbf{A})$ in the Frenet-Serret system of coordinates $(x,\ y,\ s)$, whose metric tensor reads

$$g_{ij} = \mathrm{diag}\left(1,\ 1,\ 1 + \frac{x}{\rho}\right), \tag{3.5}$$

which leads to

$$\mathcal{H} = e\Phi + \sqrt{m^2c^4 + \frac{(cp_s - eA_s)^2}{(1 + x/\rho)^2} + (cp_x - eA_x)^2 + (cp_y - eA_y)^2}\,. \tag{3.6}$$

From now on, it is convenient to treat s as the time coordinate. Consequently, due to canonical coupling, the conjugated momentum $-p_s$ will play the role of a Hamiltonian function $\tilde{\mathcal{H}}$. Solving Eq. (3.6) for p_s, we obtain

$$\tilde{\mathcal{H}} = -\left(1 - \frac{x}{\rho}\right)\sqrt{\frac{E^2}{c^2} - m^2c^2 - (p_x - eA_x)^2 - (p_y - eA_y)^2} - eA_s\,, \tag{3.7}$$

where $E = \mathcal{H} - e\Phi$. We have from special relativity that $E^2/c^2 = p^2 + m^2c^2$,this allows us to rewrite the Hamiltonian as

$$\tilde{\mathcal{H}} = -\left(1 - \frac{x}{\rho}\right)\sqrt{p^2 - (p_x - eA_x)^2 - (p_y - eA_y)^2} - eA_s\,. \tag{3.8}$$

In high-energy circular accelerators, such as those considered for this study, $p \gg p_x$ and $p \gg p_y$, and the so-called paraxial approximation can be applied. This enables the $\sqrt{1 + x} \approx 1 + x/2$ expansion for the Hamiltonian, leading to

$$\tilde{\mathcal{H}} = \left(1 + \frac{x}{\rho}\right)\left[-p + \frac{1}{2p}\left(p_x^2 + p_y^2\right)\right] - eA_s\,. \tag{3.9}$$

It is customary to assume that there is no magnetic field in the longitudinal direction. With this assumption, we only have contributions to the vector potential along s, and $A_x = A_y = 0$, i.e. $\mathbf{B} = (B_x,\ B_y,\ 0)$.

The standard approach to evaluating the contribution of the magnetic field to $\tilde{\mathscr{H}}$, eA_s, consists of expanding the magnetic field in its multipolar components.

From Maxwell's equation $\boldsymbol{\nabla}\times\mathbf{B} = 0$, one obtains the Laplace equation $\nabla^2\mathbf{A}$, which, for A_s, has a general solution that can be expressed in power series as

$$A_s = \operatorname{Re}\sum_n \left[\frac{k_n + ij_n}{(n+1)}(x+iy)^{n+1}\right], \tag{3.10}$$

which leads to the corresponding expansion of the magnetic field

$$B_y + iB_x = \sum_n (k_n + ij_n)(x+iy)^n \,. \tag{3.11}$$

The coefficients

$$k_n = \frac{1}{n!}\frac{\partial^n B_y}{\partial x^n}\bigg|_{x=y=0}, \qquad j_n = \frac{1}{n!}\frac{\partial^n B_x}{\partial y^n}\bigg|_{x=y=0} \tag{3.12}$$

are called respectively the *normal* and *skew* $2(n+1)$-polar coefficients of the magnetic field. In accelerator physics, it is customary to consider magnetic elements that generate fields with only one multipolar component. These elements are, in fact, referred to as normal or skew dipoles, quadrupoles, sextupoles, octupoles, etc. Of course, in the case of magnetic field imperfections, several multipolar components can be associated with a single magnet.

3.2 | Transverse motion

From the Hamiltonian (3.9), we can derive the equations of motion of the particle in the transverse plane. We obtain the following

$$\begin{aligned} x' &= \left(1+\frac{x}{\rho}\right)\frac{p_x}{p}, & p_x' &= \frac{p}{\rho}\left(1+\frac{x}{\rho}\right) + e\frac{\partial A_s}{\partial x}, \\ y' &= \left(1+\frac{x}{\rho}\right)\frac{p_y}{p}, & p_y' &= e\frac{\partial A_s}{\partial y}. \end{aligned} \tag{3.13}$$

To obtain an expression for the partial derivatives of A_s as a function of the x and y components of the magnetic field $\mathbf{B}$, we consider the expression of $\boldsymbol{\nabla}\times\mathbf{A}$ in the Frenet-Serret coordinates, which reads

$$\boldsymbol{\nabla}\times\mathbf{A} = \frac{\hat{x}}{1+x/\rho}\frac{\partial A_s}{\partial y} - \frac{\hat{y}}{1+x/\rho}\frac{\partial A_s}{\partial x} = B_x\hat{x} + B_y\hat{y} \tag{3.14}$$

as only the A_s component is non-zero. This leads to

$$\frac{\partial A_s}{\partial x} = -\left(1+\frac{x}{\rho}\right)B_y\,, \qquad \frac{\partial A_s}{\partial y} = \left(1+\frac{x}{\rho}\right)B_x\,, \tag{3.15}$$

which, substituted in Eq. (3.13), reads

$$\begin{aligned} x' &= \left(1+\frac{x}{\rho}\right)\frac{p_x}{p}\,, & p_x' &= \left(1+\frac{x}{\rho}\right)\left[\frac{p}{\rho} - eB_y\right] \\ y' &= \left(1+\frac{x}{\rho}\right)\frac{p_y}{p}\,, & p_y' &= e\left(1+\frac{x}{\rho}\right)B_x\,. \end{aligned} \tag{3.16}$$

Recalling the definition of beam rigidity in Eq. (3.3), we can rewrite the equations of motion as second-order differential equations using the fact that $p = eB\rho$. This leads to

$$\begin{aligned} x'' &= \frac{1}{\rho} + \frac{x}{\rho^2} + \frac{B_y}{B\rho}\left(1+\frac{x}{\rho}\right)^2\,, \\ y'' &= \frac{B_x}{B\rho}\left(1+\frac{x}{\rho}\right)^2\,. \end{aligned} \tag{3.17}$$

If we consider only linear terms for the magnetic fields B_x and B_y, these equations can be expressed in the form

$$z'' + K_z(s)z = 0\,, \tag{3.18}$$

where z stands for x or y, and the function $K(s)$ represents the effect of the linear magnetic fields the particle is subject to in the accelerator. For a circular accelerator of length L the periodic condition $K_z(s) = K_z(s+L)$ holds. This equation with the periodic condition is referred to in the literature as *Hill's equation*.

An Ansatz for the solution of Hill's equation is in the form

$$z(s) = A\sqrt{\beta_z(s)}\cos\left(\psi_z(s)\right)\,, \tag{3.19}$$

i.e. a harmonic oscillator where the amplitude $\beta_z(s)$ and phase advance $\psi_z(s)$ depend on s. When substituted into Hill's equation, this results in a relation between $\psi_z(s)$ and $\beta_z(s)$, namely

$$\frac{1}{\sqrt{\beta_z(s)}}\frac{\mathrm{d}}{\mathrm{d}s}\left(\beta_z(s)\psi_z(s)\right) = 0\,, \tag{3.20}$$

which can be solved as

$$\psi_z(s) = \int_0^s \frac{\mathrm{d}s'}{\beta_z(s')} \tag{3.21}$$

and a non-linear equation for $\beta_z(s)$:

$$\frac{1}{2}\beta_z\beta_z'' - \frac{1}{4}\beta_z'^2 + K_z(s)\beta_z^2 = 1\,. \tag{3.22}$$

The phase advance over the ring is called *tune*:

$$\nu_z = \frac{1}{2\pi}\oint \frac{\mathrm{d}s'}{\beta_z(s')}\,. \tag{3.23}$$

3.3 | Courant-Snyder ellipse

As we are interested in the transverse motion of the particle, we want to consider its evolution each time it crosses the position $s = s_0$, i.e. we want to consider the Poincaré section of dynamics. At each iteration, we will have a phase advance of ψ_z equal to $2\pi\nu_z$.

It is possible to decouple the envelope dynamics described by $\beta_z(s)$ from the transverse motion of the particles with a coordinate transformation, which leads to the definition of the Courant-Snyder ellipse and other important quantities in accelerator physics.

From Eq. (3.19), we find that $z'(s)$ reads

$$z'(s) = -\frac{z}{\beta_z(s)}(\alpha_z(s) + \tan\psi_z(s)) \tag{3.24}$$

where $\alpha_z = -\beta_z'/2$. We then consider for our coordinate transformation the angular variable $\phi_z = \psi_z$ and the generating function

$$F = \int \mathrm{d}z\, z' = -\frac{z^2}{2\beta_z}(\alpha_z + \tan\phi_z)\,, \tag{3.25}$$

which then yields the canonical action variable I_z

$$I_z = \frac{\partial F}{\partial\phi_z} = \frac{z^2}{2\beta_z}(1+\tan^2\phi_z) = \frac{1}{2\beta_z}\left[z^2 + (\beta_z z' + \alpha_z z)^2\right]. \tag{3.26}$$

In the new variables, the Hamiltonian corresponding to Hill's equation

$$\mathcal{H} = \frac{z'^2}{2} + \frac{K_z z^2}{2}\,, \tag{3.27}$$

reduces to the simple expression

$$\mathcal{H}(\phi, I, s) = \frac{I}{\beta(s)}\,, \tag{3.28}$$

which takes into account the derivative $\partial F/\partial s$, and from this new Hamiltonian we find that the equation of motion for the variable ϕ_z reads $\phi_z' = 1/\beta(s)$.

We are now interested in making ϕ_z proportional to s, and removing any dependence on the β function in the equations of motion. To achieve this, we define

$$\omega_z = \frac{2\pi\nu_z}{L}\,, \tag{3.29}$$

where, we recall, L is the circumference of the accelerator and ν_z the tune defined in Eq. (3.23). Then we have the final change of variables $(\phi_z, I_z) \to (\tilde{\phi}_z, \tilde{I}_z)$, which is defined by the generating function

$$G(\phi_z, \tilde{I}_z) = \tilde{I}_z\left(\omega_z s - \int_0^s \frac{\mathrm{d}s'}{\beta(s')}\right) + \phi\tilde{I}\,, \tag{3.30}$$

which results in the Hamiltonian

$$\mathcal{H}(\tilde{\phi}_z, \tilde{I}_z) = \omega_z\tilde{I}_z\,, \tag{3.31}$$

i.e. the well-known Hamiltonian of a harmonic oscillator (note how $I_z = \tilde{I}_z$).

From this final Hamiltonian, one can introduce and operate with normalized Cartesian coordinates

$$\hat{z} = \sqrt{2I_z}\cos\tilde{\phi}_z\,, \quad \hat{p}_z = \sqrt{2I_z}\sin\tilde{\phi}_z\,, \tag{3.32}$$

and consequently treat the transverse linear motion on both the $\hat{x}-\hat{p}_x$ and $\hat{y}-\hat{p}_y$ planes using an intuitive normalized Cartesian Hamiltonian

$$\mathcal{H}(\hat{x},\, \hat{p}_x,\, \hat{y},\, \hat{p}_y) = \frac{\omega_x}{2}(\hat{x}^2 + \hat{p}_x^2) + \frac{\omega_y}{2}(\hat{y}^2 + \hat{p}_y^2)\,. \tag{3.33}$$

The Hamiltonian of Eq. (3.33) describes circular trajectories in decoupled phase spaces $(\hat{x},\, \hat{p}_x)$ and $(\hat{y}\,, \hat{p}_y)$. Moreover, there are two corresponding action variables, namely,

$$I_x = \frac{\hat{x}^2 + \hat{p}_x^2}{2}\,, \quad I_y = \frac{\hat{y}^2 + \hat{p}_y^2}{2}\,, \tag{3.34}$$

can be defined. I_x and I_y follow the standard definition of the trajectory area divided by 2π and are conserved. However, for historical reasons, the value $2I_z$ is called Courant-Snyder invariant.

From its definition in the physical coordinates $(z,\, z')$, given in Eq. (3.26), it is possible to draw the constant-I surfaces in the (z, z') phase space, as in Fig. 3.2, which correspond to concentric ellipses, as the expanded form reads:

$$I_z = \frac{1}{2\beta_z}\left[z^2 + (\alpha z + \beta z'))^2\right] = \frac{1}{2}\left(\gamma z^2 + 2\alpha z z' + \beta z'^2\right), \tag{3.35}$$

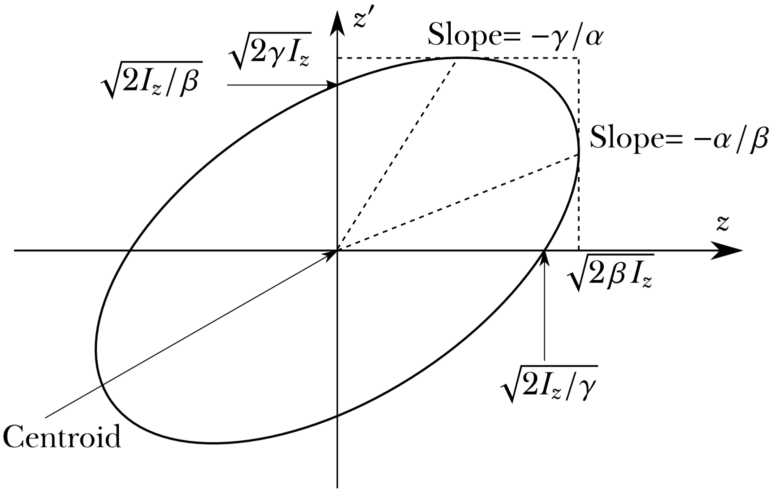

FIGURE 3.2: The Courant-Snyder ellipse $\gamma z^2 + 2\alpha z z' + \beta z'^2 = 2I_z$. The area enclosed by the ellipse is equal to $2\pi I_z$.

where we have defined $\gamma = (1+\alpha^2)/\beta$. The area of the ellipse is equal to $2\pi I_z$, and is conserved at any value of s. It can be observed, finally, how the $(z, z') \longrightarrow (\hat{z}, \hat{p}_z)$ coordinate transformation modifies the physical coordinates ellipses into circles with the same area, from which their name *"normalized coordinates"*.

A single particle following the linear transverse dynamics will have its own constant Courant-Snyder invariant. When, instead, we want to consider a beam distribution, a standard property, called *emittance* is defined as the average of the Courant-Snyder invariant:

$$\epsilon_z = \langle I_z \rangle \ . \tag{3.36}$$

The emittance is related to the second moments of the beam distribution in $(\hat{z}, \hat{p}_z)$. In fact, averaging over I_z and ϕ_z in the definitions of $\hat{z}$ and $\hat{p}_z$ given in Eq. (3.32), we obtain the following

$$\left\langle \hat{z}^2 \right\rangle = \beta_z \epsilon_z, \qquad \left\langle \hat{p}_z^2 \right\rangle = \gamma_z \epsilon_z, \qquad \left\langle \hat{z}\,\hat{p}_z \right\rangle = -\alpha_z \epsilon_z \, , \tag{3.37}$$

from there, using the definition of I_z yields

$$\epsilon_z = \sqrt{\left\langle \hat{z}^2 \right\rangle \left\langle \hat{p}_z^2 \right\rangle - \left\langle \hat{z}\,\hat{p}_z \right\rangle^2} \, . \tag{3.38}$$

The beam emittance can then be considered as the average Courant-Snyder invariant of a distribution or as the area (up to a 2π factor) of the orbit of the

RMS particle of the beam. A useful implication of this is that a Gaussian beam distribution in $(\phi_z,\ I_z)$ coordinate assumes the following practical form

$$\rho_z = \frac{1}{\epsilon_z}\exp\left(-\frac{I_z}{\epsilon_z}\right). \tag{3.39}$$

3.4 | Non-linear beam dynamics

The transverse dynamics we treated so far takes into consideration only the effects of a linear magnetic field (we recall the step between Eq. (3.17) and Eq. (3.18), where we dropped all non-linear terms for the magnetic fields B_x and B_y), so that this approach takes into account only the elements generated by a set of ideal dipole and quadrupole magnets.

To include higher-order terms of the magnetic field power series, it is possible to include non-linear terms directly into Hill's Hamiltonian. This can be done to represent both the unavoidable higher-order magnet imperfections inside the accelerator machine, or to represent explicit sextupolar and octupolar elements, which one might want to include in the accelerator lattice.

As Hill's Hamiltonian is equivalent to two uncoupled harmonic oscillators, non-linear components can be included in the Hamiltonian as anharmonic perturbation. We start by considering higher-order terms $n \geq 2$ of the power series A_s in Eq. (3.10), and we perform the change of variables $(x,\ y) \to (\hat{x}, \hat{y})$. We then see that the non-linear part of the Hamiltonian reads:

$$\mathcal{H}_{\text{nlin}}(\hat{x}, \hat{p}_x, s) = \operatorname{Re}\sum_{n\geq 2}\left[\frac{k_n(s) + i j_n(s)}{(n+1)}\left(\sqrt{\beta_x(s)}\,\hat{x} + i\sqrt{\beta_y(s)}\,\hat{y}\right)^n\right]. \tag{3.40}$$

To approximate this expression to a simpler form, we introduce the quantity $\beta(s) = \beta_y(s)/\beta_x(s)$, and its value $\overline{\beta}$ averaged over the accelerator circumference, which reads

$$\overline{\beta} = \oint \mathrm{d}s\,\frac{\beta_y(s)}{\beta_x(s)}. \tag{3.41}$$

We can now substitute the strengths $k_n(s)$ and $j_n(s)$ (which, we recall, represent the effect of a normal or a skew magnetic field $(2n+2)$) with the integrated coefficients K_n, J_n, which will be scaled by the value of $\beta_x(s)$ and $\beta_y(s)$, that is, we weight the integral average with the envelope value of the beam where the magnetic elements are placed. These coefficients read

$$K_n = \oint \mathrm{d}s\, k_n(s)\beta_x^{\frac{n}{2}}(s), \qquad J_n = \oint \mathrm{d}s\, j_n(s)\beta_x^{\frac{n}{2}}(s). \tag{3.42}$$

With this notation, the non-linear Hamiltonian has the simpler form

$$\mathcal{H}_{\text{nlin}}(\hat{x}, \hat{p}_x) = \text{Re} \sum_{n \geq 2} \left[\frac{K_n + i J_n}{(n+1)} (\hat{x} + i \overline{\beta}^{-1/2} \hat{y})^n \right] . \tag{3.43}$$

From this Hamiltonian, one can for example write a simple beam model with one degree of freedom and normal multipoles

$$\mathcal{H}(\hat{x}, \hat{p}) = \omega \frac{\hat{x}^2 + \hat{p}^2}{2} + \sum_{n > 2} K_n \frac{x^{n+1}}{(n+1)} , \tag{3.44}$$

such a simple model can be used to understand many phenomena caused by non-linear effects.

In an accelerator, non-linear effects can be used to represent either unwanted elements, such as magnet imperfections, or to represent specifically added elements generating a non-linear magnetic field, such as sextupoles and octupoles. These components can be introduced into an accelerator lattice to correct specific unwanted effects, like *chromaticity*, i.e. the fact that particles with different momentum are differently focused by quadrupoles. Chromaticity, specifically, can be controlled by the introduction of sextupole magnets. Another important source of non-linearities is space charge effects and *beam-beam interaction*, caused by the electromagnetic interaction of charged particles with other charged particles, respectively, in the same or in another beam during collisions.

The introduction of non-linear elements in a circular accelerator is the cause of three main effects [48]: amplitude-dependent detuning, excitation of non-linear resonances, and reduction of the dynamic aperture. We will present the first two phenomena very briefly and focus a little more on the core characteristics of the last one.

Amplitude-dependent detuning

Adding non-linear elements has the inevitable consequence of making the tune, i.e. the rotation frequency of the harmonic oscillator, an amplitude-dependent function. In the linear Hamiltonian (3.33), the frequency Ω is given by

$$\Omega = \frac{\partial \mathcal{H}}{\partial I} = \omega , \tag{3.45}$$

where, we recall, $I = (\hat{x}^2 + \hat{p}^2)/2$. The tune Ω is constant at any I, therefore, all particles have the same tune.

If we now add an octupolar component to the Hamiltonian, that is, an $n = 3$ element of the power series in Eq. 3.44, the new Hamiltonian is

$$\mathcal{H} = \omega \frac{\hat{x}^2 + \hat{p}^2}{2} + \frac{K_3}{5} x^4 = \omega I + \frac{K_3}{5} I^2 \cos^4 \phi \, . \tag{3.46}$$

Averaging over the angular variable ϕ, one obtains

$$\langle \mathcal{H} \rangle = \omega I + \frac{3}{40} K_3 I^2 , \tag{3.47}$$

and

$$\Omega(I) = \frac{\partial \langle \mathcal{H} \rangle}{\partial I} = \omega + \frac{3K_3}{20} I \, . \tag{3.48}$$

There is now a linear dependence of the tune on the action I, and each particle will have a different rotation frequency depending on its amplitude.

The averaging approach used here to obtain an expression of the amplitude detuning highlights only the first-order effects in the frequency. For more complex Hamiltonians, describing multiple non-linear components, deriving a complete analytical expression of the detuning is not always a trivial task.

It is possible to numerically evaluate the amplitude-dependent detuning in single-particle tracking simulations, as the tune can be measured by performing a numerical estimate of the fundamental frequency of the orbit. We will present the topic of tune evaluation later in Chapter 7, in the context of dynamic indicators, as tune determination is the foundation for consolidated tools in accelerator physics like Frequency Map Analysis.

Non-linear resonances

If the tunes ω_x and ω_y satisfy a 1D or 2D resonance condition, the non-linear magnetic field can eventually lead to severe particle loss. A theoretical approach to this phenomenon is presented in [40, 49].

When the frequency ω_x or ω_y is close to a 1D resonant condition $n\omega_z/2\pi \in \mathbb{Q}$, according to the Poincaré-Birkhoff theorem, presented in Section 1.5.1, a chain of islands with extra fixed points appears. These islands, in regular accelerator operations, may reduce the dynamic aperture (for which the definition is given in Section 3.6) and, close to separatrices, cause the onset of chaotic motion. When a resonance is crossed due to small, undesired variations of the magnetic field, which cause oscillations of ω_x and ω_y values, a growth in beam emittance may be observed [50], affecting beam lifetime.

Other than 1D resonances, in a system with two degrees of freedom, one can have a 2D resonant condition between the ω_x and ω_y frequencies, i.e. $m\omega_x + n\omega_y = 2\pi\ell$, with $\ell \in \mathbb{Q}$. Only difference resonances ($m > 0$, $n < 0$) are stable,

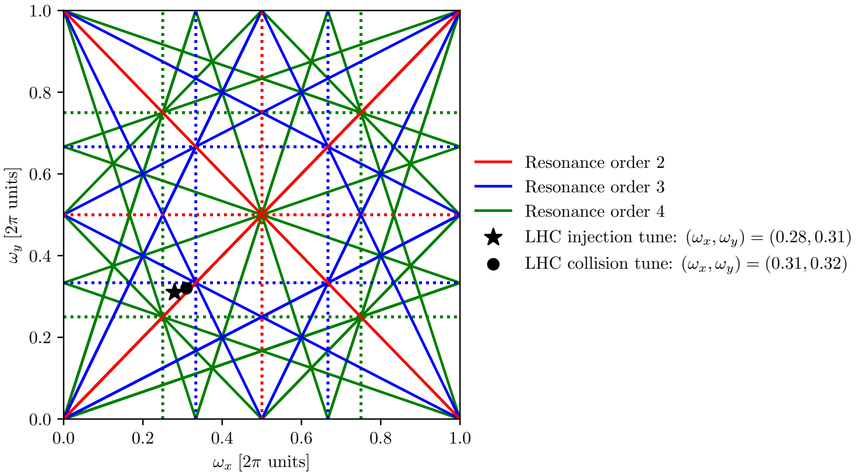

FIGURE 3.3: Resonance diagram in the $(\omega_x,\ \omega_y)$ space up to order 4, that is, $|m|+|n| = 4$. The resonances are evaluated on the fractional part of ω_x and ω_y. Dotted lines represent 1D resonances, continuous lines represent 2D resonances. The two characteristic working fractional tunes for the LHC are also reported on the resonance diagram.

although they contribute to the motion coupling between the two planes, while sum resonances (when m and n have the same signs) result in unstable motion.

The possible 1D and 2D resonances (up to order 4) are represented by lines in the (ω_x, ω_y) diagram in Fig. 3.3, where different colours show the resonance order. As higher-order resonances are generally weaker than lower-order ones, the accelerator working point should be selected far from the main resonances; the LHC does so by operating at fractional tunes $(\omega_x, \omega_y) = (0.28, 0.31)$ during injection and $(\omega_x, \omega_y) = (0.31, 0.32)$ during collisions [51]. Note that, in the accelerator literature, frequencies and tunes are reported in units of 2π.

3.5 | One-turn maps

A standard tool in accelerator physics to inspect the transverse dynamic of a particle in an accelerator magnetic lattice is one-turn maps. A one-turn map M is the Poincaré map of the circular accelerator in section $(s = s_0)$, and is given by composing single-element maps:

$$\mathrm{M} = \mathrm{M}^{(L)} \circ \mathrm{M}^{(L-1)} \circ \cdots \circ \mathrm{M}^{(2)} \circ \mathrm{M}^{(1)}\,, \tag{3.49}$$

where each $\mathrm{M}^{(i)}$ represents an element along the circular accelerator lattice, which might be, for example, a drift space without magnets, a dipole bending magnet, a quadrupole, or a higher order magnetic element.

The map M transforms the phase space coordinates $\hat{\mathbf{x}} = (\hat{x}, \hat{p}_x, \hat{y}, \hat{p}_y)$ of a particle into new coordinates $\mathbf{x}'$ which correspond to the particle after one full turn (see Fig. 1.1).

In this framework, the effect of each magnetic element on the phase coordinates of the beam can be written, in an analogy with geometrical optics, as the action of a 4×4 matrix on the coordinate vector. This matrix corresponds to the symplectic flow of the Hamiltonian for a given magnetic field.

When considering only the linear components in the magnetic lattice, the resulting Poincaré map for $\hat{\mathbf{x}}$ reads as a decoupled harmonic oscillator

$$\begin{pmatrix} \hat{x} \\ \hat{p}_x \\ \hat{y} \\ \hat{p}_y \end{pmatrix}_{n+1} = \begin{pmatrix} \cos\omega_x & \sin\omega_x & 0 & 0 \\ -\sin\omega_x & \cos\omega_x & 0 & 0 \\ 0 & 0 & \cos\omega_y & \sin\omega_y \\ 0 & 0 & -\sin\omega_y & \cos\omega_y \end{pmatrix} \begin{pmatrix} \hat{x} \\ \hat{p}_x \\ \hat{y} \\ \hat{p}_y \end{pmatrix}_n . \tag{3.50}$$

In general, it is not possible to compute exactly the transfer map of a non-linear element. Therefore, approximation techniques become necessary. The standard approach that is used in standard tracking codes such as SixTrack [52], is the *one-kick approximation*, i.e. it is assumed that the higher-order polynomial effects on the magnetic potential are all located at a precise position s_l and act with a $\delta(s - s_l)$ potential.

The main advantages of this approximation is the fact that the resulting one-turn map M maintains its symplectic character and enables efficient tracking. This approximation holds when the higher-order magnetic contributions are small in length.

A one-turn map with a single non-linear contribution, added with the one-kick approximation at $s = s_0$, will then read

$$\begin{pmatrix} \hat{x} \\ \hat{p}_x \\ \hat{y} \\ \hat{p}_y \end{pmatrix}_{n+1} = R(\omega_x, \omega_y) \begin{pmatrix} \hat{x} \\ \hat{p}_x + \operatorname{Re} \sum_r \frac{K_r + iJ_r}{r} (\hat{x} + i\sqrt{\beta}\hat{y})^r \\ \hat{y} \\ \hat{p}_y - \operatorname{Im} \sum_r \frac{K_r + iJ_r}{r} (\hat{x} + i\sqrt{\beta}\hat{y})^r \end{pmatrix}_n , \tag{3.51}$$

where now the β term, which also appears in the definition of K and J is evaluated at $s = s_0$ due to the one-kick approximation.

This shape of the map inspired the investigation of 2D and 4D maps in the form of

$$\begin{pmatrix} \hat{\mathbf{x}} \\ \hat{\mathbf{p}} \end{pmatrix}_{n+1} = \mathrm{R}(\omega) \begin{pmatrix} \hat{\mathbf{x}} \\ \hat{\mathbf{p}} + \mathbf{f}(\hat{\mathbf{x}}) \end{pmatrix}_n , \tag{3.52}$$

which are referred to as *Hénon-like maps*, due to the well-known map introduced in Ref. [53]:

$$\begin{pmatrix} \hat{x} \\ \hat{p}_x \end{pmatrix}_{n+1} = R(\omega) \begin{pmatrix} \hat{x} \\ \hat{p}_x + \hat{x}^2 \end{pmatrix}_n . \tag{3.53}$$

These models, despite their simplicity, already manifest multiple features that are observed in a beam under non-linear magnetic fields and have been used in multiple studies to investigate such features in the context of accelerator physics, especially in the context of dynamic aperture measurements [54, 55]. These maps were also used as a fundamental building block for the application of Normal Form theory to betatron motion [40].

3.6 | Dynamic aperture

As shown before, the linear transverse motion can be described as an always stable harmonic oscillator with two degrees of freedom. When instead non-linearities are introduced, the stability of the system is affected and the occurrence of hyperbolic points and resonances makes the motion of various initial conditions chaotic, eventually leading to their loss as they hit the mechanical aperture of the accelerator.

In this scenario, where the region of stable motion in the phase space is affected by the non-linear elements in the Hamiltonian, we can introduce the concept of *Dynamic Aperture* (DA), as the extent of the phase-space region where stable motion occurs up to a given number of turns N.

A complete discussion of the definition of DA, its computation, and its accuracy can be found in Refs. [54, 55], which provide a fundamental starting point on the topic. In the context of single-particle tracking, DA is defined over the number of turns N as the radius of a hypersphere whose volume is equal to the volume of the phase space where stable motion occurs up to N turns. Note how this definition neglects the island of stability, which might be given by the Poincaré-Birkhoff theorem.

The value of (N) must be adapted for a suitable time frame. In a mathematical sense, stable motion implies a bounded motion for $N \to \infty$. In our accelerator context, stable motion and particle stability can be linked to a maximum number of turns N_{max}, where the value of N_{max} is set on the basis of the specific application under consideration, e.g. in the LHC a standard 10-hour luminosity fill, which corresponds to, using the revolution frequency of $11.245\,\text{kHz}$ [51], $\sim 10^9$ turns.

A consolidated numerical method for evaluating the DA in 4D symplectic mappings that model betatron motion is presented in Ref. [54].

Let us operate on a 4D phase space on which we have a one-turn map M. If we consider an ensemble of initial conditions defined on a polar grid ($x = r\cos\phi, p_x = 0, y = r\sin\phi, p_y = 0$), $0 \leq \phi \leq \pi/2$, where x, y are expressed in units σ_x, σ_y, i.e. nominal beam emittance units, and we track them for up to

$N_{\max}$ turns to assess their stability, then we can define DA as:

$$DA(N) = \frac{2}{\pi}\int_0^{\pi/2} r(\phi; N)\, d\phi \equiv \langle r(\phi; N)\rangle \tag{3.54}$$

where $r(\phi; N)$ is the last stable amplitude, i.e. $x^2+y^2 < r_{\max}$ for every iteration of M, not disconnected from the origin for up to N turns in the direction ϕ.

In addition to this consolidated "radial scan" method, other techniques have been studied to improve the convergence speed of numerical DA measurements, such as the one presented in Ref. [56], where a Support Vector Machine algorithm is employed to perform an optimized sampling and border detection of the stable region of the phase space.

3.6.1 | Dynamic aperture scaling laws

Simulating entire sets of initial conditions on different one-turn maps is a computationally intense task that becomes unsustainable when considering extremely high $N_{\max}$ values or complex symplectic tracking models[1]. Moreover, the multipolar components of the various superconducting magnets are known only with limited precision, so one has to perform parametric studies to consider different realizations of the magnetic lattice. Because of these reasons, realistic timescales in tracking simulation are still out of reach for proper accelerator physics research.

This limitation motivated the search for a robust model for the time dependence of DA, as such a model could offer insights into the long-term evolution of DA by extrapolating short-term tracking simulation data. The most recent developments on the topic of DA scaling laws can be found in [57] and references therein.

The models presented in [57] are based on the Nekhoroshev theorem. Previous models formulated scaling laws using both the KAM theorem and the Nekhoroshev estimate, theorizing the presence of a stable core with KAM tori and an increasingly chaotic region where Nekhoroshev-like estimates for stability times apply. However, such models presented some internal discrepancies, such as the possibility to fit non-physical parameters or the strong correlation between free parameters [58, 59], motivated the usage of a scaling law exclusively based on the Nekhoroshev theorem. This is justified by the fact that the condition for the applicability of the stability-time estimate provided by the Nekhoroshev theorem is more general than the existence conditions of the KAM tori.

---

[1] Researches like [55] present simulations in $N_{\max} \sim 10^6 - 10^7$, while instead it would be necessary to reach values $\sim 10^9$.

In this context, the Nekhoroshev theorem can be used to provide an estimate of the number of turns $N(r)$ for which the orbit of an initial condition with amplitude r remains bounded. The estimate has a functional form that reads:

$$\frac{N(r)}{N_0} = \sqrt{\frac{r}{r_*}} \exp\left[\left(\frac{r_*}{r}\right)^{\frac{1}{\kappa}}\right] . \tag{3.55}$$

A more generalized form of this estimate reads

$$\frac{N(r)}{N_0} = \left(\frac{r}{r_*}\right)^{\lambda} \exp\left[\left(\frac{r_*}{r}\right)^{\frac{1}{\kappa}}\right] . \tag{3.56}$$

From this working hypothesis, the latest scaling law inspected in [57], based on inverting the functional form of the Nekhoroshev estimate, reads:

$$DA(N) = \frac{\rho_*}{\left[-2\mathrm{e}\lambda \mathcal{W}_{-1}\left(-\frac{1}{2\mathrm{e}\lambda}\left(\frac{\rho_*}{6}\right)^{1/\kappa}\left(\frac{8}{7}N\right)^{-1/(\lambda\kappa)}\right)\right]^{\kappa}} , \tag{3.57}$$

where $\mathcal{W}$ is the Lambert-$\mathcal{W}$ function [60]. The free parameters in this equation are ρ_*, κ, and possibly λ, unless it is set at $1/2$. The parameter ρ_* is related to the Nekhoroshev parameters in Eq. (3.55) with the following relation:

$$\rho_* = \left(\frac{\kappa}{2e}\right)^{-\kappa} r_* . \tag{3.58}$$

3.7 | Fundamentals of longitudinal dynamics

Although the focus of this work is on the transverse beam dynamics, it is important to include an essential presentation of the core concepts behind the longitudinal dynamics, i.e., the theory describing synchrotron oscillations. A particle that exhibits a longitudinal displacement with respect to the reference trajectory, or that has a longitudinal momentum different from the reference, will also manifest a different transverse dynamics, with a mechanism called *syncro-betatron coupling*. The main effects of syncro-betatron coupling can be represented as a turn-dependent *modulation* of transverse tunes.

In high-energy circular accelerators, the acceleration of particles is achieved via the use of time-varying electromagnetic fields. The accelerating fields are generated in dedicated straight elements, called RF cavities. In these cavities, a high-frequency accelerating voltage V is generated along the longitudinal direction with a specified angular frequency ω_{rf}, and reads

$$V = V_0 \sin\left(\omega_{\mathrm{rf}} t + \phi_s\right) , \tag{3.59}$$

where V_0 is the amplitude of the RF voltage and ϕ_s is a phase factor.

When the momentum of a particle in an accelerator changes, its revolution frequency f also changes, following a relation that reads:

$$\frac{\mathrm{d}f}{f} = \left(\frac{1}{\gamma_r^2} - \alpha_\mathrm{p}\right)\frac{\mathrm{d}p}{p}\,, \tag{3.60}$$

where γ_r is the Lorentz factor and α_p is referred to as the momentum compaction factor, it depends on the lattice, and it is the ratio between the relative orbit difference (given by the different trajectory in the magnetic lattice) and the relative momentum error

$$\alpha_p = \frac{1}{C}\frac{\mathrm{d}\Delta C}{\mathrm{d}\delta} = \frac{1}{C}\oint \frac{D(s)\,\mathrm{d}s}{\rho}\,, \tag{3.61}$$

where C is the path length of the reference orbit, δ is the fractional off-momentum $\Delta p/p$, and $D(s)$ is the dispersion function [43], which quantifies the change in orbit effects given by fractional differences in momentum δ along the various components of the magnetic lattice.

From this equation we can distinguish two separate regimes. At $\left(\gamma_r^{-2} < \alpha_p\right)$, which corresponds to low energies, the frequency of the revolution decreases with increasing momentum. At $\left(\gamma_r^{-2} > \alpha_\mathrm{p}\right)$, which corresponds to high energies, it increases. The energy corresponding to $\gamma_\mathrm{tr} = 1/\sqrt{\alpha_\mathrm{p}}$ is referred to as *transition energy*, as it delimits the two regimes.

Taking into account a particle with longitudinal phase $\phi = \phi_s$, momentum p_0, and revolution period T_0, we will refer to this particle as *synchronous particle*. When designing an accelerator, we must have that the angular frequency of the RF cavity must match the frequency of the synchronous particle. Such a requirement reads as follows

$$\omega_\mathrm{rf} = h\omega_0\,, \tag{3.62}$$

where $\omega_0 = \beta_0 c/R_0$ is the angular revolution frequency of the synchronous particle with β_0, R_0 denoting the speed and average orbit radius of the synchronous particle, respectively, and h is an integer known as the harmonic number, which also represents the number of equally spaced synchronous positions that can be exhibited along the circular accelerator.

The energy gained by the synchronous particle in each passage through the RF cavity will then be dependent on ϕ_s and equal to $\Delta E = eV_0 \sin(\phi_s)$. However, in a real beam, we will have a spread of particles with different particle momenta, and each of these particles will follow a different orbit, due to the different interactions with the accelerator magnetic lattice. Due to such off-momentum orbit and speed differences, each of these off-momentum particles will have a different revolution frequency than the reference particle and, therefore, will receive a different ΔE from the RF cavity.

In the regime below the transition energy $\gamma < \gamma_{\mathrm{tr}}$, a higher-momentum particle will arrive at the RF cavity ahead of the synchronous particle, i.e. ($\phi_1 < \phi_s$), and will have a lower ΔE than the synchronous particle, causing a decrease in its phase. On the contrary, a particle with a lower momentum will arrive at the RF cavity behind the synchronous particle, i.e. ($\phi_2 > \phi_s$), and have a higher ΔE than the synchronous particle, which causes instead an increase in its phase. In the regime above the transition energy $\gamma > \gamma_{\mathrm{tr}}$, the correlation between the difference in ΔE and phase variation is inverted.

In Fig. 3.4, we show a simple scheme for an accelerating synchronous particle for both regimes. We can observe how the two regimes require the synchronous particle to be at a different RF voltage phase to achieve a stable accelerating regime. In Fig. 3.5, instead, we show a sketch of a stationary synchronous particle above the transition energy, along with the resulting potential well described by the RF voltage frequency.

The resulting motion in the longitudinal plane, related to the potential well given by the RF voltage frequency, is called *synchrotron motion*, which is characterized by *synchrotron oscillations*. The fractional off-momentum deviation is then defined as

$$\delta = \frac{\Delta p}{p_0} = \frac{\omega_0}{\beta^2 E}\frac{\delta E}{\omega_0}\,. \tag{3.63}$$

From this we then obtain the equations of motion for the longitudinal variables.

$$\begin{aligned} \frac{\mathrm{d}\delta}{\mathrm{d}t} &= \frac{\omega_0}{2\pi\beta^2 E} eV_0\left[\sin(\phi) - \sin(\phi_s)\right]\,, \\ \frac{\mathrm{d}\phi}{\mathrm{d}t} &= h\omega_0\eta\delta, \end{aligned} \tag{3.64}$$

where η is the *slip factor* and reads

$$\eta = \frac{\Delta\omega/\omega_0}{\Delta p/p_0}\,, \tag{3.65}$$

and assumes positive values below the transition energy and negative values above the transition energy.

When considering small oscillation amplitudes, we can treat the synchrotron motion as that of a harmonic oscillator, where we consider the linearized equation of motion in the variable $\Delta\phi = \phi - \phi_s$. This approach leads to the differential equation

$$\frac{\mathrm{d}^2}{\mathrm{d}t^2}\Delta\phi - \frac{h\omega_0^2 eV\eta\cos(\phi_s)}{2\pi\beta^2 E}\Delta\phi = 0\,. \tag{3.66}$$

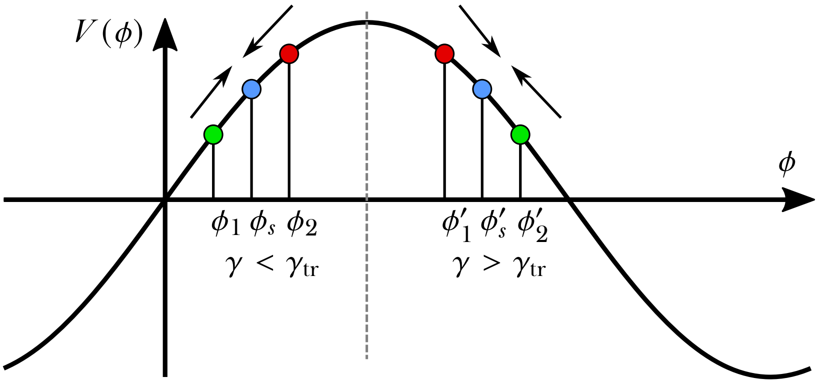

FIGURE 3.4: Sketch of the different V provided at particles with different ϕ for an accelerating synchronous particle, and consequent phase evolution respectively in the regime below transition energy (left, $\gamma < \gamma_{\text{tr}}$), and in the regime above transition energy (right, $\gamma > \gamma_{\text{tr}}$). ϕ_s and ϕ'_s represent the synchronous particle phase at $\gamma < \gamma_{\text{tr}}$ and $\gamma > \gamma_{\text{tr}}$, respectively. ϕ_1 and ϕ_2 are respectively the phase of a particle with higher and lower longitudinal momentum, the same goes for ϕ'_1 and ϕ'_2. The frequency of the RF voltage provides a restoring force towards ϕ_s, causing a different effect on the phase depending on the value of γ.

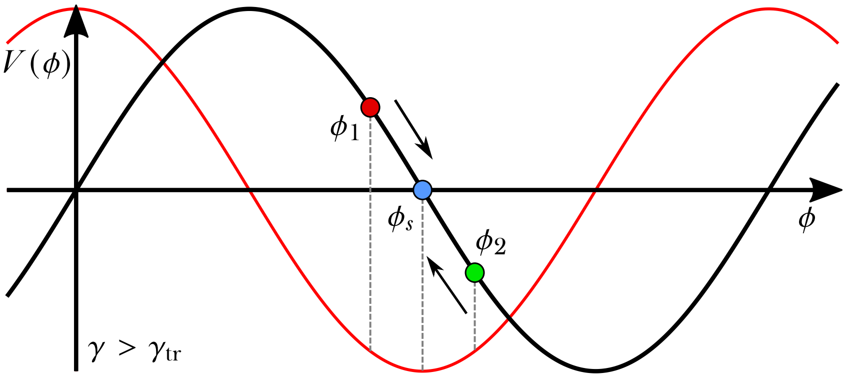

FIGURE 3.5: Sketch of the different V provided at particles with different ϕ for a stationary synchronous particle above transition energy. The synchronous particle ϕ_s receives no energy from the RF voltage, while particles at different phase receive a restoring force towards ϕ_s. The frequency of the RF voltage (black curve) describes a potential well with the minimum corresponding to the synchronous particle (red curve).

We then have the following condition for phase stability

$$\eta \cos(\phi_s) < 0. \tag{3.67}$$

The separatrix given by the equations of motion delimits different stable areas in the phase space. The area of stable motion is called *RF bucket*.

Particles with small off-momentum deviations undergo a synchrotron oscillation during their orbit. This oscillation periodically alters the magnetic lattice effect on their transverse dynamics as well, leading to what we referred to as syncro-betatron coupling.

In the context of particle tracking simulations (which also include longitudinal dynamics, will be a 6D tracking), different sets of longitudinal variables can be used along the transverse ones [61]:

$$\begin{aligned}
&\xi = s\frac{\beta}{\beta_0} - \beta ct\,, &&\tau = \frac{s}{\beta_0} - ct\,, &&\zeta = s - \beta_0 ct\,;\\
&\delta = \frac{p - p_0}{p_0}\,, &&p_\tau = \frac{1}{\beta_0}\frac{E - E_0}{E_0}\,, &&p_\zeta = \frac{1}{\beta_0^2}\frac{E - E_0}{E_0}\,;
\end{aligned} \tag{3.68}$$

where variables in the same columns are canonically conjugate. The different variables can be easily related to each other:

$$\begin{aligned}
&\xi = \beta\tau = \frac{\beta}{\beta_0}\zeta\,,\\
&\delta = \beta p_\tau + \frac{\beta - \beta_0}{\beta_0} = \beta\beta_0 p_\zeta + \frac{\beta - \beta_0}{\beta_0}\,.
\end{aligned} \tag{3.69}$$

Part II

Probing the diffusive behaviour of accelerator systems

4 | Probing the diffusive behaviour in circular accelerators

The content of this chapter, with the due adaptations, has resulted in the article by C. E. Montanari, A. Bazzani, M. Giovannozzi *“Probing the diffusive behaviour of beam-halo dynamics in circular accelerators”*, which has been published in Eur. Phys. J. Plus in November 2022 (Ref. [62]).

In this chapter, the properties of the Fokker-Planck equation (2.55) with diffusion coefficient as in Eq. (2.64), in particular that of the outgoing current at a boundary condition, are studied in detail by means of analytical models and by means of numerical simulations. These analyses are then considered in the context of the transverse losses in a circular accelerator, leading to the definition of an optimal protocol to extract the information about the diffusion coefficient by performing a sequence of well-chosen variations of the position of the boundary condition. An important part of our analysis focuses on the determination of the accuracy and robustness of the proposed protocol, which are key aspects for experimental determination of the form of the diffusion coefficient.

The plan of the chapter is as follows. In Section 4.2, we analyse some important characteristics of the FP process presented in the previous chapter, with a focus on the outgoing current and its behaviour under various conditions, such as stationary or semi-stationary equilibrium. In Section 4.3, we discuss how our model can describe the outgoing currents obtained from outward or inward changes of the position of the boundary condition and how such currents can be split into two processes with distinct timescales. In Section 4.4, the results presented in the previous sections are used to define a protocol to reconstruct the diffusion coefficient of the FP process. The results of detailed numerical simulations are presented and discussed, quantifying the performance of the proposed method. Finally, in Section 4.5 some conclusions are drawn, while details about the numerical integration of the FP process are discussed in Appendix 4.A and some analytical calculations are presented in Appendices 4.B and 4.C.

4.1 | State of the art in diffusion measurements

The concept of using a diffusive model to describe the behaviour of beam halo and characterize the transverse loss rate is not a novel concept, as achieving a valid modelling of such a phenomenon can lead to a better characterization of long-term losses and beam-halo formation.

A rather broad literature exists on the topic of diffusive models applied on accelerator machines, see, e.g. Refs. [8, 13–15, 17–20] and references therein.

An interesting line of research, which provided a valid approach for gathering local information about the value of the diffusion coefficient, is given by the usage of collimator scans presented in [16]. Collimator scans can be used to probe beam-halo dynamics and, in particular, to reconstruct the behaviour of the diffusion coefficient as a function of transverse amplitude [9, 63, 64]. The collimator scan method has been intensively used at the LHC: it is based on small displacements of the jaws combined with the measurement of the beam losses. The displacements can be either inward or outward, and depending on the direction, the local losses feature a different behaviour. Inspection of such features at different amplitudes finally provides local information on the diffusion coefficient.

The latest diffusion measurements, based on [9] diffusive framework, were taken during LHC Run 2 [65], and provided a consistent collection of collimator scan data that provided an overview of the halo diffusive phenomenology [64].

Finally, the framework on which this work is based has been developed and proposed in [6, 7], where the long-term behaviour of beam dynamics and particle losses in circular accelerators is described by means of a global diffusive model. In this framework, the evolution of the beam distribution is described by means of a Fokker-Planck equation, in which the diffusion coefficient represents the key quantity to describe the beam dynamics. An excellent agreement has been observed between the collected data and the predictions from the FP model, where the approach consists of fitting the values of the model parameters I_* and κ to the collected data.

4.2 | Some considerations on Fokker-Planck processes

We treat our problem by using the 1D action variable I, representing the non-linear invariant of the system. We consider the rescaled action variable $I \to I/\sigma^2$, and express the action in units of the RMS beam emittance, and therefore this action will be a dimensionless quantity. A second natural scale of our problem is given by I_*, as can be derived from the functional form of the diffusion coefficient (2.64), and, in fact, in several cases, the analyses presented in the rest of this chapter will be carried out in terms of the dimensionless variable I/I_*.

As for the initial condition for the beam distribution, we use the exponential distribution

$$\rho_0(I) = \exp(-I)\,, \tag{4.1}$$

obtained by the transformation of the standard Gaussian distribution in physical variables. We also note that, for future analysis, it might be interesting to consider beam distributions made of combinations of exponential distributions, as this could be used to simulate the behaviour of a beam with overpopulated tails.

In Ref. [7], a value of κ around 0.33 was found to be the best fit to the data measured during the experimental studies in the LHC, and for this reason this value is used in the numerical simulations presented in this study, although this choice does not hint at any universality of this value. Unless specified, we also consider $\epsilon = 1$ in all simulations.

4.2.1 | Outgoing current

In a generic diffusive process, the outgoing current at the absorbing boundary condition at I_a is defined as

$$J_\mathrm{a}(t) = D(I_\mathrm{a})\frac{\partial \rho(I,t)}{\partial I}\bigg|_{(I_\mathrm{a},t)}\,. \tag{4.2}$$

Equation (2.59) provides a means to obtain an analytical estimate of the current lost at the absorbing barrier (see Appendix 4.B for mathematical details). We consider the change of variable

$$x(I) = -\int_I^{I_\mathrm{a}} \frac{1}{D^{1/2}(I')}\,\mathrm{d}I'\,, \qquad \rho_x(x,t) = \rho(I,t)\sqrt{D(I)}\,, \qquad x_\mathrm{a} = x(I_\mathrm{a}) = 0\,, \tag{4.3}$$

and the FP problem in the Smoluchowsky form

$$\frac{\partial \rho_x}{\partial t} = \frac{1}{2}\frac{\partial}{\partial x}\frac{\mathrm{d}V(x)}{\mathrm{d}x}\rho_x + \frac{1}{2}\frac{\partial^2 \rho_x}{\partial x^2} \quad \text{where} \quad V(x) = -\ln\left(D^{1/2}(x)\right)\,. \tag{4.4}$$

Assuming an initial distribution of the form $\delta(x - x_0)$, where $x_0 \in]-\infty, 0]$, and approximating the potential $V(x)$ at x_0 as $-\nu\, x$, the following expression is obtained for the outgoing current at $x_a = 0$

$$J_\mathrm{a}(x_0, t) = \frac{|x_0|}{t\sqrt{2\pi t}} \exp\left(-\frac{(x_0 + \frac{\nu}{2}t)^2}{2t}\right) , \tag{4.5}$$

where ν, the linearization of the potential (4.4) at x_0 with $D(I)$ given by Eq. (2.64) in the new coordinates has the following expression

$$\nu = \frac{1}{2\kappa}\frac{1}{I(x_0)}\left(\frac{I_*}{I(x_0)}\right)^{\frac{1}{2\kappa}} \exp\left[-\left(\frac{I_*}{I(x_0)}\right)^{\frac{1}{2\kappa}}\right] . \tag{4.6}$$

We note that Eq. (4.5) can be applied to a generic distribution ρ_0 through a convolution.

$$J_\mathrm{a}(t) = \int J_\mathrm{a}(x, t)\rho_x(x)\,\mathrm{d}x . \tag{4.7}$$

We also note that Eqs. (4.5) and (4.6) inevitably provide an underestimate of the actual current lost [66], as the actual drift term is a positive increasing function for $I \ll I_*$. However, we expect an accurate description of local behaviour close to the absorbing boundary condition, i.e. we obtain a good estimate of the current lost for initial distributions that are close enough to the absorbing barrier at $I = I_\mathrm{a}$.

4.2.2 | Stationary system with a constant source

Consider a diffusive process within the region $[I_0, I_\mathrm{a}]$, with an absorbing boundary condition $\rho(I_\mathrm{a}, t) = 0$, and $\rho(I_0, t) = 1$ as a constant source over time. Regardless of the shape of the initial distribution ρ_0, the system will eventually relax to its equilibrium distribution $\rho_\mathrm{eq}(I)$, characterized by a constant outgoing current at I_a. Such a distribution satisfies the following equation

$$\frac{\partial}{\partial I}D(I)\frac{\partial}{\partial I}\rho_\mathrm{eq}(I) = 0 , \tag{4.8}$$

whose solution is given by

$$\rho_\mathrm{eq}(I) = \alpha\int_I^{I_\mathrm{a}} \frac{1}{D(x)}\,\mathrm{d}x , \quad \alpha = \frac{1}{\displaystyle\int_{I_0}^{I_\mathrm{a}} \frac{1}{D(x)}\,\mathrm{d}x} . \tag{4.9}$$

The relaxed system features a constant outgoing current given by

$$J_\mathrm{a}(t) = D(I_\mathrm{a})\frac{\partial\rho_\mathrm{eq}}{\partial I}\bigg|_{(I_\mathrm{a},t)} = \alpha , \tag{4.10}$$

which is directly linked to the integral of the diffusion coefficient. For a Nekhoroshev-like diffusion coefficient, we have the analytical expression

$$\begin{aligned}\rho_{\text{eq}}(I) &= \alpha \int_{I}^{I_{\text{a}}} \exp\left[2\left(\frac{I_*}{x}\right)^{\frac{1}{2\kappa}}\right] \mathrm{d}x \\ &= 2\alpha\ \kappa x \left[-2\left(\frac{I_*}{x}\right)^{\frac{1}{2\kappa}}\right]^{2\kappa} \Gamma\left(-2\kappa, -2\left(\frac{I_*}{x}\right)^{\frac{1}{2\kappa}}\right)\Bigg|_{I}^{I_{\text{a}}},\end{aligned} \tag{4.11}$$

where Γ is the upper incomplete gamma function

$$\Gamma(s, x) = \int_{x}^{\infty} t^{s-1}\, e^{-t}\, \mathrm{d}t\,. \tag{4.12}$$

When the system is out of equilibrium, an analytical description of the outgoing current can be obtained using the formula in Eq. (4.5), where, instead of performing a convolution between Eq. (4.5) and ρ_0, we perform a convolution with $\rho_0 - \rho_{\text{eq}}$. The resulting outgoing current is added to the constant value α (the mathematical details of such procedures are illustrated in Appendix 4.c).

4.2.3 | Semi-stationary regime for a real system

When working with a Nekhoroshev-like diffusion coefficient, its exponentially small values for $I \ll I_*$ generate a stable-core region with extremely low diffusion rates (see Fig. 2.1). This observation can be shown by computing the time of the maximum outgoing current for an initial distribution $\delta(I - I_0)$. We consider the time derivative of Eq. (4.5)

$$\frac{\partial J_{\text{a}}(x_0, t)}{\partial t} = \frac{\sqrt{2}x_0\left[12t + (\nu t - 2x_0)\,(\nu t + 2x_0)\right]}{16\sqrt{\pi t^7}} \exp\left(-\frac{(x_0 + \frac{\nu}{2}t)^2}{2t}\right), \tag{4.13}$$

which is zero for two values of t of opposite sign, and the positive one is

$$t_{\text{max}}(x_0) = \frac{2\left(\sqrt{\nu^2 x_0^2 + 9} - 3\right)}{\nu^2}\,. \tag{4.14}$$

Taking into account the diffusion coefficient of Eq. (2.64) in the change of variable Eq. (4.3), we have that

$$x_0(I_0) = -\int_{I_0}^{I_{\text{a}}} \exp\left[\left(\frac{I_*}{I}\right)^{\frac{1}{2\kappa}}\right] \mathrm{d}I\,. \tag{4.15}$$

We observe that the modulus of the integral of Eq. (4.15) increases exponentially for $I_0 \ll I_*$. Likewise, the value of ν, given in Eq. (4.6), decreases exponentially in the same range of values of I_0, which characterize a strong exponential variation for $t_{\max}$ as a function of I_0. This fact suggests that the contribution to the outgoing current at an absorbing barrier at time t is mainly determined by the initial conditions near I_0, with $t_{\max}(I_0) \approx t$. Therefore, given a generic initial distribution $\rho_0(I)$ and an absorbing boundary condition at I_{a}, after a transient time t, the system relaxes to a condition where the current $J_{\mathrm{a}}(t)$ is determined mainly by $\rho_0(I_0)$, where I_0 satisfies $t_{\max}(I_0) \approx t$. Taking into account the exponential increase in $t_{\max}(I)$, we have a core region that is slowly eroded by the diffusive process. Outside this core region, the system behaves as in a semi-stationary regime, characterized by a very slowly varying source at I_0.

The evolution of this semi-stationary process can be approximated by modifying the α term in Eq. (4.9) as

$$\rho_{\mathrm{eq}}(I, t) = \alpha(t) \int_I^{I_{\mathrm{a}}} \frac{1}{D(x)}\, \mathrm{d}x\,, \tag{4.16}$$

where here $\alpha(t)$ depends on the value of the initial distribution $\rho_0(I_0)$, and can be estimated by

$$\alpha(t) = \frac{\rho_0\left(I_0(t)\right)}{\displaystyle\int_{I_0(t)}^{I_{\mathrm{a}}} \frac{1}{D(x)}\, \mathrm{d}x}\,, \tag{4.17}$$

in which $I_0(t)$ is obtained by inverting Eq. (4.15) to determine $I_0(x_0)$, and Eq. (4.14) to obtain $x_0(t_{\max})$. When the two functions are combined, $I_0(t)$ is determined.

This behaviour can be observed in Fig. 4.1, where a Nekhoroshev-like diffusive process is simulated for a time long enough to reach the semistationary regime. Here, we consider the distribution obtained after prolonging the simulation of the system presented in Fig. 2.1 with $\kappa = 0.33$, and compare it to ρ_{eq} from Eq. (4.9), using α obtained from Eq. (4.17). A global offset between the two curves is observed, which clearly highlights the limits of the approximation.

4.3 | Reconstruction of the diffusion coefficient of a FP process

We now consider the problem of modelling the variation of the outgoing current after a change in position I_{a} of the absorbing boundary condition, under

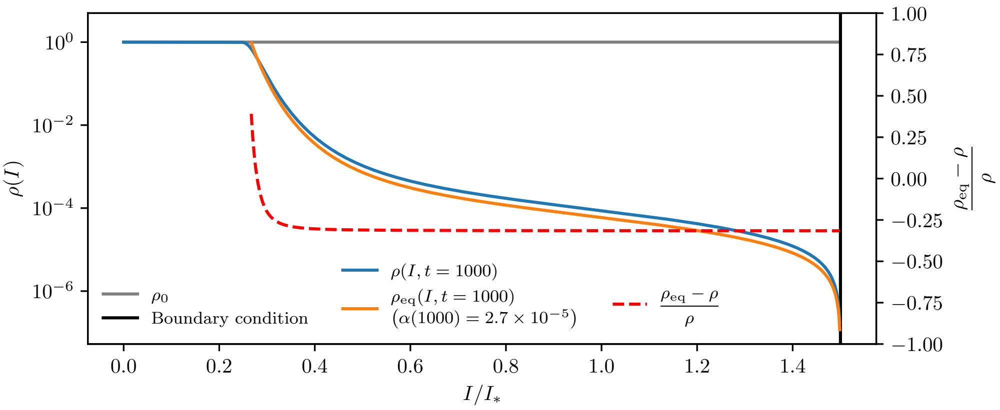

Figure 4.1: Initial uniform distribution for the simulation shown in Fig. 2.1 after numerical integration at $t = 1000$ [a. u.], compared to the estimate of $\rho_{\rm eq}$ from Eq. (4.9), with $\alpha(t)$ computed with Eq. (4.17). (Simulations parameters: ($I_* = 1.0\,[\sigma^2]$, $\kappa = 0.33$)).

the hypothesis that the movement is fast enough to be considered instantaneous and that the movement is performed over a short distance while the system is in the semi-stationary regime described in the previous section. The ultimate goal consists of defining a method to examine the information about the shape of the diffusion coefficient $D(I)$ contained in the outgoing current measured after the instantaneous movement of the boundary condition. This, in view of reconstructing the characteristics of the FP process under analysis, which corresponds to evaluating the values of the two parameters I_* and κ defining $D(I)$.

We define two types of outgoing current, namely *global current*, i.e. the outgoing current observed from a slow core erosion process while keeping the absorbing boundary condition fixed, and *recovery current*, i.e. the current observed after the absorbing boundary condition is instantaneously moved, and the system relaxes to a new semi-stationary regime.

We start by modelling the shape of the recovery current for a stationary system with a fixed source, both for inward and outward movements of the absorbing boundary. Furthermore, we recall that this mimics what is done experimentally when trying to measure the diffusion equation by scanning the position of some collimators jaws [9, 10, 12, 16, 20, 63, 64]. Afterwards, we try to adapt the models to a system in a semi-stationary regime, characterized by a source evolving with time.

4.3.1 | Moving the absorbing boundary condition inwards

Let us consider a system in equilibrium with a constant source $\rho(I_0, t) = 1$, and an absorbing boundary condition $\rho(I_\mathrm{a}, t) = 0$, and assume that the boundary condition is instantaneously moved inwards to $\rho(I'_\mathrm{a}, t) = 0$, with $I_0 < I'_\mathrm{a} < I_\mathrm{a}$. After this change, the equilibrium distribution varies, and the new equilibrium distribution is given by

$$\rho'_\mathrm{eq}(I) = \beta \int_I^{I'_\mathrm{a}} \frac{1}{D(x)}\,\mathrm{d}x\,, \tag{4.18}$$

where β is a constant such that $\rho'_\mathrm{eq}(I_0) = 1$, and compared with the constant α of Eq. (4.9), we have $\alpha < \beta$. The graphs of ρ_eq and ρ'_eq are shown in Fig. 4.2 (top).

To apply the analytical formulae presented in the previous section, we need to calculate the difference distribution $\rho^*(I)$. Assuming that the original system starts from the equilibrium distribution in Eq. (4.9), we obtain

$$\begin{aligned}
\rho^*(I) = \rho_\mathrm{eq}(I) - \rho'_\mathrm{eq}(I) &= \alpha \int_I^{I_\mathrm{a}} \frac{1}{D(x)}\,\mathrm{d}x - \beta \int_I^{I'_\mathrm{a}} \frac{1}{D(x)}\,\mathrm{d}x \\
&= \alpha \left(\int_I^{I'_\mathrm{a}} \frac{1}{D(x)}\,\mathrm{d}x + \int_{I'_\mathrm{a}}^{I_\mathrm{a}} \frac{1}{D(x)}\,\mathrm{d}x \right) - \beta \int_I^{I'_\mathrm{a}} \frac{1}{D(x)}\,\mathrm{d}x \\
&= \alpha \int_{I'_\mathrm{a}}^{I_\mathrm{a}} \frac{1}{D(x)}\,\mathrm{d}x - (\beta - \alpha) \int_I^{I'_\mathrm{a}} \frac{1}{D(x)}\,\mathrm{d}x \\
&= \rho^*_\mathrm{app} - (\beta - \alpha) \int_I^{I'_\mathrm{a}} \frac{1}{D(x)}\,\mathrm{d}x\,.
\end{aligned} \tag{4.19}$$

The shape of $\rho^*(I)$ is shown in Fig. 4.2 (bottom). This function, restricted to the interval $I \in [I_0, I'_\mathrm{a}]$, is increasing monotonically, with a maximum in I'_a. Given the Nekhoroshev-like form of the diffusion coefficient, the decrease to zero when $I \to I_0$ is exponentially fast, while in the region close to I'_a, the function remains almost constant to the value ρ^*_app that can be used as the lowest-order approximation of $\rho^*(I)$.

In Fig. 4.3, we compare the simulated current with its analytical estimate, obtained by computing the convolution with the distribution $\rho^*(I)$ of Eq. (4.19), which are in very good agreement (i.e. with a difference not greater than 10%). In the same figure, the analytical approximation based on the convolution with ρ^*_app is shown, and even in this case the agreement is very good (i.e. with a difference not greater than 10%).

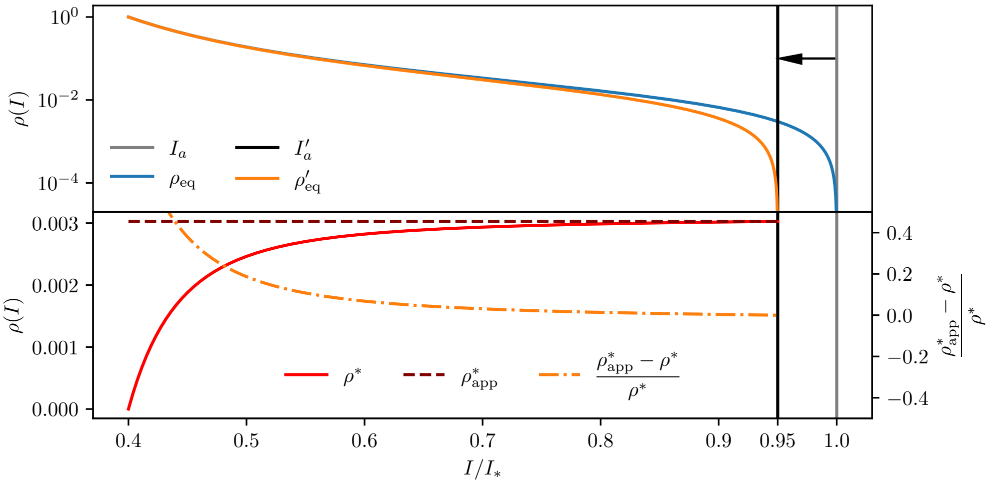

Figure 4.2: Top: Equilibrium distribution for $I_{\rm a}/I_* = 1.0$ compared with the equilibrium distribution for $I'_{\rm a}/I_* = 0.95$. Bottom: Difference between the two equilibrium distributions. (Simulations parameters: $I_* = 1.0\,[\sigma^2]$, $\kappa = 0.33$, $I_0/I_* = 0.4$).

4.3.2 | Moving the absorbing boundary condition outwards

We now consider a system in equilibrium with a constant source $\rho(I_0,t) = 1$, and an absorbing boundary condition $\rho(I_{\rm a},t) = 0$, and assume that this boundary condition is instantaneously moved outward to $\rho(I''_{\rm a},t) = 0$, with $I_0 < I_{\rm a} < I''_{\rm a}$. The new equilibrium distribution is given by

$$\rho''_{\rm eq}(I) = \gamma \int_I^{I''_{\rm a}} \frac{1}{D(x)}\,{\rm d}x\,, \tag{4.20}$$

where γ is a constant such that $\rho''_{\rm eq}(I_0) = 1$, and compared with the constant α of Eq. (4.9), we have $\gamma < \alpha$. The graphs of $\rho_{\rm eq}(I)$ and $\rho''_{\rm eq}(I)$ are shown in Fig. 4.4 (top).

To properly define the difference distribution in the new interval $[I_0, I''_{\rm a}]$, we need to extend the definition of the equilibrium distribution $\rho_{\rm eq}(I)$, namely

$$\rho_{\rm eq}(I) = \begin{cases} \alpha \displaystyle\int_I^{I_{\rm a}} \frac{1}{D(x)}\,{\rm d}x & \text{if } I \le I_{\rm a} \\ 0 & \text{if } I > I_{\rm a}\,, \end{cases}\,, \tag{4.21}$$

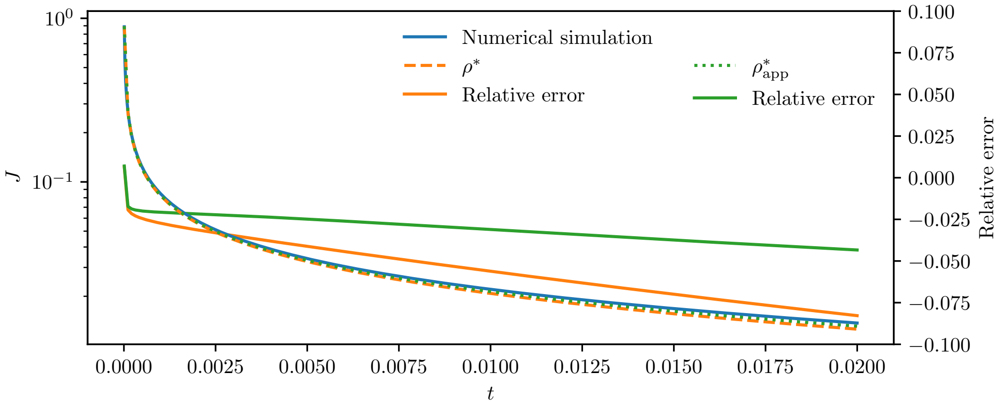

FIGURE 4.3: Comparison between the current generated by the inward displacement of the absorbing boundary condition shown in Fig. 4.2, its analytical estimate based on $\rho^*(I)$, and the analytical estimate based on ρ^*_{app}.

which leads to the following expression for the difference distribution

$$\rho^*(I) = \begin{cases} -\gamma \displaystyle\int_{I_\text{a}}^{I''_\text{a}} \frac{1}{D(x)}\,\mathrm{d}x + (\alpha - \gamma) \displaystyle\int_{I}^{I_\text{a}} \frac{1}{D(x)}\,\mathrm{d}x & \text{if } I \leq I_\text{a} \\ -\gamma \displaystyle\int_{I}^{I''_\text{a}} \frac{1}{D(x)}\,\mathrm{d}x & \text{if } I > I_\text{a}\,, \end{cases} \tag{4.22}$$

which is a negative distribution, with a minimum at I_a and with $\rho^*(I_0) = \rho^*(I''_\text{a}) = 0$.

A plot of $\rho^*(I)$ is shown in Fig. 4.4 (bottom), and we note that this distribution leads to a negative outgoing current that needs to be combined with the stationary current of the equilibrium process to obtain the actual outgoing current.

While in the interval $[I_0, I_\text{a}]$ a constant approximated distribution function can be a reasonable assumption, in the interval $[I_\text{a}, I''_\text{a}]$ a different approximation is needed. Under the assumption that the outward step $I''_\text{a} - I_\text{a}$ is small, a linear approximation from $\rho^*(I_\text{a})$ to $\rho^*(I''_\text{a})$ can be considered, namely

$$\rho^*_{\text{app}}(I) = \begin{cases} -\gamma \displaystyle\int_{I_\text{a}}^{I''_\text{a}} \frac{1}{D(x)}\,\mathrm{d}x & \text{if } I \leq I_\text{a} \\ -\gamma \left(\dfrac{I''_\text{a} - I}{I''_\text{a} - I_\text{a}}\right) \displaystyle\int_{I_\text{a}}^{I''_\text{a}} \frac{1}{D(x)}\,\mathrm{d}x & \text{if } I > I_\text{a}\,. \end{cases} \tag{4.23}$$

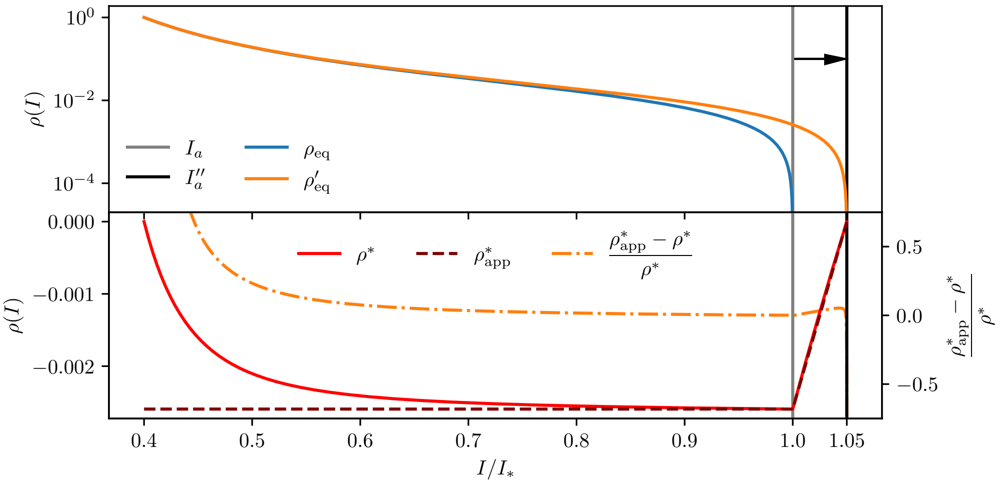

Figure 4.4: Top: Equilibrium distribution for $I_{\rm a}/I_* = 1.0$ compared with the equilibrium distribution for $I''_{\rm a}/I_* = 1.05$. Bottom: Difference between the two distributions. (Simulations parameters: $I_* = 1.0\ [\sigma^2]$, $\kappa = 0.33$, $I_0/I_* = 0.4$).

In Fig. 4.5, we compare the simulated current with its analytical estimate, obtained by computing the convolution with the distribution $\rho^*(I)$ of Eq. (4.22), which is in good agreement (i.e. with a difference not greater than $10-15\%$). In the same figure, the analytical approximation based on convolution with $\rho^*_{\rm app}$ is shown, and even in this case the agreement is excellent (i.e. with a difference not greater than 5%).

4.3.3 | Moving the absorbing boundary condition in a semi-stationary system

In Section 4.2.3 we have seen how it is possible to describe a diffusive process, after a transient time, as a semi-stationary process in which a stable core is slowly eroded over an exponentially long time, with an approximated timescale given by Eq. (4.15). If the position of the absorbing boundary condition is changed when the system is in this semi-stationary state, and the new position is close to the original one, so that it is characterized by a timescale of the same order of magnitude, the stationary part of the system, i.e. the relaxed part outside the stable-core, will relax to a new configuration in a time that is short compared to the timescale of the stable-core erosion.

Being the timescale of the recovery-current process orders of magnitude shorter than the evolution of the global current, the variation of the shape of

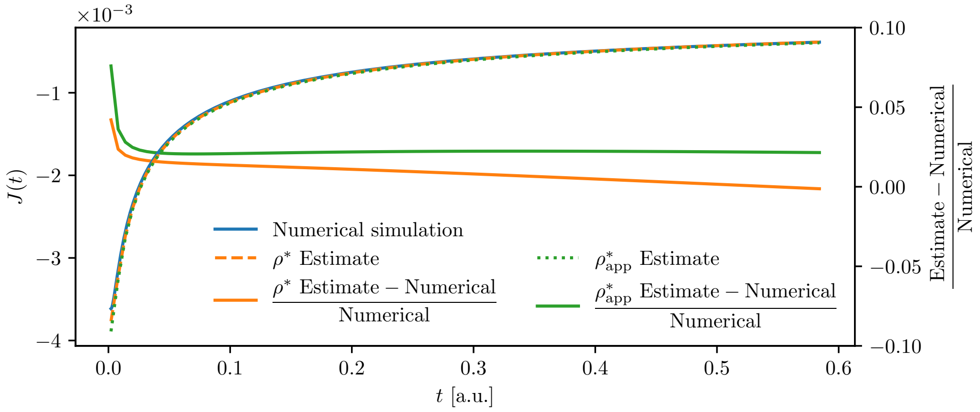

FIGURE 4.5: Comparison between the current generated by the outward displacement of the absorbing boundary condition shown in Fig. 4.4, its analytical estimate based on $\rho^*(I)$, and the analytical estimate based on the approximation ρ^*_{app}.

the core is so slow that it can be neglected. Therefore, we can treat this situation as a source in a fixed position with a slow-varying intensity $\alpha(t)$.

Normalizing a recovery current

Due to the previous assumptions, one can define a normalization procedure to be applied to the recovery current to make it independent of the characteristics of the global current. We are interested in reducing the problem to the ideal case of a constant source at I_0 and a constant unitary outgoing current at the absorbing boundary condition I_a, instead of a system with a slow-varying global current $\alpha(t)$. This approach is tested by simulating the same Nekhoroshev-like FP system twice: first, by keeping the absorbing boundary fixed; second, by executing some instantaneous changes of the absorbing boundary position. With this approach, we gather information on the value of the semi-stationary current $\alpha(t)$, thus enabling the transformation of the process with a moving boundary to a system with a fixed source.

We define the normalized recovery current as the current obtained in the measurement with the moving absorbing barrier divided by the current $\alpha(t)$, obtained in the measurement with fixed boundary. The normalized recovery current has a unitary value when the absorbing boundary condition is not changed and has normalized maximum and minimum, respectively, for the inward and outward movements of the absorbing boundary condition. The behaviour of the normalized recovery current can be related to the ideal stationary systems described above, for which analytical approximations are known.

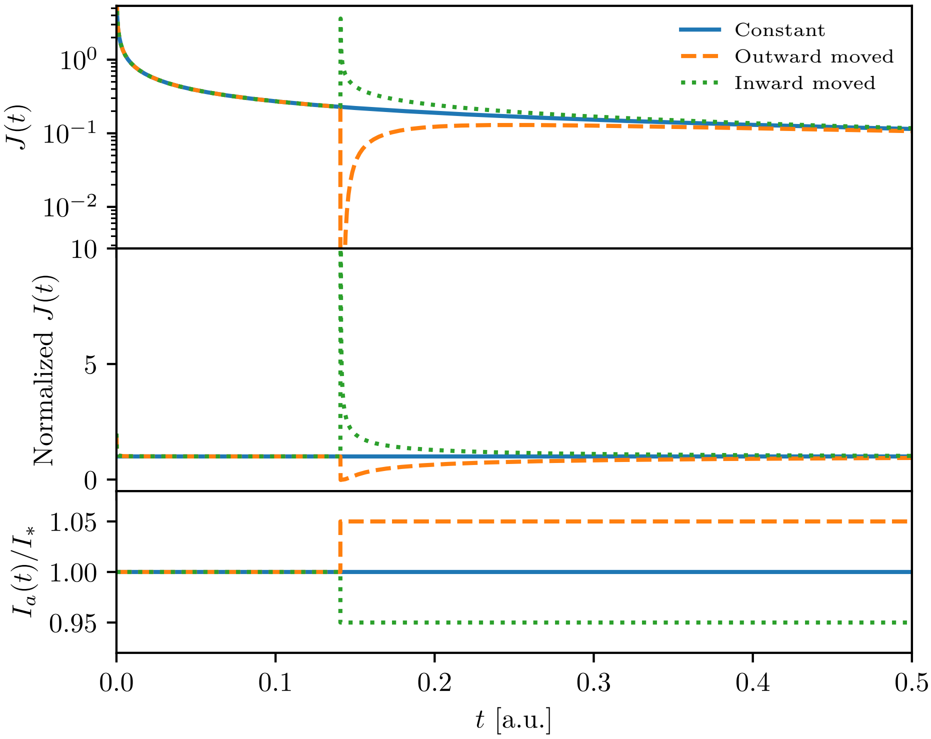

FIGURE 4.6: Top: Evolution of the outgoing current for three diffusive processes with different boundary conditions. Middle: Evolution of the normalized outgoing current. Bottom: Changes to the absorbing boundary condition in the three scenarios. (Simulations parameters: $I_* = 1.0\,[\sigma^2],\ \kappa = 0.33$).

In Fig. 4.6, an example of such a procedure is shown (centre) together with the evolution of the outgoing current (top) and the corresponding variation of the position of the boundary condition (bottom). It is worth mentioning that for every change in I_a the value of $\alpha(t)$ changes according to Eq. (4.17), although for small variations of the absorbing boundary condition, a Taylor expansion can be applied.

Normalizing a recovery current without knowledge of the global current

Whenever it is not possible to repeat two complete measurements in the same process, i.e. one with and one without changes in the position of the boundary condition, the normalization procedure defined previously needs to be adapted.

Ideally, the best strategy consists of waiting long enough after each change in the position of the absorbing boundary to reach an equilibrium and to accomplish the recovery process so that the outgoing current measured before the change in the boundary position and after the long wait is a pure global current. This would approximately correspond to a complete relaxation of the difference distribution resulting from the boundary movement. Therefore, in this way, the outgoing current can be used to reconstruct the shape of the global current and to perform the normalization procedure.

However, some additional hurdles should be considered: Since we do not have prior knowledge of the value of $D(I)$, we do not know the timescales of the recovery currents or those of the core-eroding process. Furthermore, even though a good fraction of the recovery process is achieved very quickly, complete recovery, corresponding to complete relaxation of the difference distribution ρ^*, could take an exponentially long time, possibly beyond the computing capabilities. Hence, it might not be possible to perform such a long measurement in a particle accelerator. Therefore, it is necessary to define a protocol that enables quantitative criteria to establish whether or not an assumed recovery time is long enough to ensure a meaningful reconstruction of the behaviour of the FP process, possibly including an estimate of the uncertainty in the reconstruction of the global current.

A possible solution, compatible with these constraints, consists of the combination of three movements of the boundary condition, where, for each value of the action to be probed, an outward-inward-outward sequence of movements is performed. These three steps must be performed with a fixed movement size ΔI and with a fixed relaxation time Δt between the movement of the boundary condition and the next. The optimal values for ΔI and Δt are discussed in the next section. A visualization of this protocol is provided in Fig. 4.7 (bottom), where the change in the boundary condition in three steps is highlighted and repeated three times, and the corresponding evolution of the outgoing current is given (top), calculated from numerical simulations. For comparison, the situation corresponding to the constant position of the boundary condition is also shown.

We remark that variants of the proposed three-step movement are indeed possible and that this proposal is also motivated by the wish not to introduce unnecessary complications. It is also important to stress that the assumption of performing small and equal movements of the position of the absorbing barrier for the three steps implies that Δt should also be the same for the steps, since the relaxation time should be approximately the same for all steps.

This three-step sequence of absorbing-barrier changes is performed at different values of the global current, and this basic sequence can be repeated by performing it at different action values. The resulting sequence of alternating recovery currents provides an approximation of the evolution of the global current with a sequence of upper- and lower-bound values at different times, which can be interpolated and used for the construction of a global current estimate. These limits provide a degree of uncertainty directly related to the chosen value Δt, as the longer Δt, the lower the degree of uncertainty in the reconstruction of the global current. A more detailed discussion of a possible quantitative definition of the optimal choice of the relaxation timescale Δt, together with the effects of using shorter relaxation times, is discussed in the next section.

To reconstruct the global current, an upper- and lower-bound estimate are derived by considering the last values of the inward and outward recovery currents, respectively. Two extra points are added to the upper- and lower-bound estimates, with the goal of covering the maximum time span for reconstructing the global current: The last measured global current value before the first boundary movement is added to both estimates; the last value of the last recovery current measured, which, being an outward recovery current, was already part of the lower-bound estimate, is also added to the upper-bound estimate. This explains why in Fig. 4.8 (centre) the estimates coincide at the beginning and end of the interpolation interval. The two sets of upper-bound and lower-bound points are each interpolated with a univariate cubic spline, and the average function of these two interpolating functions is taken as the estimate of the global current.

We remark that the univariate cubic spline is taken with a number of knots so that the second derivative does not change sign. This ensures that the resulting global current estimate meets the expected features of the actual global current. In particular, it avoids local oscillations that might be generated by a simple interpolation of the upper-bound and lower-bound points. The result of this approach is shown in Fig. 4.8 where a fraction of the data presented in Fig. 4.7 is used to reconstruct the global current, and an excellent general agreement (i.e, with a difference not greater than 5%) with the actual global current is clearly visible.

4.3.4 | Reconstructing $D(I)$ from the normalized recovery currents

After the proposed reconstruction protocol is performed, a series of normalized recovery currents, obtained for different positions of the boundary condition, are available. All these curves are then used to reconstruct the shape of $D(I)$ using a fit procedure.

Thanks to the normalization procedure, every normalized recovery current can be considered as an individual and independent relaxation process, as in a system in equilibrium with a fixed source. Therefore, we can consider as ex-

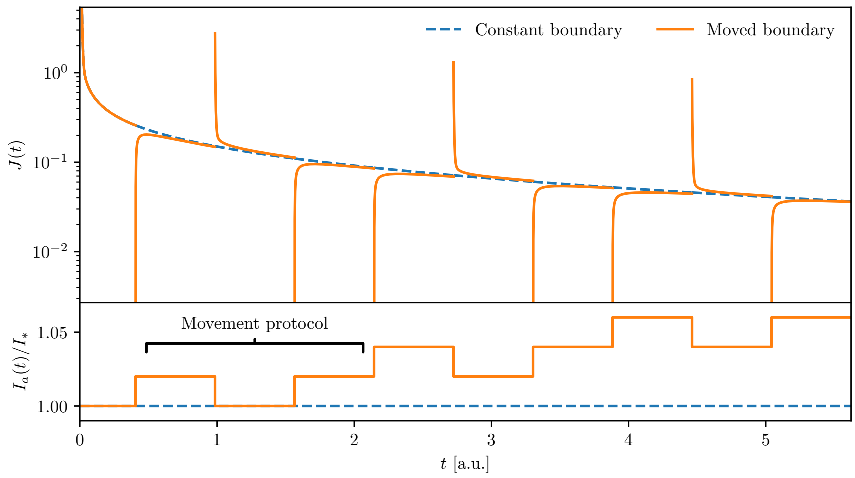

FIGURE 4.7: Example of the proposed three-step protocol with a direct comparison between the condition with and without the variations in the position of the absorbing boundary condition. In this figure, the protocol is executed three times. The top plot shows the evolution of the outgoing current, while the bottom one shows the corresponding evolution of the position of the absorbing boundary condition. Note how the repetition of the three-step protocol moves progressively the absorbing boundary outwards. (Simulations parameters: $I_* = 1.0\ [\sigma^2],\ \kappa = 0.33$).

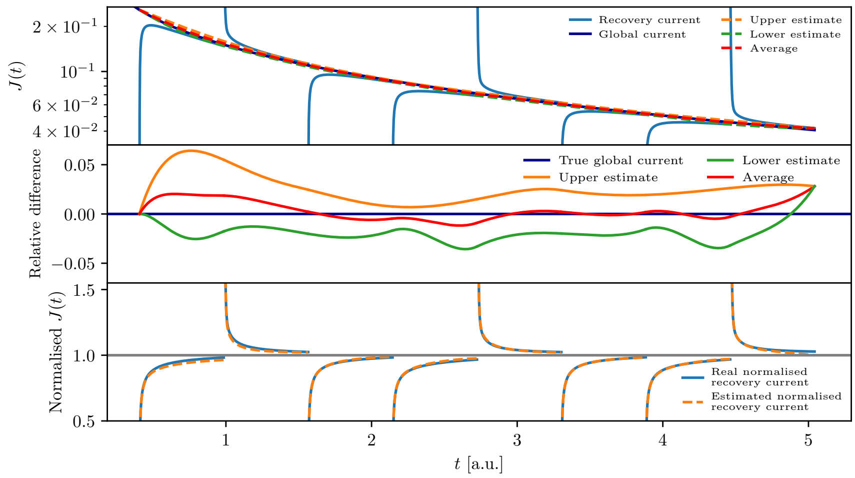

FIGURE 4.8: Example of the reconstruction process of the global current applied to a fraction of the data shown in Fig. 4.7. Top: Outgoing current from the process with constant boundary (dark blue) and with varying boundary conditions (light blue), along with the three components of the interpolation process. Middle: Relative difference, between the lower, average, or upper estimate of the global current and the true global current, of the interpolation procedure. Bottom: Comparison between the actual recovery current and the reconstructed one.

pected current the convolution of the analytical current, presented in Eq. (4.5), with one of our approximated difference distribution ρ^*, according to Eq. (4.7). From a normalized recovery current obtained from an inward movement, we expect a relaxation curve characterized by an equivalent process with an initial distribution given by Eq. (4.19), where the value of ρ^*_{app} is calculated considering $\alpha = 1$, due to the normalization performed, the integral being calculated over the appropriate action interval. Likewise, for a recovery current from an outward movement, we expect a curve characterized by an equivalent process with an initial distribution given by Eq. (4.23), where we consider $\gamma = 1$, due to the normalization performed, the integral being computed over the appropriate action interval. Assuming a Nekhoroshev-like form for $D(I)$, the goal is to determine the values of the two parameters I_* and κ, which is obtained by a standard non-linear least squares algorithm applied to the currents obtained during the execution of the proposed protocol. The strong non-linearity of the functions involved in the least-squares fit makes the reconstruction of I_* and κ a difficult task, and alternative approaches have been tried. A possibility consists in performing a coarse scan of the (I_*, κ) parameter space to identify an initial guess of the model parameters, and then performing a finer scan around the initial guess. In this approach, the distance between the numerical value of the recovery current and the one obtained from the analytical model for a given pair of (I_*, κ) values is evaluated, and the minimum provides either the initial estimate of the parameters or their optimal value. This strategy has been successfully applied to the analysis of beam data reported in [67]. Another aspect of the fit is the strong correlation between the model parameters, typically of the order of a Pearson product-moment coefficient of 0.9, which is likely linked with the strongly non-linear function to be minimized. The impact of the strong correlation between the model parameters can be mitigated by the approach based on parameter scanning rather than looking for the minimum with standard routines to perform numerical optimization.

4.4 | Numerical results

To test the validity of the proposed procedure and obtain a complete overview of its performance and limitations in the reconstruction of $D(I)$, several numerical simulations of diffusive processes with a Nekhoroshev-like diffusion coefficient have been performed using the protocol described in Section 4.3. Special emphasis is placed on establishing the reliability of the proposed procedure as a function of the values of ΔI and Δt used in the protocol of variation of the position of the boundary conditions.

4.4.1 | Simulation parameters

As an initial condition, we consider the distribution in Eq (4.1), and note that all action variables are dimensionless and expressed either in units of sigma of the beam or in units of I_*. We then consider a Nekhoroshev-like diffusive system characterized by the parameters obtained from the studies reported in Ref. [7], namely $I_* = 20.0\ [\sigma^2]$, $\kappa = 0.33$. Such a system, as can be seen from Figs. 2.1 and 4.1, is compatible with the semi-stationary regime and hence with the application of the proposed procedure.

Different values of the starting position I_a/I_* of the absorbing boundary condition have been considered. Although most of our assumptions are valid for the $I_a/I_* < 1$ regime, we also consider starting positions near I_* and beyond I_*, i.e. in the saturation region of $D(I)$, to evaluate how robust the method is under non-ideal conditions.

For each configuration, after an initial time delay when a semi-stationary regime is reached, ten repetitions of the three-step protocol (outward-inward-outward), shown in Fig. 4.7, have been performed. Several values of ΔI, i.e. the action change of the position of the boundary condition, have been used to assess the presence of an optimal value for the reconstruction procedure. We observe that at the end of a simulation, the position of the absorbing boundary condition has changed from I_a/I_* to $(I_a + 10\Delta I)/I_*$.

Several relaxation time values Δt have been considered to evaluate reconstruction performance at different levels of equilibrium. We note that an empirical relaxation time has been defined as the time for which a normalized recovery current is expected to recover the 99.9% of the value of the original global current. This ideal time is computed using full knowledge of $D(I)$, using our analytical current estimate Eq. (4.5), and considering an outward movement of the absorbing boundary condition of size ΔI from the initial position of the absorbing boundary. It is stressed that, in general, we should assume that such relaxation time is not known when reconstructing the value of the diffusion coefficient. It is also worth mentioning that a criterion based on a complete 100% recovery of the global current cannot be used in practice, as this would require exponentially long simulation times needed to reach the relaxation of the inner part of the distribution, with negligible differences with respect to the 99.9% case. Different fractions of this ideal time have been used when performing our procedure, and we evaluate how times shorter than the ideal relaxation time impact the quality of our final fit, as the system is still in a non-equilibrium regime when the next absorbing boundary movement occurs.

When working with the data sets generated by the various numerical simulations, a post-processing step is performed on the normalized recovery currents before executing the final fit procedure for reconstruction of $D(I)$. It consists of selecting a fraction of the data representing the normalized recovery currents, i.e. only the normalized recovery current data up to a given percentage of the full recovery. For example, if we decide to filter out normalized data beyond the 90% recovery, it means that we discard values that are lower than 1.1 for inward normalized recovery currents and values that are higher than 0.9 for outward normalized recovery currents. We recall that, in the context of a normalized recovery current, a full recovery implies a value of 1.0 as a normalized recovery current.

This post-processing step is shown in Fig. 4.9, where two different values of the fraction of the relaxation time between boundary movements are used in numerical simulations. In both simulations, the boundary movement starts after an equal waiting time. In the left plot, the normalized recovery currents, reported in Fig. 4.8, are shown together with two different filtering levels. On the right, the same system is simulated using a shorter fraction of the relaxation time, and the recovery currents are shown together with the same filtering levels presented in the left plot. The much shorter time leads to only a partial recovery of the currents between boundary condition changes. For these sets of normalized recovery currents, the filtering levels displayed lead to almost no data reduction.

By selecting different levels of data filtering, it is possible to assess how this choice affects the accuracy of the reconstruction of $D(I)$. It should be noted that our analytical approximation of Eq. (4.5) performs best when describing the evolution of a distribution near the absorbing boundary condition [66]. Furthermore, the recovery current features an exponential-like decay that makes the analytical approximation less accurate over long timescales. For this reason, investigating the dependence of the reconstruction performance on the fraction of data selected is very relevant.

4.4.2 | Analysis of the reconstruction performance

Numerical exploration of the FP process involves a scan of several simulation parameters, leading to a large hyperspace of possible configurations. For this reason, we focus on the most ideal configurations, i.e. those that provide the best reconstruction performance, and then show how the other parameters affect the reconstruction accuracy of I_* and κ.

After each execution of the proposed three-step protocol described in Section 4.3 and shown in Fig. 4.7, we end up with two outward and one inward recovery currents. In every configuration explored, we observe better reconstruction results when only the recovery currents from the outward step are considered. On the other hand, considering only the inward recovery currents or all currents simultaneously, poorer performance and numerical instabilities

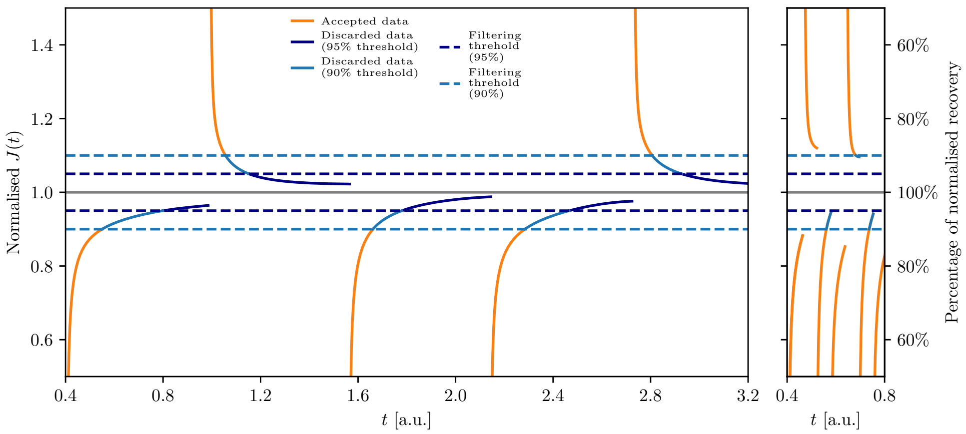

FIGURE 4.9: Left: normalized recovery current, shown already in Fig. 4.8, together with two filtering levels. The boundary movements are performed after an initial evolution time $t = 0.4$ [a. u.], and the relaxation time Δt between one boundary movement and the next one is equal to $\Delta t = 0.58$ [a. u.]. Right: the same system is simulated with the same initial evolution time $t = 0.4$ [a. u.] and one order of magnitude shorter relaxation time $\Delta t = 0.058$ [a. u.], the resulting normalized recovery currents have not relaxed long enough to reach the 95% filtering level. When the selected filtering level is not reached by the normalized recovery currents, the whole dataset is used for the fit reconstruction and no parts are discarded.

are observed. This is explained by the fact that when the position of the absorbing boundary is moved inward, we are cutting in a distribution that is not necessarily in the perfect equilibrium configuration defined in our approximations. On the other hand, when we move the boundary condition outward, we obtain a much more reliable observable of the distribution that populates the new available action interval, when evolving towards the new equilibrium state. It is possible to observe this behaviour in Fig. 4.10, where the relative error in the reconstruction of κ and I_* is shown for the three types of fit as a function of the fraction of the ideal relaxation time Δt for two values of I_a/I_*, representing the inner part of the stable-core region (left) and close to the regime change of $D(I)$ (right). In the inner region, even small fractions of relaxation time provide a good reconstruction of the fit parameters (i.e. with a difference not greater than $10 - 15\%$). Furthermore, the three types of analysis, based on outward-only, inward-only, and inward and outward recovery currents, provide results with comparable accuracy for longer fractions of the relaxation time.

However, in the transition region, only longer fractions of relaxation time provide a good reconstruction of the fit parameters (i.e. with a difference not

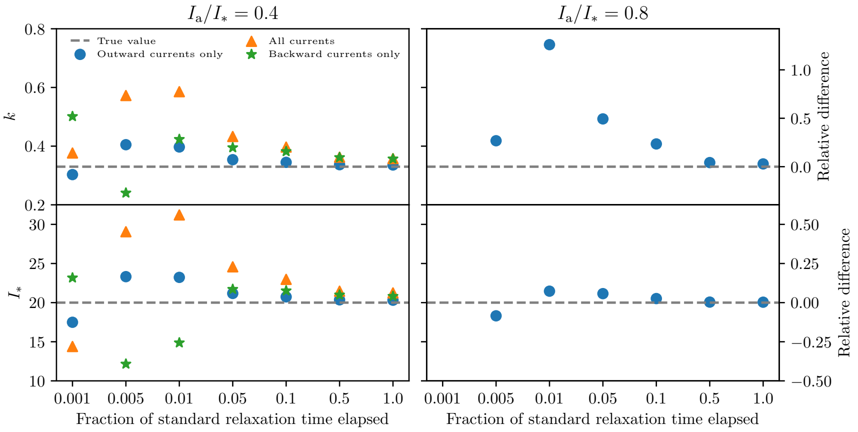

Figure 4.10: Fit results for I_* and κ as a function of the relaxation time Δt for two values of I_a/I_*, using different subsets of the numerical data. Left: for $I_a/I_* = 0.4$, a good reconstruction performance (i.e. with a difference not greater than 20%) is observed even for short fractions of the ideal relaxation time. A rather similar performance is observed for the three types of analysis, the one based on the outward currents having the best performance. Right: for $I_a/I_* = 0.8$, only the cases corresponding to longer fractions of the relaxation time feature a good performance. Moreover, only the analysis based on the outward currents is displayed, as the other two features either failures or large errors in the fit. (Simulation parameters: initial $I_a/I_* = 0.4$, boundary step $\Delta I = 0.1\sigma^2$, 10 repetitions of the three-step procedure, data up to a maximum current recovery of 90%).

greater than 20%) and the only applicable type of analysis is based on outward recovery currents. The other two analyses feature failures or larger errors in the fit, which are generated by the behaviour of the inward recovery current. Based on the observed behaviour, in the following plots, we will display only results from the reconstruction based on the outward recovery currents. The reasons for the poor performance of the reconstruction of I_* and κ when inward recovery currents are considered are at least twofold. The first reason stems from the fact that by cutting the distribution with the inward movement of the boundary condition, the system enters a non-equilibrium regime, in which the recovery current features sizeable variations. If enough time passes, the system reaches a new equilibrium, and the recovery current is much more reliable for the reconstruction of I_* and κ, as observed in Fig. 4.10. The second reason is of purely numerical origin, but somewhat linked to the first one, as when an inward step is performed, the equilibrium distribution is cut and the sharp edge needs to be smoothed by applying a logistic function to the cut distribution

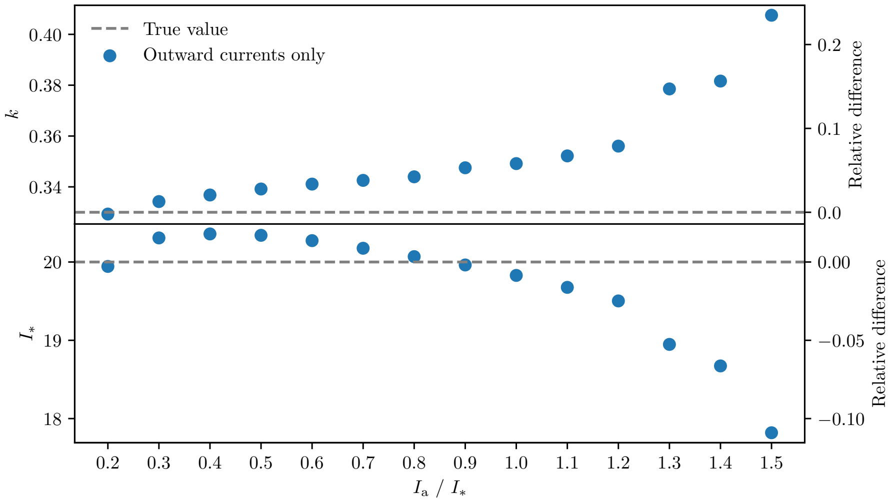

Figure 4.11: Fit results for I_* and κ as a function of the initial value of I_a/I_*. The reconstruction performance is excellent for $I_a/I_* \le 1$, while for larger values the relative error increases. (Simulation parameters: boundary step $\Delta I = 0.1\sigma^2$, relaxation time $\Delta t = 0.5$, 10 repetitions of the three-step procedure, data up to a maximum current recovery of 90%).

(see the discussion in Appendix 4.A). This has potentially harmful effects on the generated recovery current, which is subsequently used to reconstruct the model parameters. Note that the first argument is even more applicable to the case of data from beam experiments, as observed from the data analyses carried out recently and discussed in Ref. [67].

In Fig. 4.11, the reconstruction error for the two fit parameters is shown as a function of the starting position of the absorbing boundary I_a/I_*. Performance is excellent for $I_a/I_* \le 1$ (i.e. with a difference not greater than 5%), while outside this region the reconstruction error increases. This behaviour is to be expected, as a recovery current mainly carries local information about $D(I)$. Therefore, if only the region $I_a/I_* > 1$ is sampled, the information about $D(I)$ reflects only its quasi-linear regime (see Fig. 2.1). Such incomplete information inevitably affects the performance of the final fit, as it prevents an accurate reconstruction of the strongly non-linear part of the diffusion coefficient. This result also suggests that, after the fit parameters have been determined, one can verify whether the action interval explored was suitable for an accurate reconstruction of the functional form of the diffusion coefficient.

The plots in Fig. 4.11 provide some insight into the dependence of the reconstruction performance as a function of a single parameter, while the others

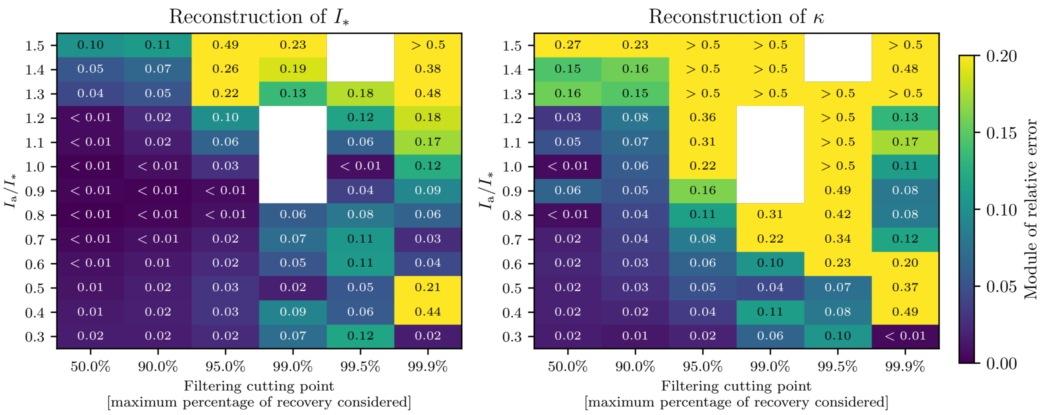

Reconstruction of I_*

I_a/I_*	50.0%	90.0%	95.0%	99.0%	99.5%	99.9%
1.5	0.10	0.11	0.49	0.23		> 0.5
1.4	0.05	0.07	0.26	0.19		0.38
1.3	0.04	0.05	0.22	0.13	0.18	0.48
1.2	< 0.01	0.02	0.10		0.12	0.18
1.1	< 0.01	0.02	0.06		0.06	0.17
1.0	< 0.01	< 0.01	0.03		< 0.01	0.12
0.9	< 0.01	< 0.01	< 0.01		0.04	0.09
0.8	< 0.01	< 0.01	< 0.01	0.06	0.08	0.06
0.7	< 0.01	< 0.01	0.02	0.07	0.11	0.03
0.6	< 0.01	0.01	0.02	0.05	0.11	0.04
0.5	0.01	0.02	0.03	0.02	0.05	0.21
0.4	0.01	0.02	0.03	0.09	0.06	0.44
0.3	0.02	0.02	0.02	0.07	0.12	0.02

Reconstruction of κ

I_a/I_*	50.0%	90.0%	95.0%	99.0%	99.5%	99.9%
1.5	0.27	0.23	> 0.5	> 0.5		> 0.5
1.4	0.15	0.16	> 0.5	> 0.5		0.48
1.3	0.16	0.15	> 0.5	> 0.5	> 0.5	> 0.5
1.2	0.03	0.08	0.36		> 0.5	0.13
1.1	0.05	0.07	0.31		> 0.5	0.17
1.0	< 0.01	0.06	0.22		> 0.5	0.11
0.9	0.06	0.05	0.16		0.49	0.08
0.8	< 0.01	0.04	0.11	0.31	0.42	0.08
0.7	0.02	0.04	0.08	0.22	0.34	0.12
0.6	0.02	0.03	0.06	0.10	0.23	0.20
0.5	0.02	0.03	0.05	0.04	0.07	0.37
0.4	0.02	0.02	0.04	0.11	0.08	0.49
0.3	0.02	0.01	0.02	0.06	0.10	< 0.01

Figure 4.12: 2D view of the reconstruction performance as a function of the cut in the recovery current, as applied in Fig. 4.9, and of the initial value of I_a/I_*. It is clearly seen how certain values of the cut provide a consistent increase in reconstruction performance. White regions indicate a failure in convergence in the final fit procedure. (Simulation parameters: relaxation time $\Delta t = 1$, boundary step $\Delta I = 0.1\sigma^2$, 10 repetitions of the three-step, data up to a maximum current recovery of 90%).

are kept fixed. However, in the following figures, the relative error of the reconstruction procedure is shown as a function of two parameters. The colour code represents the relative difference between the reconstructed values (from the proposed protocol) and the true values (used in numerical simulations of FP processes) of I_* and κ that describe $D(I)$. The scale is limited to a relative difference of 20%, which is assumed as a threshold to identify poor performance. Note that the white cells represent the cases in which the reconstruction procedure failed.

Figure 4.12 shows the relative error as a function of the cut in recovery current performed during post-processing and I_a/I_*. The performance of the reconstruction approach improves when the recovery currents are cut. This depends on the fact that our approach is local, i.e. accurate to describe the system's behaviour close to the boundary condition. The longer the recovery time, the less local the information collected from the current. For this reason, the reconstruction performance plots are based on recovery currents cut at 90%.

Regarding the reconstruction performance as a function of the relaxation time Δt, Fig. 4.13 shows the behaviour, including the dependence on I_a/I_*. In this case, the longer the relaxation time, the better the reconstruction performance. In particular, longer relaxation times allow for a better reconstruction even for large values of I_a/I_*. It should be noted that, in the case of short relaxation times, good overall performance can only be achieved by working at $I/I_* \ll 1$. Combining the results of the last two analyses, we conclude that the

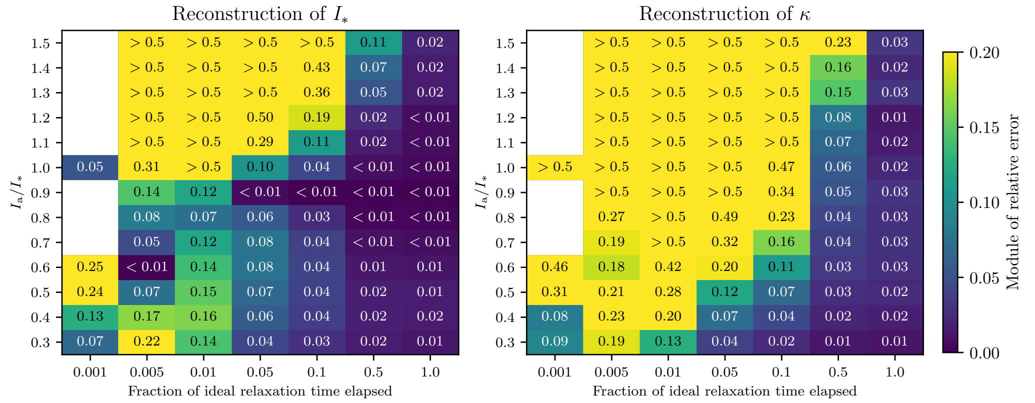

FIGURE 4.13: 2D view of the reconstruction performance as a function of the relaxation time Δt and the initial value of I_a/I_*. It is clearly seen how the reconstruction performance improves for longer relaxation times. However, the method proves to be rather robust for fractions of ideal time up to 5% provided $I_a/I_* < 0.6$. White regions indicate a failure in convergence in the final fit procedure. (Simulation parameters: boundary step $\Delta I = 0.1\sigma^2$, 10 repetitions of the three-step procedure, data up to a maximum current recovery of 90%, if smaller values of Δt lead to a normalized recovery below 90%, all the normalized recovery current data are used for the reconstruction).

best approach to an accurate determination of I_* and κ consists of increasing the relaxation time between successive changes in the position of the boundary condition and cutting the data from the recovery currents.

Figure 4.14 shows the 2D plot of reconstruction performance as a function of the number of repetitions of the three-step procedure and I_a/I_*. It can be seen with the higher number of repetitions how the performance improves. This is naturally linked to the fact that repeating the three-step procedure implies sampling a larger extent of the phase space, thus probing more accurately the behaviour of the diffusion coefficient as a function of the action. It is also clearly visible that from six repetitions of the three-step procedure, a good reconstruction is obtained for $I_a/I_* < 1$.

Finally, the impact of ΔI is shown in Fig. 4.15, where the performance is represented as a function of ΔI and I_a/I_* is represented. We see that performance is not strongly affected by the choice of ΔI, i.e. relative error fluctuations are less than 10% for differences of an order of magnitude in ΔI. However, it is important to highlight two facts that could suggest a choice in the size of the change in position of the absorbing boundary condition: (1) the ideal relaxation time is directly proportional to the size of the absorbing boundary movement; (2) a too small ΔI could lead to a too local sampling in the action space, thus

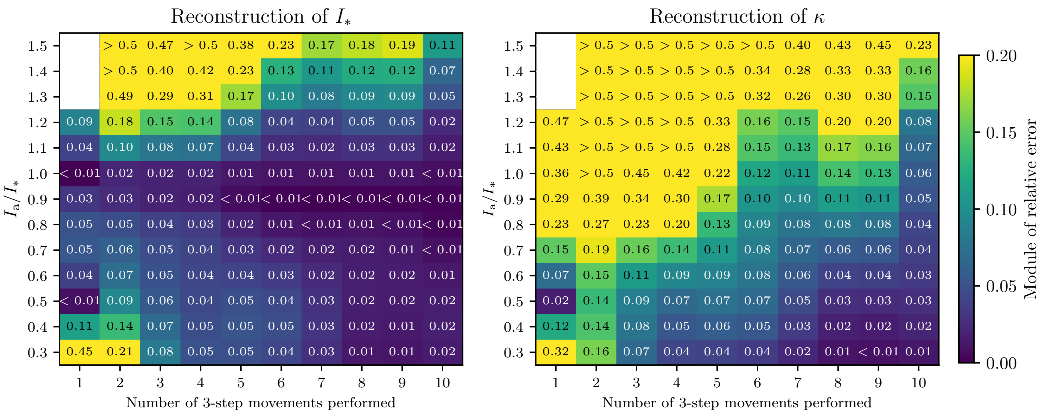

FIGURE 4.14: 2D view of the reconstruction performance as a function of the number of three-step movements and of I_a/I_* starting positions. It is clearly seen how the performance increases with the number of three-step movements, as larger regions of phase space are explored (as in Fig. 4.7). White regions indicate a failure in convergence in the final fit procedure. (Simulation parameters: relaxation time $\Delta t = 0.5$ [a. u.], boundary step $\Delta I = 0.1\sigma^2$, which is $\Delta I/I_* = 0.005$, data up to a maximum current recovery of 90% is considered).

negatively affecting the final reconstruction of $D(I)$.

4.5 | Final remarks

Beam-halo scans, performed with movable collimator jaws, have been used intensively to study the diffusive behaviour of the beam halo in circular accelerators and seem to be a very useful tool to study this special regime of beam dynamics in the absence of beam instrumentation capable of providing diagnostic tools to study beam-halo dynamics.

The main result of this chapter is the identification of an efficient protocol to test the shape of a diffusion coefficient consistent with the stability time estimate of the Nekhoroshev theorem. The protocol has been scrutinized by means of detailed numerical simulations, but it is clear that eventually it should be tested with beam measurement data. Two aspects should be highlighted: although the framework presented in this article is one-dimensional, i.e. considering non-linear beam dynamics in one degree of freedom, we believe that it can be applied to cases representing systems with two degrees of freedom (as shown in Ref. [7]). Furthermore, the proposed approach does not rely on previous knowledge of the beam distribution, which is a clear advantage for applications.

The proposed protocol relies on the idea that it is possible to separate the

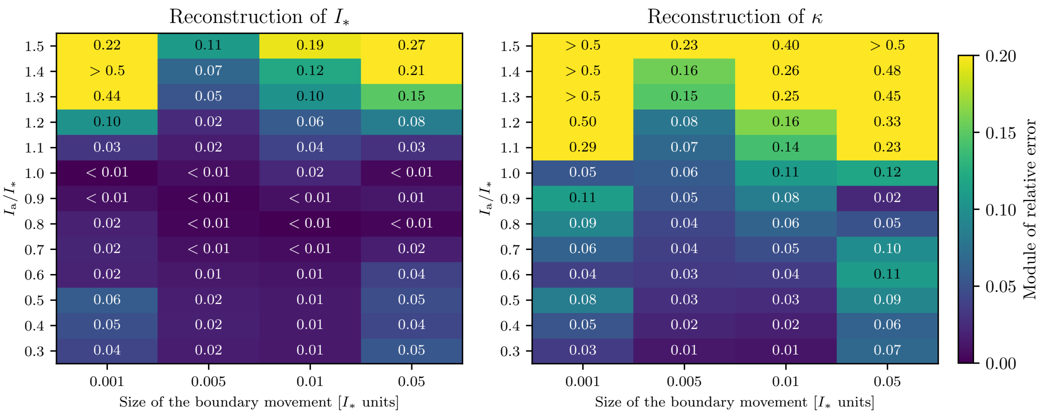

Reconstruction of I_*

I_a/I_*	0.001	0.005	0.01	0.05
1.5	0.22	0.11	0.19	0.27
1.4	> 0.5	0.07	0.12	0.21
1.3	0.44	0.05	0.10	0.15
1.2	0.10	0.02	0.06	0.08
1.1	0.03	0.02	0.04	0.03
1.0	< 0.01	< 0.01	0.02	< 0.01
0.9	< 0.01	< 0.01	< 0.01	0.01
0.8	0.02	< 0.01	< 0.01	< 0.01
0.7	0.02	< 0.01	< 0.01	0.02
0.6	0.02	0.01	0.01	0.04
0.5	0.06	0.02	0.01	0.05
0.4	0.05	0.02	0.01	0.04
0.3	0.04	0.02	0.01	0.05

Reconstruction of κ

I_a/I_*	0.001	0.005	0.01	0.05
1.5	> 0.5	0.23	0.40	> 0.5
1.4	> 0.5	0.16	0.26	0.48
1.3	> 0.5	0.15	0.25	0.45
1.2	0.50	0.08	0.16	0.33
1.1	0.29	0.07	0.14	0.23
1.0	0.05	0.06	0.11	0.12
0.9	0.11	0.05	0.08	0.02
0.8	0.09	0.04	0.06	0.05
0.7	0.06	0.04	0.05	0.10
0.6	0.04	0.03	0.04	0.11
0.5	0.08	0.03	0.03	0.09
0.4	0.05	0.02	0.02	0.06
0.3	0.03	0.01	0.01	0.07

FIGURE 4.15: 2D view of the reconstruction performance as a function of ΔI and I_a/I_*. The best performance is achieved for $\Delta I = 0.005\sigma^2$, but the dependence on ΔI is very weak (Simulation parameters: relaxation time $\Delta t = 0.5$ [a. u.], 10 repetitions of the three-step procedure, data up to a maximum current recovery of 90%).

measured outgoing current into a global current, i.e. the general outgoing current loss that is measured from the exponentially slow erosion of the stable core of the beam, and a recovery current, i.e. the current following a change of the position of the boundary condition, which corresponds to a non-equilibrium state. By performing an alternating three-step sequence of outward-inward-outward boundary-condition changes, which can easily be done by means of collimator scans, it is possible to reconstruct the global current of the erosion process and use that to normalize the recovery currents. Each normalized recovery current ultimately contains local information on the diffusion coefficient without the need of prior knowledge on the form of the initial distribution in the action space and can be used for estimating its global shape.

The performance of this protocol has been tested by means of many numerical simulations of Fokker-Planck processes performed in various configurations to evaluate the reliability and limits of our approach. The protocol was shown to be capable of reconstructing with precision and good accuracy (i.e. with an error not greater than $10 - 15\%$) the diffusion coefficient parameters when performed in a phase-space region where the diffusion coefficient has an exponential evolution, i.e. for $I/I_* < 1$, the relaxation time between changes in the boundary conditions is long enough so that the system reaches an equilibrium state and multiple amplitudes have been probed. For this last condition, the optimal number of amplitudes to be sampled is highly dependent on the detail of the diffusion process; however, from the simulations it appears that about six sequences of three-step absorbing boundary changes covering the $I/I_* < 1$ region are a good choice.

The analysis also highlighted how good reconstruction performance can be achieved by considering only the outgoing recovery currents in the final fitting reconstruction and by discarding part of the recovery current data beyond a certain level, as it is more prone to reconstruction errors and more difficult to characterize with our analytical formulas. It is worth stressing that the reconstruction performance proves to be good even if the optimal conditions are not met. Most importantly, the procedure provides useful information on possible shortcomings present in the data set under consideration, such as a high uncertainty band in the global current reconstruction, or a reconstructed value of I_* that indicates that the probed phase-space region is outside the optimal interval $I/I_* < 1$. In these cases, the protocol should be reapplied under better conditions, e.g. by adjusting the range of actions probed to satisfy the condition $I/I_* < 1$.

Thanks to the positive and encouraging results of the analysis presented here, we are confident that the measurement protocol is a powerful tool for probing the non-linear diffusive behaviour in an accelerator like the LHC, although it should be stressed that it is of general applicability in any circular accelerator. Therefore, the logical next step is the proposal of a dedicated beam measurement, at the LHC or elsewhere, performed under the optimal conditions considered in this chapter, which will complete the investigations presented in this chapter. In the meantime, available data from collimator scans collected at the LHC (but not with the proposed protocol) have been analysed under the assumption of the proposed functional form for the diffusion coefficient. Very promising results have been obtained that support pursuing this line of research and will be presented in the next chapter.

Appendices

4.A | Numerical integration of the Fokker-Planck equation using the Crank-Nicolson method

For executing the numerical integration of a FP equation in the form of Eq. (2.59), we used the Crank-Nicolson integration scheme [42], which is a finite difference method, second-order and implicit in time. It can be shown that this scheme is unconditionally stable for many differential equations [68].

To obtain valid numerical results of the integration of the FP equation with a Nekhoroshev-like diffusion coefficient as in Eq. (2.64), and to obtain a consistent evaluation of the outgoing current in different scenarios, we have to properly evaluate the stiffness of the problem and, consequently, adapt the fineness in both time and space discretization. Moreover, regarding the simulation of an instantaneous change in position of the absorbing boundary condition, a rigorous protocol must be established, especially when considering the inward displacements of the boundary condition, for which some additional precautions must be taken.

The outgoing current, defined in Eq. (4.2), is obtained by directly computing, in between each integration step, the numerical derivative of ρ at the absorbing boundary position.

A Nekhoroshev-like diffusion coefficient has the main characteristic of varying by various orders of magnitude over the accessible range of the action variable, meaning that if we want to simulate the entirety of a diffusive phenomenon, we must take into consideration such a wide range of values in the integration process. This becomes mostly critical when the process to be simulated is the recovery current that occurs after a variation in the position of the boundary condition, such as the ones described in Section 4.3.

The recovery current is mainly dependent on variations in the equilibrium distribution that are various orders of magnitude lower, in absolute value, than the core part of the distribution (refer to Figs. 4.1 and 4.3). It is therefore necessary to choose a time and space discretization fine enough to obtain numerical estimates that are not seriously affected by the integration error. To do that, we performed a convergence test for a single recovery current in every scenario we wanted to analyse. In this convergence test, we gradually increased the fineness of the discretization, until we measured a relative difference between the numerical results not higher than 1%.

When it comes instead to reproduce the instantaneous change of the position of the absorbing boundary condition in the integration scheme, we perform a resampling of the distribution ρ at the time of the boundary change, while keeping the same fineness for the spatial discretization. However, in an outward movement, this process is straightforward, as there is no artificial change to the existing distribution ρ to be taken into account, and we just add an empty region with no singular points. Instead, for the case of an inward movement, we do have to make a cut inside the ρ distribution, corresponding to the movement performed by the absorbing boundary. Such a cut generates an inconsistency between the non-zero value of ρ at the new position of the boundary condition and the zero condition imposed by the absorbing boundary condition. This inconsistency leads to a divergence in the analytical definition of the outgoing current and undefined behaviours in the numerical integration. Therefore, we apply to the cut distribution a sharp damping, right next to the newly positioned absorbing boundary condition, generated by a logistic function $f(I)$ defined as

$$f(I) = \frac{1}{1 + e^{\frac{I - I_{\mathrm{a}} + \ell}{\ell}}} \,, \tag{4.24}$$

where ℓ is the extent of the range of action values where the damping occurs and is taken equal to twice the fineness of the spatial discretization, and I_{a} is the position of the absorbing boundary condition after the inward movement. In this way, $\rho_d(I) = \rho(I) f(I)$ represents a distribution that is smooth enough to avoid instabilities in numerical integration. The sharpness of this damping is directly proportional to the fineness of the spatial sampling, and its effects are included in the convergence tests.

4.B | Analytical estimate of the outgoing current for a FP process

We are interested in finding an accurate analytical approximation for the outgoing current of a FP process like Eq. (2.59). We start by applying the following change of variables

$$x = -\int_I^{I_{\mathrm{a}}} \frac{1}{D^{1/2}(I')} \, \mathrm{d}I' \,, \qquad \rho_x(x,t) = \rho(I,t) \frac{\mathrm{d}I}{\mathrm{d}x} = \rho(I,t)\sqrt{D(I)} \,, \tag{4.25}$$

which leads to

$$\frac{\partial \rho_x}{\partial t} = \frac{1}{2} \frac{\partial}{\partial x} \left[\frac{1}{D^{1/2}} \frac{\mathrm{d}D^{1/2}}{\mathrm{d}x} \rho_x \right] + \frac{1}{2} \frac{\partial^2 \rho_x}{\partial x^2} \,, \tag{4.26}$$

where $D = D\left(I(x)\right)$. Introducing the effective potential $V(x) = -\ln\left(D^{1/2}(x)\right)$, we obtain the Smoluchowsky form [69]

$$\frac{\partial \rho_x}{\partial t} = \frac{1}{2} \frac{\partial}{\partial x} \frac{\mathrm{d}V(x)}{\mathrm{d}x} \rho_x + \frac{1}{2} \frac{\partial^2 \rho_x}{\partial x^2} \,. \tag{4.27}$$

Equation (4.27) can be made self-adjoint by means of the following change of variables

$$\rho_x(x,t) = \exp\left[-\frac{V(x)}{2} \right] p(x,t) \,, \tag{4.28}$$

and Eq. (4.27) is cast into the following form

$$\frac{\partial p}{\partial t} = \frac{1}{4} \left[\frac{\mathrm{d}^2 V}{\mathrm{d}x^2} - \frac{1}{2} \left(\frac{\mathrm{d}V}{\mathrm{d}x} \right)^2 \right] p + \frac{1}{2} \frac{\partial^2 p}{\partial x^2} \,. \tag{4.29}$$

The general solution of Eq. (4.29) can be written as

$$p(x,t) = \sum_{\lambda} c_{\lambda}(t)\phi_{\lambda}(x)\,, \tag{4.30}$$

where an expansion using the eigenfunctions $\phi_{\lambda}(x)$ of the operator on the r.h.s. of Eq. (4.29) has been used, namely

$$2\left\{-\frac{1}{4}\left[\frac{\mathrm{d}^2V}{\mathrm{d}x^2} - \frac{1}{2}\left(\frac{\mathrm{d}V}{\mathrm{d}x}\right)^2\right] - \lambda\right\}\phi_{\lambda}(x) = \frac{\mathrm{d}^2\phi_{\lambda}}{\mathrm{d}x^2}\,, \tag{4.31}$$

and $c_{\lambda}(t) = c_{\lambda}(0)e^{-\lambda t}$. This choice of eigenfunctions is motivated by the working hypothesis that $p(x, t \to +\infty) = 0$, i.e. the system will eventually relax to a zero distribution.

Using the orthogonality and completeness properties of $\phi_{\lambda}(x)$,

$$\int \phi_{\lambda}(x)\phi_{\lambda}(x')\,\mathrm{d}x = \delta(\lambda - \lambda') \tag{4.32}$$

$$\sum_{\lambda} \phi_{\lambda}(x)\phi_{\lambda}(x') = \delta(x - x')\,, \tag{4.33}$$

and considering the initial condition

$$\rho_x(x,0) = \exp\left[-\frac{V(x)}{2}\right]p(x,0) \tag{4.34}$$

$$p(x,0) = \sum_{\lambda} c_{\lambda}(0)\phi_{\lambda}(x)\,, \tag{4.35}$$

we have that

$$c_{\lambda}(0) = \int \exp\left[\frac{V(x)}{2}\right]\rho_x(x,0)\phi_{\lambda}(x)\,\mathrm{d}x\,, \tag{4.36}$$

and the solution for an initial Dirac delta distribution $\rho_x(x,0) = \delta(x - x_0)$ can be written as

$$\rho_x(x,t) = \exp\left[\frac{V(x_0) - V(x)}{2}\right]\sum_{\lambda} e^{-\lambda t}\phi_{\lambda}(x_0)\phi_{\lambda}(x)\,, \tag{4.37}$$

and the outgoing current at an absorbing boundary in $x = 0$, which in the original variables corresponds to $I = I_{\mathrm{a}}$, reads

$$J(t) = \frac{1}{2}\frac{\partial \rho_x}{\partial x}\bigg|_{(0,t)}\,. \tag{4.38}$$

If the potential is linearized, i.e. $V(x) \simeq -\nu x$, then there is an analytic solution to the eigenvalue problem in Eq. (4.31)

$$-2\left[\lambda - \frac{\nu^2}{2}\right]\phi_\lambda(x) = \frac{\mathrm{d}^2\phi_\lambda}{\mathrm{d}x^2}\,, \tag{4.39}$$

and if we replace this solution in Eq. (4.38), we obtain the expression for the outgoing current

$$J(x_0, t) = \frac{|x_0|}{t\sqrt{2\pi t}} \exp\left(-\frac{(x_0 + \frac{\nu}{2}t)^2}{2t}\right)\,, \tag{4.40}$$

which has dimension t^{-1}. Furthermore, the linearization ν of the potential $V(x)$ near $x = x_0$ reads

$$\nu = \frac{\frac{1}{2\kappa}}{I(x_0)}\left(\frac{I_*}{I(x_0)}\right)^{\frac{1}{2\kappa}} \exp\left[-\left(\frac{I_*}{I(x_0)}\right)^{\frac{1}{2\kappa}}\right]\,, \tag{4.41}$$

which can be inserted into Eq. (4.5), to obtain an analytical estimate of the outgoing current.

4.C | Outgoing current for a system with infinite source

To make use of the analytical estimate of the outgoing current presented in Appendix 4.B, we need to slightly modify certain steps to adapt to the different non-zero equilibrium distribution ρ_{eq}, as the original calculations are carried out under the assumption that $\rho(I, t \to +\infty) = 0$, and modifications to Eq. (4.35) need to be made and then propagated.

Under these new conditions, the expansion of the solution of the diffusive problem in Eq. (4.30) can be modified according to

$$p(x,t) = \sum_\lambda c_\lambda(t)\phi_\lambda(x) + \exp\left[\frac{V(x)}{2}\right]\rho'_{\mathrm{eq}}(x)\,, \tag{4.42}$$

where $\rho'_{\mathrm{eq}}(x) = \rho_{\mathrm{eq}}(I(x))\frac{\mathrm{d}I}{\mathrm{d}x}$ is the equilibrium distribution of our system, while considering the change of variables necessary to work with the self-adjoint diffusive problem in the Smoluchowsky form. The various considerations about $c_\lambda(t)$ and $\phi_\lambda(x)$ are unchanged. The values $c_\lambda(0)$ should be recomputed and from the expansion in Eq. (4.42), we obtain

$$\rho'(x,0) = \exp\left[-\frac{V(x)}{2}\right]p(x,0) \tag{4.43}$$

$$p(x,0) = \sum_\lambda c_\lambda(t)\phi_\lambda(x) + \exp\left[\frac{V(x)}{2}\right]\rho'_{\mathrm{eq}}(x)\,, \tag{4.44}$$

which then leads to

$$\begin{aligned} c_\lambda(0) &= \int \exp\left[\frac{V(x)}{2}\right] \left\{\rho'(x,0) - \rho'_{\text{eq}}(x)\right\} \phi_\lambda(x)\,\mathrm{d}x \\ &= \int \exp\left[\frac{V(x)}{2}\right] \rho^*(x,0)\phi_\lambda(x)\,\mathrm{d}x\,, \end{aligned} \tag{4.45}$$

where, $\rho^*(x,t)$ stands for the difference between the actual and the equilibrium distribution, still to be reached, and in this framework, the rest of the analytic current estimate, i.e. Eq. (4.40), still applies.

5 | Diffusion measurements at the CERN LHC

The content of this chapter, with the due adaptations, has resulted in the proceedings by C. E. Montanari, A. Bazzani, M. Giovannozzi, A. A. Gorzawski, and S. Redaelli *"Testing the Global Diffusive Behaviour of Beam-Halo Dynamics at the CERN LHC Using Collimator Scans"*, which were presented as a poster at IPAC'22 in June 2022 (Ref. [67]).

In Chapter 4, we presented an optimal method to measure the diffusion coefficient of a beam halo, based on the characteristics of the outgoing current, given by a Fokker-Planck equation with a Nekhoroshev-like diffusion coefficient. In this chapter, we apply this method to the available LHC collimator scan data, which was gathered during Run 2, however, not using the optimized measurement protocol devised in the previous chapter.

As this measurement campaign was tailored to a different model of diffusion, the data was gathered with a different protocol, which inevitably does not meet all the optimal requirements highlighted in the previous chapter. This inevitably required an adjustment of the reconstruction procedure to account for the differences between the optimal and the actual measurement protocol.

The chapter is structured as follows. In Section 5.1, we present the LHC collimation system. In Section 5.2, we present the collimator scan data and the diffusion coefficient reconstruction, together with the necessary adjustments applied to the reconstruction procedure to account for the differences between the optimal and the actual measurement protocol. Finally, some conclusive remarks are given in Section 5.3.

5.1 | The LHC collimation system

The LHC layout [1] can be summarized in a geometric scheme composed of eight straight insert regions (IR) and eight circular arc segments. A simple scheme of this layout is reported in Fig. 5.1, left. Within this circular scheme, the main particle physics experiments are located in IR1, IR2, IR5 and IR8, namely, ATLAS [70], ALICE [71], CMS [72], and LHCb [73]. In these four IRs, the two beams intersect and interact in what is referred to as an Interaction Point (IP). The RF cavities for accelerating the beams are in IR4 and IR6 hosts the beam extraction system. Finally, IR3 and IR7 are dedicated, respectively, to the longitudinal and transverse collimation system.

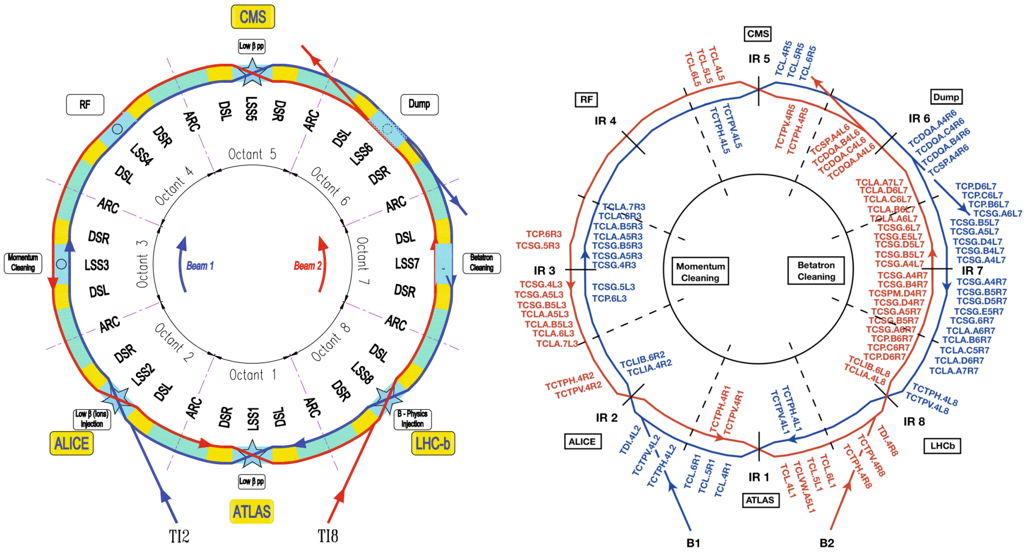

FIGURE 5.1: Left, layout of the LHC. The ring follows an eightfold symmetry. Each octant hosts a Long Straight Sector (LSS) surrounded by two Dispersion Suppressor regions (DSR and DSL). Each octant is connected by an arc (ARC). (From Ref. [1]). Right, LHC collimation system layout in blue and red for Beam 1 and Beam 2, respectively. (From Ref. [74])

The LHC collimation system is a fundamental component of machine operation and safety [75, 76]. It has multiple functions, such as cleaning the beam halo, protecting the machine against unexpected and anomalous losses [77], and reducing the background noise in experimental IPs [78, 79].

The collimation system counts more than 120 individual collimators. Most of these collimators are movable devices made up of two movable jaws made of solid material, which can be brought at different distances from the circulating beam [80]. A summary of the various collimators positioned along the LHC layout is reported in Fig. 5.1, right. These jaws are straight and parallel to the beam and have a tapering at both ends, along the axis of the beam. The distance between the start and end of the tapering, where the jaw material is straight, is called the active length of the collimator. Some photos and schemes of these LHC collimators are reported in Fig. 5.2.

At IR7, where the betatronic collimation system is located, we have an effective cleaning stage of halo particles that happen to have an excessively large amplitude of the betatron oscillation. This is called *betatron cleaning*. To achieve effective betatron cleaning, we require that the magnetic lattice optics in the col-

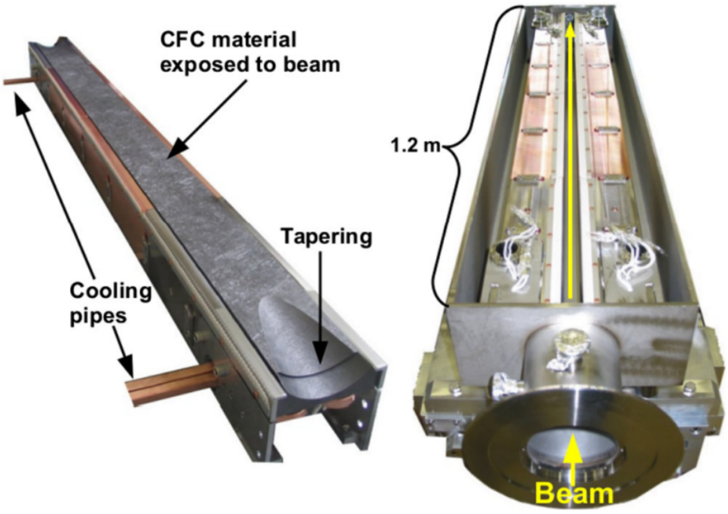

Figure 5.2: Left picture, jaw of a secondary collimator, made of carbon-fiber composite (CFC) and water cooled through copper pipes. Right picture, two collimator jaws are installed in a collimator tank. (From Ref. [81])

limation region has very low dispersion and high β function values. With such an optics setup, particles with high transverse displacement also feature high betatron displacement.

In IR3, instead, a *momentum cleaning* of particles takes place. In that region, conversely, a high dispersion value is kept, so that the high transverse displacement is mainly caused by high momentum offset.

To safely clean the beam halo without damaging the magnets or other components of the machine, the LHC collimation system works on the basis of a multistage process. This multistage process consists of a *hierarchy* of individual collimators with the purpose of progressively cleaning and controlling the loss of particles. A scheme of this hierarchy is presented in Fig. 5.3.

Primary collimators, which are also known as *Target Collimator Primary* (TCP), are those placed closest to the edge of the beam and form the first stage of collimation. The purpose of this first collimation stage is to intercept and dispose of beam halo particles, i.e. it is the stage at which the beam halo actually gets intercepted above a certain threshold. When interacting with the primary collimator matter, the primary particles may exhibit various scattering behaviours, from acquiring an angular kick to depositing energy and producing secondary particles.

These particles, scattered by the TCPs, form the secondary halo, which is then tackled by the secondary collimators *Target Collimator Secondary-Graphite*

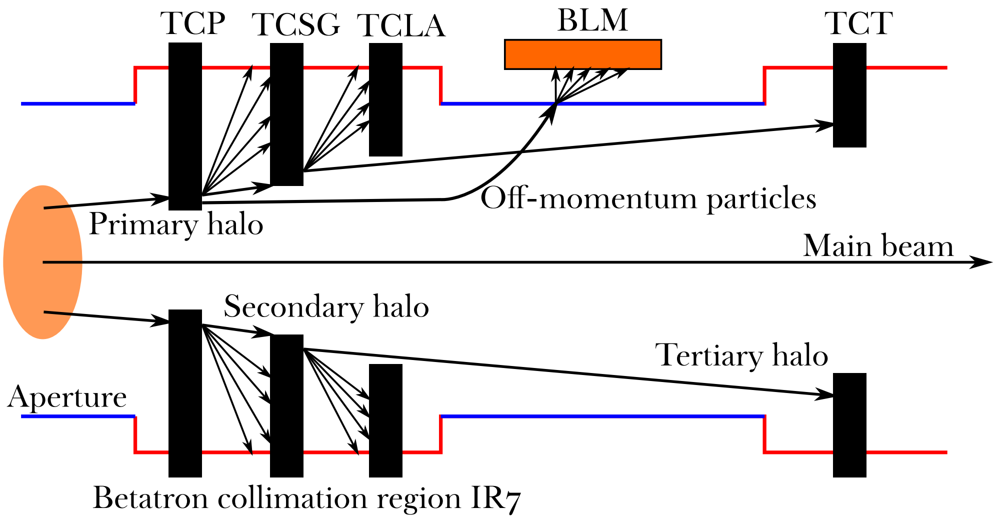

FIGURE 5.3: Scheme of the multistage collimation system in the LHC. The hierarchy includes primary (TCP), secondary (TCSG) and tertiary (TCT) collimators and shower absorbers (TCLA). Particles in the primary halo interact with the TCP and are scattered to the TCSGs. The hadronic showers coming from the TCSGs are finally absorbed by the TCLAs, and TCTs are in place to protect the aperture bottlenecks of the triplet quadrupoles. Part of the secondary halo interacts with the ionization chambers of the BLMs, and provide an indirect measurement of the primary halo. (Scheme based on Ref. [82])

(TCSG). The particles leaving the collimator finally form the tertiary halo, which finally interacts with the active absorbers, *Target Collimator Long Absorber* (TCLA), which are installed downstream of the TCSGs, and *Target Collimator Tertiarys* (TCTs), which make up a third final collimation stage for local protection for the aperture bottlenecks in the machine, i.e. in the triuplet quadrupoles.

Such a hierarchy offers various advantages over a simple single-stage collimation system. It ensures that particles that have been incorrectly outscattered at larger amplitudes and modified energies, constituting the so-called *secondary beam-halo*, will be mainly absorbed by the next stages of collimation and not by other fragile parts of the machine. Moreover, the interaction of beam-halo particles with the primary collimator produces hadronic showers whose products can reach the cold magnets downstream of the cleaning region, possibly leading to unwanted quenches.

In IR7, there are 3 sets of collimators that cover the horizontal, vertical, and skew planes, as they have been shown to provide satisfactory cleaning [83].

The collimator hierarchies for these planes are, respectively, denominated by the letters C, D, and B. That is, the horizontal target primary collimator is called TCP.C. In IR3, the dispersion is only in the horizontal plane and only one set of collimators is installed to perform the longitudinal cleaning.

A multi-stage collimation system allows one to distribute the beam loads over a large controlled area. However, it also leads to a significant increase in the machine impedance, i.e. the level of self-interaction of the charged particle beam, mediated by the machine environment [84], which can be an important cause of beam instability and losses. Collimators are the single highest contributors of LHC impedance at top energy [85], as their resistive wall tends to be the element closest to the beam. Therefore, a multi-stage collimation system has to be configured so that it balances beam load distribution and impedance contributions efficiently. Active studies are ongoing to optimize the collimation system to minimize the beam losses and the machine impedance, see, e.g. Ref. [86].

The secondary particle showers represent the point of observation to measure the amount of primary particles absorbed by the TCPs. To quantify this amount, the LHC is equipped with multiple ionization chambers, which make up the beam loss monitor (BLM) system [87, 88]. The charged particles that pass through the ionization chambers finally provide a measure of Gy/s, which can be converted into a corresponding measure of protons/s lost using a measured calibration factor, evaluated by controlled collimator-induced losses [89], which are also quantified in parallel by the *DC Beam Current Transformer* (DCBCT) [90], which measures the number of protons in the circulating beam by measuring the magnetic field, induced by the moving beam. A picture of an LHC BLM is presented in Fig. 5.4. The calibrated BLM data are the precise loss signal that we finally expect to use to reconstruct the diffusion behaviour in the transverse plane.

5.2 | Analysis of experimental data

Between 2016 and 2018, collimator scans were performed at the CERN LHC with physics beams at 6.5 TeV [64]. During these scans, one of the jaws of the primary collimators in IR7 was moved inward and outward in small steps, starting at $5\sigma_{\text{nom}}$, where the nominal sigma value σ_{nom} is evaluated for a nominal emittance $\varepsilon_{\text{nom}} = 3.5\,\mu\text{m}$.

The scan was performed after executing a beam-based alignment [92] of the collimator, which is a procedure in which the TCP jaws are progressively positioned closer to the beam until the halo is touched. By performing such a procedure, one is sure that the centre of the collimator gap is precisely posi-

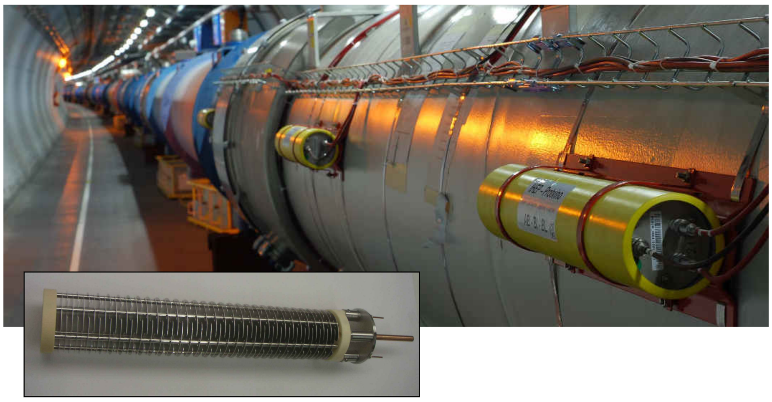

Figure 5.4: Top picture, ionization chambers of the LHC BLM system, mounted on the side of the LHC Magnets. Bottom picture, inner structure of a BLM ionization chamber. (From Ref. [91])

tioned around the local closed orbit.

The measurement is performed with the local beam loss monitoring (BLM) system and is provided in unit of Gy/s with 1 Hz sampling rate, processed over different *Running Sums* (RS), evaluated by a real-time processing system implemented on FPGA [93]. In this implementation, a time window is moved over the signal sampled by the device, and the maximum peak measured in the time window is considered the final measurement, which is finally reported in Gy/s, RSs range from a minimum of 40 µs to a maximum of 83.89 s. A list of the various RS defined in the measurement system is presented in Table 5.1.

The IR7 TCPs dedicated to the vertical plane and to the horizontal plane (namely, TCP.D and TCP.C) were used to perform a collimator scan of the beam halo on both Beam 1 and Beam 2, performing a sequence of inward steps, with pauses of a few seconds between each step, followed by a train of outward steps, with pauses ranging from ~ 30 seconds to almost two minutes between steps. The scraping was first performed on the vertical plane and then on the horizontal plane.

During the scraping, the BLM data were recorded by the ionization chambers placed after the collimator hierarchy. Two dedicated sets of BLMs are placed for the two separate planes and are considered in our analysis depending on the plane that is undergoing scraping. In Fig. 5.5 we present the data collected during fill 6052 of type RS06, i.e. sampling the maximum spike measured by the BLM over a time window of 10.24 ms. Here, the collimator jaw positions are reported in millimetres from the centre of the beam, measured after the beam-based alignment. The two different BLM planes reading is reported.

Signal Name	Time Windows		Refreshing		Data formats	
	Number of 40 µs steps	Duration [ms]	Number of 40 µs steps	Duration [ms]	FPGA/VME	Measurement and Logging DB (rate: 1 Hz) [Gy/s]
RS01	1	0.04	1	0.04	Maximum of sum values observed from the last readout	Maximum of sums normalized to window length
RS02	1	0.08	1	0.04		
RS03	2	0.32	1	0.04		
RS04	8	0.64	1	0.04		
RS05	16	2.56	2	0.08		
RS06	64	10.24	2	0.08		
RS07	256	81.92	64	2.56		
RS08	16384	655.36	64	2.56		
RS09	32768	1310.72	2048	81.92	Last calculated sums observed in the last readout	Last calculated sum normalized to window length
RS10	131072	5242.88	2048	81.92		
RS11	524288	20971.52	16384	655.36		
RS12	2097152	83886.08	16384	655.36		

Table 5.1: Specifications of the various Running Sums (RSs) that are defined in the FPGA based data gathering system of the BLMs. (Ref. [94])

It should be noted that these collimator scans were not performed using an optimal protocol such as that proposed in the previous chapter. In fact, complete inward scans, followed by outward scans, were used instead of a sequence of in/out steps. Furthermore, jaw movements were not always performed leaving enough time for the system to relax to its equilibrium state. This can be observed from the fact that, between most outward steps, the loss signal still has a non-negligible positive first derivative when the next collimator outward step is performed, suggesting that a recovery current process was still ongoing when the jaw was moved, as the expected global current process has negative or close to zero first derivative. This suggests that an ideal resting time between steps was not achieved before the next collimator step.

Due to these two characteristics of the measurement protocol used during the collimation scan, some of the working hypothesis made in the previous chapter, which ultimately allow the reconstruction of $D(I)$ by fitting the normalized recovery current, may not hold. More specifically, we lack the upper bound to reconstruct the global current, and we cannot be sure that the beam tail distribution after an outward step follows Eq. (4.22).

To address these characteristics and shortcomings of the data, we had to consider only a subset of the data and modify some of the elements of the fitting procedure.

To address the lack of alternating jaw movements, we selected a region of in-

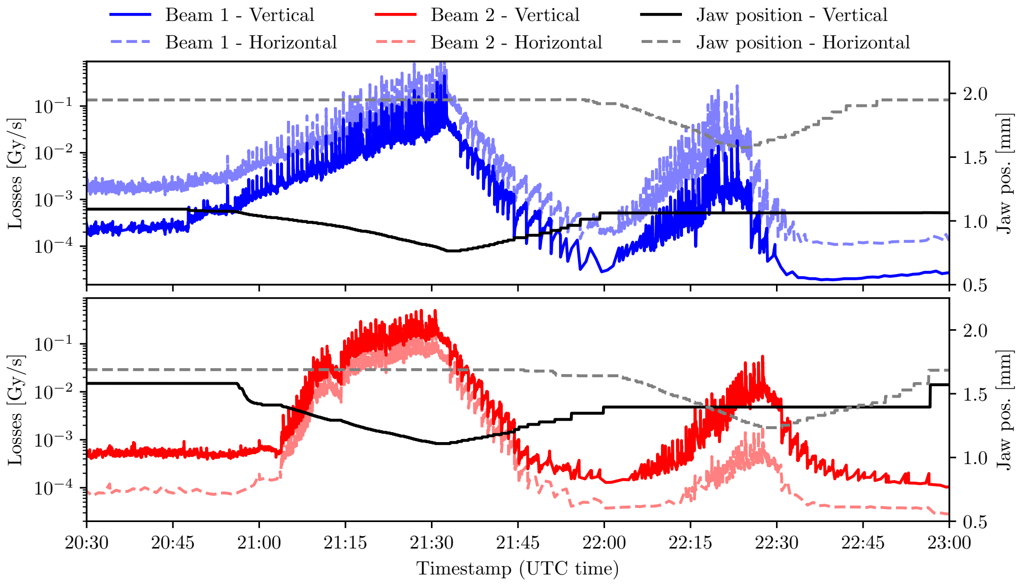

FIGURE 5.5: Beam loss data from the two separate BLM monitors corresponding to the TCPs on the vertical and horizontal planes, using RS06 (i.e. the maximum spike over a time window of 10.24 ms), for Beam 1 and Beam 2, and positions of IR7 TCP jaws measured in the vertical and horizontal plane for the collimator scans carried out in fill 6052. The data acquired represent a complete collimator scan on both planes. The jaw positions are considered from the beam centre position, measured after a beam-based alignment. (Data from Ref. [64])

terest (ROI) in which many outward steps were performed with almost regular sampling, with loss signals exhibiting the features we expect to see from a recovery current. This decision is motivated by the fact that the simulation study presented in the previous chapter shows how recovery currents induced by outward steps are much more reliable for reconstruction purposes than those induced by inward steps.

In Fig. 5.6 we present the portion of the data collected in Fill 6052 that we finally selected. Unfortunately, only the scraping performed in the vertical plane meets our quality requirements to apply the fitting of our diffusive model.

The measured collimator jaw position is converted to measured beam sigma units σ using the nominal optical parameters and the measured value of the beam emittance, taking into account the position of the beam centre. The nominal optical parameters were considered as the measured β-beating level, i.e. the difference between the measured optical functions and the expected nominal values, was in the few percent level as expected from regular LHC

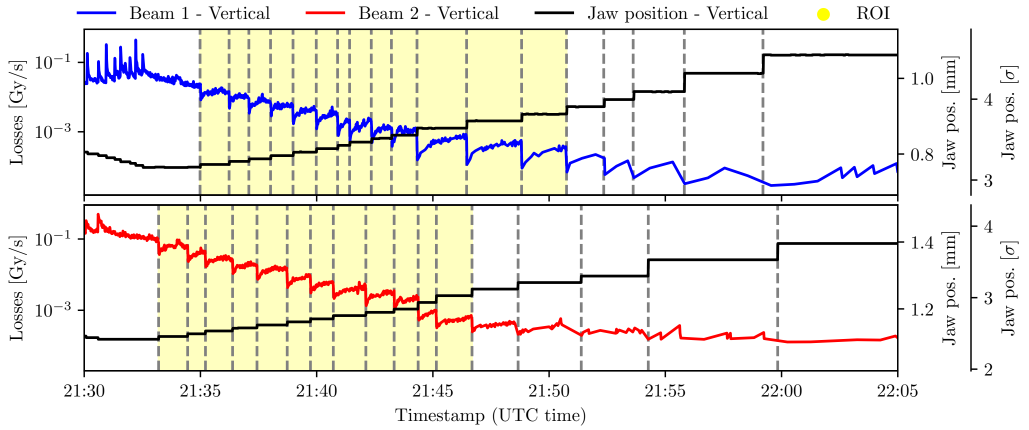

FIGURE 5.6: Selected data from Fill 6052 (i.e. Fig. 5.5). The data shown correspond to outward jaw movements in the vertical plane. The yellow-marked region of interest (ROI) represents a subset of data meeting our quality requirements for applying the fitting of our diffusive model. The jaw positions are considered from the beam centre position, measured after a beam-based alignment. A corresponding position measured in σ units is also reported. (Data from Ref. [64])

operation [95]. To convert the Gy/s units of the BLM signal to protons/s, we used a calibration factor F [89] dependent on the TCP jaw position. This calibration factor F is calculated from the BLM loss data and the intensity lost recorded by the DCBCTs during the collimator steps. The coefficient reads

$$F = \left(-9.0 \times 10^{-14}\sigma + 6.2 \times 10^{-13}\right)^{-1} , \tag{5.1}$$

where σ is the position of the collimator jaw in sigma units.

The absence of alternating jaw movements implies a lack of information for constructing an upper-bound estimate of the global current. Moreover, since the jaw movements were not always performed to allow enough time for the system to relax to its semi-stationary state, we cannot make strong assumptions on the global current value by only interpolating the end points of the outward recovery currents.

To address this issue, we define an initial estimate of the global current shape $J_{\text{eq}}^{\text{est}}(t)$, by constructing a Cubic Spline Interpolation (CSI) passing through the end points of the sequence of outward recovery currents, following the same methodology as presented in the previous chapter. This “fundamental CSI”, has the features we expect to observe from a global current we expect to observe from a Nekhoroshev-like Fokker-Planck process. However, by just interpolating the end points, it does not take into account missing recovery due to collimator steps being performed too quickly.

To include this missing information, the fundamental CSI has been multiplied by different constant terms to represent possible different levels of partial recovery of $J_{\mathrm{R}}(t)$. This procedure is shown in Fig. 5.7. One can see how the fundamental CSI represents the initial lowest estimate of global current, while the different multiplicative constants introduce different gap levels after the terminating points of the recovery currents. This multiplicative can then be treated as a free parameter for reconstructing missing information.

Finally, the rapid sequence of jaw movements introduces another issue: the difference distribution ρ^* cannot be described with certainty by Eq. (4.22), or its approximated form by Eq. (4.23). To address this issue, we replace the $D(I)$-dependent integral terms in Eq. (4.23) with the approximation

$$\rho^*_{\mathrm{app}}(I) = \begin{cases} -M & \text{if } I \leq I_{\mathrm{a}} \\ -\left(\frac{I'_{\mathrm{a}}-I}{I'_{\mathrm{a}}-I_{\mathrm{a}}}\right) M & \text{if } I > I_{\mathrm{a}} \end{cases}, \tag{5.2}$$

where M is a fixed constant for each jaw movement that represents an unknown amount of out-of-equilibrium distribution.

A scan is performed on different combinations of the multiplicative factor of the CSI and of M, while keeping track of the χ^2 achieved by the fitting routine that determines the values of the model parameters κ, I_*. The result of this procedure is shown in Figs. 5.8 and 5.9, where one can observe the existence of an optimal configuration of parameters and the good reconstruction performance achieved by such a configuration. The optimal fit results for Beam 1 and Beam 2 data are reported in Table 5.2.

Beam / Plane	CSI	M	κ	I_* $[\sigma]$
Beam 1 / V	$\times 1.5$	750	0.59 ± 0.03	21 ± 2
Beam 2 / V	$\times 1.5$	1000	0.85 ± 0.02	39 ± 8

TABLE 5.2: Results of the fit procedure of κ and I_* for the selected data in the vertical plane, along with corresponding setup obtained for the CSI multiplicative constant and M value for (5.2).

Note that the values reported in [7], namely $\kappa = 0.33$ and $I_* \simeq 21$, were obtained for Beam 2 and considering the diffusion in the vertical plane. It should be stressed that these previous measurements were performed with non-colliding bunches, whereas in the beam measurements analysed here, beam-beam effects were present.

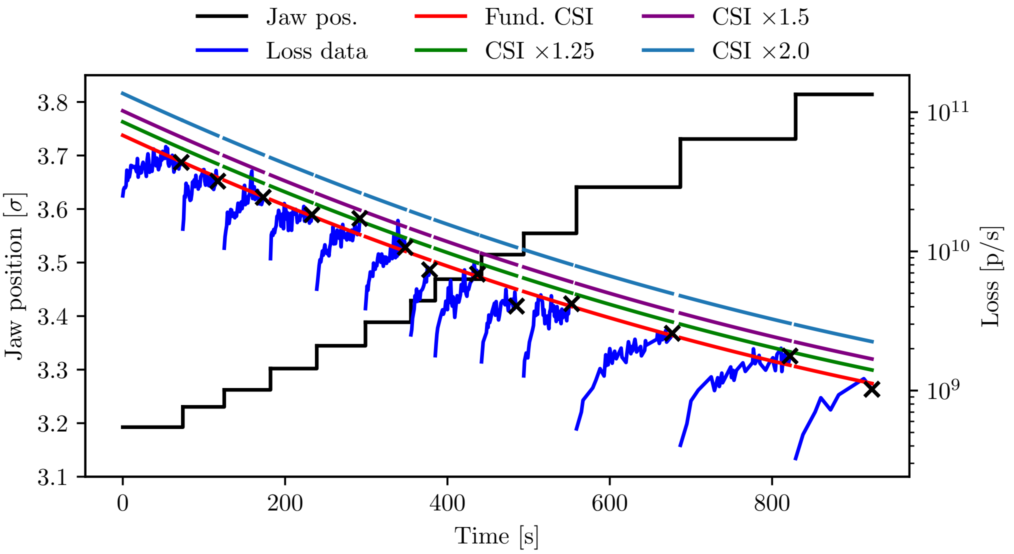

Figure 5.7: Possible estimates of $J_{\mathrm{eq}}(t)$ for Beam 1 data. An initial estimate is made starting from a Cubic Spline Interpolation (CSI) with positive second derivative passing through the end points of the measured recovery currents (red line). The various curves are obtained by multiplying the fundamental CSI by a constant term, and represent estimates of the partial recovery currents. The multiplicative constant considered is reported in the plot legend.

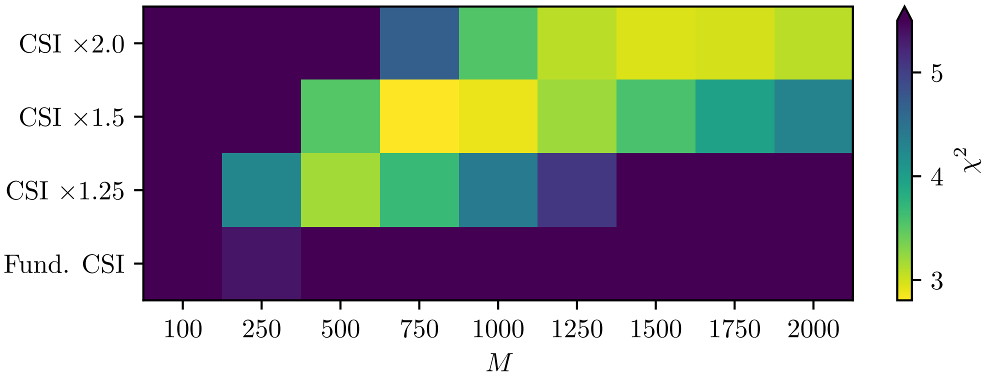

Figure 5.8: Fit performance of κ and I_* for Beam 1 data, using different combinations of CSI multiplicative constants and values of M for Eq. (5.2). The color map shows the existence of an optimal pair of values at (CSI ×1.5, 750).

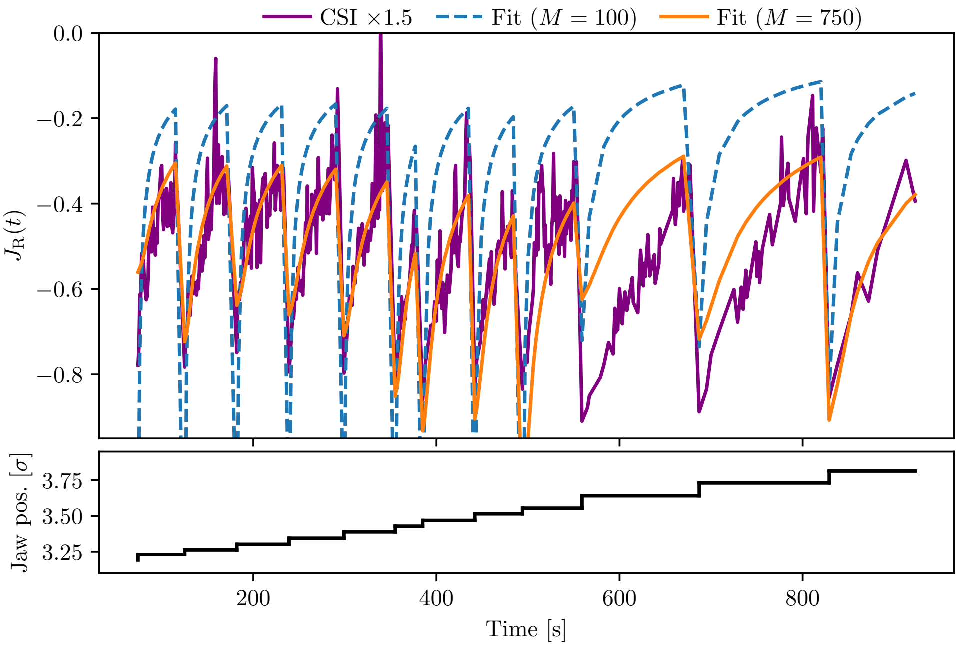

FIGURE 5.9: Fit results for Beam 1 data for two M values, considering the recovery current obtained by using the optimal CSI multiplicative constant $\times 1.5$. The optimal M value (orange) outperforms a lower M value (blue) and manages to reconstruct the shape of the recovery currents.

5.3 | Final remarks

Despite the differences between the approach used to collect the data during LHC Run 2 and the optimal one suggested by the numerical studies performed on the Nekhoroshev-like Forkker-Planck diffusive model, we were able to analyse the loss signal measured by the BLMs during collimator scans, and obtain a promising reconstruction of the recovery currents, which are ultimately the indicator of diffusive-like behaviour.

To address missing information in the data, due to the different measurement protocol used, we had to adapt some of the key elements of our fitting procedure. That is, we had to define a new method for reconstructing the global current estimate and we had to consider a different form for the difference distribution ρ^*. This led to good reconstruction performances and promising insights into the global diffusive behaviour of the LHC beam halo.

Future collimator scans during the LHC Run 3 will focus on acquiring beam data using the proposed optimized experimental method, to characterize more accurately the presence of non-linear diffusive behaviour.

6 | Application of the diffusive model to describe beam losses in the presence of wire compensators

In this chapter, we examine the case of beam-beam wire compensators, which play an important role in counteracting the detrimental effects of beam-beam interactions in the LHC. Our original contribution to this field is the application of our diffusive model to assess the long-term effects of wire compensators on beam losses and emittance.

Through the study of the LHC Beam 2 data, collected during a Run 2 measurement campaign, we aim to understand the effectiveness of wire compensators in mitigating beam-beam effects without causing unwanted effects such as increased emittance. The results of this analysis provide insight into the potential benefits of utilizing wire compensators in present and future accelerator design and show how this diffusive model can be applied to assess long-term effects of new components in the accelerator via inspection of the beam loss data.

The chapter is structured as follows. In Section 6.1, we present the generalities of wire compensators and their implementation in the LHC. In Section 6.2, we give an overview of the data gathered during the dedicated wire compensators' measurement campaign in Run 2. In Section 6.3, we discuss how our diffusive model can be applied to the data and, in Section 6.4, we present the results of the analysis. Finally, in Section 6.5, we draw our conclusions and discuss the potential future applications of the diffusive model in light of the results and difficulties encountered in this analysis.

6.1 | Generalities on the LHC beam-beam wire compensators

One of the most significant limits in the present LHC design and the future HL-LHC is given by the electromagnetic interactions between the two counter-rotating beams in the shared sections of the machine that occur around the interaction points [3]. These beam-beam interactions lead to what can be distinguished as head-on beam-beam effects, which occur when the beam bunches overlap at the interaction point, and long-range beam-beam effects, occurring when the two beams are transversely separated in the remaining part of the shared region.

In the LHC, the beams are set in collision with a *crossing angle*, which has the purpose of separating bunches immediately upstream and downstream of the collision point [3] to reduce the strength of long-range beam-beam effects. However, an increase in the crossing angle also implies a reduction in integrated luminosity, that is, the total number of collisions that have occurred over a given period of time, typically measured in inverse femtobarns fb^{-1} [96], as the overlap of the bunches decreases. A schematic visualization of two different crossing angles and their consequent effect on beam separation and bunch overlap is presented in Fig. 6.1. The nominal full crossing angle for LHC is set at $\theta_c = 285\,\mu\mathrm{rad}$, while for HL-LHC the expected baseline parameter will be set at $\theta_c = 500\,\mu\mathrm{rad}$ [2].

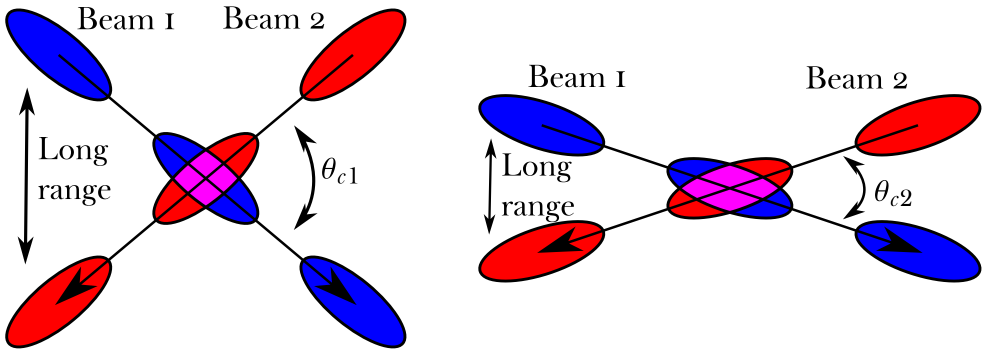

FIGURE 6.1: Schematic visualization of two different full crossing angles and their consequent effect on beam separation and bunch overlap. As $\theta_{c1} > \theta_{c2}$, the bunches are more separated in the first case (left), while the bunch overlap is larger in the second case (right). The long-range beam-beam effects are also more significant in the second case.

To address long-range beam-beam effects while maintaining a small crossing angle, a corrective approach based on electromagnet lenses was presented in [97]. The concept of wire compensators can be traced back to the early 2000s, when the resemblance between long-range beam-beam kicks and the $1/r$ dependence of a kick caused by a DC wire was observed [19, 97]. This similarity is more accurate with larger beam-beam separations. Since the initial proposal, various experiments have been conducted, including installing and testing different types of wires at facilities such as the RHIC [98] at Brookhaven National Laboratory, DAFNE [99] at INFN in Italy, and at the CERN Super Proton Synchrotron (SPS) CERN [100, 101]. In 2015, a study was conducted using a resonance compensation criterion to optimize the position and current of the wires [102], where it was shown that the non-linear kicks from distributed long-range beam-beam interactions could be approximated by two equivalent kicks on either side of the IP. A sketch of the concept of compensation given by beam-beam wire compensators, which we will refer to as BBCW, is presented in Fig. 6.2. In the sketch, the weak-strong approximation is represented [103, 104], i.e. it is assumed that one beam, called *strong beam*, will not be affected by the other beam, called *weak beam* that, in contrast, experiences kicks caused by the electromagnetic fields generated by the strong beam.

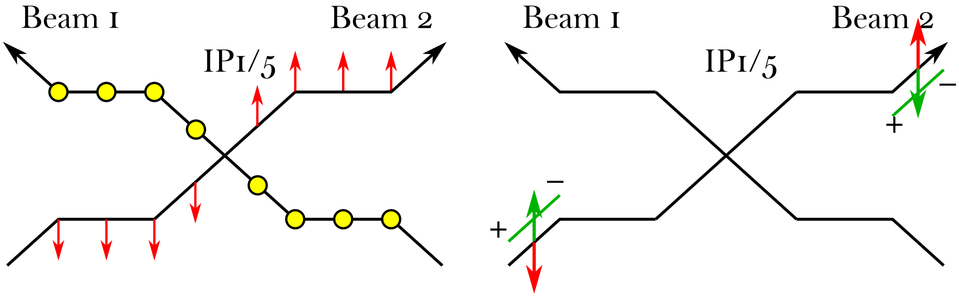

FIGURE 6.2: Left, sketch of the long-range beam-beam effects experienced by Beam 2 from Beam 1, assuming the weak-strong approximation (i.e. we consider the effect of Beam 1 on Beam 2 and not vice versa). Right, sketch of the principle of the compensation given by the BBCW. The long-range beam-beam effects (red arrow) are compensated by the DC wires (green arrow), which are placed in the beam path before and after the interaction point.

The BBCW has been tested in multiple iterations on various accelerator complexes (a complete list of experimental applications up to early 2022 is available in [105]).

In LHC, BBCW are installed for Beam 2 only, as it was the only beam that was expected to operate with a coronograph [106], which is a device that is expected to allow transverse beam-halo measurements in the future and allow inspection of beam-halo properties with and without BBCW. The wires are embedded in the tertiary collimators placed upstream and downstream of IP1 and IP5 [107]. These wire collimators are still part of the collimator hierarchy, presented in Section 5.1, and are placed near the IPs to locally protect the superconducting triplet quadrupoles from debris generated at the interaction point. A scheme of a wire collimator, along with a picture of one of the collimators deployed in the LHC, is reported in Fig. 6.3.

A collimator hosts two separate wires (one per jaw), and each wire can carry up to 350 A. These two separate wires are cabled in series so that they have the

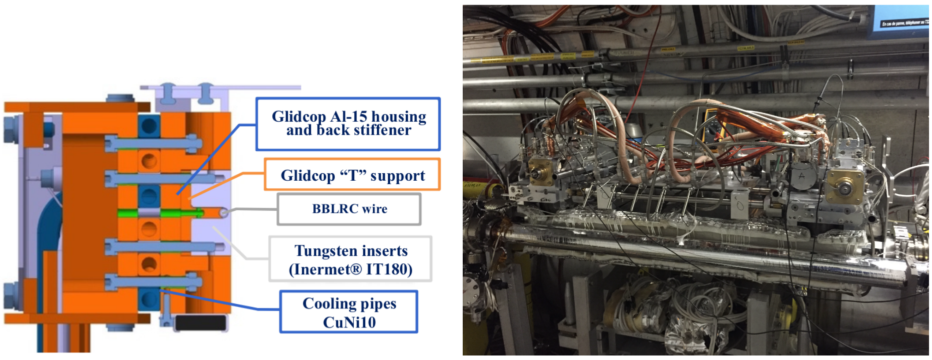

FIGURE 6.3: Left: section view of a wire collimator. These collimators are composed of tungsten jaws into which a copper wire with a thin silicon dioxide insulator is embedded (from Ref. [107], details on the components can be found in references therein). Right: photo of the wire collimator currently installed in the LHC on the left side of IP5 (from Ref. [105]).

same polarity. This configuration enables a specific 2-jaw powering setup with the characteristics of doubling the odd multipolar strength of the kick, while the even ones cancel out. This choice is motivated by the need to compensate for octupolar resonances [108]. The two possible configurations are presented in Fig. 6.4. The first, called the *single wire* configuration, powers only the internal wires. The second one, called *quadrupolar configuration*, powers both wires.

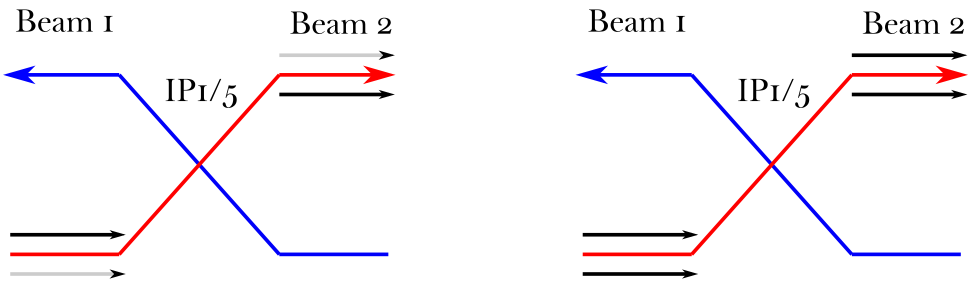

FIGURE 6.4: Left, sketch of the single wire configuration, where only one wire per pair is powered. Right, quadrupolar configuration, where both wires in each pair are powered to compensate the octupolar resonances.

6.2 | Overview of experimental data

For the application of our diffusive framework, we consider the experimental data gathered at the CERN LHC during the 2018 LHC Machine Development (MD) programme, during the BBCW measurements campaign [108]. More specifically, we consider the data gathered during fill 7386, as it has the configuration closest to an operational scenario.

During this MD measurement, the BBCW prototypes installed for Beam 2 were tested in various long-range beam-beam-dominated scenarios. During fill 7386, three trains of symmetric bunches, that is, bunches that fill the same slots in Beam 1 and Beam 2, enabling collisions only at IP1 and IP5, were tested at flat-top energy with collisions at different crossing angles, smaller than the nominal one to enhance long-range beam-beam effects. In this operational-like fill, the wire compensators were set in the quadrupolar configuration. The calibrated loss signals measured by the various BLMs for the two beams are shown in Fig. 6.5, note that the measurement unit is in protons/s, since we are considering calibrated losses, which are a combination of the original Gy/s BLMs signal located in IR7 [109], converted into an estimate of the corresponding protons lost by a conversion factor established with dedicated measurements and simulation studies [110]. In addition to the BLM data, the beam intensity measured by the DCBCTs, the current in the wire, the octupole powering, and the crossing angles are also reported.

The BLM data for Beam 1 and Beam 2 in units of protons/s represents a high-precision measure of protons lost over time. Instead, the DCBCT data provide a measurement of the intensity of the beam in number of protons over time. This measurement is not sensitive enough; it can be seen from the plot how the measured intensity does not distinguish the different regimes of losses highlighted by the BLM data and maintains a steady linear decrease. This difference in sensitivity makes the BLM data a fundamental tool for inspecting the different regimes of losses in the transverse plane.

BBCW and octupole magnets powering are reported in Ampere. BBCW wires can be found in either an *off* state, namely at $0\,\mathrm{A}$, or in an *on* state, namely at $350\,\mathrm{A}$. Instead, the octupoles are found at two different current values, namely $260\,\mathrm{A}$ and $-560\,\mathrm{A}$. It is important to highlight how the switch of state for both systems requires a non-negligible amount of time; this will be thoroughly discussed in the next section.

It is possible to see how the data provide a variety of crossing angle configurations, along with on-off alternations of both BBCW power and octupoles current. Qualitatively, one can see how the BBCW equipped in Beam 2 do lead to a lower BLM loss signal when they are turned on, while turning them

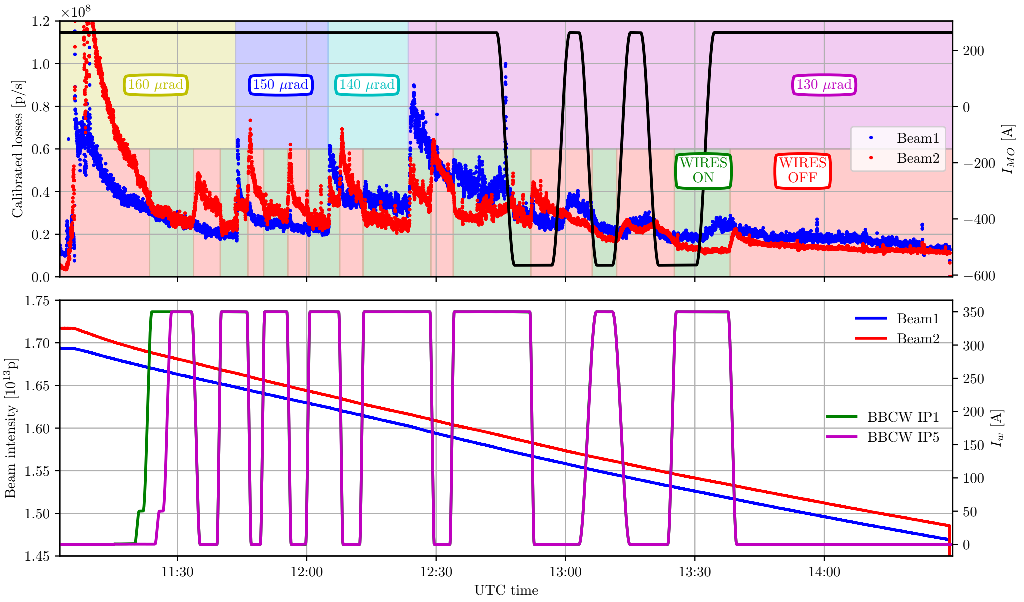

FIGURE 6.5: Overview of the data gathered during fill 7386. BLM calibrated losses and DCBCT beam intensity measurements were taken at different combinations of crossing angles, wire power, and octupole power.

off leads to a strong peak in the losses measured by the BLMs.

We will now discuss how our diffusive framework can be applied to this loss signal, along with some necessary considerations on how one must preprocess and interpret these data before applying the model.

6.3 | Application of the diffusive model

Let us consider the Fokker-Planck equation presented in Eq. (2.59), with the Nekhoroshev-like form of the diffusion coefficient. We recall that the system is fully characterized by the three free parameters ϵ, I_*, and κ.

To apply this model to the BLM data and reconstruct $D(I)$ for the various states of the system, we perform a fitting approach inspired by the procedure used in the work of Bazzani et al. [7], where the same Fokker-Planck model is used to reconstruct the evolution of the normalized beam intensity.

From the collected BLM and DCBCT data, we want to construct a measure of the normalized intensity of the beam as a function of the number of turns. We first convert the measurements from seconds to the number of turns, considering that in LHC Run2, a reference proton at 6.5 TeV performs 11245 turns every second. We then evaluate the relative intensity lost over an interval $[N_0, N_1]$, as the DCBCT data are not sensitive enough to measure the small differences in the loss rates, we consider the amount of protons lost from the integrated BLM signal, and we take the DCBCT value registered at the beginning of the interval considered as the reference intensity, as it is the moment at which the first peak in the BLM losses was measured. This procedure is illustrated in Fig. 6.6.

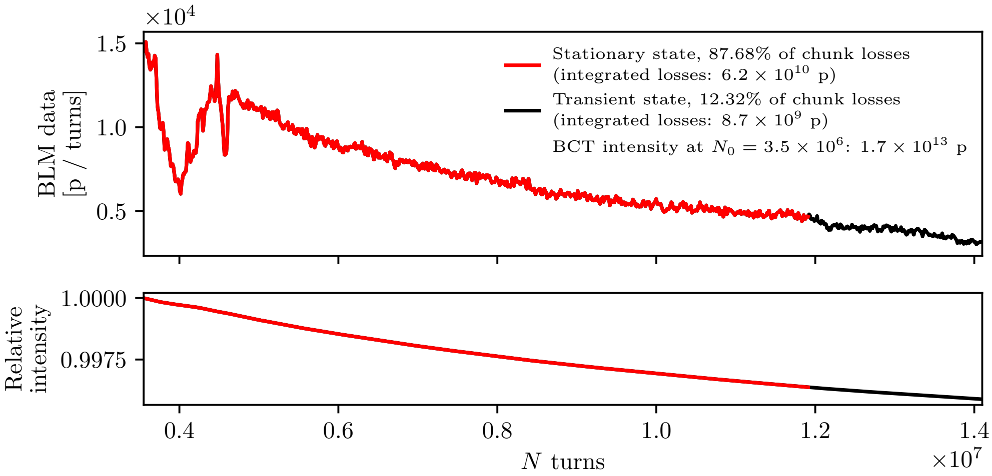

Figure 6.6: Example of the procedure used to evaluate the relative intensity lost over an interval $[N_0, N_1]$. The BLM signal is integrated over the interval, and the DCBCT value registered at $N_0 = 3.5\times10^6$ turns is used as the reference intensity. A comparison between the integrated losses measured in the stationary state of the chunk and the transient state, whose definition is given later and in Fig. 6.7, is also reported. As the losses in the transient state are much lower than the losses in the stationary state, our working hypothesis still holds.

In addition to the various assumptions made to allow the application of the special form of the diffusion coefficient, it is important to note that this model has the strong assumption that $D(I)$ does not evolve over time. This implies that the magnetic lattice of the accelerator must not manifest stronger variations than those given by the small stochastic perturbation. Such an assumption requires some preliminary consideration on the BLM loss signal that we have at hand.

When the BBCW, the crossing angle, and the octupoles are in a stationary state, we can state that the parameters of the Fokker-Planck equation can be considered as constant over time. We can define this state as stationary and have the beam distribution $\rho(I,t)$ following the evolution defined by the Fokker-Planck equation.

When, instead, a variation in any of the accelerator elements occurs, e.g. a BBCW is switched on or the crossing angle is varied, the parameters of the Fokker-Planck equation vary as well into a new value. This variation does not necessarily occur in a negligible time. As can be seen in Fig. 6.7. In fact, switching the BBCW DC current to the target voltage takes a significant number of seconds, leading to a time interval in which the system is in a transient state. During such a transient state, we cannot make assumptions about the evolution of the transverse beam or the evolution of the values of ϵ, I_*, and κ, and therefore we are forced to discard these data slices.

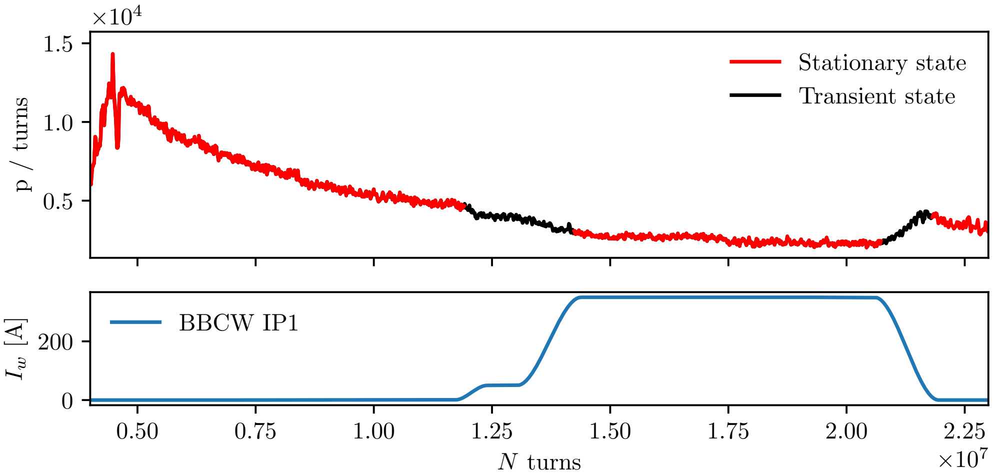

FIGURE 6.7: Visualization of the difference between stationary state and transient state for a data slice. We define as stationary state the time interval in which all the parameters of the system are in a steady state, while the transient state is the time interval in which the system is undergoing a variation. Here, the BBCW DC current is switched on to the target value, causing a transient state along the process.

In Fig. 6.8, we show the BLM data for Beam 2 divided into enumerated chunks where the system is in stationary state. We can see how the stationary states are generally longer than the transient states, except for the part where the octupoles change powering.

We assume that the beam distribution at the end of a stationary state can be used as the initial condition of the next stationary state. Therefore, we completely neglect the transient state losses between the two stationary states. However, to justify this approach, we must verify that the integrated loss in the transient state is significantly smaller than the integrated loss in the stationary state.

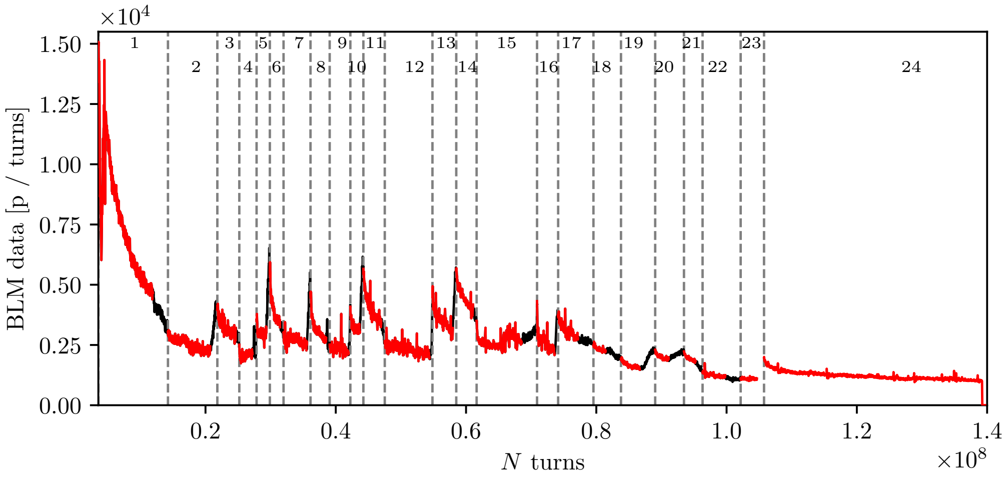

Figure 6.8: Experimental data for Beam 2 divided in chunks, where each chunk is in a stationary state. Each chunk is characterized by a different set of parameters, and the system is in a transient state when the parameters are changed. Each chunk has a number assigned, which will be used to identify it for the rest of the analysis. Red corresponds to stationary state data, while black represents transient state data.

In Fig. 6.9, this comparison is shown for each individual chunk, and it is possible to see how the interval where the octupole state changes has higher relative transient losses. Such comparable losses led us to the decision not to inspect this chunk of data characterized by varying octupole currents, and we performed the fitting procedure only on the data up to those variations. It must be noted that also chunks 5 and 10 display a comparable level of high losses in the transient state; this is mainly due to the fact that, for these two specific chunks, a change in parameters was performed after a very short number of turns, compared to the other chunks. Such a short time, inevitably, makes the losses in the stationary state almost comparable to those in the transient state.

After defining the properties of the data to be inspected, we fit our diffusive model following the same procedure as in the work of Bazzani et al. [7]. We consider a Gaussian beam in the action variable I, as an initial condition. This then gives us the following exponential distribution

$$\rho_0(I) = \sigma^{-2} \exp\left(-\frac{I}{\sigma^2}\right) \tag{6.1}$$

where σ^2 stands for the measured beam emittance. For convenience, it is possible to scale the action variable $I \to I/\sigma^2$, which corresponds to the setting

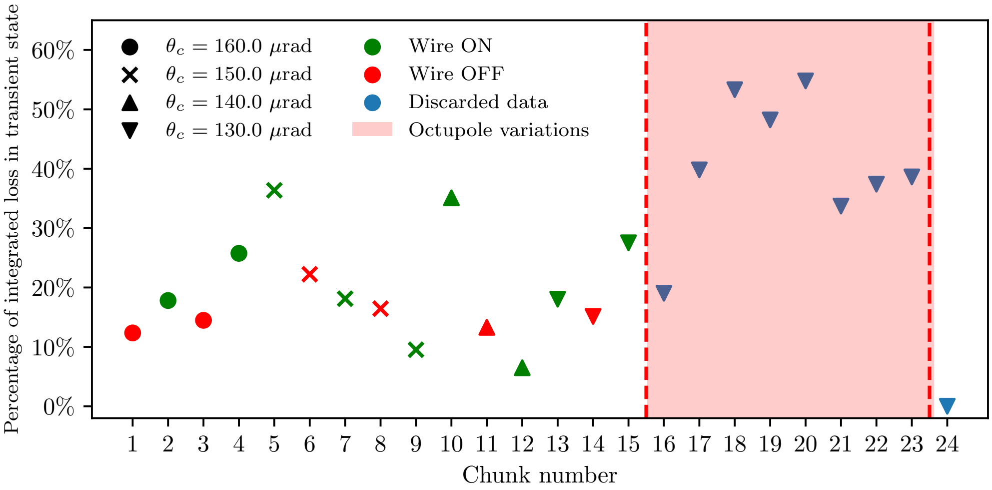

FIGURE 6.9: Comparison of the integrated losses in transient state and in stationary state for each chunk of data. The chunk number follows the nomenclature defined in Fig. 6.8. A higher relative loss in the transient states can be seen for the chunk where the octupoles current is changed.

$\sigma = 1$ in the simulations without affecting the beam loss rate. As for the absorbing boundary condition, we consider the position of the TCPs in IR7, which were set at nominal position. To fit the data, we then scan the values κ and I_*, and integrate the evolution of the FP equation (2.59) as a function of the number of turns. The parameter ϵ^2 is then fixed by requiring that the initial and final values of the relative intensity, evaluated at the beginning and at the end of the fragment, are equal. The scan in κ and I_* is first performed as a brute-force grid scan on a range of candidate values; then a least-square fitting is performed with starting point on the best parameters found with the preliminary scan.

As we assume that the beam distribution at the end of a stationary state can be used as the initial condition of the next stationary state, we can use the evolved beam distribution as the initial condition for the next chunk. This procedure, iterated for all parts, finally gives us the reconstructed $D(I)$ for the various states of the system. Note that this working hypothesis forces us to include in the fitting process also chunk 5 and chunk 10, despite their significant relative losses in the transient state.

6.4 | Numerical results

We perform the fitting procedure using the data for both Beam 1 and Beam 2. As the wires are installed on Beam 2 only, we do not expect to observe a significant difference between $D(I)$ reconstructed on the Beam 1 chunks with wire on and wire off. However, the data of Beam 1 are useful for understanding the effects of different crossing angles on the system and assessing the performance of the fitting procedure.

Beam 1 data

We first consider the data of Beam 1 divided in chunks only where the crossing angle is varied. In Fig. 6.10, we show the relative intensity loss, along with the fit reconstruction. Note that we considered Beam 1 data up to the point at which the octupole current is varied. In Fig. 6.11, we show the reconstructed $D(I)$ for the various crossing angles, with the resulting parameters reported in Tab. 6.1.

We can see how $D(I)$ increases as the crossing angle is lowered, as expected from the fact that long-range beam-beam effects become more important, and we can also observe how, in general, the fitting procedure manages to reproduce the data with high precision, as can be seen from the plotted fit residual in Fig. 6.10.

θ_c	160 µrad	150 µrad	140 µrad	130 µrad
I_*	90 ± 30	123 ± 10	140 ± 30	63.33 ± 0.02
κ	0.72 ± 0.06	0.72 ± 0.01	0.73 ± 0.03	0.6250 ± 0.0003
ϵ^2	6.8×10^{-7}	1.1×10^{-6}	2.8×10^{-6}	5.3×10^{-6}

Table 6.1: Fit parameters for the reconstructed $D(I)$ for the data of Beam 1 divided in chunks where the crossing angle is varied. The uncertainty reported represents the standard deviation of the fit parameters evaluated by the least-squares method.

We now inspect the data of Beam 1 divided in chunks where the wire compensators, acting on Beam 2, are switched on and off. A comparison of the reduced χ^2 values of the fit for the two different slicing methods is shown in Fig. 6.12. We can see that the reduced χ^2 values are mainly lower when smaller fragments are considered, but not consistently, as some individual chunks achieve a higher reduced χ^2 value than the fit performed on entire chunks with the same crossing angle. We can also observe how the reduced χ^2 value ranges between various orders of magnitude for the different smaller

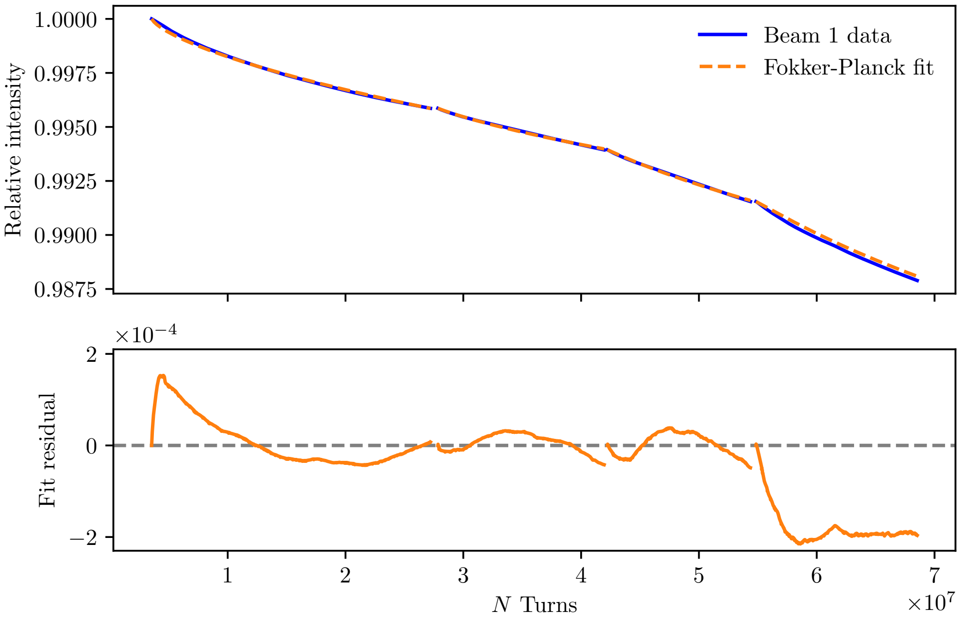

FIGURE 6.10: Relative loss of intensity for the data of Beam 1 divided in chunks where the crossing angle is varied. The fit reconstruction is also shown. A good agreement between the data and the fit is observed.

fragments. This suggests that in some individual situations, overfitting issues may occur, especially in the cases where the reduced χ^2 value drops the most.

We can see how the reconstructed $D(I)$, presented in Fig. 6.13, although manifesting differences, does not show a consistent different diffusion value between the two states, as the wires appear to affect the diffusion coefficient inconsistently. Furthermore, extreme differences are also obtained from the $D(I)$ reconstruction of the whole section, also at lower I values, where the diffusion is expected to be close to orders of magnitude lower than its value at higher I values. This suggests that the fitting procedure might be affected by overfitting when the chunks are too small and not rich enough in information, giving non-physical results.

From this analysis, it is impossible to detect a consistent effect of the wires on the diffusion coefficient of Beam 1, which leads to the conclusion that the impact of the BBWC on Beam 1 is negligible, and therefore the data analysis should not take into account the status (on or off) of the wire.

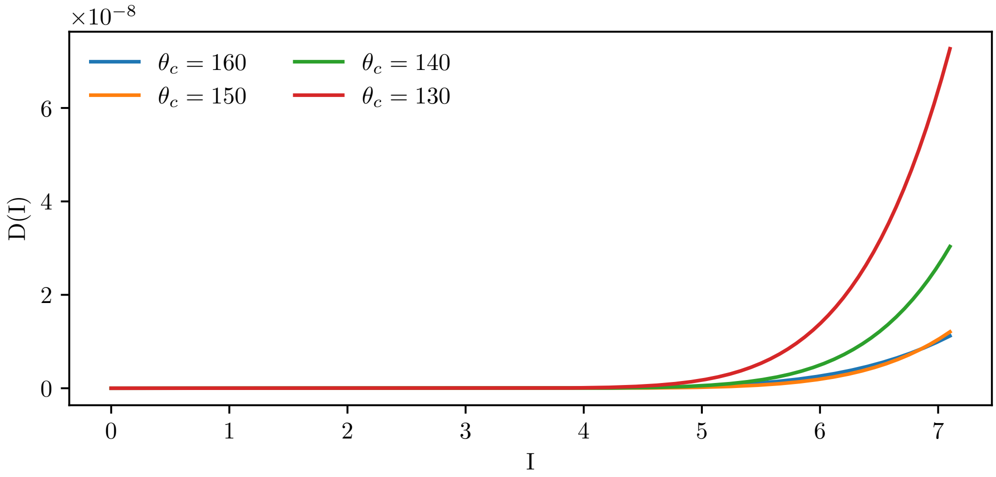

FIGURE 6.11: Reconstructed $D(I)$ for the data of Beam 1 divided in chunks where the crossing angle is varied. The $D(I)$ increases as the crossing angle is lowered.

Beam 2 data

Now we inspect the data of Beam 2, where the wires are installed. We consider the data divided into chunks as presented in Fig. 6.8. In Fig. 6.14, we show the relative intensity loss, along with the fit reconstruction. In Fig. 6.15, we show the reconstructed $D(I)$ for the various crossing angles and the various states of the wire.

It can be seen that, in general, the fit reconstruction is able to reproduce the data quite well. Furthermore, it is possible to see how the reconstructed $D(I)$ is consistently different when the wires are switched on and off, with generally higher diffusion values when the wires are off. This is in agreement with the expectation that the wires are able to reduce the long-range beam-beam effects and thus the diffusion. Moreover, it is possible to see how such a reconstructed $D(I)$ for the wire on also has lower values for low I amplitudes. This suggests that indeed the BBCWs might provide better long-term stability of the beam.

The values of the two parameters, I_* and κ, are shown in Fig. 6.16 and, in this case, no significant patterns can be observed in the evolution of the parameters for the different states of the system. However, a strong correlation can be observed between κ and I_*. A similar correlation was also observed and commented on in Chapter 4. In future studies, this correlation trend will be investigated and tackled by imposing the same κ value on multiple fittings, as this parameter is expected to depend only on the geometry of the phase space and, therefore, to be constant in physical systems with the same phase-space

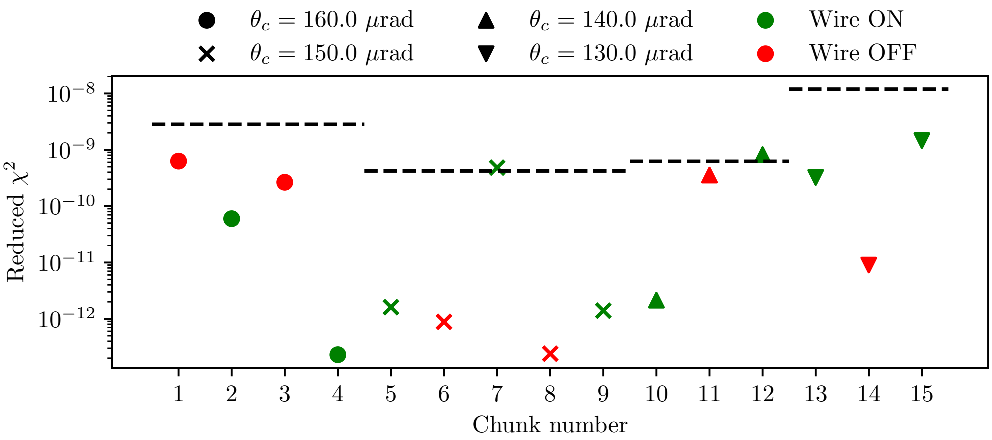

FIGURE 6.12: Comparison of the reduced χ^2 values of the fit for the two different chunking methods of Beam 1. The black dashed lines represent the reduced χ^2 obtained when fitting the entire data chunk with the same crossing angle, without considering the wire status. The reduced χ^2 values vary over multiple orders of magnitude when smaller chunks are considered, and in two cases is higher than the reduced χ^2 obtained by the larger chunk fitting. This may suggest overfitting issues for when the reduced χ^2 exhibits the lowest values. The numbers representing the chunks follow the nomenclature in Fig. 6.8.

dimensionality.

6.5 | Final remarks

We have performed an initial study of the effects of the BBCWs on the long-term beam dynamics of the LHC using our diffusive framework. We have used the data of the LHC Beam 1 and Beam 2, collected during an MD measurement campaign of Run 2, and we have reconstructed the diffusion coefficient of various system configurations. Ultimately, we have found that the wires are able to reduce the long-range beam-beam effects and thus the diffusion. Moreover, we have observed that our model suggests that the wires are consistently able to reduce intensity loss. As expected, the model did not highlight significant BBCWs effects on Beam 1.

As noted in the overview of the experimental data, a large portion of the data had to be discarded because of the large losses occurring during transient periods. Moreover, multiple chunks considered in the analysis are character-

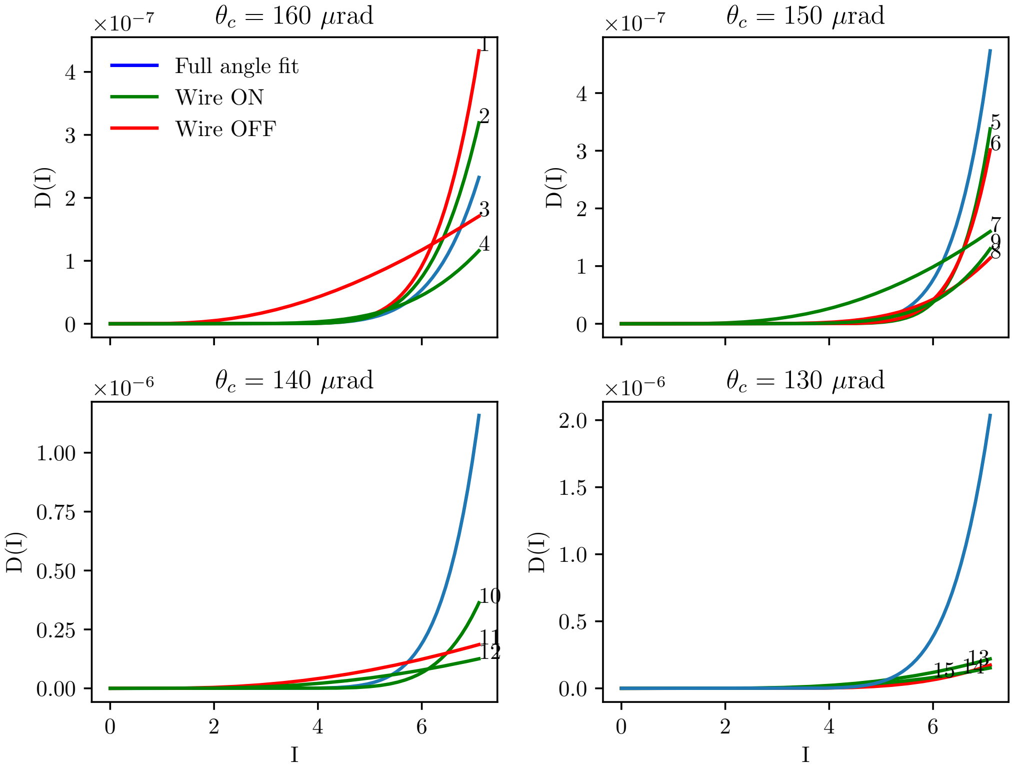

Figure 6.13: Reconstructed $D(I)$ for the data of Beam 1 divided in chunks where the wire compensators are switched on and off, compared with the $D(I)$ reconstructed using the full chunk corresponding to the crossing angle. The $D(I)$ does not show a consistent different diffusion value between the two states and, in many situations, the values obtained for $D(I)$ on the smaller samples obtain extremely different results from the full fitting result for low values of I. This suggests overfitting issues. The numbers representing the chunks follow the nomenclature in Fig. 6.8.

ized by a very short time span, which might be too short to be representative of long-term beam dynamics. This is a limitation of the collected data that could have had a significant impact on the results.

However, the promising results obtained in the fit reconstruction seem to suggest that this diffusive framework may provide some insight into the long-term effects of BBCWs on beam dynamics. This has motivated us to consider a different data collection strategy for the scheduled MD measurements of LHC Run 3. More specifically, we planned to measure the BLM losses while keeping the BBCWs on and off for longer time spans to better characterize the long-term effects of the wires.

Additionally, we planned to perform collimation scans with BBCWs on and

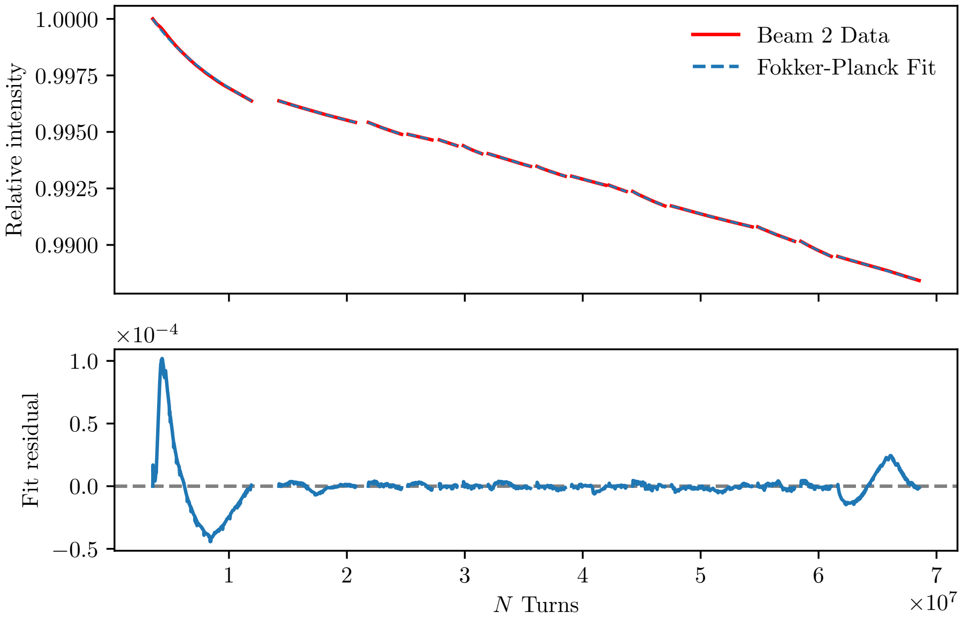

FIGURE 6.14: Relative intensity loss and fit reconstruction for the data of Beam 2 divided in chunks, following the nomenclature of Fig. 6.8. The fit reconstruction shows a very good agreement with the data, as can be seen from the fit residuals.

off, in order to directly inspect the beam tail population and measure $D(I)$ following the protocol presented in Chapter 4. The purpose was to compare the values obtained with the two different methodologies.

Both of these strategies in the data gathering have been successfully implemented during a MD measurement campaign of LHC Run3 [111], and the results will be presented in a future work.

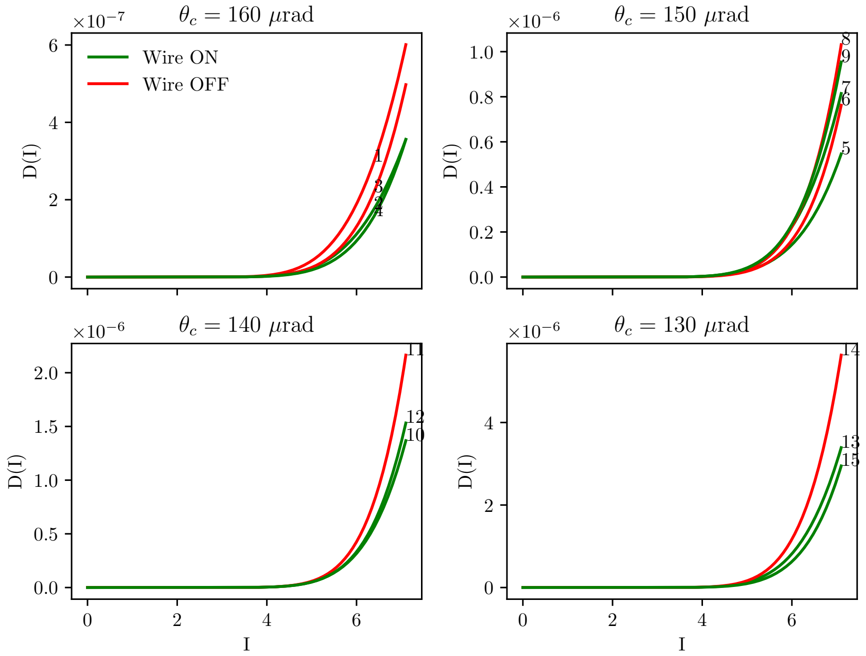

FIGURE 6.15: Reconstructed $D(I)$ for the data of Beam 2 divided in chunks, following the nomenclature of Fig. 6.8. It can be seen how the reconstructed $D(I)$ is consistently different when the wires are switched on and off, with, in general higher diffusion values when the wires are off. The only exception is given by chunk 6, with a crossing angle of θ_c =150 µrad.

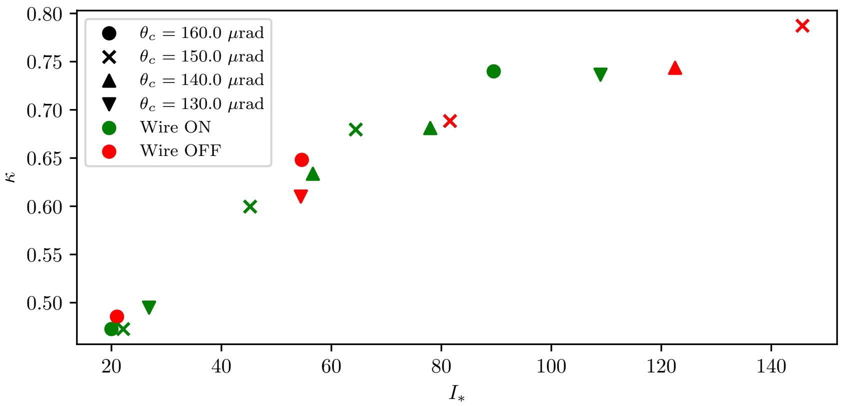

FIGURE 6.16: Evolution of the parameters I_*, and κ, for the Beam 2 data divided in chunks, following the nomenclature of Fig. 6.8. No significant patterns can be observed as a function of the crossing angle, except a strong correlation between κ and I_*.

Part III

Dynamic indicators for the detection of regular and chaotic motion

7 | Overview of dynamic indicators

The content of this chapter, with the due adaptations, has resulted in the article by A. Bazzani, M. Giovannozzi, C. E. Montanari, G. Turchetti *"Performance analysis of indicators of chaos for non-linear dynamical systems"*, currently under internal peer review.

After investigating the applicability of a Nekhoroshev-like diffusive models to the study of beam loss data, we now switch our focus to the topic of single-particle tracking and, consequently, to the problem of characterizing the long-term dynamics of non-linear symplectic maps, which of course includes realistic accelerator one-turn maps.

In this chapter, we focus on the identification of chaotic behaviour in the orbits of complex dynamical systems by using dynamic indicators. Dynamic indicators have been already proposed, and new ones have been designed with the goal of enhancing the detection of chaos in numerical simulations. The difficulty lies in forecasting chaotic behaviour by analysing orbits of a restricted length. To inspect the properties of these indicators, and assess which ones are the best performing, we carry out an accurate analysis of the performance of the indicators briefly introduced to classify the orbits of a 4D modulated polynomial symplectic map, namely a 4D Hénon map that is considered a reference model for several applications.

The chapter is structured as follows. In Section 7.1, we give a brief introduction on the topic of chaos indicators, as well as a summary of the dynamic indicators under analysis; in Section 7.2 we define mathematically and discuss in some detail the chaos indicators considered; in Section 7.3 we discuss their numerical implementation; in Section 7.4 we present the numerical results and rank the different indicators in terms of classification efficiency, in particular, studying their predictive power. Finally, some conclusions are drawn in Section 7.5. In addition, we report some detail on the computational cost of implementing indicators using parallel computing facilities in Appendix 7.A, while some considerations on the time dependence of indicators are presented in Appendix 7.B.

7.1 | Introduction

The study of the long-term evolution of Hamiltonian systems is a very difficult task from both a theoretical and a numerical point of view. The KAM theory [112] cannot be used to solve the stability problem for Hamiltonian systems in more than two dimensions. Therefore, great effort has been devoted to improving time stability estimates after the celebrated Nekhoroshev theorem [21]. However, the existence of chaotic layers in phase space strongly affects the long-term evolution of the orbits, and for this reason, numerical indicators have been proposed to detect the chaotic character of orbits using a limited number of time iterations.

For a given Hamiltonian model, one has to tackle the problem of comparing the performance of the various indicators to assess which one provides the optimal classification of the orbits. In applications, this task must be accomplished taking into account the characteristics of the physical problem under consideration. For instance, in the field of accelerator physics, the study of the charged-hadron motion in the magnetic lattice of a circular accelerator is often devoted to the determination of the region of phase space in which bounded motion occurs. The extent of such a region is called dynamic aperture and involves studying the stability of orbits of a 6D polynomial symplectic map in a neighbourhood of an elliptic fixed point, up to $10^8 - 10^9$ iterations (see, e.g., [40]). An exhaustive analysis of the phase-space topology is clearly beyond the current computational capabilities. Therefore, indicators of chaos turn out to be extremely useful to reduce the amount of computational time needed to assess the character of orbits (regular or chaotic). This task may be affected by the presence of orbit diffusion in phase space, which occurs in chaotic layers. The presence of small stochastic effects, which naturally arise in physical systems, may prevent orbit trapping near regular regions, the so-called stickiness phenomenon [25, 113], thus inducing diffusive behaviour in phase space.

It is worth noting that polynomial symplectic maps are not only central for the analysis of accelerator physics problems, as they are also present in other domains and have been intensively studied to understand the phase space structure of Hamiltonian systems [114], and are a fundamental tool for long-term integration of orbits [40].

The main result of this chapter is to show that it is possible to determine a classification performance ranking of the main commonly used chaotic indicators when applied to a generic 4D cubic polynomial symplectic map of Hénon-like form (see, e.g., [40]), which is an excellent prototype dynamical system for applications.

The indicators of chaos are typically based on the existence of positive Lyapunov characteristic exponents, and their numerical performance is strongly affected in the regions where sticky orbits are present.

The family of Fast Lyapunov indicators (FLI) [24] has been proposed to distinguish the regions of regular and chaotic motion for symplectic maps [25]. They also proved to be suitable for distinguishing resonant regions in phase space and to visualize the Arnold web of resonances where slow diffusion occurs [32]. These indicators are based on the evolution of an initial deviation vector and provide the linear response of the tangent map along an orbit. When considering one or more initial deviation vectors, the result depends on the direction of the initial deviation vectors. To overcome this, the linear response to a random displacement vector with zero mean value and unit variance was recently proposed [115]. The trace of the corresponding covariance matrix defines the square Lyapunov Error (LE), which is similar to FLI. Furthermore, the invariants of the covariance matrix of order $k > 1$ are asymptotically related to the sum of the first k Lyapunov exponents. However, unlike the Generalized Alignment Index ($GALI^{(k)}$) indicators [30, 31], these invariants do not depend on the initial deviations [116]. Recently, a couple of approaches have been proposed to improve the performance of some indicators, namely applying the Weighted Birkhoff averaging [117] or the Mean Exponential Growth of Nearby Orbit ($MEGNO$) [118], which is used to filter the oscillations and to improve the accuracy by averaging on map iterations [119, 120].

To calculate the sensitivity to small deviations along an orbit, the Reversibility Error Method (REM) can be used [28, 29]. In this case, the linear response to the forward evolution in the presence of small random noise is considered, followed by the unperturbed backward evolution. The covariance matrix of the random process, which provides the final deviation from the initial condition in the limit of zero noise amplitude, can be computed, and its invariants quantify the violation of reversibility. The first invariant for the forward-backward process BF is the square of the reversibility error, which is equal to the sum of the squares of Lyapunov errors computed at each iteration of the map. This invariant can be compared with the results for REM, when the stochastic perturbation is generated by the finite numerical precision present in both the forward and backward directions.

Finally, a completely different indicator introduced by J.Laskar [26, 27] is represented by the Frequency Map Analysis FMA, which computes the variation of the main frequency of a given orbit considering different orbit lengths to detect the chaotic character.

7.2 | Definition and main properties of indicators of chaos

7.2.1 | Frequency Map Analysis

Originally introduced by J. Laskar in the field of celestial mechanics, the Frequency Map Analysis (FMA) rapidly expanded outside the initial domain of application (see, e.g., [26, 27, 121–135] for a selected list of references, with special emphasis on accelerator-related applications) is a numerical method to inspect the global dynamics of multidimensional Hamiltonian systems, taking advantage of the quasiperiodicity of regular orbits located on KAM tori.

Given a Hamiltonian system $H(I,\theta) = H_0(I)+\varepsilon H_1(I,\theta)$, where for $\varepsilon = 0$ the Hamiltonian $H_0(I)$ is integrable and $(I, \theta$ are action angle variables in $\mathbb{R}^n \times \mathbb{T}^n$, where $\mathbb{T}$ represents a one-dimensional torus. If the system is nondegenerate,

$$\det\left(\frac{\partial \nu(I)}{\partial I}\right) = \det\left(\frac{\partial^2 H_0(I)}{\partial I^2}\right) \neq 0\,, \tag{7.1}$$

the application

$$F : I \in \mathbb{R}^n \longrightarrow \nu \in \mathbb{R}^n \tag{7.2}$$

is a diffeomorphism on its image. This means that the invariant tori are equally identified by the action variables I or by their corresponding frequency vector ν. For a nondegenerate system, when ε is sufficiently small, the KAM theorem [33–35], states that there still exists a set of initial conditions of positive measure that correspond to regular orbits on invariant tori, for which, according to Pöschel [136], a similar diffeomorphism still applies.

Based on this theoretical framework, it is possible to distinguish between regular orbits on the KAM tori, which feature a discrete structure for Fourier components defined by the harmonic of the fundamental frequencies, and chaotic orbits, which exhibit a complex structure in the Fourier spectrum [135]. In this sense, FMA is a technique that performs numerical evaluations of the frequency vector ν from a time series corresponding to a certain interval $[i, i+n]$, for different values of i. In case of a regular orbit lying on a KAM tori, the frequency vectors for various i will agree up to the precision of the numerical method used to determine the frequency. On the other hand, a chaotic orbit will have ν that evolves over different intervals, showing fluctuations in frequency space [133].

To achieve an accurate numerical evaluation of fundamental frequencies, multiple studies have been carried out to improve standard algorithms such as the Fast Fourier Transform (FFT) or the Average Phase Advance (APA) [26, 137–139]. In the work of Bartolini et al. [140], the fundamental frequency is evaluated using an FFT combined with a Hanning filter and an interpolation algorithm, resulting in a closed-form formula for the fundamental frequency. In recent studies [141], the frequency determination carried out using the average phase advance algorithm is improved by applying the weighted Birkhoff averaging [142], which will be used in the sequel to perform the evaluation of FMA. More precisely, we define FMA_n as the Euclidean distance between two vectors defined by the fundamental frequencies ν_1 and ν_2, evaluated respectively over the time intervals $[0, n/2]$ and $[n/2, n]$ of the orbit. An initial condition on a KAM torus has FMA_n converge to zero when $n \to \infty$. In contrast, an initial condition in a chaotic layer will converge to an asymptotic value for FMA_n bounded away from zero.

7.2.2 | Lyapunov Error invariants

Let $M(\mathbf{x}, n)$ be a time-dependent symplectic map with $\mathbf{x} \in \mathbb{R}^{2d}$ where the first d components of $\mathbf{x}$ are the space coordinates and the last d their conjugate moments. Denoting by DM the Jacobian matrix $(DM)_{ij} = \partial M_i/\partial x_j$ and by $\mathbf{x}_n$ the orbit after n iterations, the corresponding tangent map $\mathsf{L}_n(\mathbf{x})$ is defined by

$$\begin{aligned} &\mathbf{x}_n = M(\mathbf{x}_{n-1}, n-1) \equiv M_n(\mathbf{x}), && \mathbf{x}_0 = \mathbf{x}; \\ &\mathsf{L}_n(\mathbf{x}) = DM(\mathbf{x}_{n-1}, n-1)\,\mathsf{L}_{n-1}(\mathbf{x}) \equiv DM_n(\mathbf{x}), && \mathsf{L}_0 = \mathsf{I}, \end{aligned} \tag{7.3}$$

where $M_n(\mathbf{x}) = M(\mathbf{x}, n-1) \circ M_{n-1}(\mathbf{x})$ with $M_0(\mathbf{x}) = \mathbf{x}$.

For any initial condition $\mathbf{x}$, consider a small stochastic deviation $\epsilon\boldsymbol{\xi}$ where $\boldsymbol{\xi}$ is a unit random vector with $\langle\, \boldsymbol{\xi}\, \rangle = 0$ and a unit covariance matrix $\langle\, \boldsymbol{\xi}\, \boldsymbol{\xi}^T\, \rangle = \mathsf{I}$, where the suffix ^{T} denotes the transposed vector. Letting $\mathbf{y}_n = M(\mathbf{y}_{n-1}, n-1)$ be the orbit with initial condition $\mathbf{y}_0 = \mathbf{x}_0 + \epsilon\boldsymbol{\xi}$ the linear response $\Xi_n(\mathbf{x})$, initialized by $\Xi_0 = 0$ is given by

$$\begin{aligned} \Xi_n(\mathbf{x}) &= \lim_{\epsilon\to 0} \frac{\mathbf{y}_n - \mathbf{x}_n}{\epsilon} \\ &= DM(\mathbf{x}_{n-1}, n-1) \times \lim_{\epsilon\to 0} \frac{\mathbf{y}_{n-1} - \mathbf{x}_{n-1}}{\epsilon} \\ &= DM(\mathbf{x}_{n-1},\ n-1)\Xi_{n-1} \\ &= \mathsf{L}_n(\mathbf{x})\,\boldsymbol{\xi}\ . \end{aligned} \tag{7.4}$$

The random vector Ξ_n has zero mean and covariance matrix

$$\Sigma_n^2(\mathbf{x}) = \langle\, \Xi_n(\mathbf{x})\Xi_n^T(\mathbf{x})\, \rangle = \mathsf{L}_n(\mathbf{x})\mathsf{L}_n^T(\mathbf{x})\,. \tag{7.5}$$

Oseledet theorem [143] states that the limit

$$\lim_{n\to\infty} (\mathsf{L}_n^T \mathsf{L}_n)^{1/2n} = \mathsf{W}\, e^{\Lambda}\, \mathsf{W}^T \tag{7.6}$$

exists, where W is an orthogonal symplectic matrix and Λ is diagonal with entries $\lambda_j(\mathbf{x})$ ordered in a decreasing sequence in j.

The diagonal entries of Λ are the Lyapunov exponents, and the columns of W the corresponding Lyapunov vectors. Since the eigenvalues of $\mathsf{L}_n^T \mathsf{L}_n$ are the same as those of the covariance matrix $\mathsf{L}_n \mathsf{L}_n^T$, the two matrices have the same characteristic polynomial. Then consider the corresponding invariants $I_n^{(k)}(\mathbf{x}), k = 1, \ldots, 2d$, i.e., the coefficients of the characteristic polynomial. The first invariant $I_n^{(1)}(\mathbf{x})$, is given by the trace of the covariance matrix, namely,

$$I_n^{(1)}(\mathbf{x}) \equiv \mathrm{Tr}\big(\Sigma_n^2(\mathbf{x})\big) = \mathrm{Tr}\big(\mathsf{L}_n^T(\mathbf{x})\, \mathsf{L}_n(\mathbf{x})\big) = LE_n^2(\mathbf{x})\,, \tag{7.7}$$

which is the square of the Lyapunov error $LE_n(\mathbf{x})$. Note that it does not depend on the initial deviation vector or on the chosen orthogonal reference frame, and its asymptotic behaviour is determined by the first, i.e., largest, Lyapunov exponent λ_1.

The other invariants $I^{(k)}$ are the sum of all products that combine k distinct eigenvalues if they are simple. The geometric interpretation is straightforward. Letting $\mathbf{e}_j$ be the standard base vectors, we have $\mathsf{L}_n = (\mathbf{e}_{1\;n}, \ldots, \mathbf{e}_{2d\;n})$where $\mathbf{e}_{j\;n} = \mathsf{L}_n\, \mathbf{e}_j$. Therefore, the invariant $I_n^{(k)}(\mathbf{x})$ is the sum of the squared volumes of the $\binom{2d}{k}$ parallelotopes whose sides are the vectors $\mathbf{e}_{j_1\;n}(\mathbf{x}), \ldots, \mathbf{e}_{j_k\;n}(\mathbf{x})$.

The difference with respect to $GALI_n^{(k)}$ indicators (see Section 7.2.5), is that the $I_n^{(k)}(\mathbf{x})$ are independent of the initial displacements.

For a symplectic map, $\mathsf{L}_n(\mathbf{x})$ is a symplectic matrix, and $\Sigma_n^2(\mathbf{x}) = \mathsf{L}_n(\mathbf{x})\, \mathsf{L}_n^T(\mathbf{x})$ is symplectic and positive definite. As a consequence, ordering the eigenvalues in a decreasing sequence, we have $e^{\lambda_{j;n}} e^{\lambda_{2d-j+1;n}} = 1$. The asymptotic behaviour of the invariant $I_n^{(k)}$, $k \le 2d$ is given by

$$\lim_{n\to\infty} \frac{1}{2n} \log I_n^{(k)}(\mathbf{x}) = \lambda_1(\mathbf{x}) + \ldots + \lambda_k(\mathbf{x})\,. \tag{7.8}$$

In a region of chaotic motion, $\lambda_{j\;n}(\mathbf{x})$ are positive for $j \le d$ just as their limit $\lambda_j(\mathbf{x})$, so that $I_n^{(k)}(\mathbf{x})$ has exponential growth with n, for n sufficiently large. In a region of regular motion, $I_n^{(k)}(\mathbf{x})$ grows according to a power law $I_n^{(k)}(\mathbf{x}) \sim n^{2k}$ for $k \le d$ as all Lyapunov exponents vanish.

7.2.3 | Fast Lyapunov Indicator and Weighted Birkhoff averaging

The Fast Lyapunov Indicator [24], is one of the best known dynamic indicators, due to its straightforward implementation and its sensitiveness to the detection of chaotic structures [144]. Given $M(\mathbf{x}, n)$, its tangent map $\mathsf{L}_n(\mathbf{x})$, and an arbitrary initial unitary deviation vector $\boldsymbol{\xi}$, FLI is defined for $n \geq 1$, as:

$$FLI_n(\mathbf{x}_0, \boldsymbol{\xi}) = \ln \|\mathsf{L}_n(\mathbf{x}_0)\boldsymbol{\xi}\| \,, \tag{7.9}$$

i.e., the logarithm of the linear response $\boldsymbol{\Xi}_n(\mathbf{x})$, calculated for an arbitrary fixed deviation vector. The quantity FLI_n/n tends to the largest Lyapunov exponent as $n \longrightarrow \infty$. Therefore, in a region of regular motion, this quantity tends to zero, whereas in a region of chaotic motion it takes a positive value.

It is possible to take advantage of the properties of the logarithm in Eq. (7.9) to avoid overflows for large values of n, and to express the limit FLI_n/n as an average along the trajectory $\mathbf{x}_n$ [145]:

$$\begin{aligned} \frac{FLI_n(\mathbf{x}_0, \boldsymbol{\xi})}{n} &= \sum_{i=0}^{n-1} \frac{\ln \|\mathbf{y}_i - \mathbf{x}_i\|}{n}, \\ \mathbf{y}_i &= DM(\mathbf{x}_{i-1}, i-1)\frac{\mathbf{y}_{i-1} - \mathbf{x}_{i-1}}{\|\mathbf{y}_{i-1} - \mathbf{x}_{i-1}\|}\,, \\ \mathbf{y}_1 &= DM(\mathbf{x}_0, 0)\boldsymbol{\xi}\,. \end{aligned} \tag{7.10}$$

In the work of Das et al. [117], it is presented how the application of the Weighted Birkhoff averaging method WB_n [142] in the evaluation of FLI can lead to superconvergence properties when applied to oscillating time series. Instead of considering equal weighting $(1/n)$, the Weighted Birkhoff averaging method uses a weighting function $w\left(\frac{i}{n}\right)$, which acts similarly to a window function in spectral analysis. A function $w(t)$ that proved to be very effective in improving the convergence of quasiperiodic time series averages [142] reads as follows:

$$w(t) := \begin{cases} \exp\left[-\frac{1}{t(1-t)}\right], & \text{for } t \in (0,1) \\ 0, & \text{for } t \notin (0,1) \end{cases}. \tag{7.11}$$

Replacing the standard mean with $w(t)$ in Eq. (7.10) leads to the weighted Fast Lyapunov Indicator FLI_n^{WB}:

$$FLI_n^{WB}(\mathbf{x}_0, \boldsymbol{\xi}) = \sum_{i=0}^{n-1} w\left(\frac{i}{n}\right) \ln \|\mathbf{y}_i\| \,. \tag{7.12}$$

We expect that $FLI_n^{WB}(\mathbf{x}_0, \boldsymbol{\xi})$ converges faster than $FLI_n(\mathbf{x}_0, \boldsymbol{\xi})/n$ to their common limit in the case of regular orbits, at least.

To simplify the notation, we will refer to $FLI_n(\mathbf{x}_0, \boldsymbol{\xi})/n$ and $FLI_n^{WB}(\mathbf{x}_0, \boldsymbol{\xi})$ as $FLI_n(\boldsymbol{\xi})/n$ and $FLI_n^{WB}(\boldsymbol{\xi})$, respectively, specifying the choice made for the initial unitary displacement $\boldsymbol{\xi}$.

7.2.4 | Backward-Forward reversibility error

The reversibility error is obtained by computing the linear response of the dynamics to small additive stochastic perturbations on the orbit after n forward iterations n followed by n backward iterations

$$\begin{aligned} \mathbf{y}_{n'} &= M(\mathbf{y}_{n'-1}, n'-1) + \epsilon \boldsymbol{\xi}_{n'}\,, \qquad \mathbf{y}_0 = \mathbf{x}\,, \qquad 1 \le n' \le n\,; \\ \mathbf{y}_{n'} &= M^{-1}(\mathbf{y}_{n'-1}, 2n-n') + \epsilon \boldsymbol{\xi}_{n'}\,, \qquad n+1 \le n' \le 2n\,. \end{aligned} \tag{7.13}$$

where $\boldsymbol{\xi}_{n'}$ are random vectors with zero mean and unit covariance matrix $\langle \boldsymbol{\xi}_{n'} \rangle = 0$ and $\langle \boldsymbol{\xi}_{n'} \boldsymbol{\xi}_{n''}^T \rangle = \delta_{n'n''}$. $\boldsymbol{\xi}_{n'} = 0$ for $n' > n$. We denote by $\mathbf{x}_{n'}$ the orbit when random deviations are absent $\epsilon = 0$. This orbit enjoys the symmetry property $\mathbf{x}_{n'} = \mathbf{x}_{2n-n'}$ for $n+1 \le n' \le 2n$, so the reversibility condition $\mathbf{x}_{2n} = \mathbf{x}$ is satisfied.

The linear response for the BF process is defined by

$$\Xi_{n'}^{BF}(\mathbf{x}) = \lim_{\epsilon \to 0} \frac{\mathbf{y}_{n'} - \mathbf{x}_{n'}}{\epsilon}\,, \qquad 1 \le n' \le 2n\,, \tag{7.14}$$

and the cumulative random deviation $\Xi_{n'}^{BF}(\mathbf{x})$satisfies the recurrence

$$\begin{aligned} \Xi_{n'}^{BF} &= DM(\mathbf{x}_{n'-1}, n'-1)\, \Xi_{n'-1}^{BF}(\mathbf{x}) + \boldsymbol{\xi}_{n'}\,, \qquad 1 \le n' \le n; \\ \Xi_{n'}^{BF} &= DM^{-1}(\mathbf{x}_{2n-n'+1}, 2n-n')\, \Xi_{n'-1}^{BF} + \boldsymbol{\xi}_{n'}\,, \qquad n+1 \le n' \le 2n\,. \end{aligned} \tag{7.15}$$

From the recurrence relation of the tangent map (7.3) evaluated for n' and from the equality $DM^{-1}(M(\mathbf{x}, k), k))\, DM(\mathbf{x}, k) = \mathsf{I}$ for $k = 2n - n'$ it follows

$$\begin{aligned} DM(\mathbf{x}_{n'-1},\ n'-1) &= \mathsf{L}_{n'}(\mathbf{x})\, \mathsf{L}_{n'-1}^{-1}(\mathbf{x})\,, \\ DM^{-1}(\mathbf{x}_{2n-n'+1}, 2n-n') &= \Big(DM(\mathbf{x}_{2n-n'}, 2n-n') \Big)^{-1} \\ &= \mathsf{L}_{2n-n'}(\mathbf{x})\, \mathsf{L}_{2n-n'+1}^{-1}(\mathbf{x})\,. \end{aligned} \tag{7.16}$$

Replacing Eq. (7.16) in Eq. (7.13) we obtain the final result

$$\begin{aligned}
\Xi_n^{BF}(\mathbf{x}) &= \mathsf{L}_n(\mathbf{x}) \sum_{k=1}^{n} \mathsf{L}_k^{-1}(\mathbf{x})\, \boldsymbol{\xi}_k \,; \\
\Xi_{2n}^{BF}(\mathbf{x}) &= \mathsf{L}_n^{-1}(\mathbf{x})\, \Xi_n^{BF}(\mathbf{x}) + \sum_{k=0}^{n-1} \mathsf{L}_k^{-1}(\mathbf{x})\, \boldsymbol{\xi}_{2n-k} \\
&= \sum_{k=1}^{n-1} \mathsf{L}_k^{-1}(\mathbf{x})\, (\boldsymbol{\xi}_k + \boldsymbol{\xi}_{2n-k}) \; + \; \boldsymbol{\xi}_{2n} + \mathsf{L}_n^{-1}(\mathbf{x})\boldsymbol{\xi}_n .
\end{aligned} \tag{7.17}$$

If random deviations are present only in the forward process, the covariance matrix of Ξ_{2n}^{BF} is given by

$$\Sigma_n^{2\;BF}(\mathbf{x}) = \left\langle \Xi_{2n}^{BF}(\mathbf{x}) \big(\Xi_{2n}^{BF}(\mathbf{x})\big)^T \right\rangle = \sum_{k=1}^{n} \big(\mathsf{L}_k^T(\mathbf{x}) \mathsf{L}_k(\mathbf{x}) \big)^{-1} . \tag{7.18}$$

If random deviations are present both in the forward and backward processes, we define $\Sigma_n^{2\;BF}$ as $1/2$ the covariance matrix of Ξ_{2n}^{BF}, and the result is the r.h.s. of Eq. (7.18) where the last term of the sum $(\mathsf{L}_n^T \mathsf{L}_n)^{-1}$ is replaced by $\frac{1}{2}\,\mathsf{I} + \frac{1}{2}(\mathsf{L}_n^T \mathsf{L}_n)^{-1}$ due to the boundary condition, and asymptotically, for $n \to \infty$ the difference is negligible.

The invariants of the matrix $\Sigma_n^{2\;BF}$ provide information on the effect of small random perturbations along the orbits. If the map M is symplectic, both L_n and $\mathsf{L}_n^T \mathsf{L}_n$ are symplectic matrices and the trace of$\mathsf{L}_n^T \mathsf{L}_n$ and its inverse are equal. As a consequence, it is not difficult to check that the trace of $\left(\sum_{n'} \big(\mathsf{L}_{n'}^T \mathsf{L}_{n'}\big)^{-1}\right)^k$ and of $\left(\sum_{n'} \mathsf{L}_{n'}^T \mathsf{L}_{n'}\right)^k$ are equal and the invariants of the covariance matrices of the BF process become

$$I_n^{(k)\;BF}(\mathbf{x}) = I^{(k)} \left(\sum_{k'=1}^{n} \left(\mathsf{L}_{n'}^T(\mathbf{x})\, \mathsf{L}_{n'}(\mathbf{x}) \right)^{-1} \right) = I^{(k)} \left(\sum_{k'=1}^{n} \mathsf{L}_{n'}^T(\mathbf{x})\, \mathsf{L}_{n'}(\mathbf{x}) \right) . \tag{7.19}$$

The first invariant has a very simple relation to the Lyapunov error $LE_n(\mathbf{x})$. Explicitly, we have the following.

$$\Big(E_n^{BF}(\mathbf{x})\Big)^2 \equiv I_n^{(1)\;BF}(\mathbf{x}) = \sum_{n'=1}^{n} \mathrm{Tr}\Big(\mathsf{L}_{n'}^T(\mathbf{x})\mathsf{L}_{n'}(\mathbf{x})\Big) = \sum_{n'=1}^{n} \Big(LE_n(\mathbf{x})\Big)^2 . \tag{7.20}$$

We conclude by observing that the BF reversibility error analysis can be applied to investigate the effect of rounding errors in numerical computations [146]. Letting M_ϵ be the map evaluated with roundoff errors and M_ϵ^{-1}

its inverse, we have $M_\epsilon^{-1}(M_\epsilon(\mathbf{x})) = \mathbf{x} + O(\epsilon)$. In the IEEE 754 international standard, the precision of a real number is $\epsilon \sim 10^{-16}$. Iteration with rounding is defined by Eq. (7.13) where $\epsilon\xi_{n'}$ is missing, but M is replaced by M_ϵ. The matrix $\frac{1}{2}\,\Xi_{2n}^{BF}\left(\Xi_{2n}^{BF}\right)^T$, whose average defines the covariance matrix of the BF reversibility error, is replaced by

$$\mathsf{X}_{2n}^{BF}(\mathbf{x}) = \frac{1}{2}\,\frac{\mathbf{y}_{2n} - \mathbf{x}}{\epsilon}\,\frac{(\mathbf{y}_{2n} - \mathbf{x})^T}{\epsilon}\,. \tag{7.21}$$

This matrix has a non-zero eigenvalue, with eigenvector $\mathbf{y}_{2n} - \mathbf{x}$, and a null eigenvalue of multiplicity $2d - 1$ with eigenspace orthogonal to $\mathbf{y}_{2n} - \mathbf{x}$. The noise-induced Reversibility Error Method (REM) squared is the non-zero eigenvalue of such a matrix, equal to is trace and given by

$$\left(REM_n^{BF}(\mathbf{x})\right)^2 = \mathrm{Tr}\left(\mathsf{X}_{2n}^{BF}(\mathbf{x})\right) = \frac{1}{2}\,\frac{\mathbf{y}_{2n} - \mathbf{x}}{\epsilon}\cdot\frac{\mathbf{y}_{2n} - \mathbf{x}}{\epsilon}\,. \tag{7.22}$$

The main difference is that REM, due to rounding, is the result of a single realization with a pseudorandom error and, therefore, is affected by large fluctuations when we vary n or $\mathbf{x}$. These fluctuations are absent for the BF reversibility error previously defined, since averaging over the random deviations is carried out. The other relevant difference is that the higher-order REM invariants are zero.

Note that the implementation of REM is trivial since it does not require the evaluation of the tangent map and the computational cost is just twice the cost of the orbit computation, provided that the inverse map is explicitly known.

7.2.5 | $GALI^{(k)}$ indicators

The k-order indicators $GALI^{(k)}$ use the volumes of parallelotopes whose sides are normalized images of the k linearly independent vectors $\boldsymbol{\eta}_j$ with $1 \leq j \leq k$.

$$GALI_n^{(k)}(\mathbf{x}) = \left\|\frac{\mathsf{L}_n(\mathbf{x})\boldsymbol{\eta}_1}{\|\mathsf{L}_n(\mathbf{x})\boldsymbol{\eta}_1\|} \wedge \ldots \wedge \frac{\mathsf{L}_n(\mathbf{x})\boldsymbol{\eta}_k}{\|\mathsf{L}_n(\mathbf{x})\boldsymbol{\eta}_k\|}\right\|\,, \tag{7.23}$$

where $\wedge$ stands for the external product of two vectors. Their asymptotic behaviour for chaotic orbits, whose first d Lyapunov exponents are positive, is given by

$$GALI_n^{(k)} \sim e^{-n\left((\lambda_1-\lambda_2)+\ldots+(\lambda_1-\lambda_k)\right)}\,. \tag{7.24}$$

where we assume a decreasing order for the exponents.

For regular, quasi-periodic orbits, whose Lyapunov exponents vanish, the $GALI^{(k)}$ indicators decay following a power law. We recall that the Lyapunov error invariants $I_n^{(k)}$ grow exponentially with a coefficient given by the sum of the first k Lyapunov exponents for chaotic orbits, or according to a power law for regular orbits.

7.2.6 | Introducing filters

We conclude by remarking that the introduction of a filter such as $MEGNO$ that drastically reduces the numerical oscillations of the indicator of chaos [119, 147], may greatly improve the efficiency of the indicator. In principle, the oscillations disappear using suitable normal coordinates for the considered systems, but their computations face the limits and technical difficulties of perturbation theory. Referring to the phase flow that interpolates the orbits at integer times $t = n$, $MEGNO$, applied to $LE_t(\mathbf{x})$, it has the double-time average of $d \log LE_t(\mathbf{x}) / d \log t$

$$\begin{aligned} MEGNO_n(LE(\mathbf{x})) &= \left\langle\!\left\langle t \, \frac{d \log LE_t(\mathbf{x})}{dt} \right\rangle\!\right\rangle \\ \text{where} \qquad \langle f(t) \rangle &= \frac{1}{t} \int_0^t f(t') \, dt' \, . \end{aligned} \tag{7.25}$$

If the indicator $LE_n(\mathbf{x})$ grows exponentially as $e^{\lambda t}$, then $MEGNO_n(LE(\mathbf{x}))$ increases as λt. If $LE_n(\mathbf{x})$ follows the power law t^α, then $MEGNO_n(LE(\mathbf{x}))$ converges to 2α.

7.3 | Numerical implementations

7.3.1 | Models

To test the effectiveness of the proposed indicators of chaos, we consider a 4D polynomial symplectic map dependent on time, which is a generalisation of the Hénon map [40]. The origin is an elliptic fixed point, and the non-linear terms combine fixed quadratic non-linearities and variable cubic ones. The map reads:

$$\begin{pmatrix} x_{n+1} \\ p_{x,n+1} \\ y_{n+1} \\ p_{y,n+1} \end{pmatrix} = R(\omega_{x,n}, \omega_{y,n}) \begin{pmatrix} x_n \\ p_{x,n} + x_n^2 - y_n^2 + \mu \left(x_n^3 - 3 x_n y_n^3 \right) \\ y_n \\ p_{y,n} - 2 x_n y_n + \mu \left(y_n^3 - 3 y_n x_n^3 \right) \end{pmatrix} , \tag{7.26}$$

where μ represents the intensity of the cubic non-linearity and R is a 4×4 rotation matrix defined as

$$R(\omega_{x,n}, \omega_{y,n}) = \begin{pmatrix} R\left(\omega_{x,n}\right) & 0 \\ 0 & R\left(\omega_{y,n}\right) \end{pmatrix} , \tag{7.27}$$

with $R\left(\omega_{x,n}\right)$ and $R\left(\omega_{y,n}\right)$ being 2×2 rotation matrices. In the sequel, we refer to the map (7.26) as the 4D Hénon map and remark that it is often used as a reference model in applications such as accelerator physics (see, e.g., [40, 55, 57]), since it represents the dynamics generated by a magnetic lattice that includes sextupole and octupole magnets [40].

Linear frequencies $\omega_{x,n}$ and $\omega_{y,n}$ are slowly modulated as a function of time n according to

$$\begin{aligned} \omega_{x,n} &= \omega_{x,0}\left(1+\varepsilon\sum_{k=1}^{m}\varepsilon_k\cos\left(\Omega_k n\right)\right), \\ \omega_{y,n} &= \omega_{y,0}\left(1+\varepsilon\sum_{k=1}^{m}\varepsilon_k\cos\left(\Omega_k n\right)\right), \end{aligned} \tag{7.28}$$

where ε represents the modulation amplitude and the parameters ε_k and Ω_k are taken from Table 1 in [55] to model the effect of frequency modulation in a particle accelerator due to ripples in the currents of the power supplies that feed the magnets. Modulation of the linear frequency may cause the appearance of weak chaotic regions in the stability basin near the origin. We recall that the parameters ε_k have an order of magnitude of 10^{-4}.

In numerical simulations, two sets of frequencies ω_{x0} and ω_{y0} have been considered, namely $(0.168,\ 0.201)$, which is close to resonances of order 5 and 6, and $(0.28,\ 0.31)$, which are the frequencies in the transverse phase space for charged particles orbiting in the LHC at injection energy. We have analysed the performance of chaos indicators as a function of the parameters ε and μ, which have been varied in the intervals $[0, 64]$ and $[0, 1]$, respectively. Some considerations on the computational costs of implementing the various indicators of chaos in a parallel computing architecture are reported in the Appendix 7.A.

Figure 7.1 shows some survival plots for various configurations of the 4D Hénon map. A set of 300×300 initial conditions, sampled on a uniform Cartesian grid in the $x - y$ plane, choosing $p_x = p_y = 0$, is tracked up to $n_{\max} = 10^8$ turns. Grid boundaries are selected to sample a region of interest that contains the stability basin of the origin, more specifically $[0.0,\ 0.45]$ for case $(\omega_{x0},\ \omega_{y0}) = (0.168,\ 0.201)$, or $[0.0,\ 0.60]$ for case $(\omega_{x0},\ \omega_{y0}) = (0.28,\ 0.31)$. An initial condition is considered stable if its distance from the origin is less than a certain control radius r_c when $n = n_{\max}$. Otherwise, the initial condition is considered lost and its tracking is stopped, and the stability time is given by the first value n_stab for which $\sqrt{x^2_{n_\mathrm{stab}} + p^2_{x,n_\mathrm{stab}} + y^2_{n_\mathrm{stab}} + p^2_{y,n_\mathrm{stab}}} \geq r_\mathrm{c}$. The choice of r_c is rather arbitrary (we have considered $r_\mathrm{c} = 10^2$) and the dependence of the results on r_c is very weak since at that amplitude the dynamics of the 4D Hénon map is fully dominated by polynomial terms. The two rows

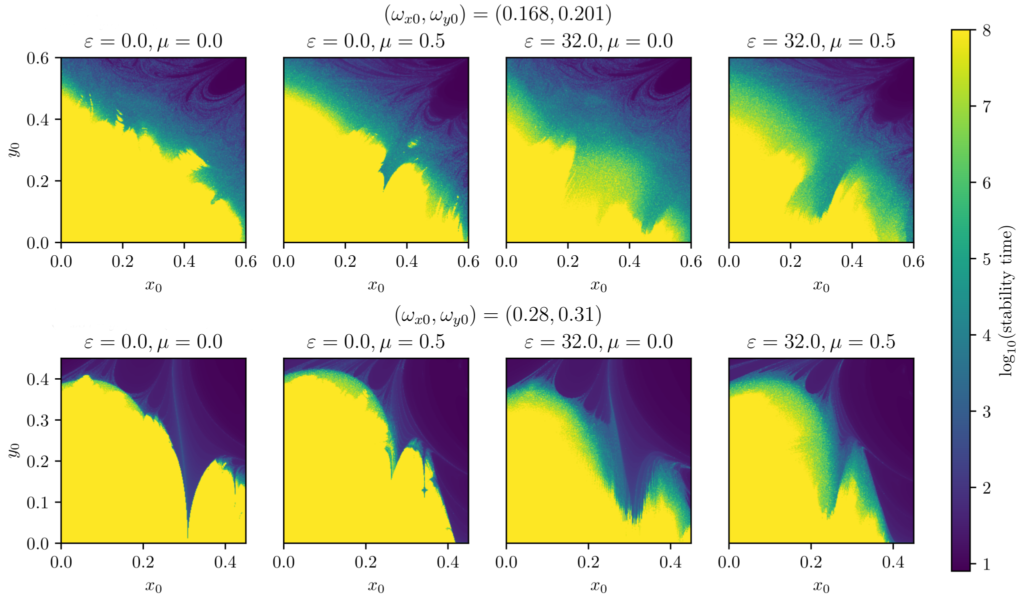

FIGURE 7.1: Survival plot for various 4D modulated Hénon maps with quadratic and cubic non-linearities. Initial conditions, sampled on an uniform Cartesian 300×300 grid in the $x - y$ plane, are tracked up to $n_{\max} = 10^8$ and are considered lost when their distance to the origin exceeds a predefined maximum radius $r_c = 10^2$. The two sets of linear frequencies feature different shapes of the stable region as can be seen by comparing the plots in the two rows. The parameters ε and μ induce additional changes, in particular the increase of the size of the transition region between stability up to $n_{\max}$ and shorter stability time. The color scale is related to the logarithm of the stability time as reported on the right.

of Fig. 7.1 show the survival plots for the two sets of frequencies considered in the studies. The shape of the stable region (yellow area) strongly depends on the frequencies, as different sets of resonances affect the dynamics. Furthermore, the impact of ε and μ is also clearly seen. The first enlarges the transition region between stable initial conditions and unstable ones, i.e., the region for which $n_{\text{stab}} < n_{\max}$, where a weak diffusion occurs, while the latter changes the shape of the stable region.

7.4 | Results of numerical investigations

In the following, we report the results of the numerical study of the dynamic indicators presented in Section 7.2, namely $\log_{10}(LE)$, FLI, FLI^{WB},

$MEGNO(LE)$, $GALI^{(4)}$, REM, and FMA. Note that we consider the logarithm of LE, as it is a quantity comparable to FLI and $MEGNO(LE)$. We first focus on the dependence of FLI on the choice of the initial displacement vector ξ, and compare it with $\log_{10}(LE)$. Next, we discuss a comparison between the convergence rate of FLI and that of FLI^{WB}. Finally, we compare the classification performance of all dynamic indicators by determining their accuracy, together with its time dependence, in reconstructing a Ground Truth (GT) evaluated at a high iteration time.

7.4.1 | Dependence on the initial displacement

The main feature of LE, compared to FLI, is its independence from the initial choice of direction of the unitary displacement vector ξ. To highlight this, in Fig. 7.2, we directly compare the calculated values of $\log_{10}(\log_{10}(LE)/n)$ with those of $\log_{10}(FLI/n)$, calculated with an initial displacement along one of the four orthonormal base vectors $\hat{x}$, $\hat{p}_x$, $\hat{y}$, and $\hat{p}_y$. These calculations are carried out for a set of 300×300 initial conditions, sampled on a uniform Cartesian grid in the $x - y$ plane. It is possible to see how, at low turn number ($n = 10^2$, top row), the different choice of displacement highlights the structures in FLI that are missing in LE. This can be explained by considering that the displacement vector is not fully aligned along the largest Lyapunov exponent yet. In contrast, these structures are missing for LE, which has smoother behaviour.

The observed differences are greatly reduced for a higher number of turns ($n = 10^4$, bottom row), as the initial displacement tends to become almost aligned along the direction corresponding to the largest Lyapunov exponent. However, despite the smaller differences between $\log_{10}(\log_{10}(LE)/n)$ and $\log_{10}(FLI/n)$, the behaviour of the various indicators is still not the same. It is worth noting how displacements along $\hat{x}$ and $\hat{y}$ produce similar structures that are, however, different with respect to the case in which displacement is carried out along $\hat{p}_x$ or $\hat{p}_y$. Globally, these observations underline the value of the invariance properties of LE, which seems to be more promising than FLI for the analyses that will be discussed in the following sections.

As this dependence on the initial displacement decreases with higher iteration numbers, we will focus only on $FLI(\hat{x})$ for the remainder of the chapter, as the rest of the results are not significantly affected by this choice.

7.4.2 | Application of Weighted Birkhoff averaging to FLI

As an additional analysis of the time dependence of chaos indicators, we compare the values obtained for FLI at different times, using the standard ap-

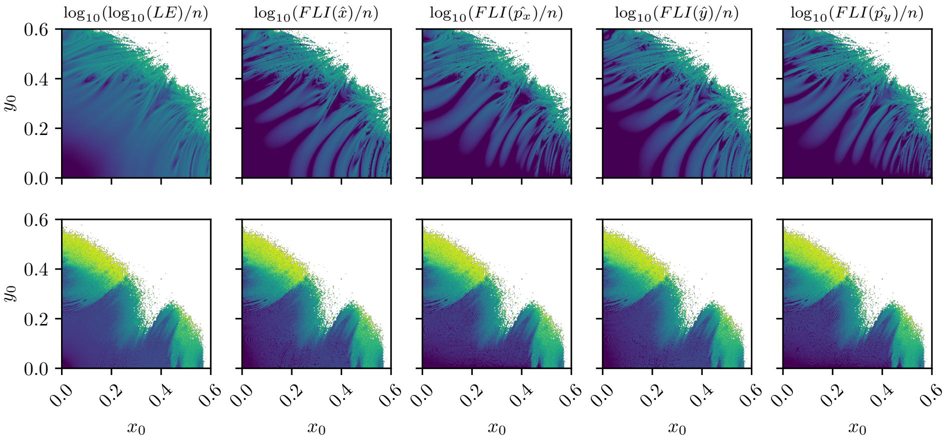

FIGURE 7.2: Color maps of $\log_{10}(\log_{10}(LE)/n)$ and $\log_{10}(FLI/n)$ indicators for a low iteration number ($n = 10^2$, top row) and a high iteration number ($n = 10^4$, bottom row). In both rows, the FLI for the four possible displacements are shown together with LE, in order to highlight the different structures shown by the indicators. It is possible to see how, for low iteration numbers, different choices of initial displacement for FLI highlight structures that do not appear in LE. The differences reduce for higher number of turns, but are still present. Note that an arrow at the bottom of the color bar means that pixels of the bottom color correspond to a value equal to or lower than the bottom value. White pixels correspond to initial conditions whose distance from the origin has exceeded a predefined radius ($r_c = 10^2$) during the tracking, before reaching the target iteration number n. (Simulation parameters used: $(\omega_{x0}, \omega_{y0}) = (0.168,\ 0.201)$, $\varepsilon = 64.0$, $\mu = 0.5$).

proach that considers the mean in Eq. (7.10), that is, FLI/n, or the variant based on the use of Birkhoff weights as in Eq. (7.12), that is, FLI^{WB}. The analysis starts considering two ensembles of regular and chaotic particles that have been classified by means of the value of the FLI indicator computed for $n = 10^8$ turns (effectively this sets a ground-truth level, as discussed in the next section). The sets are also used to calculate the time evolution of FLI/n and FLI^{WB} with the objective of evaluating possible improvements in the latter compared to the first. In Fig. 7.3 (top), the comparison is made for a subset of the set of regular initial conditions, whereas the behaviour of chaotic ones is shown in the bottom plot of the same figure. It is possible to observe how, for regular initial conditions, Birkhoff averaging consistently speeds up the convergence of FLI^{WB} to zero.

The case of chaotic initial conditions has different characteristics. In fact, a saturation region is observed for the indicator value on the order of 10^{-3} for both indicators. When this value is reached, both indicators oscillate around it.

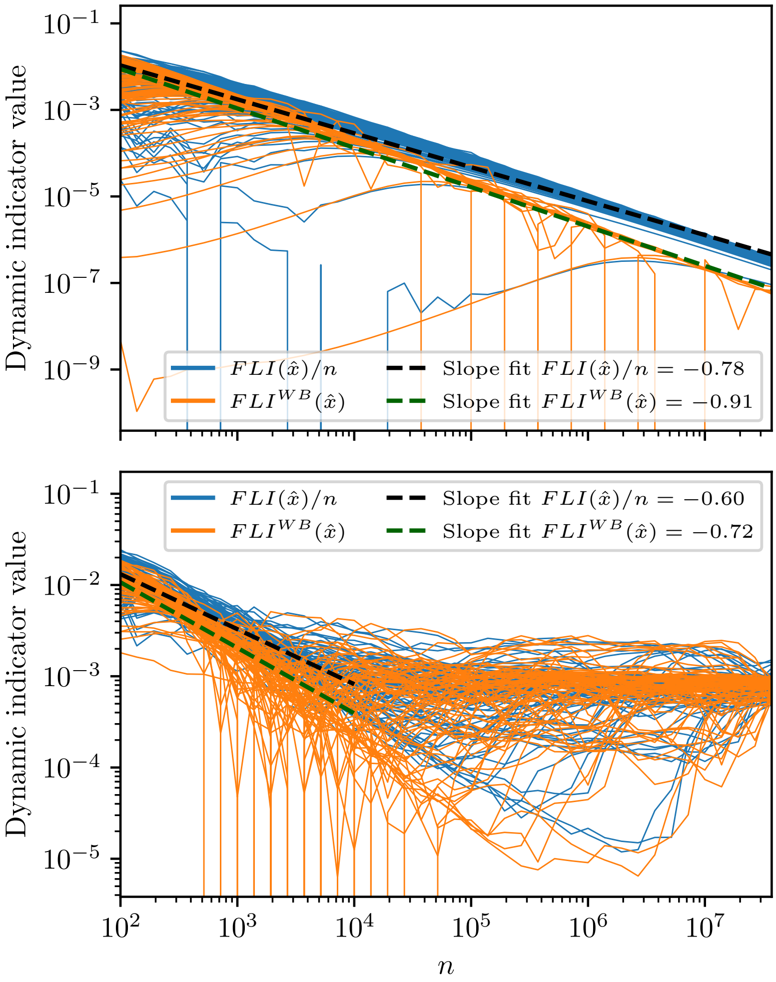

FIGURE 7.3: Time evolution of FLI computed using either a standard mean or the Birkhoff averaging. Top plot: indicators computed for a set of 100 regular initial conditions, the fit highlights a faster convergence rate for the Birkhoff averaging. Bottom plot: indicators computed for a set of 100 chaotic initial conditions. A similar improvement in convergence rate is observed for low n values, before reaching a saturation value of the indicator of the order of 10^{-3}. (Simulation parameters: $(\omega_{x0}, \omega_{y0}) = (0.28,\ 0.31)$, $\varepsilon = 32.0$, $\mu = 0.5$).

However, the slope with which this non-zero value is reached is different for the two indicators and is higher in absolute value for FLI^{WB} than for FLI/n, similar to what is observed for the case of regular orbits. It is also worth stressing the presence of initial conditions that, up to some $n = 10^6$ turns, feature a steady decrease in the value of the dynamic indicator, as if they were characterized by regular motion. However, after that, the value of the indicator suddenly increases, reaching the value that identifies chaotic orbits. This behaviour clearly defies any approach aimed at classifying initial conditions as regular or chaotic in finite time.

The improvement caused by the Birkhoff averages is also clearly visible in Fig. 7.4, where the time evolution of the distribution of the values of FLI/n (top) and FLI^{WB} (bottom) is shown. The part of the distribution corresponding to the regular initial conditions reaches its peak (yellow band) and moves toward zero with increasing n. However, the displacement towards zero is faster for FLI^{WB}. Furthermore, the peak of the distribution is sharper for FLI^{WB} than for FLI. In both graphs, a faint trace of a peak is visible corresponding to the indicator value of about 10^{-3}. This feature is remarkably similar for the two indicators, as already seen in Fig. 7.4.

This behaviour shows that the regular orbits benefit from the use of the Birkhoff averages, whereas the chaotic ones are mostly unaffected by the special averaging mechanism. These features can be exploited for the classification problem that will be addressed in the next section.

7.4.3 | Classification performance

For this analysis, we study the predictive performance of chaos indicators in terms of a binary classification of a large set of initial conditions by varying the number of iterations n. It should be stressed that this classification only concerns the behaviour of an orbit that has been detected to be stable for n_{max}.

An overview of the time dependence of the dynamic indicators and the distribution of their values observed in our numerical investigation is given in the Appendix 7.B. The main feature of interest, which constitutes the basis of this analysis, is the general tendency of dynamic indicators to create a bimodal distribution, as has also been reported for finite-time Lyapunov exponents in [148, 149]. We focus on studying the evolution of this specific characteristic, i.e., the presence of two peaks in the distribution of indicator values, as a function of time, which is the key feature used for the classification analysis.

As the complete development of the bimodal distribution requires various orders of magnitude of the number of turns, we perform our analysis on the logarithm of the seven dynamic indicators, namely $\log_{10}(\log_{10}(LE)/n)$, $\log_{10}(MEGNO(LE)/n)$, $\log_{10}(FLI/n)$, $\log_{10}(FLI^{WB})$, $\log_{10}(GALI^{(4)})$,

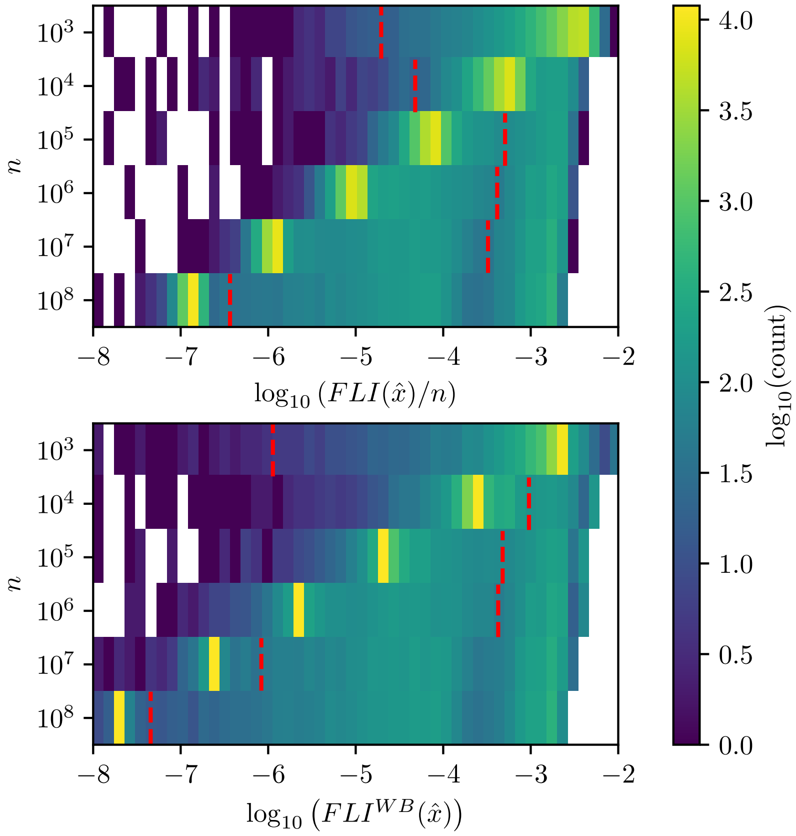

FIGURE 7.4: Time evolution of the distribution of the values of FLI (top) and FLI^{WB} (bottom) indicators for the whole set of 15684 initial conditions that survived up to $n_{\max} = 10^8$. The Birkhoff averaging leads to faster convergence towards zero of the regular initial conditions, which are represented by the yellow band. Furthermore, the width of such a band is narrower for FLI^{WB} with respect to FLI. The red dashed lines represent threshold values, defined by our algorithm, representing the attempt to perform the binary classification in regular and chaotic initial conditions. (Simulation parameters: $(\omega_{x0}, \omega_{y0}) = (0.28,\ 0.31),\ \varepsilon = 32.0,\ \mu = 0.1$).

$\log_{10}(REM)$, and $\log_{10}(FMA)$. The factor n^{-1} is included in the first two indicators to observe a comparable evolution of values over time with the two FLI indicators, since, ultimately, its presence does not alter the outcome of these studies.

To carry out this task, we first construct a ground truth (GT) for different sets of parameters for the 4D Hénon map, iterated for $n_{\max} = 10^8$. The initial conditions are then classified into a binary chaotic/regular classification scheme using the LE indicator. An example is given in Fig. 7.5 where eight cases, the same as those depicted in Fig. 7.1, are displayed. Dark colours identify regular regions of the phase space, whereas lighter colours denote chaotic regions. It is clearly seen that the frequency modulation and the presence of the cubic non-linearity increase the extent of the chaotic areas of the phase space, also generating regions in which regular and chaotic orbits are deeply intertwined.

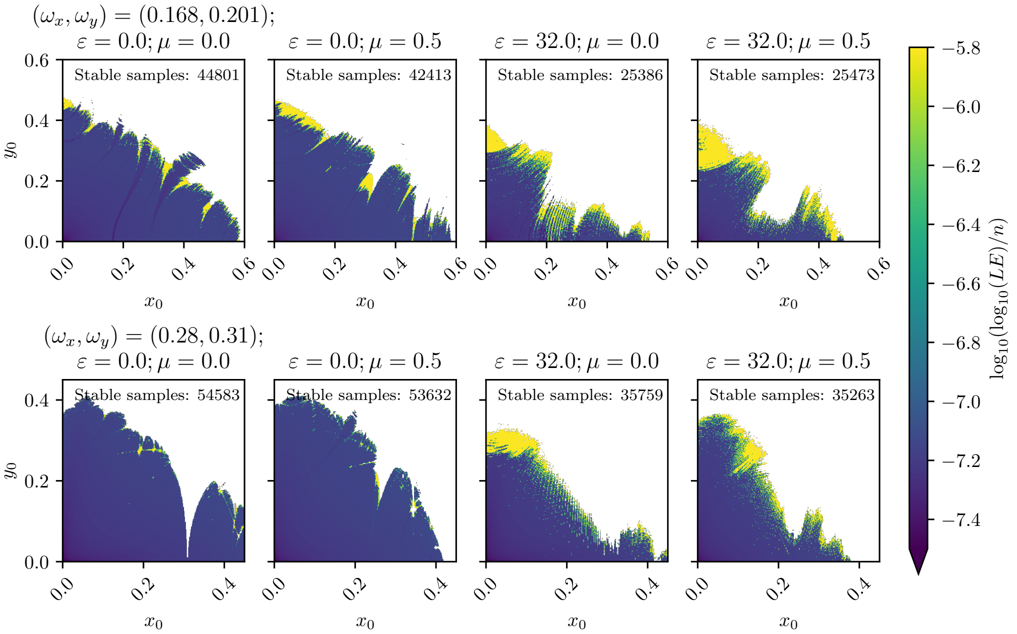

FIGURE 7.5: Distributions of $\log_{10}(\log_{10}(LE)/n)$ for various 4D modulated Hénon maps (the same cases shown in Fig. 7.1) with quadratic and cubic non-linearities. 300×300 initial conditions, sampled on an uniform Cartesian grid in the $x - y$ plane, are tracked up to $n_{\max} = 10^8$. It is possible to observe how the case for $\varepsilon = 0.0$, $\mu = 0.0$, corresponding to the absence of modulation and cubic non-linearities, lead to regular motion almost everywhere, except for a small set of initial conditions. For the other cases, extended regions of chaotic motion are visible. Note that the maximum value registered in the color maps corresponds to numerical saturation.

The GT classification is built from the distribution of the values of the dynamic indicator $\log_{10}(\log_{10}(LE)/n)$ for $n_{\max}$. The resulting distribution has a main group of regular initial conditions with low value LE, and a second group of chaotic initial conditions with higher value LE. Due to the large separation of these two clusters, a threshold value has been calculated to distinguish them using a kernel density estimation method (KDE) [150, 151] with a Gaussian kernel and different bandwidth values. This allows investigating the Mode Tree [152] of the distribution, detecting its two main modes, and setting the position of the minimum of the distribution between them. It is worth stressing that more refined approaches might be devised to detect the peaks or, equivalently, cluster the indicator values, but they have not been considered in this analysis. In fact, our focus is on the performance of the indicator in generating a suitable distribution for the classification problem, even for low values of n, not on designing a sophisticated algorithm to analyse the distribution of the indicator, including its peculiarities.

An example of the GT construction process can be seen in Fig. 7.6. Stable initial conditions up to $n_{\max}$ are identified by direct tracking (first graph from the left), and the value of the indicator LE is calculated for the set of stable initial conditions (second graph from the left). At this stage, it is possible to compute the distribution of LE and determine the threshold that separates the peaks of the bimodal distribution (third plot from the left) and provides the criterion to classify any given initial condition as regular of chaotic. Applying the computed threshold, it is possible to generate a binary map with the resulting classification (fourth plot from the left). The determination of the threshold for the case shown is rather straightforward, as the large separation between

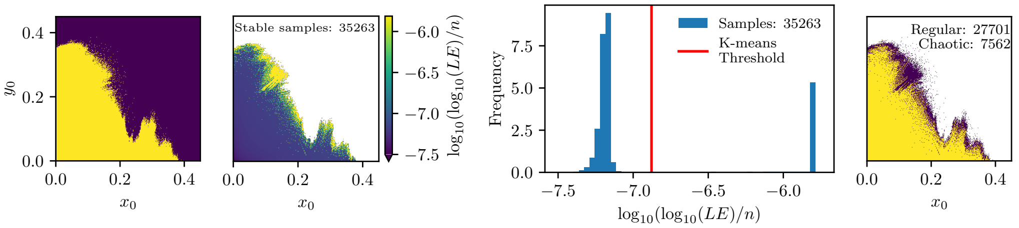

FIGURE 7.6: Ground Truth construction for a modulated Hénon map. From left to right: a survival plot of the initial conditions stable up to $n_{\max} = 10^8$ (yellow is stable, purple is unstable); distribution of the LE indicator for all stable initial conditions, evaluated at $n_{\max}$; histogram of $\log_{10}(\log_{10}(LE)/n)$, classified with a threshold evaluated with a KDE-based procedure; binary classification of regular (yellow) and chaotic (purple) initial conditions. (Simulation parameters: $(\omega_{x0}, \omega_{y0}) = (0.28,\ 0.31)$, $\varepsilon = 32.0$, $\mu = 0.5$).

the two peaks makes the actual value of the threshold not particularly relevant. However, when $n \ll n_{\max}$ the separation between the peaks decreases and the threshold value becomes essential for an efficient classification of the initial conditions.

Examples of the procedure for determining the threshold based on the indicator distribution are shown in Fig. 7.7. In the top plot, the case of REM is depicted (but it is representative of all other indicators except FMA). The use of KDE with different bandwidth clearly shows how the two peaks of the distribution can be detected. This allows the position of the threshold to be set at the location of the minimum value of the distribution in between the two peaks. The case of FMA is different since the distribution has three peaks and the standard algorithm to determine the threshold must be adapted. Therefore, KDE is used to determine the position of the three peaks, and the threshold is set at the position of the minimum of the distribution in between the two peaks with the largest amplitude.

This choice is somewhat arbitrary, but the features of the distribution clearly indicate that the performance of the indicator is limited, with little possibility of improving it. Indeed, the non-negligible fraction of initial conditions that generate the part of the distribution in between the extreme peaks cannot be clearly classified by the proposed approach, as some of them will turn chaotic, whereas other regular if the indicator would be computed over a longer time span.

Once the GT has been computed, we define as predictive performance of a dynamic indicator the accuracy in reconstructing the binary classification in the GT, that is, the ratio between the correctly labelled initial conditions and the total number of stable initial conditions. Such a reconstruction is attempted using the same strategy implemented for the determination of the GT, namely, we consider the distribution of the dynamic indicator under consideration and define a binary classification using a threshold computed via the KDE-based approach. The resulting thresholds evaluated over time for REM and FMA are visualized in detail in Fig. 7.8, while the results for the other dynamic indicators are presented in Appendix 7.B.

The accuracy performance of the dynamic indicator is then evaluated for various $n < n_{\max}$. We expect a good-performing dynamic indicator to achieve high accuracy values when it generates two separate groups, even when $n \ll n_{\max}$. Such behaviour, in fact, enables effective mode detection and consequent effective GT reconstruction. In contrast, a poor-performing dynamic indicator will need a longer tracking time before showing the presence of two separate clusters, causing the threshold determination to be unable to separate the chaotic from the regular initial conditions.

A global comparison of the classification performance of the seven dynamic

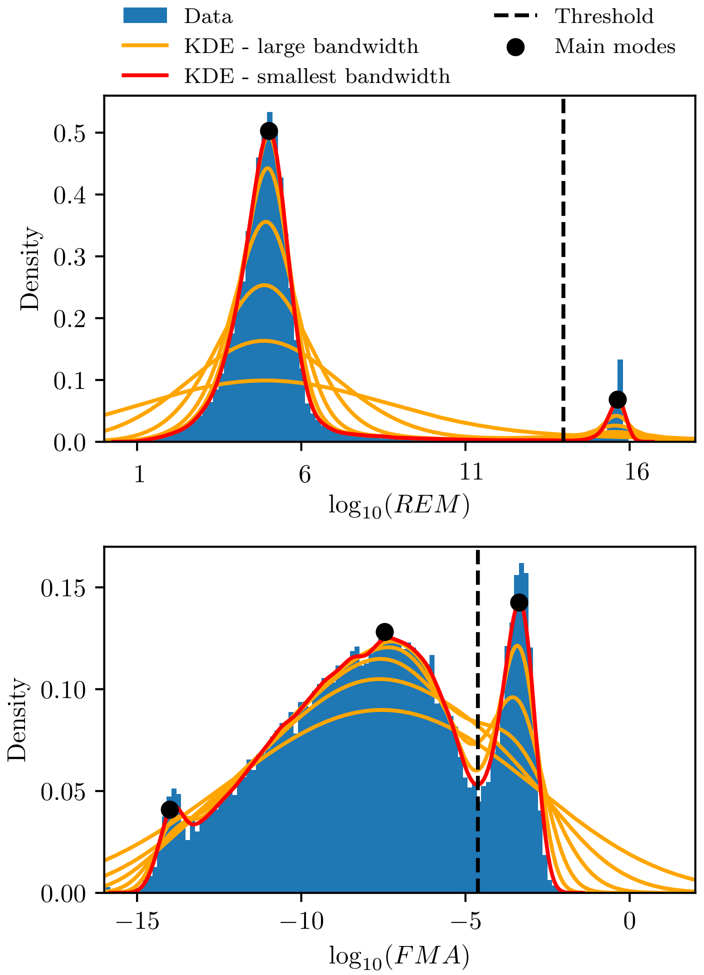

FIGURE 7.7: Example of the KDE-based procedure for computing a threshold for the binary classification (regular/chaotic) of initial conditions. Top: application to $\log_{10}(REM)$ (evaluated at $n = 10^5$). KDEs with various bandwidth are used until the two main peaks of the bi-modal distribution are detected, the threshold is then placed at the position of the minimum of the distribution between them. This procedure is applied to all dynamic indicators except for FMA. Bottom: application of the procedure to $\log_{10}(FMA)$ (evaluated at $n = 10^5$), which clearly exhibits a three-mode distribution. The procedure is applied so that it detects the three main modes of the distribution, and then sets the threshold at the minimum of the distribution between the two modes at higher values. (Simulation parameters: $(\omega_{x0}, \omega_{y0}) = (0.28,\ 0.31)$, $\varepsilon = 32.0$, $\mu = 0.5$).

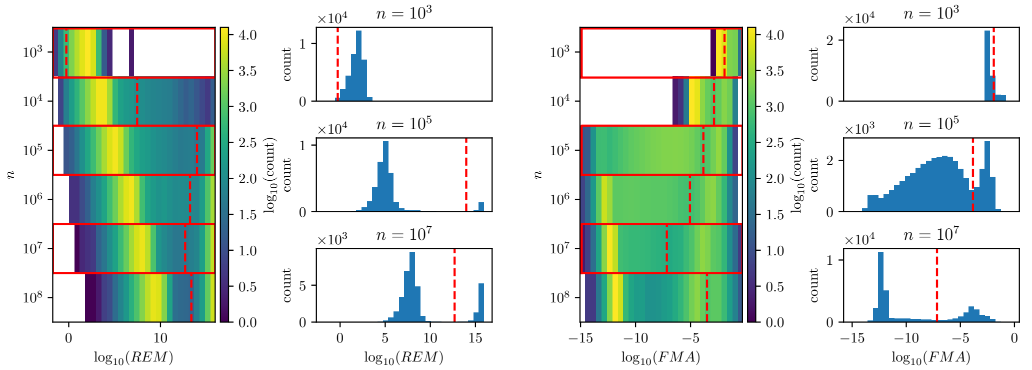

FIGURE 7.8: Distribution of values of $\log_{10}(REM)$ (left) and $\log_{10}(FMA)$ (right) as a function of time for a modulated 4D Hénon map. The red dashed lines represent threshold values, defined by our algorithm shown in Fig. 7.7, representing our criterion to distinguish regular and chaotic orbits. For low values of the iterations n, the distribution of both indicators is in general represented by a uni-modal function. For higher values of n, we can see the formation of two separate clusters in the case of REM, making the distribution bi-modal. For FMA, we have in general a different behaviour, as it tends to form a tri-modal distribution. (simulation parameters: $(\omega_{x0}, \omega_{y0}) = (0.28,\ 0.31)$, $\varepsilon = 32.0$, $\mu = 0.5$).

indicators is carried out, and the accuracy achieved by the dynamic indicators as a function of n is shown in Fig. 7.9, for different sets of parameter values for the 4D Hénon maps.

When considering the Hénon maps with $\varepsilon = 0.0$, i.e., without frequency modulation, a rather small fraction of chaotic orbits with a very mild dependence on n of the accuracy of the various dynamic indicators is observed. Furthermore, FMA differs from all other indicators, clearly showing poorer performance in terms of accuracy. All other indicators have very similar performance, the only difference being in the time at which a steplike increase in accuracy is observed, which occurs for $n = 10^3 - 10^4$, corresponding to 4-5 orders of magnitude lower than $n_{\max}$. This sudden increase in accuracy is related to the time required by dynamic indicators to generate a bimodal distribution that can be efficiently analysed using our KDE-based procedure. In this sense, it should be noted that $GALI^{(4)}$ is the most accurate indicator, as it reaches high accuracy values even at very low values of n and the gradual increase does not occur in the range of n shown in the graphs. In general, the behaviour observed for all indicators (except FMA) shows that a rather accurate prediction of GT can be achieved using the information provided by the indicators over a rather limited number of turns.

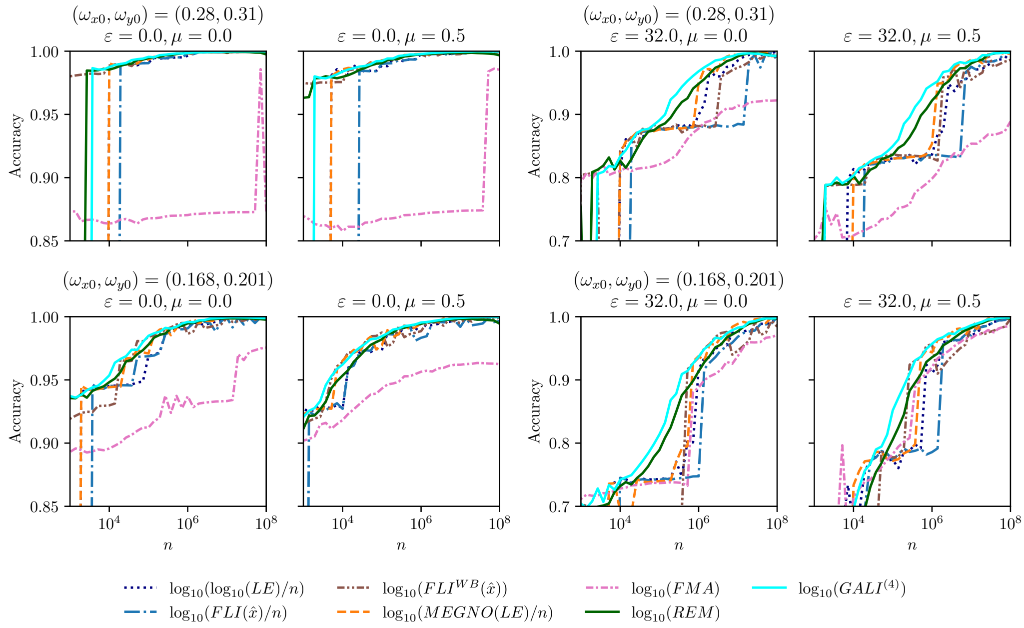

FIGURE 7.9: Time dependence of the accuracy achieved in reconstructing the Ground Truth (computed for $n_{\max} = 10^8$) by the various dynamic indicators for eight cases of the 4D modulated Hénon maps (the same cases shown in Fig. 7.1), differing by cubic non-linearities and frequency modulation.

In the case with $\varepsilon = 32.0$, i.e., with frequency modulation and a larger fraction of chaotic orbits, the situation changes dramatically. Accuracy depends rather strongly on n, suggesting that chaos detection requires a larger number of turns to be accurate. In terms of the ranking of the indicators, FMA remains the worst (this is certainly true for case $(\omega_{x0}, \omega_{y0}) = (0.28, 0.31)$, while for case $(\omega_{x0}, \omega_{y0}) = (0.168, 0.201)$ a better performance is observed). REM and $GALI^{(4)}$, are the best values in a wide range of values of n. Furthermore, they do not show any sudden jump in accuracy because of their well-behaved distribution. Finally, we remark that beyond $n = 10^6 - 10^7$, the precision of all indicators is very similar.

To provide a quantitative assessment of the performance of the dynamic indicators, we define a performance estimate as

$$\frac{1}{2}\int_4^6 \text{Accuracy}(10^x)\,\mathrm{d}x\,, \tag{7.29}$$

i.e., the integral of the accuracy achieved and displayed in Fig. 7.9 normalized to the integral of the ideal case with unit accuracy throughout the turn interval. The reasons for such a definition are twofold: First, it avoids the possible bias introduced by indicators that are more efficient in detecting the chaotic behaviour at low number of turns but that are not so efficient afterwards; second, it probes the predictive power of the indicator by setting an upper bound that is lower than the turn number used for determining the GT. Equation (7.29) has been numerically evaluated using the trapezoidal rule and considering 50 values of n equally spaced on a logarithmic scale over the interval $10^4 - 10^6$. The performance estimate values for the dynamic indicators for the various Hénon maps are reported in Table 7.1.

Performance estimates have been ranked in decreasing order, separating the various cases considered in our analyses. $GALI^{(4)}$ turns out to be the highest scorer in all cases, followed by REM. Then we find $MEGNO$ and $FLI^{WB}(\hat{x})$, while FMA tends to be the last in this ranking. The error associated with each performance estimate value is provided by the variation of the accuracy whenever the automatic threshold value is varied by ±5%. This quantity provides information on the robustness of the accuracy against perturbation of the threshold: A small value indicates a high stability of the numerical values. It is also worth noting that the performance estimates of the best dynamic indicators are correlated with small values of the corresponding error.

Important insights on the performance of the various indicators can be gained by looking at the relative identification error in terms of false positive, i.e., when a regular orbit is classified as chaotic, and false negative, i.e., when a chaotic orbit is classified as regular. A false negative is almost unavoidable, according to the behaviour shown in Fig. 7.3, unless the indicator is calculated over a very large number of turns, which means accepting a very limited predictive power of the indicator. However, the behaviour of the two types of errors reveals interesting features of the various indicators. An overview of the dependence of false positive and false negative errors is shown in Fig. 7.10, where relative errors are displayed as functions of the turn number for the map configurations considered in the first row of Fig. 7.9.

The behaviour of the false positive error reveals a fundamental difference between FMA and the other indicators. In fact, FMA shows an error value that is only slightly dependent on the turn number and drops to small values for very large n. For the other indicators, for a low number of turns, this type of error is large, and then, around 10^4 turns, it drops essentially to zero. This feature is related to the fact that, for a low number of turns, the bimodal structure is not yet present. It is also worth noting that, for the case of $FLI^{WB}(\hat{x})$ the Birkhoff averaging introduces a clear improvement by pushing the position of the sudden drop to zero of the false positive error to a lower number of turns.

The false negative error increases sharply at a turn number close to that corresponding to the abrupt decrease in the false positive error. After this turn number, two behaviours are observed: In the first case, the error level is ap-

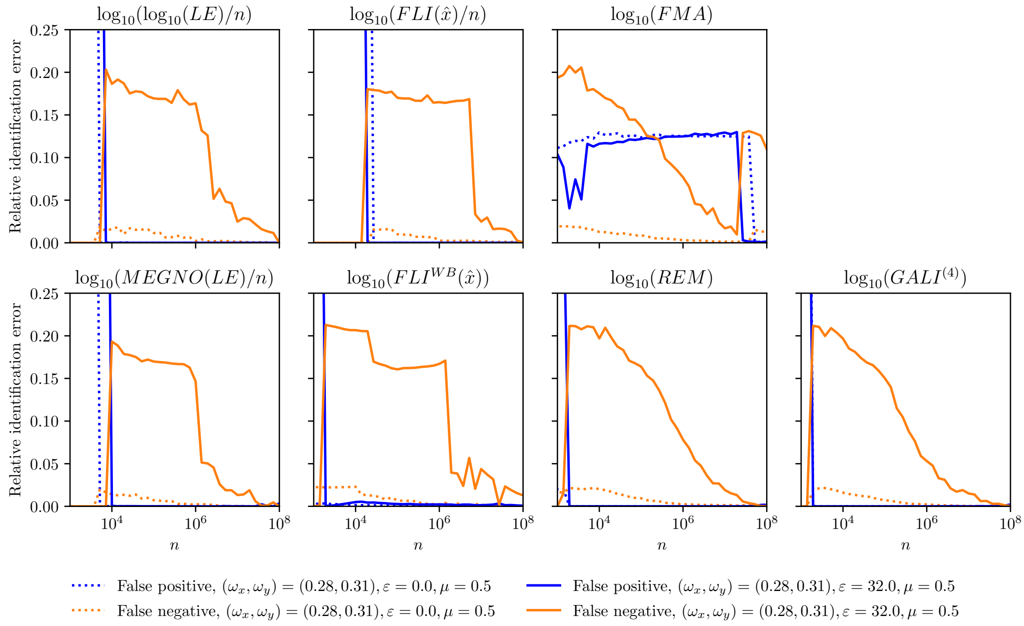

FIGURE 7.10: Identification errors for the various indicators as a function of the number of turns for the cases displayed in the first row of Fig. 7.9.

proximately constant until it drops to a low value after $n \approx 10^7$. This value is relatively close to that used to determine the GT, which indicates a limited predictive power of the indicator. In the second case, the error level decreases almost linearly as a function of n. This is the key to achieving good performance and is the feature shown by REM and $GALI^{(4)}$. It should be noted that FMA also behaves in this way, i.e., with a linear decrease in the false positive error. However, when the false negative error drops, a jump in the false positive error is observed. This error then shows a decrease that is almost negligible up to $n_{\max}$. These characteristics, related to the characteristics of the distribution of the FMA values, prevent this indicator from reaching a good performance level.

As a last comment, these features are always present, but frequency modulation strongly enhances the errors.

7.5 | Conclusions

In this chapter, various numerical indicators to identify the chaotic character of orbits of Hamiltonian systems have been presented and discussed in detail. The powerful Birkhoff averages were used to improve the convergence rate of an indicator in the case of regular initial conditions. The goal of our analysis is to evaluate the performance of the indicators in terms of accuracy in the binary classification of an orbit identified by its initial conditions, as regular or chaotic. An important element in this assessment is whether the correct classification can be achieved by using the information over a limited number of turns, i.e., whether an early chaos detection can be effectively performed, which is equivalent to probing the predictive power of dynamic indicators.

The dynamical system that has been selected as a test bed for performance analyses is a 4D Hénon-like symplectic map, with or without cubic non-linearity and with or without frequency modulation. This choice is justified by the relevant applications of this map to understand long-term stability problems in particle accelerators. Several configurations have been considered and, for each case, a ground truth classification has been determined with $n = 10^8$ iterations. The various indicators have been used to provide an estimate of the classification performance with respect to ground truth as a function of the number of turns used. The classification is based on the bimodal feature of the indicator value distributions, which points out two clusters associated with regular and chaotic orbits. To define a classification threshold, we use a KDE-based algorithm to determine the position of the distribution minimum between the two modes.

A ranking of the performance of the various indicators has been established, with $GALI^{(4)}$ slightly outperforming the other indicators in all cases considered, immediately followed by REM. Then we find FLI^{WB} and $MEGNO(LE)$. Modulation of the linear frequencies significantly reduces the predictive power of each indicator. It should be noted that the identification errors of the various indicators are largely dominated by the wrong labelling of the initial conditions as regular.

The conclusions drawn for the case of the 4D Hénon-like map are generic for a polynomial Hamiltonian system in a neighbourhood of elliptic fixed points. Hence, these results can be particularly useful for applications such as non-linear beam dynamics. The specific choice of an indicator to predict the chaotic character should take into account the performance evaluated in our analysis, as well as the computational efforts needed to compute the various indicators. In this sense, REM could be a very interesting candidate due to its good performance combined with computational efficiency, which is particularly suitable for reducing the CPU time required for the numerical integration of complex physical systems.

Appendices

7.A | Computational costs for evaluating the indicators of chaos

Evaluation of a dynamic indicator requires a variable amount of computational cost, which could affect the feasibility and efficiency of specific implementations or favour the usage of specific dynamic indicators. Here, we focus our considerations on the specific case of a discrete map with a known analytic expression for both the tangent and the inverse maps.

For LE, FLI, and $MEGNO(LE)$, the main computational effort consists of tracking the value of $\mathsf{L}_n(\mathbf{x})$, along the orbit of $\mathbf{x}$. This implies the additional memory requirement to store a matrix of size $2d \times 2d$ and the execution of matrix-matrix and matrix-vector multiplications at each iteration. It should be noted that an important feature of these indicators is that their evaluation at a target iteration number n also provides their value for all lower iteration numbers. This feature frees up additional computational costs for the analysis of the evolution of the dynamic indicator value over time.

$GALI^{(k)}$ requires the evaluation of $\mathsf{L}_n(\mathbf{x})$ to calculate the normalized k images of $\boldsymbol{\eta}_j$ with $1 \leq j \leq k$. A practical and fast method for computing the norm of external products in Eq. (7.23) is given in [116], where it is proven that $GALI^{(k)}$ is equal to the product of singular values z_j, of A, where A is a $2d \times k$ matrix that reads

$$A = \begin{pmatrix} \left(\frac{\mathsf{L}_n(\mathbf{x})\boldsymbol{\eta}_1}{\|\mathsf{L}_n(\mathbf{x})\boldsymbol{\eta}_1\|}\right)_1 & \cdots & \left(\frac{\mathsf{L}_n(\mathbf{x})\boldsymbol{\eta}_k}{\|\mathsf{L}_n(\mathbf{x})\boldsymbol{\eta}_k\|}\right)_1 \\ \vdots & & \vdots \\ \left(\frac{\mathsf{L}_n(\mathbf{x})\boldsymbol{\eta}_1}{\|\mathsf{L}_n(\mathbf{x})\boldsymbol{\eta}_1\|}\right)_{2d} & \cdots & \left(\frac{\mathsf{L}_n(\mathbf{x})\boldsymbol{\eta}_1}{\|\mathsf{L}_n(\mathbf{x})\boldsymbol{\eta}_1\|}\right)_{2d} \end{pmatrix}. \tag{7.30}$$

The singular values of A can be obtained by applying the Singular Value Decomposition (SVD) method [153]. Note that the evaluation of $GALI^{(k)}$ for a target iteration number $\overline{n}$ also provides the values of $\boldsymbol{\eta}_j$ for all lower values of n. However, for each $n \leq \overline{n}$ for which we wish to evaluate $GALI^{(k)}$, a specific SVD calculation is required.

For the reversibility error indicator BF, it is possible to use Eq. (7.17) to evaluate $\Xi_n^{BF}(\mathbf{x})$ with the possibility of exploring several realizations of ξ. This requires the evaluation, for each iteration, of $\mathsf{L}_n^{-1}(\mathbf{x})$ or $\mathsf{L}_n(\mathbf{x})$, together with the evaluation of the sum with a selected or a set of selected noise realizations. This can lead to higher memory demands when several noise realizations or the time evolution of the indicator needs to be evaluated. Furthermore, its evaluation at a target iteration number $\overline{n}$ does not provide the values for $n \leq \overline{n}$, as each evaluation requires a different summation and noise realization. If the map analysed is symplectic, the corresponding invariant defined in Eq. (7.20) can be used, resulting in a computational effort comparable to the evaluation of LE.

REM, conversely, involves very little computational effort, as it does not require the evaluation of $\mathsf{L}_n(\mathbf{x})$, but only the execution of the orbit computation twice. This makes REM very attractive for applications in which no explicit or analytical expression for the tangent map is available. However, the evaluation of REM for a target iteration number n gives no information on its value for lower iteration values, as its evaluation requires separate backtracking each time.

Finally, for *FMA*, if the fundamental frequency is evaluated using FFT-based methods (see, e.g., [138, 140]), considerable effort is required in terms of memory usage, due to the necessity of storing the entire orbit of $M(\mathbf{x}, n)$, then perform the algorithm. This is not the case if the fundamental frequency is evaluated using the APA method (see, e.g., [138, 140]), as the mean can be progressively evaluated without the need to store the entire orbit history.

Modern parallel computing architectures, such as those offered in General Purpose Graphics Processing Units (GPGPU) [154], follow the single-instruction, multiple-data (SIMD) architecture, that is, they execute the same operations over large data allocations, using thread wraps of hundreds of processing cores.

To fully exploit the SIMD architecture, an algorithm must offer options for scaling up parallelization without strong penalties in terms of memory management or branching.

Tracking multiple initial conditions in discrete-time maps is one of the most straightforward processes to implement in a SIMD architecture, as it can be treated as a problem “embarrassingly parallel” [155], and multiple examples of GPGPU applications can be observed, for example, in charged particle tracking in accelerator physics [156–161].

The various indicators of chaos presented here offer, in general, a straightforward conversion to a SIMD approach, since it is immediately possible to perform the tracking and the turn-after-turn dynamic indicator evaluation of several initial conditions. This improvement alone enables mass processing of initial conditions for large values of the turn number $n_{\max}$, allowing various types of statistical analysis.

However, an exception is given by FMA when evaluated using FFT-based methods, as it requires one to keep track in memory of the orbit of any initial condition and then perform numerical estimates of the fundamental frequencies. Due to this requirement, scaling up the procedure to a large number of turns or a large number of initial conditions may lead to memory limitations.

To fully benefit from the SIMD architecture, we evaluated the fundamental frequency via the APA method with Birkhoff weights, which does not require the storage of the entire orbit but only the weighted mean phase advance, which can be progressively evaluated without high memory requirements.

A similar limitation is present in the BF reversibility error, since its direct evaluation, defined in Eq. (7.17), requires maintaining track of the entire orbit when there is interest in evaluating different realizations of ξ_n. In contrast, REM offers a straightforward GPGPU approach, since it only requires explicit forward and backward tracking, without the need to evaluate the tangent map. We recall that REM evaluates only the first invariant from a single noise realization, obtained by exploiting the numerical roundoff.

7.B | Time dependence of dynamic indicators

When considering a large amount of initial conditions to determine the properties of the corresponding orbits by means of dynamic indicators, it is possible to obtain an accurate picture of the phase-space structures, such as regions characterized by regular dynamics and regions where frequency modulation and non-linearities induce chaotic behaviour. In Fig. 7.11, the seven chaos indicators computed for $n = 10^5$ are presented for a set of initial conditions that turned out to be stable up to $n_{\max} = 10^8$. All indicators highlight a region of regular motion close to the origin and chaotic structures at higher amplitudes. Generally speaking, the various dynamic indicators reconstruct very similar shapes for the regular and chaotic regions of the phase space, with the exception of FMA. Indeed, this indicator provides a lot of structure even inside the region that is classified as regular by the other indicators, and in which the values of the other indicators are to a high degree of accuracy constant. We inspect the distribution of values of the various dynamic indicators, computed at a large number of turns. It is possible to observe the formation of bimodal or, as we shall see for the case of FMA, three-modal distributions. In Fig. 7.12, the time evolution of the distribution of the indicator value is shown. The red lines represent the threshold that we use to distinguish between regular and chaotic orbits, whose definition was given in Section 7.4.3.

The indicators $\log_{10}(LE)/n$, $FLI(\hat{x})/n$, $FLI^{WB}(\hat{x})$, and $MEGNO(LE)/n$ have a comparable behaviour and globally tend to cluster regular orbits into an ensemble peaked at near-zero values, whereas chaotic orbits are part of another cluster featuring a large spread of values, which correspond to indicator values that are orders of magnitude higher. To achieve a valid overview of the value distribution, especially its tendency to create a bimodal distribution [148, 149], we will consider the logarithm of these three indicators, i.e. $\log_{10}(\log_{10}(LE)/n)$, $\log_{10}(FLI(\hat{x})/n)$, $\log_{10}(FLI^{WB}(\hat{x}))$, and

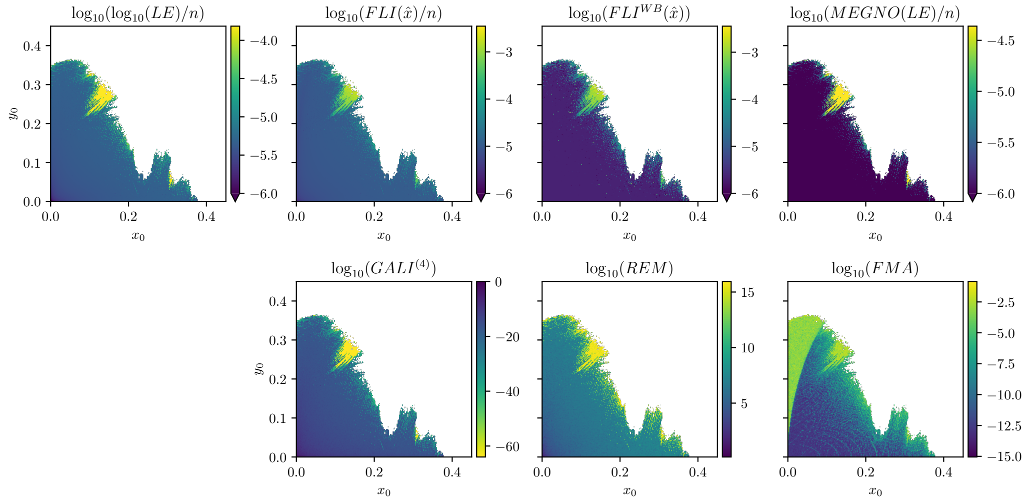

Figure 7.11: Color maps of the various dynamic indicators for a modulated 4D Hénon map evaluated at $n = 10^5$. It can be seen how the indicators globally highlight the same structures in phase space, with the exception of FMA, which also shows structures related to resonances. Note that an arrow at the top of the color bar means that pixels of the top color correspond to a value equal to or greater than the top value. White pixels correspond to initial conditions whose distance from the origin has exceeded a predefined radius ($r_c = 10^2$) during the tracking, before reaching the target iteration number $n_{\text{max}} = 10^8$. (Simulation parameters: $(\omega_{x0}, \omega_{y0}) = (0.28,\ 0.31),\ \varepsilon = 32.0,\ \mu = 0.5$).

$\log_{10}(MEGNO(LE)/n)$.

By direct inspection of the colour maps in Fig. 7.12, it can be seen how these four indicators generate bimodal distributions, with the peak corresponding to regular orbits featuring a clear trend towards zero, and this trend appears to be faster for $\log_{10}(FLI^{WB}(\hat{x}))$, and $\log_{10}(MEGNO(LE)/n)$, due to the applied filters. $\log_{10}(FLI(\hat{x})/n)$ and $\log_{10}(FLI^{WB}(\hat{x}))$ feature an increasing spread of values corresponding to chaotic orbits, a clear trend of the distribution of regular orbits toward zero. A similar trend is also observed in $\log_{10}(\log_{10}(LE)/n)$ and $\log_{10}(MEGNO(LE)/n)$, however, the current numerical implementation of LE suffers from numerical saturation for chaotic orbits that exhibit exponential growth in the values of the tangent map. This results in a limitation for the spread of values that can be observed for chaotic orbits at high numbers of turns, but, ultimately, the distinction between clusters remains.

$GALI^{(4)}$ takes values in the interval $[0, 1]$, corresponding to the range of values of the volume of the 4D parallelotope, constructed by normalized orthonormal displacements. The unit value is associated with the initial orthonormal displacement, whereas zero implies an exact chaos-induced align-

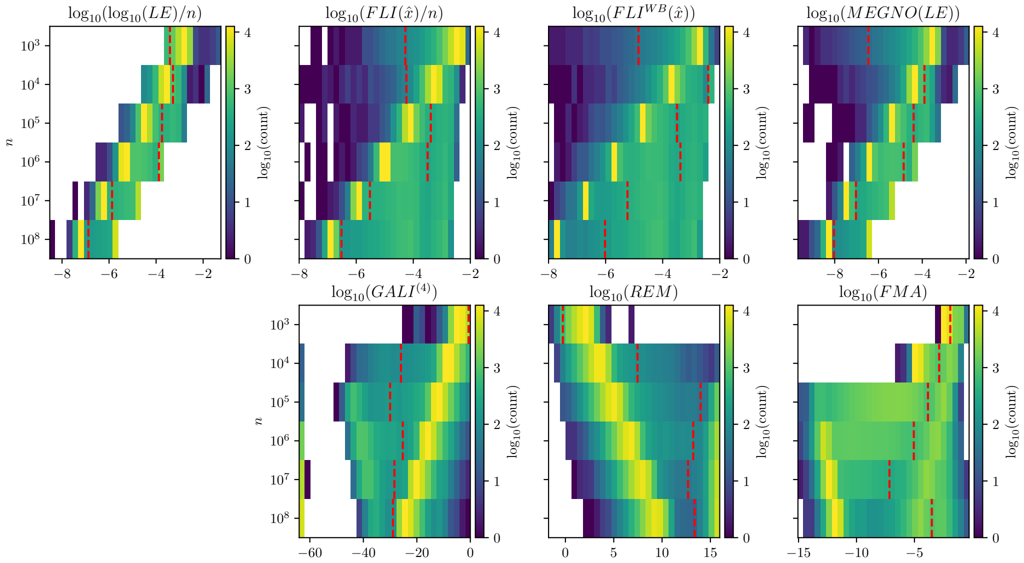

FIGURE 7.12: Distribution of values of the various dynamic indicators as a function of time for a modulated 4D Hénon map. For low values of the iterations n, the distribution is in general represented by a uni-modal function. For higher values of n, we can see the formation of either two separate clusters, making the distribution bimodal, or an individual cluster with a significant tail. $\log_{10}(FMA)$ constitutes an exception, as it evolves forming a tri-modal distribution (also shown in detail in Fig. 7.7, bottom). The red dashed lines represent threshold values, defined by our algorithm, representing our criterion to distinguish regular and chaotic orbits. (simulation parameters: $(\omega_{x0}, \omega_{y0}) = (0.28,\ 0.31),\ \varepsilon = 32.0,\ \mu = 0.5$).

ment of at least two displacement vectors along the direction of the maximum Lyapunov exponent. Inspecting the indicator distribution in logarithmic scale, i.e. $\log_{10}(GALI^{(4)})$, highlights a bimodal distribution, where the peak corresponding to the ensemble of regular orbits moves towards small values of the indicator, following a power law distribution. Moreover, an ensemble of chaotic orbits creates a tail distribution of values lower than the regular ensemble, thus creating a second, smaller-amplitude peak in the indicator distribution. The presence of the logarithm when evaluating the distribution of $GALI^{(4)}$ generates a numerical artefact. Indeed, certain chaotic orbits feature a 4D volume, computed using the SVD method, that reaches values below numerical precision, which are consequently registered as zero. We assign to these initial conditions a value of 10^{-64}, which represents a product of 4 singular values $z_j = \epsilon \sim 10^{-16}$ with extended precision. The cluster of these special initial conditions generates yet another peak in the indicator distribution that is, nevertheless, irrelevant in future considerations about the classification of orbits.

The dynamic indicator REM is also considered on a logarithmic scale to better understand its behaviour. The measured Euclidean distance for the case of regular orbits ranges from a few orders of magnitude higher than the numerical precision $\epsilon \sim 10^{-16}$ for small values of n. These indicator values increase with n following a power law (typically, the peak reaches 10^5 for $n = 10^5$) due to the accumulation of the numerical error. Instead, for chaotic orbits, we observe exponential growth that saturates to an almost constant value. This occurs since chaotic orbits belong to an invariant bounded set of diameter D so that the saturation value is about $\epsilon^{-1}D$. Similarly to $GALI^{(4)}$, we inspect the indicator in logarithmic scale, i.e. $\log_{10}(REM)$.

FMA is based on the evaluation of the Euclidean distance in the frequency space of the fundamental frequencies computed over different time intervals. If we inspect its distribution on logarithmic scale, we observe how the indicator converges to a three-mode distribution. This configuration consists of an ensemble of initial conditions rapidly converging to values close to numerical precision, an ensemble of initial conditions maintaining values above 10^{-5}, and a well-populated ensemble of initial conditions that connect these two ensembles (this distribution is also shown in Fig. 7.7, bottom). Inspecting the logarithm of the indicator, i.e. $\log_{10}(FMA)$, allows to inspect the full spread of values achieved by the various orbits.

$(\omega_x, \omega_y) = (0.28, 0.31)$			
$\varepsilon = 0.0; \mu = 0.0$		$\varepsilon = 0.0; \mu = 0.5$	
$\log_{10}(GALI^{(4)})$	0.99700 ± 0.00014	$\log_{10}(GALI^{(4)})$	0.9956 ± 0.0002
$\log_{10}(FLI^{WB}(\hat{x}))$	0.9966 ± 0.0005	$\log_{10}(REM)$	0.99423 ± 0.00004
$\log_{10}(MEGNO(LE)/n)$	0.9965 ± 0.0008	$\log_{10}(\log_{10}(LE)/n)$	0.99 ± 0.03
$\log_{10}(REM)$	0.99629 ± 0.00003	$\log_{10}(FLI^{WB}(\hat{x}))$	0.99 ± 0.10
$\log_{10}(\log_{10}(LE)/n)$	0.99 ± 0.05	$\log_{10}(FLI(\hat{x})/n)$	0.9080 ± 0.0016
$\log_{10}(FLI(\hat{x})/n)$	0.94 ± 0.01	$\log_{10}(MEGNO(LE)/n)$	0.90 ± 0.14
$\log_{10}(FMA)$	0.8738 ± 0.0005	$\log_{10}(FMA)$	0.8797 ± 0.0004
$(\omega_x, \omega_y) = (0.28, 0.31)$			
$\varepsilon = 32.0; \mu = 0.0$		$\varepsilon = 32.0; \mu = 0.5$	
$\log_{10}(GALI^{(4)})$	0.9453 ± 0.0014	$\log_{10}(GALI^{(4)})$	0.924 ± 0.002
$\log_{10}(REM)$	0.9329 ± 0.0003	$\log_{10}(REM)$	0.9096 ± 0.0003
$\log_{10}(MEGNO(LE)/n)$	0.93 ± 0.08	$\log_{10}(MEGNO(LE)/n)$	0.90 ± 0.09
$\log_{10}(\log_{10}(LE)/n)$	0.924 ± 0.011	$\log_{10}(\log_{10}(LE)/n)$	0.888 ± 0.015
$\log_{10}(FLI^{WB}(\hat{x}))$	0.913 ± 0.007	$\log_{10}(FLI^{WB}(\hat{x}))$	0.88 ± 0.02
$\log_{10}(FMA)$	0.869 ± 0.003	$\log_{10}(FLI(\hat{x})/n)$	0.843 ± 0.009
$\log_{10}(FLI(\hat{x})/n)$	0.863 ± 0.007	$\log_{10}(FMA)$	0.797 ± 0.005
$(\omega_x, \omega_y) = (0.168, 0.201)$			
$\varepsilon = 0.0; \mu = 0.0$		$\varepsilon = 0.0; \mu = 0.5$	
$\log_{10}(GALI^{(4)})$	0.9896 ± 0.0004	$\log_{10}(GALI^{(4)})$	0.9909 ± 0.0004
$\log_{10}(REM)$	0.98682 ± 0.00009	$\log_{10}(MEGNO(LE)/n)$	0.99 ± 0.09
$\log_{10}(FLI^{WB}(\hat{x}))$	0.986 ± 0.002	$\log_{10}(REM)$	0.98850 ± 0.00012
$\log_{10}(\log_{10}(LE)/n)$	0.981 ± 0.003	$\log_{10}(FLI^{WB}(\hat{x}))$	0.988 ± 0.002
$\log_{10}(FLI(\hat{x})/n)$	0.980 ± 0.016	$\log_{10}(\log_{10}(LE)/n)$	0.99 ± 0.07
$\log_{10}(FMA)$	0.9319 ± 0.0010	$\log_{10}(FLI(\hat{x})/n)$	0.980 ± 0.015
$\log_{10}(MEGNO(LE)/n)$	0.9 ± 0.2	$\log_{10}(FMA)$	0.9510 ± 0.0009
$(\omega_x, \omega_y) = (0.168, 0.201)$			
$\varepsilon = 32.0; \mu = 0.0$		$\varepsilon = 32.0; \mu = 0.5$	
$\log_{10}(GALI^{(4)})$	0.903 ± 0.003	$\log_{10}(GALI^{(4)})$	0.914 ± 0.003
$\log_{10}(REM)$	0.8880 ± 0.0004	$\log_{10}(REM)$	0.8915 ± 0.0004
$\log_{10}(MEGNO(LE)/n)$	0.87 ± 0.09	$\log_{10}(MEGNO(LE)/n)$	0.89 ± 0.11
$\log_{10}(\log_{10}(LE)/n)$	0.863 ± 0.016	$\log_{10}(FMA)$	0.881 ± 0.007
$\log_{10}(FLI(\hat{x})/n)$	0.849 ± 0.012	$\log_{10}(\log_{10}(LE)/n)$	0.88 ± 0.02
$\log_{10}(FLI^{WB}(\hat{x}))$	0.849 ± 0.007	$\log_{10}(FLI^{WB}(\hat{x}))$	0.870 ± 0.012
$\log_{10}(FMA)$	0.843 ± 0.004	$\log_{10}(FLI(\hat{x})/n)$	0.850 ± 0.017

Table 7.1: Performance estimate of the dynamic indicators for the various Hénon map configurations, evaluated using Eq. (7.29) over the interval $n = 10^4 - 10^6$. Values are ranked in decreasing order. It is clearly seen that $GALI^{(4)}$ is the highest scorer and REM is the second-best scorer in most of the cases considered. The uncertainty in the performance estimate is evaluated by applying a variation of the calculated thresholds of $\pm 5\%$.

8 | Analysis of the beam dynamics in HL-LHC with dynamic indicators

In this final chapter, we make use of the insights on the behaviour of dynamic indicators presented in the previous chapter to analyse the phase-space properties of a realistic HL-LHC lattice. As modern tracking codes are able to perform the tracking of many particles in parallel, thanks to the use of modern GPU architectures, we can inspect numerous initial conditions and thus enable new statistical analyses of the phase-space properties of the lattice.

From the analysis performed on the Hénon map, along with the performance classification study, we know that the dynamic indicators $GALI^{(k)}$ and REM are the most performant in quickly investigating the chaotic behaviour of the orbits. Along with these indicators, we also include the FLI and FLI^{WB} indicators, which are also very useful for achieving a numerical estimate of the maximal Lyapunov exponent, and the FMA indicator, to compare its results with other indicators in the presence at different levels of modulation.

As the final goal of this line of research is to assess the relation between the existence of large chaotic regions in the phase space to the occurrence of Nekhoroshev-like diffusive behaviour, we therefore look forward to the information provided by dynamic indicators, which might offer a more direct insight about the presence of a Nekhoroshev-like long-term evolution.

The chapter is structured as follows. In Section 8.1, we provide specific details on the implementation of the shadow particle method to evaluate dynamic indicators, as current tools do not offer an analytic expression of the tangent map. In Section 8.2, we go into the technical details of the numerical implementation of the dynamic indicators, as well as the details of the model used for the analysis. In Section 8.3, we present the results of the analysis of the phase-space properties of the HL-LHC lattice, and in Section 8.4, we discuss some characteristics of the indicators. Finally, in Section 8.5, we analyse the details of the beam dynamics highlighted by the dynamic indicators, which are of interest in the context of the Nekhoroshev-like scaling laws and in determining the time evolution of selected indicators. In Section 8.6, we conclude the chapter with a summary of the results and a discussion of future work.

8.1 | Evaluation of dynamic indicators for complex systems

In the previous chapter, we observed how some dynamic indicators, such as FLI and $GALI^{(k)}$, require the evaluation of the evolution of an initial displacement using the tangent map $DM(\mathbf{x}, n)$. For a simple model, such as the Hénon map, an analytic expression of $DM(\mathbf{x}, n)$ is available, enabling us to directly evaluate expressions such as Eq. 7.10 directly.

Conversely, when realistic accelerator models are considered, which are the result of the concatenation of the transfer maps of thousands of magnetic elements, it is currently not feasible to obtain a complete and practical application of the analytic expression of the tangent map. This requires the use of numerical methods to evaluate the tangent map, which is a computationally expensive task. An alternative method to evaluate the linear response of the system to a small initial displacement is the use of a so-called "shadow particle" [162].

The shadow particle method consists of approximating the limit $\epsilon \to 0$, which appears in the first row of Eq. (7.4), with an ϵ of small but finite value, performing orbit tracking of both the initial condition $\mathbf{x}_0$ and the displaced initial condition $\mathbf{y}_0 = \mathbf{x}_0 + \epsilon\boldsymbol{\xi}$, and then evaluating the estimate $\Xi_n(\mathbf{x}) = \frac{\mathbf{y}_n - \mathbf{x}_n}{\epsilon}$.

When tracking $\mathbf{x}_n$ and $\mathbf{y}_n$, it is also necessary to reset the distance between $\mathbf{x}_n$ and $\mathbf{y}_n$ to the initial value ϵ in all τ iterations, while maintaining the same direction. This is done to avoid spurious effects in the evaluation of the linear response that could be caused by an excessive distance between the two orbits [162], which is especially expected for chaotic orbits.

This periodically modified $\mathbf{y}'_n$, for a given value of τ, reads

$$
\begin{aligned}
\mathbf{y}'_0 =& \mathbf{y}_0 \, ; \\
\mathbf{y}'_i =& M(\mathbf{x}_{i\tau-1}, i\tau - 1) M(\mathbf{x}_{i\tau-2}, i\tau - 2) \cdots \\
& \cdots M(\mathbf{x}_{(i-1)\tau}, (i-1)\tau) \left[\mathbf{x}_{(i-1)\tau} + \epsilon \, \frac{\mathbf{y}'_{i-1} - \mathbf{x}_{(i-1)\tau}}{\left\| \mathbf{y}'_{i-1} - \mathbf{x}_{(i-1)\tau} \right\|} \right] , \qquad 0 \le i \le n/\tau \, ,
\end{aligned}
\tag{8.1}
$$

which, for $\tau = 1$, reduces to

$$
\begin{aligned}
\mathbf{y}'_0 &= \mathbf{y}_0 \, ; \\
\mathbf{y}'_i &= M(\mathbf{x}_{i-1}, i - 1) \left[\mathbf{x}_{i-1} + \epsilon \, \frac{\mathbf{y}'_{i-1} - \mathbf{x}_{i-1}}{\left\| \mathbf{y}'_{i-1} - \mathbf{x}_{i-1} \right\|} \right] .
\end{aligned}
\tag{8.2}
$$

Implementing this method in the definition of FLI/n, FLI^{WB}, and $GALI^{(k)}$ is a straightforward task and ends with replacement of the evaluation of the tangent map $DM(\mathbf{x}, n)$ with the evaluation of a shadow particle for each displacement direction $\boldsymbol{\xi}$ we want to consider.

This estimation method has been widely used in the literature due to its simplicity of implementation; however, in multiple studies [162, 163] it has been highlighted how the choice of both the value of ϵ and the time interval τ between displacement resets to ϵ can significantly affect the final evaluation of $\Xi_n(\mathbf{x})$ and consequently the dynamic indicators relying on it.

8.2 | Implementation of dynamic indicators in accelerator tracking codes

8.2.1 | GPU parallel tracking of particles

As noted in Appendix 7.A, in the context of map tracking, single-particle tracking falls into the category of "embarrassingly parallel" computational problems [155], that is, a problem that offers trivial parallelization opportunities on many processing units. This is because the tracking of a single particle is independent of the tracking of other particles, since beam intensity-dependent effects are neglected, and the only information that needs to be shared between different particles is the lattice information. This makes the tracking of many particles a very suitable problem for parallelization in a GPU architecture, which is designed following the SIMD paradigm (Single Instruction Multiple Data) [154].

Since 2021, a new symplectic tracking framework named Xsuite [164] has been under development at CERN. Xsuite is a collection of Python packages that extends the features offered by the SixTrack code [165], following modern programming paradigms and allowing efficient parallelization in both CPU and GPU architectures by generating optimized C code on the fly. More specifically, the Xtrack tracking package in Xsuite offers the possibility to track particles in realistic accelerator lattices on GPU architectures, thus enabling the tracking of large numbers of initial conditions at significantly shorter times. The application of GPUs in accelerator physics simulations has already been used in multiple studies, ranging from Hollow Electron Lens to charged particle tracking studies [156–161]. Among these various studies, the implementation of the GPU version of Xsuite was specifically used to enable new statistical studies on Hollow Electron Lens [160].

The code structure of Xsuite allowed us to easily implement, within the GPU workflow, the fundamental elements for the dynamic indicators' evaluation, such as the normalization of shadow particles, and it made it possible to track a large amount of initial conditions. The possibility of tracking a large number of initial conditions is one of the main motivations of this study, as a combination of large scans and dynamic indicators might lead to better insights into the phase-space features of realistic accelerator lattices.

8.2.2 | Computational effort for evaluating chaos indicators

The dynamic indicators showcased in the previous chapter require different computational efforts in terms of memory requirements or additional operations needed, on top of a reference single-particle tracking mechanism. As discussed in Appendix 7.A, considering these different requirements can favour the choice of a specific dynamic indicator, depending on the analysis to be performed and the available computational resources. We recall here the main considerations for each indicator concerning the usage of the shadow-particle method.

Current particle tracking frameworks do not offer practical tools for obtaining an analytic expression of the tangent map. To overcome this issue, the shadow particle method gives us a straightforward method to numerically evaluate the chaotic behaviour of a complex magnetic lattice made up of multiple non-linear elements.

For FLI, the main computational effort consists in tracking the orbit of two particles, namely the initial condition and the shadow particle, i.e. the initial condition with an initial displacement included. This value increases if there is interest in inspecting different initial displacements at the same time. Similarly, $GALI^{(k)}$ requires the evaluation of $k+1$ particles per initial condition, namely, the unperturbed initial condition and k shadow particles with orthogonal displacement.

REM and FMA do not need to track shadow particles. REM however requires a forward and backward tracking, doubling the computational effort in a way comparable to FLI. FMA, instead, only requires forward tracking to evaluate the fundamental frequency, that is, the tune, at different time intervals. Depending on the method used to evaluate the tune, memory requirements could vary, for example, using FFT-based algorithms to evaluate the fundamental frequency requires storing the complete orbit, while methods based on the average phase advance algorithm may be implemented without this need. Details regarding this issue are discussed in the Appendix 7.A, as excessive memory requirements may lead to the impossibility to rely on SIMD architectures due to the current limits of GPU on board memory. In the context of this study, we evaluated the tune using the average phase advance method with Birkhoff weights proposed in [141], which provides superconvergence and can be evaluated in a single forward tracking pass, without the need to store the entire orbit history.

8.2.3 | Models

For our studies, we used a realistic accelerator lattice implementation based on version 1.4 of the HL-LHC layout and optics [166] of Beam 1. We performed single-particle tracking without beam-beam interaction at top energy 7.0 TeV. As we consider a configuration with colliding proton beams at top energy, we have the machine tunes set at $\omega_x = 62.31$, $\omega_y = 60.32$ and β^* set at 0.15 m at IP1 and IP5. The nominal emittance of the beam is set at 2.5 µm. The tracking simulation has its starting point set at IP3. At this location, the β functions for the two planes are β_x =117.83 m and β_y =219.64 m. The lattice implementation is based on the MAD-X code [167] and is available in the Pymask repository [168].

The MAD-X magnetic lattice comprises 60 realizations (also called seeds) of the magnetic field imperfections that have been measured in the various magnets installed in the ring. These realizations are usually used to gather a broad statistic of the results in a simulation experiment. These seeds offer a good representation of different levels of non-linear effects, and they can be used to study the impact of machine imperfections on the formation of chaotic regions in the phase space.

From this set of 60 realizations, we picked two representative samples, namely, the one scoring the best and worst dynamic aperture values on a tracking up to $n = 10^5$ turns. The dynamic aperture is defined as the volume of the connected phase-space region where the particles exhibit a bounded motion for at least n turns [55, 169]. We evaluated the dynamic aperture using a 100×100 uniform grid, sampling initial conditions in the $x - y$ transverse plane, with all other variables set to zero. The largest connected component of initial conditions that survived tracking up to $n = 10^5$ turns was considered to be in the dynamic aperture region.

See Fig. 8.1 for a visualization of these two seeds. The resulting survival plot for the tracking done up to $n = 10^5$ turns is reported, where one can see how the different realizations lead to a different portrait in the phase space.

To inspect the performance of the dynamic indicators, we sampled initial conditions on a uniform Cartesian grid of 300×300 particles in the $x - y$ plane, with transverse moments p_x and p_y set to zero. The boundaries of the Cartesian grid were manually selected based on the scan results presented in Fig. 8.1, to have a square region of interest (ROI) focused on the dynamic aperture region highlighted at $n = 10^5$. The boundary of the selected ROI is coloured red.

The longitudinal variable ζ was set at three values to inspect different levels of tune modulations induced by synchrotron motion, respectively, at 0.0 m, at 0.15 m, which is halfway close to the bunch separatrix, and at 0.3 m, which is very close to the bucket separatrix. See Fig. 8.2 for an illustration of the chosen

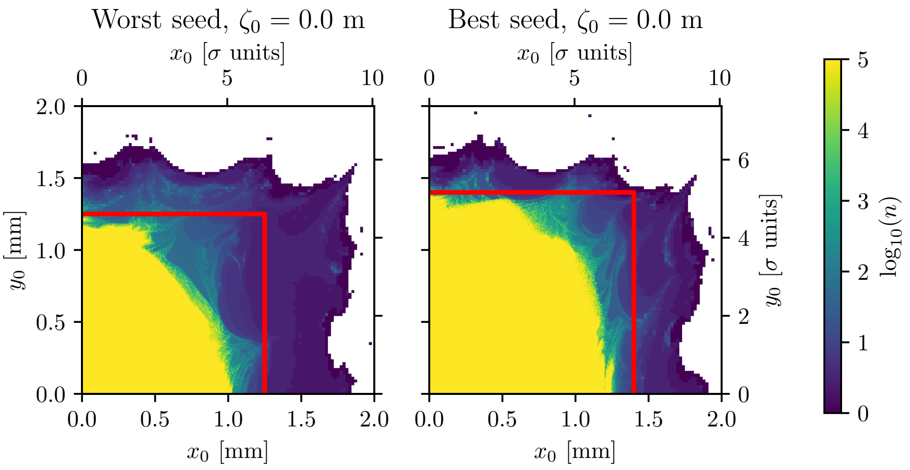

Figure 8.1: Survival plot up to $n = 10^5$ turns of two different seeds of a realistic HL–LHC lattice of Beam 1, without beam-beam interaction, at 7.0 TeV. The two seeds achieved, the worst and best dynamic aperture value out of the selection of 60 seeds available. The initial conditions consist of a 100×100 grid over the x–y plane. A region of interest (ROI) is highlighted in red on the two survival plots, and represents the choice of boundaries for the finer sampling we performed for our dynamic indicator analysis.

ζ values, which are based on the tracking results of multiple initial conditions with different initial ζ values and x, p_x, y, p_y set to zero.

8.3 | Chaos detection studies

The dynamic indicators presented in the previous section, namely FLI/n, FLI^{WB}, $GALI^{(k)}$, REM, and FMA, were evaluated for the HL-LHC lattices up to $n = 10^5$ turns. The results of the evaluation of these indicators are presented in the following sections.

Note how we present most of the value distributions on a logarithmic scale, since the indicators are expected to follow either a power-law distribution or an exponential one. The logarithmic scale allows us to better inspect the tails of the distribution and the general tendencies of these indicators to create bimodal distributions, with the sole exception of FMA, which, as we have seen from the results in the previous chapter when considering a modulated Hénon map, tends to generate a trimodal distribution.

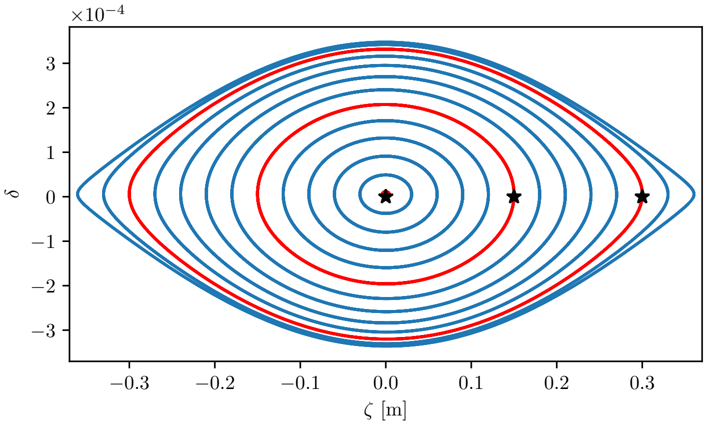

FIGURE 8.2: Tracking of initial conditions with different ζ values up to $n = 10^3$ on the HL-LHC lattice with best seed. The tracking highlights the classic structure, with the hyperbolic fixed points placed at $\zeta \sim \pm\, 0.36\,\mathrm{m}$. The three black crosses represents the three choices of ζ_0 we decided to inspect in our dynamic indicator study.

8.3.1 | Overview of the chaotic regions of the HL-LHC lattice

The inspected 300×300 Cartesian grid of initial conditions considered in the selected ROIs gives us an overview of the phase space that ranges from zero amplitude to approximately 5 σ units of amplitude.

An initial overview of how the phase space is structured is shown in Fig. 8.3, where we report a survival plot for the various configurations of the HL-LHC, in terms of the seed used and the value of ζ_0 considered, tracked up to $n = 10^5$ turns. We can see in the various colour maps a well-defined connected region of initial conditions stable up to 10^5 turns. Outside this connected region, we observe different structures of unstable initial conditions depending on the value of ζ_0. We can observe how, as the value of ζ_0 increases, the boundary between stable and unstable initial conditions becomes less sharp.

We can now inspect these six HL-LHC configurations with chaos indicators and see what structures they highlight within the region where the particles survive up to $n = 10^5$ turns. In Fig. 8.4, we present a colour map of the values of $\log_{10}(\mathrm{FLI}(\hat{x})/n)$ evaluated in the six configurations. We can see, as expected, how chaotic regions, corresponding to the higher values of the indicator, occur at the borders of the stable region, showing, for the case of certain configurations, isolated structures that resemble islands of stability, with regular initial conditions within. These structures can be related to non-linear resonance effects. On the contrary, the internal core region is fully constituted by initial conditions with regular behaviour.

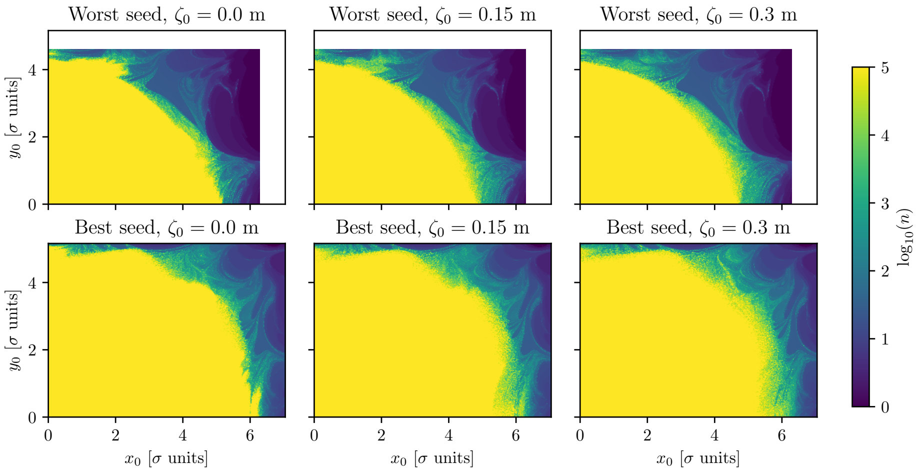

FIGURE 8.3: Survival plot up to $n = 10^5$ turns for all six configurations of the realistic HL-LHC lattice model considered. The realization given by the seed causes strong changes in the phase space structure, while the initial value of ζ_0 is related to different levels of erosion of the stable boundary.

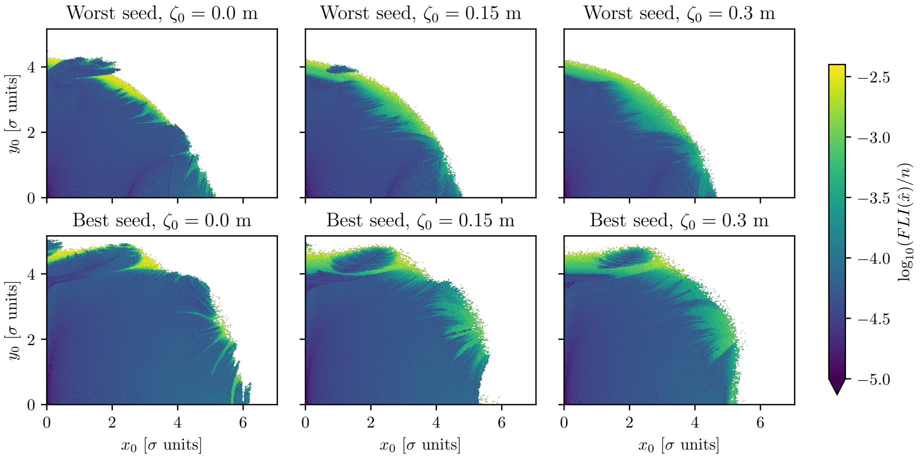

FIGURE 8.4: $\log_{10}(\text{FLI}(\hat{x})/n)$ evaluated at $n = 10^5$ for all six configurations of the realistic HL-LHC lattice model considered. The size of the chaotic structures highlighted by the indicator appears to be strongly correlated to ζ_0.

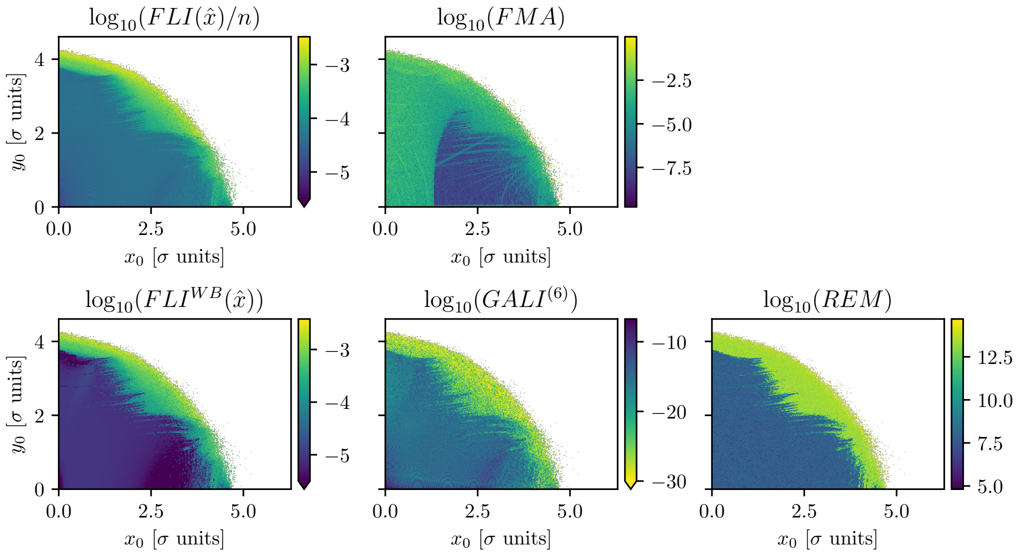

FIGURE 8.5: Colour maps of the various dynamic indicators for a realistic HL-LHC lattice, evaluated at $n = 10^5$. It can be seen how the indicators globally highlight the same structures in phase space, with the exception of FMA, which also shows additional structures. (HL-LHC lattice used: worst seed, ζ_0 =0.3 m.)

The size and shape of the chaotic regions appear to depend on both the seed and the initial value of ζ_0. We can see how increasing ζ_0 contributes to slightly enlarging the size of chaotic regions, since the introduction of stronger longitudinal dynamics causes more modulation effects in the transverse plane, leading to more chaotic initial conditions.

In Fig. 8.5, we present an overview of the various dynamic indicators in the analysis evaluated for one of the HL-LHC lattices, in the form of colour maps evaluated at $n = 10^5$. We can see how the various dynamic indicators, with the exception of FMA, tend to highlight the same regions of chaos, giving a coherent overall evaluation of the phase-space chaoticity. The exception given by FMA will be commented on in a later section.

In Fig. 8.6, we present an overview of the evolution of the value distribution of the various dynamic indicators for different values of n. We can see that, in general, dynamic indicators tend to converge into a bimodal distribution, with the sole exception of FMA, which instead converges into a trimodal distribution. This tendency confirms what we observed in the previous chapter on the modulated Hénon map.

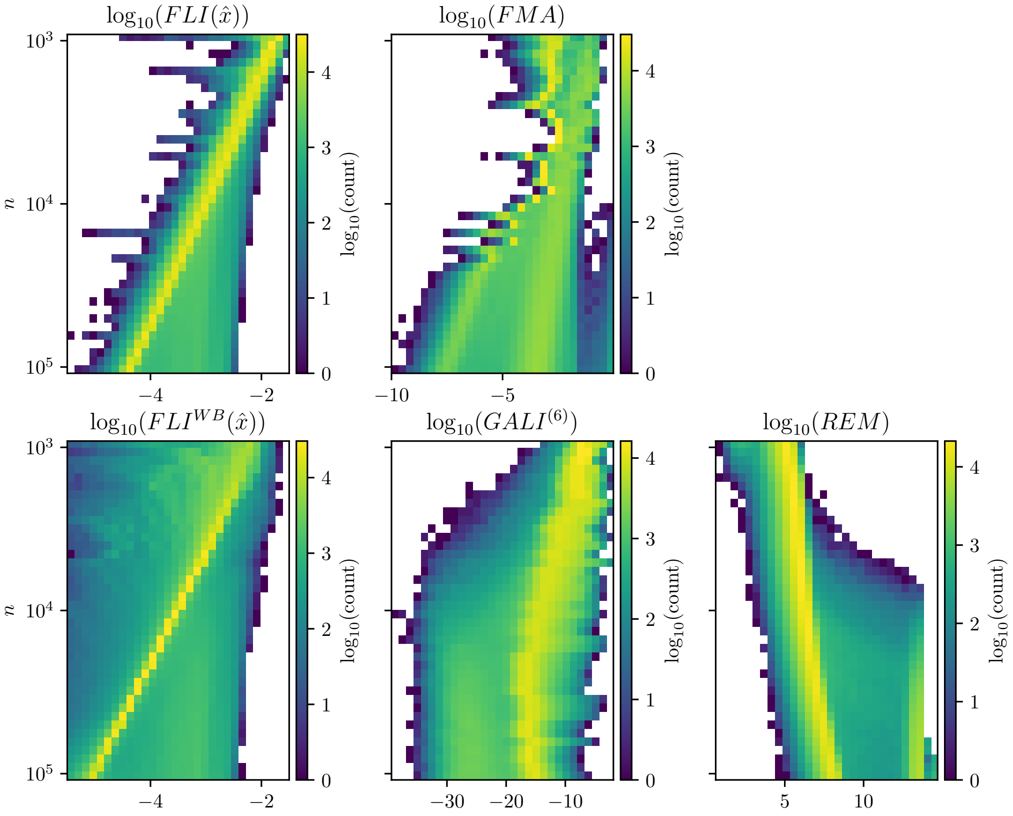

FIGURE 8.6: Distribution of values of the various dynamic indicators as a function of time for a realistic HL-LHC lattice. For low values of the number of turns n, the distribution is in general represented by a uni-modal function. For higher values of n, we can see the formation of either two separate clusters, making the distribution bi-modal, or an individual cluster with a significant tail. $\log_{10}(FMA)$ constitutes an exception, as it evolves forming a tri-modal distribution. (HL-LHC lattice used: worst seed, ζ_0 =0.3 m.)

8.4 | Some features of dynamic indicators

8.4.1 | FLI dependence on the initial displacement

FLI, by definition, depends on the initial choice of the direction of the unitary displacement vector ξ, which implies that different structures can be highlighted in the phase space.

To assess the magnitude of these differences, in Fig. 8.7, we compare the calculated values of $\log_{10}(FLI)$, calculated at $n = 10^5$ with an initial displacement along one of the six orthonormal vectors, namely $\hat{x}$, $\hat{p}_x$, $\hat{y}$, $\hat{p}_y$, $\hat{\zeta}$, and $\hat{\delta}$. The comparison is made against the mean value computed for the six possible initial displacements, and the standard deviation is also presented.

It is possible to see how the different choice of initial displacement highlights different structures in the regular region, whereas chaotic regions tend to assume the same final value. This difference is also highlighted by the standard deviation since the chaotic regions at the border of the stable domain generally show a low standard deviation, whereas the stable regions at lower amplitude have higher values.

This result is expected, since chaotic initial conditions are characterized by a large maximal Lyapunov exponent, which leads different initial displacements to eventually align along it after a high enough number of turns. In contrast, regular initial conditions do not exhibit this preferential direction and lead to a different value of FLI depending on the choice of the initial displacement.

8.4.2 | Use of Birkhoff weights with FLI

To quantify the convergence improvements given by the Birkhoff weights, we compare the values obtained for FLI at different times for one of the HL-LHC lattices, using either the standard approach that considers the mean in Eq. (7.10), that is, FLI/n, or the weighted mean based on the use of Birkhoff weights as in Eq. (7.12), that is, FLI^{WB}.

In this analysis, we consider two ensembles of regular and chaotic particles that have been classified by means of the value of the FLI indicator computed for $n = 10^5$ turns. Inevitably, this evaluation does not reach the level of reliability achieved by the ground truth evaluated in the previous chapter, which was evaluated at $n = 10^8$. Therefore, there could be some misclassified particles in our sampling. To overcome this issue as much as possible, we consider regular particles those that have reached a final value of $\log_{10}(\mathrm{FLI}/n) < -4.5$, and, as chaotic particles, we consider those that have reached a final value of $\log_{10}(\mathrm{FLI}/n) > -2.5$. This arbitrarily thresholding is based on the expected

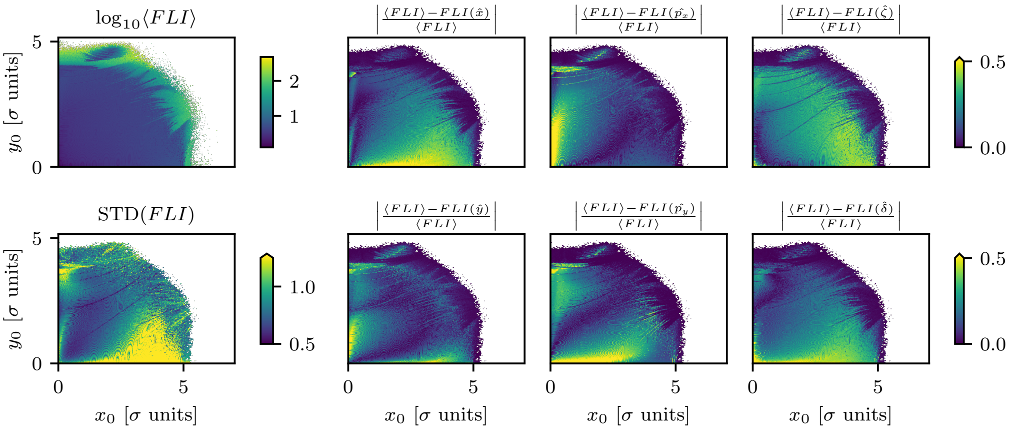

FIGURE 8.7: Overview of FLI evaluated at $n = 10^5$ using as initial displacement any of the six base vectors $\hat{x}$, $\hat{p}_x$, $\hat{y}$, $\hat{p}_y$, $\hat{\zeta}$, and $\hat{\delta}$. The two colour maps on the left show the mean and the standard deviation of all six evaluations of FLI, the others show the values of FLI for each of the six initial displacements as relative difference from the mean value. (HL-LHC lattice used: best seed, ζ_0 =0.3 m.)

properties of the dynamic indicator FLI and considers a subset of initial conditions that have already manifested clear regular or chaotic behaviour at 10^5 turns, while excluding those that do not yet have a clear classification.

The sets are then used to inspect the time evolution of both FLI/n and FLI^{WB}, to assess possible classification improvements in the latter compared to the first. These improvements can be, for example, an increased convergence rate in the indicator value or an increased spread between the values of regular and chaotic initial conditions.

In Fig. 8.8 (left), the comparison between the two indicators is made for a subset of the set of regular initial conditions. It is possible to observe how, for regular initial conditions, Birkhoff averaging does not seem to significantly improve the convergence rate, although it does introduce a constant shift towards a smaller indicator value gap that improves the overall performance of the indicator.

In Fig. 8.8 (right), we show the comparison for the subset of chaotic initial conditions. In this case, a saturation region is observed for the indicator value of the order of $10^{-3} - -10^{-4}$ for both indicators. When this value is reached, both indicators oscillate around it. However, the slope with which this non-zero value is reached is different for the two indicators and is higher in absolute value for FLI/n than for FLI^{WB}. This, combined with the fact that both indicators showed a similar convergence rate for regular initial conditions, suggests

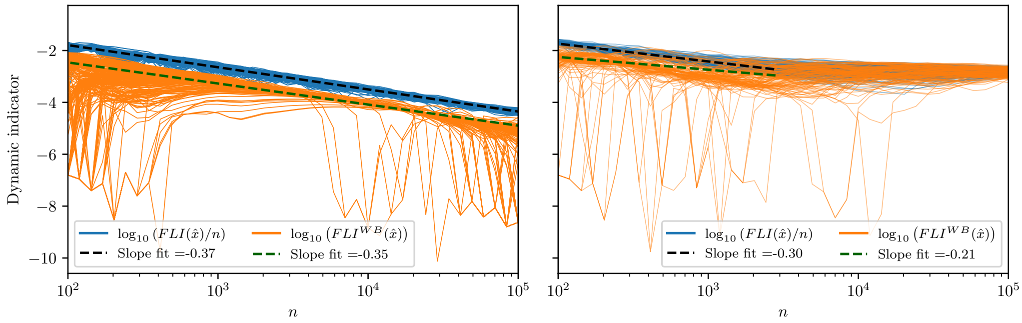

FIGURE 8.8: Time evolution of FLI computed using either a standard mean (FLI/n) or the Birkhoff averaging (FLI^{WB}). Left plot: indicators computed for a set of 100 regular initial conditions, the fit highlights an almost identical convergence rate for the two indicators, although the Birkhoff averaging introduces a constant shift towards a smaller indicator value, which represents already an improvement. Right plot: indicators computed for a set of 100 chaotic initial conditions. A slight difference in convergence rate is observed for low n values, before reaching a saturation value of the indicator of the order of 10^{-3}−−10^{-4}. (HL-LHC lattice used: worst seed, ζ_0 =0.3 m.)

a greater difference in the convergence rate of regular and chaotic initial conditions for FLI^{WB}, compared to that of FLI/n. We must also point out how some chaotic initial conditions exhibit large fluctuations in FLI^{WB} before the saturation point, reaching values comparable to the regular initial conditions.

Despite these isolated oscillations, the improvement brought about by the Birkhoff averages can be appreciated by comparing the evolution of the value distribution of $\log_{10}(FLI/n)$ and $\log_{10}(FLI^{WB})$ reported in Fig. 8.6, since there the time evolution of the value distribution is shown for all the initial conditions shown in Fig. 8.5. The part of the distribution corresponding to the regular initial conditions reaches its peak (yellow band) and moves toward zero with increasing n. However, the displacement towards zero is faster for FLI^{WB}, and the peak is also narrower, potentially allowing for a better classification method, as seen in the previous chapter. It should be stressed that, as already mentioned, the lower values of FLI^{WB} are not due to a steeper slope, but to a constant initial offset. In both graphs, a faint trace of a peak is visible that corresponds to the indicator value of about 10^{-3}. This feature is remarkably similar for the two indicators, as already seen in Fig. 7.4.

When applied to a modulated Hénon map, as discussed in Section 7.4.2, the Birkhoff weights applied to FLI provided a slight improvement in the convergence of regular initial conditions to zero, as well as an overall benefit in highlighting the two separate clusters of initial conditions. In the current context, this difference in convergence was not appreciated to a comparable extent; however, a slight improvement was observed in cluster sharpness and separation, suggesting that Birkhoff weights still offer a certain improvement with respect to the plain *FLI* classification of chaotic orbits.

8.4.3 | Dependence of *FMA* from the longitudinal dynamics

As observed in Appendix 7.B, the chaotic structures highlighted by *FMA* are very different from those highlighted by the other dynamic indicators. This is due to the fact that *FMA* is generally sensitive to tune changes, which are not necessarily related to chaotic dynamics, but rather related to the presence of resonances or tune modulation.

To further highlight this characteristic of *FMA*, we can observe how the indicator is particularly sensitive to the presence of longitudinal dynamics. Indeed, the longitudinal dynamics couples with the transverse one, also introducing tune modulation via a finite value of the chromaticity. In Fig. 8.9, we present *FMA* evaluated for the best seed for three values of ζ_0, and we compare the resulting structures with those highlighted by FLI^{WB}. Two essential features can be observed. The first is that the chaotic regions at the border of the stable region resemble very much for the two indicators, which show that their behaviour is similar. The second is a strong difference between the two indicators in the region close to the vertical axis. This difference grows significantly as a function of ζ_0. With increasing values of ζ_0 the chaotic region detected by *FMA* extends toward the origin along the vertical axis. Furthermore, the width of this chaotic region increases with ζ_0. It is quite clear that the chaotic behaviour detected by *FMA* is an artefact related to the presence of a strong modulation of the tunes. In this sense, this observation suggests that the use of *FMA* to identify chaotic regions in phase space is taken with a grain of salt whenever modulation of linear tunes is present.

Another feature emerges when considering the evolution of the distribution of indicator values as a function of time. In fact, if we compare the evolution of the value distribution of *FMA*, we can observe, in Fig. 8.5, how *FMA* evolves into a trimodal distribution for one of the lattices around $n = 10^4$. Unlike the other dynamic indicators, which show a tendency to create a bimodal distribution.

8.4.4 | General performance of *REM*

In the previous chapter, the performance of different dynamic indicators was evaluated using a modulated Hénon map and applying a clustering approach to detect chaotic orbits. This analysis showed that the *REM* indicator is

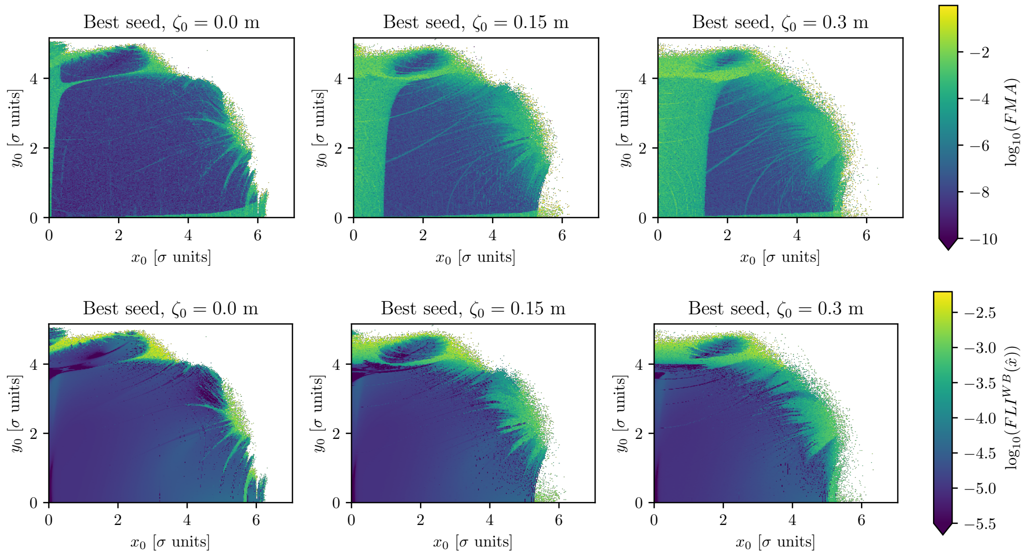

Figure 8.9: $\log_{10}$(FMA) (top row) and $\log_{10}(\mathrm{FLI}^{WB}(\hat{x}))$ (bottom row) evaluated on the same seed for three values of ζ_0 at $n = 10^5$. The differences between the two indicators are enhanced with larger values of ζ_0.

capable of highlighting chaotic structures faster than Lyapunov-based dynamic indicators such as FLI^{WB}. Mainly because of its ability to distinguish regular orbits from chaotic ones in a well-defined bimodal distribution, as the numerical error is quickly amplified by the chaotic character of the orbits.

When applying REM to the HL-LHC lattices, we observe a similar behaviour, i.e. the ability to clearly highlight chaotic regions in the phase space. In Fig. 8.5, we can qualitatively compare the results obtained by REM, calculated for an example seed, with those obtained with FLI^{WB}. We can observe how REM tends to highlight chaotic regions qualitatively sharper than FLI^{WB}, reproducing the same behaviour observed in the modulated Hénon map, although, for this analysis, we lack the possibility to define a ground truth to be used to compare the results of the various indicators.

The behaviour of the distribution of the indicator values can be appreciated by comparing the evolution of the value distribution of $\log_{10}(REM)$ and $\log_{10}(FLI^{WB})$ as a function of time, as shown in Fig. 8.6. In fact, $\log_{10}(REM)$ tends to a bimodal distribution much faster than $\log_{10}(FLI^{WB})$ and in such a way that a threshold to detect chaotic initial conditions would be almost independent of n. Therefore, we can conclude that the promising performance of REM in highlighting chaotic structures in the phase space, along with its straightforward numerical implementation, makes it a very interesting tool for studying phase-space structures in realistic accelerator lattices.

8.5 | Analysis of the beam dynamics using dynamic indicators

8.5.1 | Considerations on stability time and Lyapunov time

It is of interest to inspect the average value of the Lyapunov time T_L, that is, the inverse of the maximum Lyapunov exponent [163], for different values of the amplitude in the $x-y$ space. The maximum Lyapunov exponent is estimated directly by the dynamic indicators FLI/n or FLI^{WB}. In particular, we are interested in evaluating whether T_L follows a Nekhoroshev-like scaling law, which would indicate that the chaotic regions are those contributing to the diffusion-like process that has been introduced in the proposed framework. In other words, we want to inspect whether T_L scales with the amplitude I of an initial condition, as in Eq. (1.45). This study is motivated by the well-known fact that the dynamic aperture follows a Nekhoroshev-like evolution [57], discussed in Section 3.6, which implies a scaling law that describes an exponential reduction in the stability time T_s of the initial conditions as a function of their initial action I.

To make use of our numerical simulation data and inspect T_s and T_L as functions of the initial radius $r=\sqrt{x^2+y^2}$ of an initial condition, we evaluated the mean values of T_s and T_L for a set of initial conditions in the amplitude interval $[r-\Delta r/2, r+\Delta r/2]$ and the angular sector comprised between $[0, \pi/2]$. The mean values of T_s and T_L are then calculated for each interval and the resulting values are plotted as a function of r. Note that for our Nekhoroshev-like scaling laws, I and r are related by $I=r^2$.

To evaluate an optimal choice for Δr, we first calculate the mean values of T_s and T_L for a range of values of Δr, and compare the resulting curves directly. We then select the value of Δr as the best compromise between statistical fluctuations and loss of information. In Fig. 8.10, we present the results of this analysis for both T_s and T_L, applied to one of the realizations of the HL-LHC lattice. We can see that the best compromise is achieved for $\Delta r = 0.2\sigma$, which is the value used in the following.

To estimate the Lyapunov time T_L, we can use FLI/n or FLI^{WB}, as both provide an estimate of the maximal Lyapunov exponent and therefore of T_L. In Fig. 8.11, we present the results of this analysis for the same seed of the HL-LHC lattice. For regular orbits, the maximal Lyapunov exponent is zero and, therefore, T_L is infinite. For chaotic orbits, however, the maximal Lyapunov

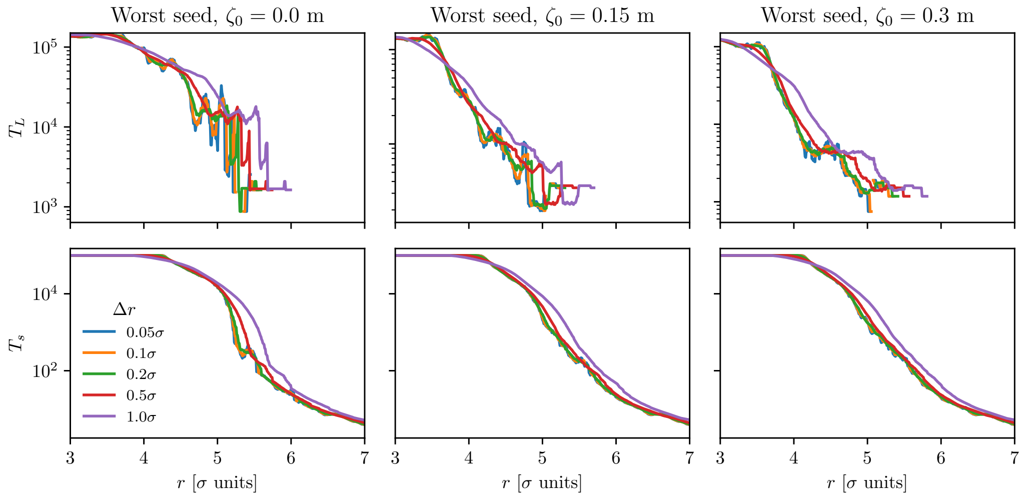

FIGURE 8.10: Mean values of T_s and T_L as a function of r for some values of Δr. The best compromise between statistical fluctuations and loss of information is achieved for $\Delta r = 0.2\sigma$.

exponent is finite and therefore T_L is finite as well. However, since the FLI/n and FLI^{WB} dynamic indicators are evaluated at a finite time n, it is inevitable to observe a non-zero value of the maximal Lyapunov exponent, and hence a finite value of T_L, also for regular orbits. This can be observed in Fig. 8.11, since for values of r corresponding to the regular regions of the phase space, i.e. close to zero, T_L as computed using FLI/n tends to 10^5, the maximum number of turns used in the numerical simulations. The situation is different for the case of FLI^{WB}. In fact, thanks to its superconvergence properties, it provides the same mean T_L value as FLI/n for r in the chaotic regions, i.e. it corresponds to large values of r. Moreover, it provides higher values of T_L for r corresponding to regular regions. Based on this observation, we will use FLI^{WB} to derive T_L in the following.

When comparing directly T_L and T_s, as shown in Fig. 8.12, we can observe that the two times exhibit a similar behaviour with respect to r: they both exhibit a saturated plateau for low r, corresponding to the region dominated by regular orbits, and an exponential decay beyond certain values of the radius, which varies in sharpness and position depending on the value of ζ_0. In the same figure, we also show different evaluations of T_L based on FLI^{WB}, evaluated at different values of n, which clearly show how the value of T_L for regular orbits increases with the value of n, while the value of T_L for chaotic orbits converges to a value that can be considered true. Another important feature is clearly seen in the same figure, namely that T_L extends over a reduced range of

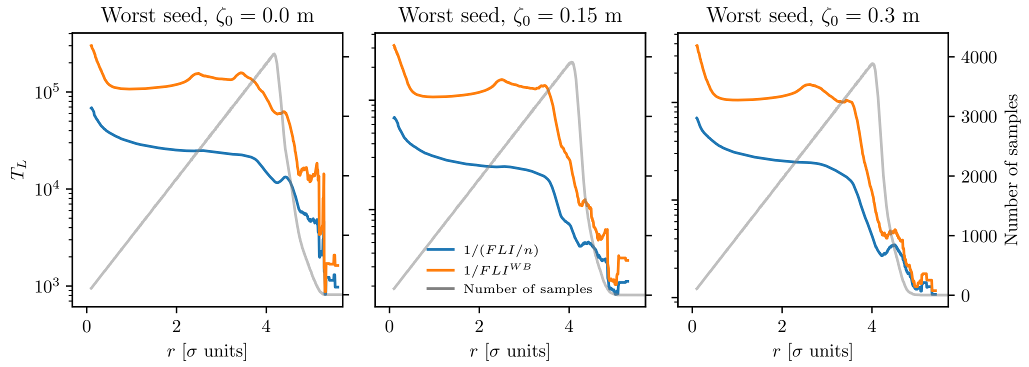

FIGURE 8.11: Mean values of T_{L} as a function of r with $\Delta r = 0.2\sigma$ for three values of the ζ_0 variable. The results presented refer to FLI/n and FLI^{WB}, both evaluated at $n = 10^5$. For high values of r, the two indicators provide similar results, while for low values of r, FLI^{WB} provides a higher value of T_{L}. This is linked to the faster convergence rate of FLI^{WB} to the true value of the indicator, and hence of the maximal Lyapunov exponent. The grey line indicates the number of stable initial conditions that are inside the interval $[r - \frac{\Delta r}{2}, r + \frac{\Delta r}{2}]$ and the angular sector comprised in the interval $[0, \pi/2]$, that are used to evaluate the mean. The change of slope corresponds to the transition between the stable region and the unstable one.

r values. This is due to the choice that the indicator values have been evaluated only for orbits that are stable up to 10^5 turns, which clearly explains why, on the other hand, T_{s} extends over a wider range of r values.

The curves shown so far are obtained by a process of averaging of the raw data. To better understand the actual situation, the distributions of T_{L} and T_{s} as functions of r are shown in Fig. 8.13. There, the distributions are represented using a colour map, and the mean values are highlighted by the red curves. We can observe how the distributions feature a spread that correlates with the value of r, i.e. it shrinks towards small values of r and grows with increasing values of r. For the case of T_{s}, this effect is really striking, since for the values of r corresponding to the stable region of phase space, the distribution of T_{s} is a delta centred on the value of 10^5. In fact, the behaviour of the width of the distributions is not a surprising feature, since the value of r is somewhat correlated with the presence of regular or chaotic orbits.

It is worth noting that given the shape of the distributions, the mean value does not correspond to the most probable one, i.e. the position of the maximum of the distribution. Therefore, we have evaluated the curves that represent the most probable values of T_{s} and T_{L} and used them for the following analyses. However, it turned out that the results of the fit discussed below are

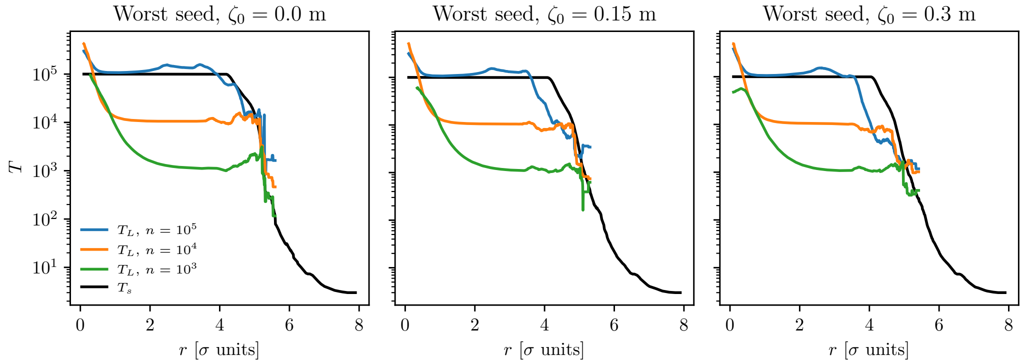

Figure 8.12: Mean values of T_L and T_s as a function of r for $\Delta r = 0.2\sigma$. The values of T_L are evaluated using FLI^{WB} evaluated for three values of n. The convergence process of the reconstructed T_L is clearly visible. Differences and similarities of T_L and T_s are clearly visible. Also visible is the worsening of similarities between T_s and T_L for increasing values of the ζ_0 variable.

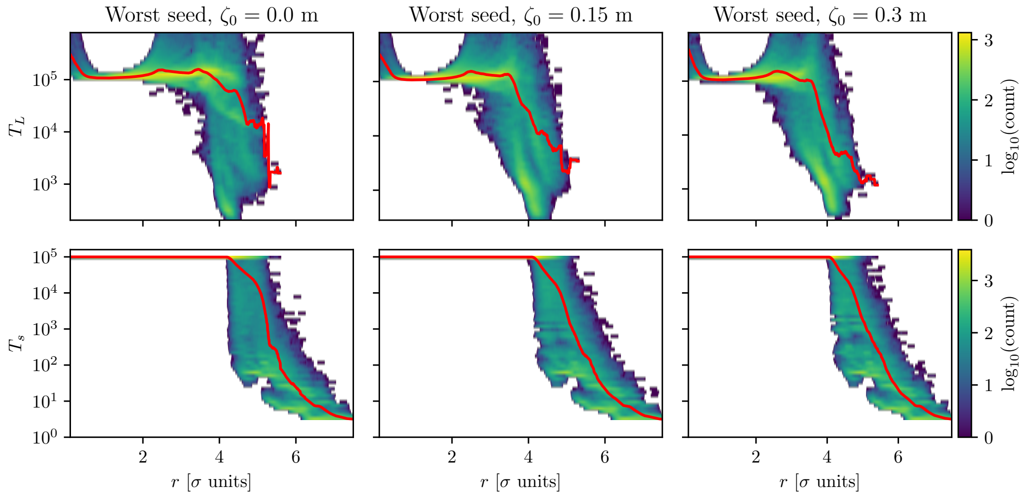

Figure 8.13: Distribution of values of T_L (top) and T_s (bottom) as a function of r for $\Delta r = 0.2\sigma$. The red lines represent the mean value of the distributions, which correspond to the black or blue lines of Fig. 8.12.

much less stable and because of this observation, the use of the most probable value of the distributions of T_s or T_L was abandoned, and the use of the mean value was retained for the rest of the analyses.

We now want to study the possibility of fitting a Nekhoroshev-like function

$$T = T_0 \exp\left[-\left(\frac{I_*}{I_0}\right)^{\frac{1}{2\kappa}}\right] \tag{8.3}$$

to both T_L and T_s, and analyse both the fit goodness and the dependence of the values of T_0, I_*, and κ for the various combinations of realizations and values of ζ_0. As this scale law ranges over multiple orders of magnitude, we consider the logarithm of T, and fit the following function:

$$\log(T) = \log(T_0) - \left(\frac{I_*}{I_0}\right)^{\frac{1}{2\kappa}} \, . \tag{8.4}$$

We first perform an initial brute-force search on a grid of values of T_0, I_0^*, and $1/(2\kappa)$, and then perform a more refined search around the best values found in the first step using the least squares method. The initial coarse-grained search is motivated by the non-linear nature of the fit, which makes it difficult to find the best values of the parameters with a simple gradient-descent method.

As we have seen in Figs. 8.12 and 8.13, and as we discussed previously, the evaluation of T_L and T_s is inevitably affected by the nature of numerical simulations that are carried out over a finite number of turns, in our case $n = 10^5$. Because of this, when performing the fit, we have to consider only the fraction of the data that does not show any saturation, which is determined by the finite number of turns used in numerical simulations.

To make an accurate selection of the numerical data to be used for the fit, we perform the fit on various data sets selected near the region of transition between the regular and chaotic regimes. We then choose the data cut that provides the best fit, using as a figure of merit the reduced χ^2 of the fit.

Figure 8.14, shows the result of the fitting procedure of T_L and T_s, applied to two HL-LHC realizations, both with $\zeta_0 = 0.3\,\mathrm{m}$. We can see how different choices of data selection lead to differences in the values of the fit parameters, and the optimal choice of the data selection, and hence of the fit parameters, can be made considering the value of the reduced χ^2, which is also shown. Note that the value of the reduced χ^2 is evaluated on the logarithmic equation (8.4).

We use the reduced χ^2 as a figure of merit to select the best data cut that does not include saturated samples or exclude chunks of unsaturated data. We select an initial data cut at a r value that exhibits a clear saturation behaviour, that is, a value of T_s equal to 10^5 or a value that oscillates around 10^5 for T_L.

Next, we evaluate the reduced χ^2 by gradually increasing the starting value of r, in steps of $0.1\ \sigma$, following a gradient descent-like procedure until we find a local minimum. We can see how the reduced χ^2 value shows a rapid decrease as we remove saturated data, and after the local minimum, only a minor variation is observed.

In Table 8.1, we report the fit parameters obtained for the six combinations of HL-LHC lattice realizations and the variable ζ_0 we have considered. We can observe how, in general, the fit routine obtains small error estimates for all data sets on T_s. However, for the case of T_L, small errors are observed for all cases except for $\zeta_0 = 0.0\,\mathrm{m}$, probably because of the small extent of chaotic regions, due to the absence of longitudinal-induced transverse tunes modulation.

We can also observe that in the fit of T_s, the exponent $1/(2\kappa)$ has a comparable value for the six configurations considered. This is an interesting feature, since κ is a parameter related to the dimensionality of the phase space and is therefore expected to be a constant for all the different seeds. Similarly, I_* shows a coherent behaviour, as it appears to be strongly correlated with the choice of the seed, while the value of ζ_0 does not induce very relevant variations of I_*.

Regarding the fit of T_L, except for the case with $\zeta_0 = 0.0\,\mathrm{m}$, we can observe how the values of $1/(2\kappa)$ are comparable only for the same seed, the best seed being the closest to the value achieved for the corresponding fit of T_s. Furthermore, I_* has values that are compatible with each other within the fit errors and comparable to the case of the fit of T_s. All this suggests that the scaling laws for T_s and T_L are not necessarily the same and, as we will see shortly, this can be related to similar results in the literature.

In the work of Morbidelli et al. [170], an overview of the relationship between Lyapunov time T_L and macroscopic instability time is presented, a concept that can be connected to our measure of stability time T_s. In particular, the authors distinguish between two different regimes, depending on the characteristics of the Hamiltonian dynamical system under study and the possible presence of low-order resonances overlapping together.

The first regime is called *resonance overlapping regime*, and is characterised by the presence of overlapped low-order resonances. In this case, T_s is expected to have a polynomial relationship with T_L, i.e. $T_\mathrm{s} \sim T_\mathrm{L}^{\beta}$, with some positive α, β. The second regime is called the *Nekhoroshev regime*, and it is shown by the authors how such a regime cannot follow a universal polynomial relation between T_s and T_L, but could instead follow an exponential one, i.e. $T_\mathrm{s} \sim \exp(T_\mathrm{L})$. This indicates that there is no universal relationship between T_s and T_L, as the actual regime depends on the specific characteristics of the Hamiltonian system under study.

If we assume, as we have done so far and verified using the data of numerical

T_s fit		$\zeta_0 = 0.0\,\mathrm{m}$	$\zeta_0 = 0.15\,\mathrm{m}$	$\zeta_0 = 0.3\,\mathrm{m}$
Worst seed	$1/(2\kappa)$	2.94 ± 0.02	3.0 ± 0.2	3.03 ± 0.08
	I_*	131 ± 2	119 ± 7	109 ± 5
	$\log_{10}(T_0)$	-1.23 ± 0.04	-0.95 ± 0.08	-0.81 ± 0.06
	Red. χ^2	0.069	0.021	0.014
Best seed	$1/(2\kappa)$	2.9997 ± 0.0004	3.03 ± 0.07	3.00 ± 0.08
	I_*	220 ± 40	208 ± 28	206 ± 23
	$\log_{10}(T_0)$	-2.2 ± 0.3	-1.9 ± 0.3	-1.819 ± 0.004
	Red. χ^2	0.086	0.055	0.028
T_L fit		$\zeta_0 = 0.0\,\mathrm{m}$	$\zeta_0 = 0.15\,\mathrm{m}$	$\zeta_0 = 0.3\,\mathrm{m}$
Worst seed	$1/(2\kappa)$	1 ± 3	1.88 ± 0.01	1.9 ± 0.1
	I_*	2500 ± 1600	100 ± 40	104 ± 31
	$\log_{10}(T_0)$	-3 ± 17	1.9 ± 0.3	1.5 ± 0.3
	Red. χ^2	0.049	0.010	0.014
Best seed	$1/(2\kappa)$	1.5 ± 1.0	2.94 ± 0.08	2.7 ± 0.1
	I_*	1700 ± 400	108 ± 25	98 ± 27
	$\log_{10}(T_0)$	-4 ± 5	1.1 ± 0.3	1.5 ± 0.3
	Red. χ^2	0.018	0.003	0.016

TABLE 8.1: Results of the fit of a Nekhoroshev-like scaling law on T_s and T_L data obtained from the six combinations of HL-LHC realizations and ζ_0 values considered. The error reported is that associated to the fit procedure and represents the standard deviation of the fit parameters evaluated by the least-squares method. The reduced χ^2 is also reported.

simulations, that both T_s and T_L follow a Nekhoroshev-like scaling law, we can derive the following relation between the two quantities, namely:

$$\frac{T_\mathrm{s}}{T_{0,\mathrm{s}}} = \exp\left[\left(\frac{I_{*,\mathrm{s}}}{I_{*,\mathrm{L}}}\right)^{1/2\kappa_\mathrm{s}} \left(\log\frac{T_\mathrm{L}}{T_{0,\mathrm{L}}}\right)^{\kappa_\mathrm{L}/\kappa_\mathrm{s}}\right] . \tag{8.5}$$

If $\kappa_\mathrm{L}/\kappa_\mathrm{s} = 1$, we can recover a polynomial relation between T_s and T_L of the form $T_\mathrm{s} = \alpha T_\mathrm{L}^{\beta}$, with $\alpha = T_{0,\mathrm{s}}/(T_{0,\mathrm{L}})^{(I_{*,\mathrm{s}}/I_{*,\mathrm{L}})^{1/2\kappa_\mathrm{s}}}$ and $\beta = (I_{*,\mathrm{s}}/I_{*,\mathrm{L}})^{1/2\kappa_\mathrm{s}}$. If, on the other hand, $\kappa_\mathrm{L}/\kappa_\mathrm{s} \neq 1$, the relation assumes the form $T_\mathrm{s} = \alpha \exp\left(\beta \log\left(T_\mathrm{L}/T_{0,\mathrm{L}}\right)^{\kappa_\mathrm{L}/\kappa_\mathrm{s}}\right)$, with $\alpha = T_{0,\mathrm{s}}$ and $\beta = (I_{*,\mathrm{s}}/I_{*,\mathrm{L}})^{1/2\kappa_\mathrm{s}}$. It is worth noting that in our case the exponential relation between T_s and T_L includes a dependence on the logarithm of T_L, which is nonetheless different from the regimes described in Ref. [170]. The parameters of the relation found in the numerical simulations performed using the HL-LHC magnetic lattices are listed in Table 8.2.

Relation T_s, T_L		$\zeta_0 = 0.0\,\mathrm{m}$	$\zeta_0 = 0.15\,\mathrm{m}$	$\zeta_0 = 0.3\,\mathrm{m}$
Worst seed	$\kappa_\mathrm{L}/\kappa_\mathrm{s}$	2 ± 6	1.56 ± 0.08	1.56 ± 0.09
	α	$(5.9 \pm 0.5) \times 10^{-2}$	$(1.1 \pm 0.2) \times 10^{-1}$	$(1.6 \pm 0.2) \times 10^{-1}$
	β	$(1.6 \pm 3.1) \times 10^{-4}$	1.4 ± 1.6	1.1 ± 1.0
Best seed	$\kappa_\mathrm{L}/\kappa_\mathrm{s}$	2.0 ± 1.3	1.03 ± 0.03	1.13 ± 0.06
	α	$(0.7 \pm 0.5) \times 10^{-2}$	$(1.2 \pm 0.7) \times 10^{-2}$	$(1.51 \pm 0.01) \times 10^{-2}$
	β	$(2.2 \pm 2.0) \times 10^{-3}$	7 ± 6	9 ± 8

Table 8.2: Parameters of the relation between T_s and T_L obtained from the fit parameters reported in Table 8.1. All the parameters are evaluated assuming the case $\kappa_\mathrm{L}/\kappa_\mathrm{s} \neq 1$.

The parameters found show sizeable differences between the various cases, confirming the difference in dynamics and the fact that the relationship between T_s and T_L is strongly model dependent. It should also be noted that the values of the parameters for the case $\zeta_0 = 0.0$ exhibit strong differences from those obtained for $\zeta_0 \neq 0$ values. This can be mainly related to the fit performance obtained for the fit of the Nekhoroshev law on T_L for these cases.

Of all the cases inspected, neglecting those with $\zeta_0 = 0.0\,\mathrm{m}$ because of their high uncertainty in the parameters, we see that the one with the best seed and $\zeta_0 = 0.15\,\mathrm{m}$ appears to have the ratio $\kappa_\mathrm{L}/\kappa_\mathrm{s}$ comparable to one, if we consider the propagated uncertainty. If we then compute the corresponding parameters α and β for this specific case, we have, respectively, $\alpha = (0.2 \pm 3.3) \times 10^{-9}$ and $\beta = 7 \pm 6$. Note that α is compatible with the zero value, which implies a degeneracy of the polynomial law. This degeneracy is already visible in the large error affecting the value of α evaluated for case $\kappa_\mathrm{L}/\kappa_\mathrm{s} \neq 1$. This degeneracy might suggest an insufficient amount of information in the available data for performing this kind of parametric estimation. Future investigations will consider a different sampling of the initial conditions to reconstruct the dependence of T_L and T_s on the radius with higher resolution at the most significant amplitudes.

8.5.2 | Time evolution of $GALI^{(k)}$ for chaotic orbits

The $GALI^{(k)}$ indicators depend on the value of the parameter k that assumes the values $2 \leq k \leq 2N$, where N is the number of degrees of freedom of the system, which, in our case, is $N = 3$. For $k = 6$ we find that the choice for the linearly independent initial displacements corresponds to the six base vectors $\hat{x}$, $\hat{y}$, $\hat{p}_x$, $\hat{p}_y$, $\hat{\zeta}$, and $\hat{\delta}$, and there is a single indicator. On the other hand, for lower values of k, we can select the subspace of initial displacements among several possibilities and explore the chaotic behaviour of the system in that specific subspace.

The choice of k has consequences on the convergence rate of the indicator for regular and chaotic orbits. A complete overview of the different expected behaviours of $GALI^{(k)}$ for different values of k is given in [171] where a number of Hamiltonian systems are presented and considered in detail.

If the orbit is chaotic, $GALI^{(k)}$ converges to zero exponentially fast with the law

$$GALI^{(k)} \propto \exp\left[-t\left((\lambda_1 - \lambda_2) + (\lambda_1 - \lambda_3) + \cdots + (\lambda_1 - \lambda_k)\right)\right] , \tag{8.6}$$

where λ_1 is the largest Lyapunov exponent and $\lambda_2 > \lambda_3 > \cdots > \lambda_k$ are the next $k - 1$ Lyapunov exponents in decreasing order. If we assume $\lambda_1 \gg \lambda_2$, we see that the exponential decay of $GALI^{(k)}$ is bounded by $\exp(-tk\lambda_1)$.

In contrast, if the orbit is regular, $GALI^{(k)}$ varies with time according to different laws depending on the value of k and the choice of displacements. That is, we have

$$GALI^{(k)} \propto \begin{cases} \text{constant} & \text{if } 2 \le k \le N \\ \frac{1}{t^{2(k-N)-m}} & \text{if } N < k \le 2N \text{ and } 0 \le m < k - N \\ \frac{1}{t^{k-N}} & \text{if } N < k \le 2N \text{ and } m \ge k - N \end{cases} . \tag{8.7}$$

Let us now consider the behaviour of $GALI^{(k)}$ for an ensemble of 10 chaotic initial conditions, obtained from the worst seed configuration and $\zeta_0 = 0.3\,\mathrm{m}$, which scored a close to identical value with the $FLI^{WB}(\hat{x})$ dynamic indicator evaluated at $n = 10^5$, suggesting a similar maximal Lyapunov exponent. A mean of an ensemble of particles is considered in order to reduce the fluctuations of individual conditions and highlight the evolution trend of the dynamic indicator. We expect both $GALI^{(2)}$ and $GALI^{(4)}$ to exhibit a similar exponential decay, regardless of the choice of displacement, with $GALI^{(4)}$ showing a decay rate roughly double that of $GALI^{(2)}$. To verify this, we pick the 10 initial conditions with a value greater than 10^{-3} with $FLI^{WB}(\hat{x})$, evaluated at $n = 10^5$, as such value is related to chaotic behaviour.

The results are shown in Fig. 8.15. The mean values of $GALI^{(2)}$ and $GALI^{(4)}$ follow an exponential decay in agreement with expectations. All displacement choices exhibit the same decay with a different offset. Note that the pair $(\hat{\zeta}, \hat{\delta})$ exhibits a faster decay rate compared to the other displacement choices $GALI^{(2)}$. $GALI^{(6)}$ is also reported for the sake of comparison of the decay rates.

8.6 | Conclusions and future work

In this chapter, we used a set of dynamic indicators to study the beam dynamics generated by a realistic accelerator magnetic lattice. Given the ability of dynamic indicators to provide information on the chaotic character of the dynamics, they can be used to probe the long-term dynamics of charged particles in a circular accelerator, in order to gain insights on the phase-space structures and the scaling laws governing the beam dynamics, which are closely linked to stability and diffusive behaviour.

Five indicators have been considered, namely FLI/n, FLI^{WB}, $GALI^{(k)}$, REM, and FMA, based on the experience gained from the study of the dynamics generated by the Hénon map. The computational aspects and numerical implementation of these indicators have been discussed, and they were then tested on an HL-LHC realistic accelerator lattice, and the information provided by each indicator was discussed, also with emphasis on their features.

We have observed that the REM indicator performs mostly as expected, while the FMA is strongly affected by the tune modulation induced by the longitudinal motion that couples with the transverse one by means of the non-zero chromaticity. In a way, this is comparable to the behaviour observed on the modulated Hénon map in the presence of tune modulation.

The indicators have also been used to attempt a detailed characterization of the beam dynamics. We have observed how the Lyapunov time, provided with improved convergence rates by FLI^{WB}, can be used to inspect the presence of a Nekhoroshev-like scaling law for the dynamics, and how such value is related to both the lattice realizations and the longitudinal dynamics. This suggests that such a concept can indeed be used to inspect the presence of extended chaotic structures in the phase space, which might be related to long-term Nekhoroshev-like diffusive behaviour. Furthermore, the time evolution of the indicators $GALI^{(k)}$ has been studied for chaotic initial conditions, highlighting some properties, while its use to study the geometry of regular orbits will be the topic of future studies.

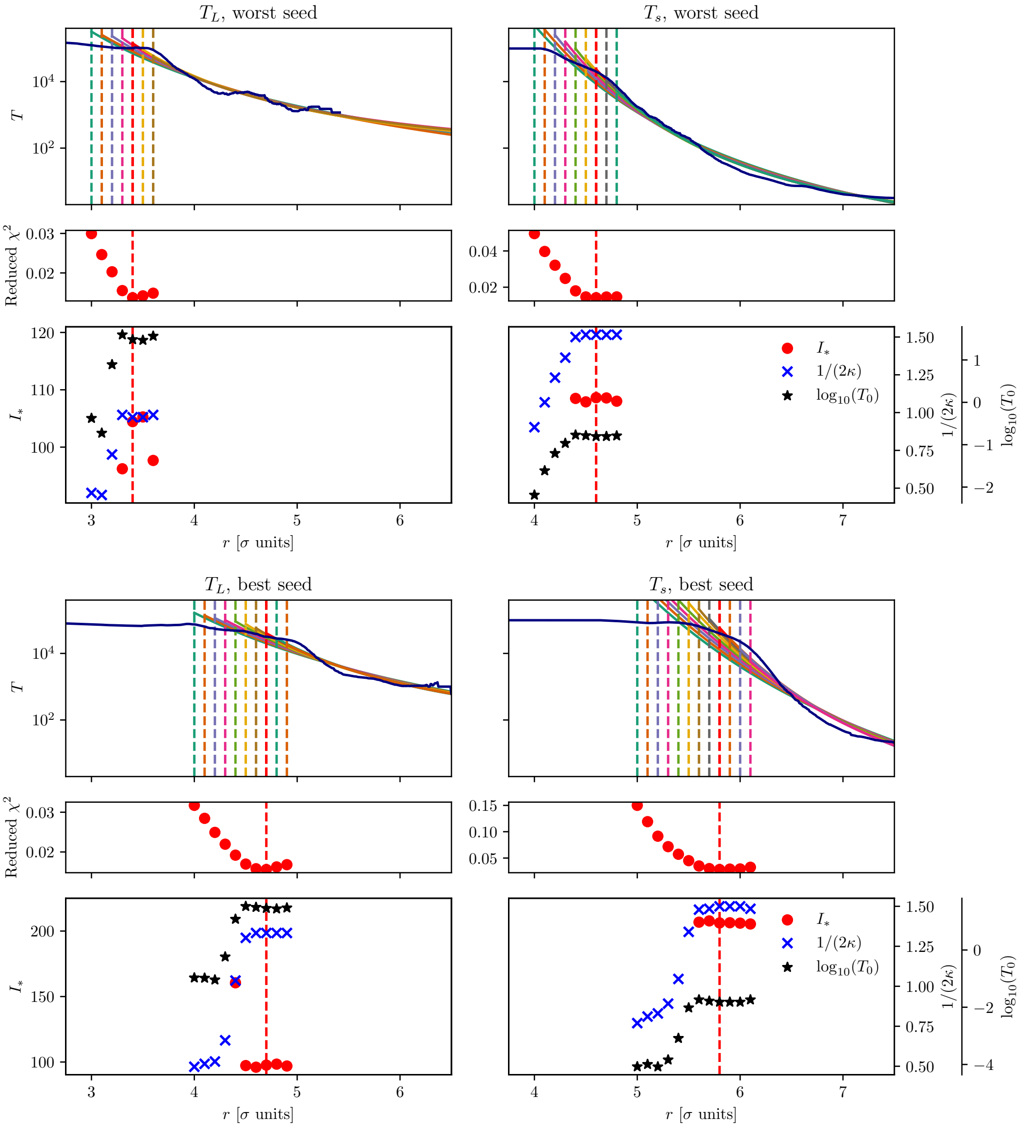

FIGURE 8.14: Results of the fit of T_L and T_s for two HL-LHC realizations (top row, worst seed with $\zeta_0 = 0.3\,\mathrm{m}$; bottom row, best seed with $\zeta_0 = 0.3\,\mathrm{m}$). Multiple slices of data are considered close to the transition point at which the data begins to manifest clear saturation due to the finite tracking time. The best fit is chosen by considering the minimum of the reduced χ^2 for the various data cuts considered. This minimum value is highlighted with a vertical red dashed line. The values of the fit parameters for the various cuts are also shown.

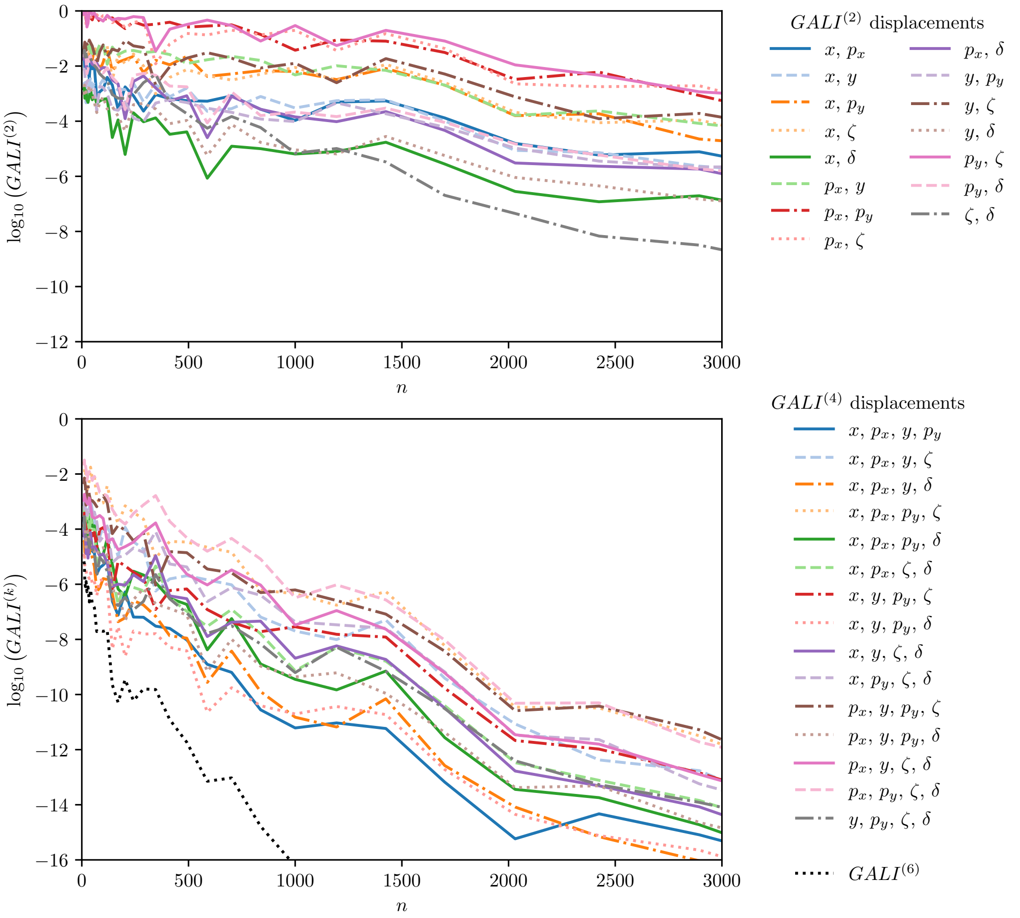

FIGURE 8.15: Mean value evolution of $GALI^{(2)}$ and $GALI^{(4)}$ for various displacement choices, and of $GALI^{(6)}$. An ensemble of 10 chaotic initial conditions with similar $FLI^{WB}(\hat{x})$ evaluated at $n = 10^5$ was considered. The mean value of the three $GALI$ indicators follow an exponential decay, which is in agreement with the expected behaviour for chaotic orbits. $GALI^{(4)}$ shows roughly double the decay rate of $GALI^{(2)}$. The displacement choice $(\hat{\zeta}, \hat{\delta})$ in $GALI^{(2)}$ has a decay rate faster than the other choices. (HL-LHC lattice used: worst seed, ζ_0 =0.3 m.)

Conclusions

In this thesis, we reviewed a novel diffusive framework for describing the long-term behaviour of the betatron motion in circular accelerators. The framework consists of a Fokker-Planck model with a diffusive coefficient having a functional form related to the stability-time estimate of the Nekhorohsev theorem. Such a framework has the purpose to provide better insights on the evolution of the beam distribution, as well as to provide a better understanding on the formation of beam halo and of the scaling laws governing beam losses.

To test the functional form of the diffusion coefficient, consistent with the stability time estimate of the Nekhoroshev theorem, we have proposed and scrutinized through detailed numerical simulations an optimal measurement protocol, which uses collimator scans with a specific pattern and timing. This protocol consists of separating the measured loss signal into a global current and a recovery current, and reconstructing the global current to normalize the recovery current. The performance of the protocol was simulated in various configurations and found to be capable of reconstructing the parameters of the diffusion coefficient with good accuracy, especially when performed in a phase-space region where the diffusion coefficient has an exponential evolution. The protocol was also shown to provide useful information on possible shortcomings in the data set used for the analysis, such as a high uncertainty band in the global current reconstruction or a reconstructed value of I_* that indicates that the probed phase space region is outside the optimal interval.

A variant of this protocol was then applied on existing LHC Run 2 collimator scan data, which were collected using a non-optimized protocol. Despite the non-ideal measurement protocol used, we were able to analyse BLM loss signals during collimator scans and obtain a promising reconstruction of recovery currents, indicating a behaviour that is compatible with a Nekhoroshev-like diffusive dynamics. To address missing information in the dataset, we adapted key features of our fitting procedure, leading to good reconstruction performance and insight into the global diffusive behaviour of the LHC beam halo. As some collimator scans carried out in the LHC 2022 run were performed using our proposed optimal protocol, we expect to be able to more accurately characterize non-linear diffusive behaviour, which will be the outcome of future work.

Another application of this general diffusive framework was the analysis of the long-term effects of beam-beam wire compensators on beam losses. The promising results obtained in the various fit reconstructions provided, in general, positive insight on the beam-halo dynamics, suggesting that the wires do not have unwanted side effects on the beam dynamics and that our diffusive model might be a promising tool to assess these long-term effects. Here, as well, future studies will be performed using the recent data collected during the 2022 LHC run, which were collected using a better approach that allows keeping under control the beam-halo evolution.

Regarding the domain of single-particle effects, we considered the analysis of the performance of dynamic indicators aimed at detecting chaotic behaviour in the orbits of symplectic dynamical systems. After measuring the classification performance of various indicators on a modulated Hénon map, we have determined which are the best performing ones, in terms of correctly assessing the chaotic character of an orbit using a minimal number of turns. On the basis of the findings of these studies, the best indicators have been applied to the study of the beam dynamics in realistic magnetic lattices of the LHC luminosity upgrade.

This analysis provided some interesting elements on the connection between Nekhoroshev scaling laws for stability times and the presence of large chaotic regions in the phase space, in terms of Lyapunov time, measured by means of the FLI^{WB} dynamic indicator. In fact, it has been possible to show that both the stability time and the Lyapunov time follow the same Nekhoroshev-like scaling law, although with different model parameters. Moreover, the $GALI$ dynamic indicator was used to first inspect its time dependence for chaotic orbits, while the analysis of the geometry of the orbits is a topic of future studies.

In general, the less known dynamic indicators explored in these studies provided interesting results that are worthy of further inspection and will eventually be included in the toolbox of an accelerator physicist.

The research line presented in this thesis still requires more steps and developments to be considered fully complete. As we look forward to the present and future measurement opportunities offered at the CERN LHC, we hope to be able to confirm and consolidate the initial promising results achieved here.

Collimator scans performed following our requirement, as well as new beam-beam wire compensator measurements, will provide new data to be studied and used to assess the consistency of our proposed diffusive framework. This, along with further developments, shall provide better insights into the complex topic of non-linear beam dynamics and beam-halo formation.

Bibliography

[1] O. S. Brüning *et al. LHC Design Report*. CERN Yellow Reports: Monographs. Geneva: CERN, 2004. doi: 10.5170/CERN-2004-003-V-1.

[2] I. Béjar Alonso *et al. High-Luminosity Large Hadron Collider (HL–LHC): Technical design report*. Ed. by I. Béjar Alonso. CERN Yellow Reports: Monographs. Geneva: CERN, 2020. doi: 10.23731/CYRM-2020-0010.

[3] G. Arduini *et al.* "High Luminosity LHC: challenges and plans". *Journal of Instrumentation* 11(12) (Dec. 2016), p. C12081. doi: 10.1088/1748-0221/11/12/C12081.

[4] M. Benedikt *et al.* "FCC-hh: The Hadron Collider. Future Circular Collider Conceptual Design Report Volume 3". *The European Physical Journal Special Topics* 228(4) (Dec. 2019), pp. 755–1107. doi: 10.1140/epjst/e2019-900087-0.

[5] A. I. Neishtadt. "Probability phenomena due to separatrix crossing". *Chaos: An Interdisciplinary Journal of Nonlinear Science* 1(1) (1991), pp. 42–48. doi: 10.1063/1.165816.

[6] A. Bazzani, O. Mazzarisi, M. Giovannozzi, and E. Maclean. "Diffusion in stochastically perturbed Hamiltonian systems with applications to the recent LHC dynamic aperture experiments". *Proceedings, 2017 Nonlinear Dynamics and Collective Effects (NOCE) workshop on Particle Beam Physics: Arcidosso, Italy, 19 – 22 September 2017*. Ed. by S. Chattopadhyay, M. Cornacchia, and S. Di Mitri. WSP, 2019, pp. 70–85. doi: 10.1142/9789813279612_0005.

[7] A. Bazzani, M. Giovannozzi, and E. Maclean. "Analysis of the non-linear beam dynamics at top energy for the CERN Large Hadron Collider by means of a diffusion model". *Eur. Phys. J. Plus* 135(1) (2020), p. 77. doi: 10.1140/epjp/s13360-020-00123-2.

[8] L. Burnod, G. Ferioli, and J. B. Jeanneret. *Drift speed measurements of the halo in the SPS collider*. Tech. rep. Geneva: CERN, 1990. url: http://cds.cern.ch/record/205343.

[9] G. Stancari. *Diffusion model for the time evolution of particle loss rates in collimator scans: a method for measuring stochastic transverse beam dynamics in circular accelerators*. arXiv:1108.5010 [physics.acc-ph]. 2011. doi: 10.48550/ARXIV.1108.5010.

[10] G. Stancari *et al.* “Measurements of Transverse Beam Diffusion Rates in the Fermilab Tevatron Collider”. *Proc. IPAC’11* (San Sebastian, Spain, Sep. 2011). JACoW Publishing, Geneva, Switzerland, pp. 1882–1884. URL: `https://jacow.org/IPAC2011/papers/TUPZ033.pdf`.

[11] T. Sen. “Anomalous beam diffusion near beam-beam synchrobetatron resonances”. *Phys. Rev. ST Accel. Beams* 15 (10 Oct. 2012), p. 101001. DOI: `10.1103/PhysRevSTAB.15.101001`.

[12] G. Stancari *et al.* “Measurements of the effect of collisions on transverse beam halo diffusion in the Tevatron and in the LHC” (2014), 83–86. 4 p. DOI: `10.5170/CERN-2014-004.83`.

[13] M. Meddahi. “Effets faisceau-faisceau dans le collisionneur protons-antiprotons du SPS”. 1991. URL: `http://cds.cern.ch/record/223301`.

[14] T. Chen *et al.* “Measurements of a Hamiltonian system and their description by a diffusive model”. *Phys. Rev. Lett.* 68 (1 Jan. 1992), pp. 33–36. DOI: `10.1103/PhysRevLett.68.33`.

[15] A. Gerasimov. “The applicability of diffusion phenomenology to particle losses in hadron colliders”. *AIP Conference Proceedings* 292(1) (1992), pp. 375–384. DOI: `10.1063/1.45124`.

[16] K.-H. Mess and M. Seidel. “Collimators as diagnostic tools in the proton machine of HERA”. *Nucl. Instrum. Meth. A* 351(2) (1994), pp. 279–285. ISSN: 0168-9002. DOI: `10.1016/0168-9002(94)91354-4`.

[17] F. Zimmermann. “Transverse proton diffusion”. *Part. Accel.* 49(SLAC-PUB-6634) (1994), pp. 67–104. URL: `http://cds.cern.ch/record/274807`.

[18] T. Sen and J. A. Ellison. “Diffusion due to Beam-Beam Interaction and Fluctuating Fields in Hadron Colliders”. *Phys. Rev. Lett.* 77 (6 Aug. 1996), pp. 1051–1054. DOI: `10.1103/PhysRevLett.77.1051`.

[19] Y. Papaphilippou and F. Zimmermann. “Estimates of diffusion due to long-range beam-beam collisions”. *Phys. Rev. ST Accel. Beams* 5 (7 July 2002), p. 074001. DOI: `10.1103/PhysRevSTAB.5.074001`.

[20] R. F. III *et al.* “Beam Diffusion Measurements at RHIC”. *Proc. PAC’03* (Portland, OR, USA). JACoW Publishing, Geneva, Switzerland, 2003, pp. 2904–2906. DOI: `10.1109/PAC.2003.1289761`.

[21] N. Nekhoroshev. “An exponential estimate of the time of stability of nearly-integrable Hamiltonian systems”. *Russ. Math. Surv.* 32(6) (Dec. 1977), p. 1. doi: `10.1070/rm1977v032n06abeh003859`.

[22] A. Bazzani, S. Marmi, and G. Turchetti. “Nekhoroshev estimate for isochronous non resonant symplectic maps”. *Cel. Mech.* 47(4) (1990), p. 333. issn: 1572-9478. doi: `10.1007/BF00051010`.

[23] G. Turchetti. “Nekhoroshev Stability Estimates for Symplectic Maps and Physical Applications”. *Number Theory and Physics*. Ed. by J.-M. Luck, P. Moussa, and M. Waldschmidt. Vol. 47. Springer Proceedings in Physics. Berlin, Heidelberg: Springer Berlin Heidelberg, 1990, pp. 223–234. isbn: 978-3-642-75405-0. doi: `10.1007/978-3-642-75405-0_24`.

[24] C. Froeschlé, R. Gonczi, and E. Lega. “The fast Lyapunov indicator: a simple tool to detect weak chaos. Application to the structure of the main asteroidal belt”. *Planetary and Space Science* 45(7) (1997), pp. 881–886. issn: 0032-0633. doi: `https://doi.org/10.1016/S0032-0633(97)00058-5`.

[25] J. Szezech, S. Lopes, and R. Viana. “Finite-time Lyapunov spectrum for chaotic orbits of non-integrable Hamiltonian systems”. *Phys. Lett. A* 335(5) (2005), pp. 394–401. issn: 0375-9601. doi: `https://doi.org/10.1016/j.physleta.2004.12.058`.

[26] J. Laskar. “Introduction to Frequency Map Analysis”. *Hamiltonian Systems with Three or More Degrees of Freedom*. Ed. by C. Simó. Springer. Dordrecht: Springer, 1999, pp. 134–150. doi: `10.1007/978-94-011-4673-9`.

[27] J. Laskar. “Frequency map analysis and quasiperiodic decompositions”. *arXiv: Dynamical Systems* (2003). doi: `10.48550/arXiv.math/0305364`.

[28] F. Panichi, L. Ciotti and G. Turchetti. “Fidelity and reversibility in the restricted three body problem”. *Communications in Nonlinear Science and Numerical Simulation* 35 (2016), pp. 53–68. issn: 1007-5704. doi: `http://dx.doi.org/10.1016/j.cnsns.2015.10.016`.

[29] F. Panichi, K. Goździewski and G. Turchetti. “The reversibility error method (REM): a new, dynamical fast indicator for planetary dynamics”. *MNRAS* 468(1) (June 2017), pp. 469–491. issn: 0035-8711. doi: `10.1093/mnras/stx374`.

[30] Ch. Skokos, T. Bountis, Ch. Antonopoulos. "Geometrical properties of local dynamics in Hamiltonian systems: The Generalized Alignment Index (GALI) method". *Physica D* 231 (2007), p. 3054.

[31] Ch. Skokos and T. Manos. *The Smaller (SALI) and the Generalized (GALI) Alignment Indices: Efficient Methods of Chaos Detection*. Ed. by Skokos, Charalampos (Haris) and Gottwald, Georg A. and Laskar, Jacques. Berlin, Heidelberg: Springer Berlin Heidelberg, 2016, pp. 129–181. isbn: 978-3-662-48410-4. doi: `10.1007/978-3-662-48410-4_5`.

[32] V. Arnol'd, V. Kozlov, and A. Neishtadt. *Mathematical aspects of classical and celestial mechanics. Dynamical systems III; 3rd rev. version*. Vol. 3. Encyclopaedia of mathematical sciences. Heidelberg: Springer, 2006. doi: `10.1007/978-3-540-48926-9`.

[33] A. N. Kolmogorov. "On the Conservation of Conditionally Periodic Motions under Small Perturbation of the Hamiltonian". *Dokl. Akad. Nauk SSR* 98 (1954), p. 527.

[34] J. Moser. "On invariant curves of area-preserving mappings of an annulus". *Nachr. Akad. Wiss. Göttingen Math.-Phys. Kl.* II (1962), p. 1. url: `https://cds.cern.ch/record/430015`.

[35] V. Arnold. "Proof of a theorem of A.N. Kolmogorov on the preservation of conditionally periodic motions under a small perturbation of the Hamiltonian". *Russ. Math. Surv.* 18 (1963). Ed. by A. B. Givental *et al.*, p. 9. doi: `10.1007/978-3-642-01742-1_21`.

[36] N. N. Nehorosev. "Stable Lower Estimates for Smooth Mappings and for Gradients of Smooth Functions". *Mathematics of the USSR-Sbornik* 19(3) (Apr. 1973), p. 425. doi: `10.1070/SM1973v019n03ABEH001788`.

[37] L. Niederman. "Hamiltonian stability and subanalytic geometry". en. *Annales de l'Institut Fourier* 56(3) (2006), pp. 795–813. doi: `10.5802/aif.2200`.

[38] M. Guzzo. "An Overview on the Nekhoroshev Theorem". *Topics in Gravitational Dynamics: Solar, Extra-Solar and Galactic Systems*. Ed. by D. Benest, C. Froeschle, and E. Lega. Berlin, Heidelberg: Springer Berlin Heidelberg, 2007, pp. 1–28. isbn: 978-3-540-72984-6. doi: `10.1007/978-3-540-72984-6_1`.

[39] G. D. Birkhoff. "Proof of Poincaré's Geometric Theorem". *Transactions of the American Mathematical Society* 14(1) (1913), pp. 14–22. issn: 00029947. url: `http://www.jstor.org/stable/1988766`.

[40] A. Bazzani, G. Servizi, E. Todesco, and G. Turchetti. *A normal form approach to the theory of nonlinear betatronic motion*. CERN Yellow Reports: Monographs. Geneva: CERN, 1994. doi: `10.5170/CERN-1994-002`.

[41] A. Bazzani, S. Siboni, and G. Turchetti. "Diffusion in Hamiltonian systems with a small stochastic perturbation". *Physica D: Nonlinear Phenomena* 76(1) (1994), pp. 8–21. issn: 0167-2789. doi: `https://doi.org/10.1016/0167-2789(94)90246-1`.

[42] J. Crank and P. Nicolson. "A practical method for numerical evaluation of solutions of partial differential equations of the heat-conduction type". *Mathematical Proceedings of the Cambridge Philosophical Society*. Vol. 43. Cambridge University Press. 1947, pp. 50–67. doi: `10.1017/S0305004100023197`.

[43] S. Y. Lee. *Accelerator physics; 4th ed.* Singapore: World Scientific, 2019. doi: `10.1142/11111`.

[44] H. Wiedemann. *Particle accelerator physics*. Springer Nature, 2015.

[45] J. D. Jackson. *Classical electrodynamics*. 1999.

[46] A. Wolski. *Beam Dynamics in High Energy Particle Accelerators*. Imperial College Press, 2014. doi: `10.1142/p899`.

[47] M. Sands. *Physics of Electron Storage Rings: an Introduction*. Tech. rep. Stanford Linear Accelerator Center, Calif., 1970.

[48] W. Herr and E. Forest. "Non-linear Dynamics in Accelerators". *Particle Physics Reference Library : Volume 3: Accelerators and Colliders*. Ed. by S. Myers and H. Schopper. Cham: Springer International Publishing, 2020, pp. 51–104. isbn: 978-3-030-34245-6. doi: `10.1007/978-3-030-34245-6_3`.

[49] E. Wilson. "Nonlinear resonances" (May 1986). doi: `10.5170/CERN-1987-003-V-1.41`.

[50] G. Guignard. *The general theory of all sum and difference resonances in a three-dimensional magnetic field in a synchrotron*. CERN Yellow Reports: Monographs. Geneva: CERN, 1976. doi: `10.5170/CERN-1976-006`.

[51] M. Benedikt *et al. LHC Design Report*. Geneva: CERN, 2004.

[52] R. De Maria *et al. SixTrack – 6D Tracking Code*. Available at http://sixtrack.web.cern.ch/SixTrack/.

[53] M. Hénon. "Numerical study of quadratic area-preserving mappings". *Q. Appl. Math.* 27 (1969), p. 291. doi: `10.1090/qam/253513`.

[54] E. Todesco and M. Giovannozzi. "Dynamic aperture estimates and phase-space distortions in nonlinear betatron motion". *Phys. Rev. E* 53(4) (4 Apr. 1996), pp. 4067–4076. DOI: `10.1103/PhysRevE.53.4067`.

[55] M. Giovannozzi, W. Scandale, and E. Todesco. "Dynamic aperture extrapolation in presence of tune modulation". *Phys. Rev.* E57(3) (3 Mar. 1998), p. 3432. DOI: `10.1103/PhysRevE.57.3432`.

[56] F. V. der Veken *et al.* "Determination of the Phase-Space Stability Border with Machine Learning Techniques". *Proc. IPAC'22* (Bangkok, Thailand). International Particle Accelerator Conference 13. JACoW Publishing, Geneva, Switzerland, July 2022, MOPOST047, pp. 183–186. ISBN: 978-3-95450-227-1. DOI: `10.18429/JACoW-IPAC2022-MOPOST047`.

[57] A. Bazzani *et al.* "Advances on the modeling of the time evolution of dynamic aperture of hadron circular accelerators". *Phys. Rev. Accel. Beams* 22 (10 Oct. 2019), p. 104003. DOI: `10.1103/PhysRevAccelBeams.22.104003`.

[58] M. Giovannozzi and F. F. Van der Veken. "Description of the luminosity evolution for the CERN LHC including dynamic aperture effects. Part I: the model". *Nucl. Instrum. Methods Phys. Res.* A905 (2018), pp. 171–179. DOI: `10.1016/j.nima.2019.01.072`.

[59] M. Giovannozzi and F. F. Van der Veken. "Description of the luminosity evolution for the CERN LHC including dynamic aperture effects. Part II: application to Run 1 data". *Nucl. Instrum. Methods Phys. Res.* A908 (2018), pp. 1–9. DOI: `10.1016/j.nima.2018.08.019`.

[60] R. M. Corless *et al.* "On the LambertW function". *Advances in Computational Mathematics* 5(1) (Dec. 1996), pp. 329–359. ISSN: 1572-9044. DOI: `10.1007/BF02124750`.

[61] G. Iadarola and F. Van Der Veken. *Xsuite physics reference manual.* 2022. URL: `https://github.com/xsuite/xsuite/blob/main/docs/physics_manual/physics_man.pdf` (visited on 01/31/2023).

[62] C. E. Montanari, A. Bazzani, and M. Giovannozzi. "Probing the diffusive behaviour of beam-halo dynamics in circular accelerators". *Eur. Phys. J. Plus* 137(11) (2022), p. 1264. DOI: `10.1140/epjp/s13360-022-03478-w`.

[63] G. Valentino *et al.* "Beam diffusion measurements using collimator scans in the LHC". *Phys. Rev. ST Accel. Beams* 16 (2 Feb. 2013), p. 021003. DOI: `10.1103/PhysRevSTAB.16.021003`.

[64] A. Gorzawski *et al.* "Probing LHC halo dynamics using collimator loss rates at 6.5 TeV". *Phys. Rev. Accel. Beams* 23 (4 Apr. 2020), p. 044802. doi: `10.1103/PhysRevAccelBeams.23.044802`.

[65] G. Valentino *et al. End-of-Fill Diffusion and Halo Population Measurements with Physics Beams at 6.5 TeV*. Tech. rep. CERN-ACC-NOTE-2017-0049. July 2017.

[66] C. E. Montanari, A. Bazzani, and M. Giovannozzi. "Diffusive Models for Nonlinear Beam Dynamics". *Proc. IPAC'21* (Campinas, SP, Brazil). International Particle Accelerator Conference 12. JACoW Publishing, Geneva, Switzerland, Aug. 2021, TUPAB233, pp. 1976–1979. isbn: 978-3-95450-214-1. doi: `10.18429/JACoW-IPAC2021-TUPAB233`.

[67] C. E. Montanari *et al.* "Testing the Global Diffusive Behaviour of Beam-Halo Dynamics at the CERN LHC Using Collimator Scans". *Proc. IPAC'22* (Bangkok, Thailand). International Particle Accelerator Conference 13. JACoW Publishing, Geneva, Switzerland, July 2022, pp. 172–175. isbn: 978-3-95-450227-1. doi: `10.18429/JACoW-IPAC2022-MOPOST043`.

[68] J. W. Thomas. *Numerical partial differential equations: finite difference methods*. Vol. 22. Springer Science & Business Media, 2013. doi: `10.1007/978-1-4899-7278-1`.

[69] R. Hannes and F. Till. *The Fokker-Planck Equation. Methods of Solution and Applications*. Berlin, Heidelberg: Springer, 1996. doi: `10.1007/978-3-642-61544-3`.

[70] T. A. Collaboration *et al.* "The ATLAS Experiment at the CERN Large Hadron Collider". *Journal of Instrumentation* 3(08) (Aug. 2008), S08003. doi: `10.1088/1748-0221/3/08/S08003`.

[71] B. Alessandro *et al. ALICE: Physics Performance Report. ALICE physics performance : Technical Design Report*. Ed. by B. Alessandro. Vol. 32. Technical design report. ALICE. Geneva: CERN, 2005. doi: `10.1088/0954-3899/32/10/001`.

[72] S. Chatrchyan *et al.* "The CMS experiment at the CERN LHC. The Compact Muon Solenoid experiment". *JINST* 3 (2008), S08004. doi: `10.1088/1748-0221/3/08/S08004`.

[73] A. A. Alves *et al.* "The LHCb Detector at the LHC". *JINST* 3 (2008), S08005. doi: `10.1088/1748-0221/3/08/S08005`.

[74] G. AZZOPARDI, B. SALVACHUA, and G. VALENTINO. "Data-driven cross-talk modeling of beam losses in LHC collimators". *Phys. Rev. Accel. Beams* 22(8) (2019), p. 083002. DOI: `10.1103/PhysRevAccelBeams.22.083002`.

[75] R. ASSMANN *et al.* "LHC Collimation: Design and Results from Prototyping and Beam Tests". *Proceedings of the 2005 Particle Accelerator Conference*. 2005, pp. 1078–1080. DOI: `10.1109/PAC.2005.1590664`.

[76] R. W. ASSMANN *et al.* "The final collimation system for the LHC" (2006). URL: `https://cds.cern.ch/record/972336`.

[77] R. BRUCE *et al.* "Reaching record-low β^* at the CERN Large Hadron Collider using a novel scheme of collimator settings and optics". *Nucl. Instrum. Methods Phys. Res. A* 848 (Jan. 2017), pp. 19–30. DOI: `http://dx.doi.org/10.1016/j.nima.2016.12.039`.

[78] R. BRUCE *et al.* "Sources of machine-induced background in the ATLAS and CMS detectors at the CERN Large Hadron Collider". *Nucl. Instrum. Methods Phys. Res., A* 729 (2013), pp. 825–840. DOI: `10.1016/j.nima.2013.03.058`.

[79] R. BRUCE *et al.* "Collimation-induced experimental background studies at the CERN Large Hadron Collider". *Phys. Rev. Accel. Beams* 22(2) (2019), p. 021004. DOI: `10.1103/PhysRevAccelBeams.22.021004`.

[80] A. BERTARELLI *et al.* "The Mechanical Design for the LHC Collimators" (2004). URL: `https://cds.cern.ch/record/794628`.

[81] R. BRUCE *et al.* "Simulations and measurements of beam loss patterns at the CERN Large Hadron Collider". *Physical Review Special Topics – Accelerators and Beams* 17(8) (2014), p. 081004.

[82] P. D. HERMES. "Heavy-Ion Collimation at the Large Hadron Collider: Simulations and Measurements". 2016. URL: `https://cds.cern.ch/record/2241364`.

[83] J. B. JEANNERET. "Optics of a two-stage collimation system". *Phys. Rev. Spec. Top. Accel. Beams* 1 (1998), p. 081001. DOI: `10.1103/PhysRevSTAB.1.081001`.

[84] H. WIEDEMANN. "Wake Fields and Instabilities". *Particle Accelerator Physics*. Berlin, Heidelberg: Springer Berlin Heidelberg, 2007, pp. 671–727. ISBN: 978-3-540-49045-6. DOI: `10.1007/978-3-540-49045-6_19`.

[85] N. MOUNET. "The LHC Transverse Coupled-Bunch Instability". 2012. DOI: `10.5075/epfl-thesis-5305`.

[86] S. Antipov *et al.* "Low-Impedance Collimators for HL-LHC" (2018), WEYGBE4. doi: `10.18429/JACoW-IPAC2018-WEYGBE4`.

[87] B. Dehning. "Beam Loss Monitors at LHC". *CERN Yellow Reports* 2(0) (2016), p. 303. url: `https://e-publishing.cern.ch/index.php/CYR/article/view/238`.

[88] C. Zamantzas *et al.* "The LHC beam loss monitoring system's data contribution to other systems". *IEEE Nuclear Science Symposium Conference Record*. Honolulu, HI, 2007, pp. 2331–2335.

[89] A. Gorzawski and M. Giovannozzi. *Determination of BLM conversion factors for collimators scans*. in preparation. 2022.

[90] J. C. Denard. "Beam current monitors" (2009). doi: `10.5170/CERN-2009-005.141`.

[91] *LHC Beam Loss Monitoring system homepage*. url: `https://ab-div-bdi-bl-blm.web.cern.ch/` (visited on 01/31/2023).

[92] G. Valentino *et al.* "Semiautomatic beam-based LHC collimator alignment". *Physical Review Special Topics-Accelerators and Beams* 15(5) (2012), p. 051002.

[93] C. Zamantzas *et al.* "An FPGA Based Implementation for Real-Time Processing of the LHC Beam Loss Monitoring System's Data". *2006 IEEE Nuclear Science Symposium Conference Record*. Vol. 2. 2006, pp. 950–954. doi: `10.1109/NSSMIC.2006.356003`.

[94] *Running Sum (RS) definition table for the LHC Beam Loss Monitoring system*. url: `https://ab-div-bdi-bl-blm.web.cern.ch/Acquisition_system/Data_acquisition_integration_durations_20100313.htm` (visited on 01/31/2023).

[95] R. Tomás, M. Aiba, A. Franchi, and U. Iriso. "Review of linear optics measurement and correction for charged particle accelerators". *Phys. Rev. Accel. Beams* 20 (5 May 2017), p. 054801. doi: `10.1103/PhysRevAccelBeams.20.054801`.

[96] W. Herr and B. Muratori. "Concept of luminosity" (2006). doi: `10.5170/CERN-2006-002.361`.

[97] J.-P. Koutchouk. *Principle of a correction of the long-range beam-beam effect in LHC using electromagnetic lenses*. Tech. rep. Geneva: CERN, 2000. url: `http://cds.cern.ch/record/692058`.

[98] R. Calaga, W. Fischer, G. Robert-Demolaize, and N. Milas. "Long-range beam-beam experiments in the Relativistic Heavy Ion Collider". *Phys. Rev. ST Accel. Beams* 14 (9 Sept. 2011), p. 091001. DOI: `10.1103/PhysRevSTAB.14.091001`.

[99] C. Milardi *et al. Dafne Lifetime Optimization with Compensating Wires and Octupoles*. 2008. DOI: `10.48550/ARXIV.0803.1544`.

[100] F. Zimmermann. "10 Years of wire excitation experiments in the CERN SPS" (2014), pp. 153–166. DOI: `10.5170/CERN-2014-004.153`.

[101] J.-P. Koutchouk, J. Wenninger, and F. Zimmermann. "Experiments on LHC Long-Range Beam-Beam Compensation in the CERN SPS" (2004). URL: `https://cds.cern.ch/record/793423`.

[102] S. Fartoukh, A. Valishev, Y. Papaphilippou, and D. Shatilov. "Compensation of the long-range beam-beam interactions as a path towards new configurations for the High Luminosity LHC". *Phys. Rev. Spec. Top. Accel. Beams* 18 (2015), p. 121001. DOI: `10.1103/PhysRevSTAB.18.121001`.

[103] D. Pellegrini, S. Fartoukh, N. Karastathis, and Y. Papaphilippou. "Multiparametric response of the HL-LHC Dynamic Aperture in presence of beam-beam effects". *Journal of Physics: Conference Series* 874(1) (July 2017), p. 012007. DOI: `10.1088/1742-6596/874/1/012007`.

[104] D. Banfi, J. Barranco Garcia, T. Pieloni, and A. Valishev. "Weak-strong beam-beam simulations for HL-LHC" (2014). URL: `https://cds.cern.ch/record/1742126`.

[105] A. Poyet *et al. First Experimental Evidence of a Beam-Beam Long-Range Compensation Using Wires in the Large Hadron Collider*. 2022. DOI: `10.48550/ARXIV.2203.08066`.

[106] A. Goldblatt *et al.* "Design and Performance of Coronagraph for Beam Halo Measurements in the LHC" (2017), MOPG74. DOI: `10.18429/JACoW-IBIC2016-MOPG74`.

[107] L. Rossi and O. Brüning. "Progress with the High Luminosity LHC project at CERN" (2019), MOYPLM3. DOI: `10.18429/JACoW-IPAC2019-MOYPLM3`.

[108] A. Poyet *et al.* "MD3263: Beam-Beam Long-Range Compensation using DC Wires in the LHC" (2019). URL: `https://cds.cern.ch/record/2703503`.

[109] B. Salvachua and F. Follin. *Update on BLM Beam Lifetime*. Oct. 2017. url: `https://indico.cern.ch/event/670013/contributions/2740764/attachments/1534174/2402701/BSalvachua-BeamLifetime.pdf` (visited on 01/31/2023).

[110] B. Dehning *et al.* "LHC beam loss detector design: Simulation and measurements". *2007 IEEE Particle Accelerator Conference (PAC)*. 2007, pp. 4198–4200. doi: `10.1109/PAC.2007.4439981`.

[111] G. Sterbini *et al. MD8043 – Beam-beam wire compensation*. 2022. url: `https://asm.cern.ch/md-planning/lhc-requests/8043` (visited on 01/31/2023).

[112] C. L. Siegel and J. Moser. *Lectures in celestial mechanics*. Berlin, Germany: Berlin Springer Verlag, 1971.

[113] H. Kandrup, C. Siopis, G. Contopoulos, and R. Dvorak. "Diffusion and scaling in escapes from two-degrees-of-freedom Hamiltonian systems." *Chaos* 9 2 (2 1999), pp. 381–392. doi: `10.1063/1.166415`.

[114] D. Turaev. "Polynomial approximations of symplectic dynamics and richness of chaos in non-hyperbolic area-preserving maps". *Nonlinearity* 16(1) (Nov. 2002), p. 123. doi: `10.1088/0951-7715/16/1/308`.

[115] G. Turchetti, F. Panichi, S. Sinigardi, and S. Vaienti. "Errors, Correlations and Fidelity for noisy Hamilton flows. Theory and numerical examples". *Journal of Physics A: Mathematical and Theoretical* 50 (Sept. 2015). doi: `10.1088/1751-8121/aa5192`.

[116] C. Skokos, T. Bountis, and C. Antonopoulos. "Detecting chaos, determining the dimensions of tori and predicting slow diffusion in Fermi–Pasta–Ulam lattices by the Generalized Alignment Index method". *The European Physical Journal Special Topics* 165(1) (Dec. 2008), pp. 5–14. issn: 1951-6401. doi: `10.1140/epjst/e2008-00844-2`.

[117] S. Das, Y. Saiki, E. Sander, and J. A. Yorke. "Quantitative quasiperiodicity". *Nonlinearity* 30(11) (Oct. 2017), pp. 4111–4140. doi: `10.1088/1361-6544/aa84c2`.

[118] J. A. Núñez, P. M. Cincotta, and F. C. Wachlin. "Information entropy". *Celestial Mechanics and Dynamical Astronomy* 64(1) (Mar. 1, 1996), pp. 43–53. doi: `10.1007/BF00051604`.

[119] K. Goździewski, E. Bois, A. J. Maciejewski, and L. Kiseleva-Eggleton. "Global dynamics of planetary systems with the MEGNO criterion". *A&A* 378 (2001), pp. 569–586. doi: `10.1051/0004-6361:20011189`.

[120] M. F. Mestre, P. M. Cincotta, and C. M. Giordano. "Analytical relation between two chaos indicators: FLI and MEGNO". *MNRAS* 414 (2011), pp. L100–L103. doi: `10.1111/j.1745-3933.2011.01065.x`.

[121] J. Laskar. "Frequency map analysis of an Hamiltonian system". *AIP conference proceedings*. Vol. 344. 1. American Institute of Physics. 1995, pp. 130–159. doi: `10.1063/1.48978`.

[122] Y. Papaphilippou, L. Farvacque, J. Laskar, and A. Ropert. "Probing the Non-Linear Dynamics of the ESRF Storage Ring with Experimental Frequency Maps". *Proceedings of the 2003 Particle Accelerator Conference*. Vol. 1. IEEE. 2003, pp. 3189–3191. doi: `10.1109/PAC.2003.1289857`.

[123] L. Nadolski and J. Laskar. "Review of single particle dynamics for third generation light sources through frequency map analysis". *Phys. Rev. ST Accel. Beams* 6 (11 Nov. 2003), p. 114801. doi: `10.1103/PhysRevSTAB.6.114801`.

[124] T. Shun-Qiang *et al.* "Nonlinear optimization of the modern synchrotron radiation storage ring based on frequency map analysis". *Chinese Physics C* 33(2) (2009), p. 127. doi: `10.1088/1674-1137/33/2/011`.

[125] D. Shatilov, E. Levichev, E. Simonov, and M. Zobov. "Application of frequency map analysis to beam-beam effects study in crab waist collision scheme". *Phys. Rev. ST Accel. Beams* 14 (1 Jan. 2011), p. 014001. doi: `10.1103/PhysRevSTAB.14.014001`.

[126] Y. Papaphilippou. "Detecting chaos in particle accelerators through the frequency map analysis method". *Chaos* 24(2) (2014), p. 024412. doi: `10.1063/1.4884495`.

[127] T. Tydecks *et al.* "FCC-ee Dynamic Aperture Studies and Frequency Map Analysis". *Proc. IPAC'18* (Vancouver, Canada, Apr.-May 2018). JACoW Publishing, Geneva, Switzerland, pp. 244–246. doi: `10.18429/JACoW-IPAC2018-MOPMF057`.

[128] P. Zisopoulos, Y. Papaphilippou, and J. Laskar. "Refined betatron tune measurements by mixing beam position data". *Phys. Rev. Accel. Beams* 22 (7 July 2019), p. 071002. doi: `10.1103/PhysRevAccelBeams.22.071002`.

[129] E. Lega and C. Froeschlé. “Numerical investigations of the structure around an invariant KAM torus using the frequency map analysis”. *Physica D: Nonlinear Phenomena* 95(2) (1996), pp. 97–106. doi: `10.1016/0167-2789(96)00046-2`.

[130] Y. Papaphilippou and J. Laskar. “Frequency map analysis and global dynamics in a galactic potential with two degrees of freedom.” *Astronomy and Astrophysics* 307 (1996). Ed. by C. Simó, pp. 427–449. doi: `10.1007/978-94-011-4673-9_70`.

[131] Y. Papaphilippou and J. Laskar. “Global dynamics of triaxial galactic models through frequency map analysis”. *Astronomy and Astrophysics* 329 (1998), pp. 451–481.

[132] Y. Papaphilippou. “Global Dynamics of a Galactic Potential via Frequency Map Analysis”. *Hamiltonian Systems with Three or More Degrees of Freedom*. Ed. by C. Simó. Dordrecht: Springer Netherlands, 1999, pp. 523–527. isbn: 978-94-011-4673-9. doi: `10.1007/978-94-011-4673-9_70`.

[133] J. Laskar. “Application of frequency map analysis”. *The Chaotic Universe: Proceedings of the Second ICRA Network Workshop, Rome, Pescara, Italy, 1-5 February 1999*. Vol. 10. World Scientific. 2000, p. 115. doi: `10.1142/9789812793621_0006`.

[134] M. Comunian *et al.* “Frequency map analysis of a three-dimensional particle in the core model of a high intensity linac”. *Phys. Rev. ST Accel. Beams* 4 (12 Dec. 2001), p. 124201. doi: `10.1103/PhysRevSTAB.4.124201`.

[135] J. Laskar. “Frequency map analysis and particle accelerators”. *Proceedings of the 2003 Particle Accelerator Conference*. Vol. 1. 2003, 378–382 Vol.1. doi: `10.1109/PAC.2003.1288929`.

[136] J. Pöschel. “The concept of integrability on cantor sets for Hamiltonian systems”. *Celestial mechanics* 28(1) (Sept. 1982), pp. 133–139. issn: 1572-9478. doi: `10.1007/BF01230665`.

[137] J. Laskar, C. Froeschlé, and A. Celletti. “The measure of chaos by the numerical analysis of the fundamental frequencies. Application to the standard mapping”. *Physica D: Nonlinear Phenomena* 56(2-3) (May 1992), pp. 253–269. doi: `10.1016/0167-2789(92)90028-L`.

[138] R. Bartolini *et al.* “Precise measurement of the betatron tune”. *Part. Accel.* 55 (1996), pp. 1–10. url: `https://cds.cern.ch/record/316949`.

[139] R. Bartolini and F. Schmidt. *A computer code for frequency analysis of non-linear betatron motion*. Tech. rep. CERN-SL-Note-98-017-AP, 1998. URL: `https://cds.cern.ch/record/702438`.

[140] R. Bartolini *et al.* "Tune evaluation in simulations and experiments". *Part. Accel.* 52 (1995), 147–177. 29 p. URL: `https://cds.cern.ch/record/292773`.

[141] G. Russo, G. Franchetti, and M. Giovannozzi. "New Techniques to Compute the Linear Tune". *Proc. IPAC'21* (Campinas, SP, Brazil). International Particle Accelerator Conference 12. Geneva: JACoW Publishing, Geneva, Switzerland, Aug. 2021, THPAB189, pp. 4142–4145. ISBN: 978-3-95450-214-1. DOI: `10.18429/JACoW-IPAC2021-THPAB189`.

[142] S. Das and J. A. Yorke. "Super convergence of ergodic averages for quasiperiodic orbits". *Nonlinearity* 31(2) (Jan. 2018), pp. 491–501. DOI: `10.1088/1361-6544/aa99a0`.

[143] V. Oseledets. "A multiplicative ergodic theorem. Characteristic Lyapunov, exponents of dynamical systems". *Trans. Moscow Math. Soc.* 19 (1968), pp. 179–210.

[144] E. Lega, M. Guzzo, and C. Froeschlé. "Theory and Applications of the Fast Lyapunov Indicator (FLI) Method". *Chaos Detection and Predictability*. Ed. by C. Skokos, G. A. Gottwald, and J. Laskar. Berlin, Heidelberg: Springer Berlin Heidelberg, 2016, pp. 35–54. ISBN: 978-3-662-48410-4. DOI: `10.1007/978-3-662-48410-4_2`.

[145] K. T. Alligood, T. D. Sauer, and J. A. Yorke. "Chaos". *Chaos: An Introduction to Dynamical Systems*. New York, NY: Springer New York, 1996, pp. 105–147. ISBN: 978-0-387-22492-3. DOI: `10.1007/b97589`.

[146] F. Panichi, L. Ciotti, and G. Turchetti. "Fidelity and reversibility in the restricted three body problem". *Communications in Nonlinear Science and Numerical Simulation* 35 (2016), pp. 53–68. ISSN: 1007-5704. DOI: `https://doi.org/10.1016/j.cnsns.2015.10.016`.

[147] P. M. Cincotta and C. M. Giordano. "Theory and Applications of the Mean Exponential Growth Factor of Nearby Orbits (MEGNO) Method". *Chaos Detection and Predictability*. Ed. by C. Skokos, G. A. Gottwald, and J. Laskar. Berlin, Heidelberg: Springer Berlin Heidelberg, 2016, pp. 93–128. ISBN: 978-3-662-48410-4. DOI: `10.1007/978-3-662-48410-4_4`.

[148] A. Prasad and R. Ramaswamy. "Characteristic distributions of finite-time Lyapunov exponents". *Phys. Rev. E* 60 (3 Sept. 1999), pp. 2761–2766. doi: `10.1103/PhysRevE.60.2761`.

[149] J. C. Vallejo, J. Aguirre, and M. A. Sanjuán. "Characterization of the local instability in the Hénon–Heiles Hamiltonian". *Physics Letters A* 311(1) (2003), pp. 26–38. issn: 0375-9601. doi: `https://doi.org/10.1016/S0375-9601(03)00452-3`.

[150] Y.-C. Chen. "A tutorial on kernel density estimation and recent advances". *Biostatistics & Epidemiology* 1(1) (2017), pp. 161–187. doi: `10.1080/24709360.2017.1396742`.

[151] S. Weglarczyk. "Kernel density estimation and its application". *ITM Web Conf.* 23 (2018), p. 00037. doi: `10.1051/itmconf/20182300037`.

[152] M. C. Minnotte and D. W. Scott. "The Mode Tree: A Tool for Visualization of Nonparametric Density Features". *Journal of Computational and Graphical Statistics* 2(1) (1993), pp. 51–68. issn: 10618600. doi: `10.2307/1390955`.

[153] W. H. Press, S. A. Teukolsky, W. T. Vetterling, and B. P. Flannery. *Numerical Recipes 3rd Edition: The Art of Scientific Computing*. 3rd ed. USA: Cambridge University Press, 2007. isbn: 0521880688.

[154] J. Ghorpade, J. Parande, M. Kulkarni, and A. Bawaskar. "GPGPU Processing in CUDA Architecture". *CoRR* abs/1202.4347 (2012). arXiv: `1202.4347`. url: `http://arxiv.org/abs/1202.4347`.

[155] M. Giovannozzi and E. McIntosh. "Development of parallel codes for the study of nonlinear beam dynamics". *Int. J. Mod. Phys. C* 8(CERN-PS-96-047-PA. CERN-CN-96-017) (Nov. 1996), 155–170. 16 p. doi: `10.1142/S0129183197000163`.

[156] X. Pang and L. Rybarcyk. "GPU accelerated online multi-particle beam dynamics simulator for ion linear particle accelerators". *Computer Physics Communications* 185(3) (2014), pp. 744–753. doi: `10.1016/j.cpc.2013.10.033`.

[157] A. Oeftiger and S. Hegglin. "Space Charge Modules for PyHEADTAIL". *Proc. HB'16* (Malmö, Sweden, Jul. 2016). JACoW Publishing, Geneva, Switzerland, pp. 124–129. doi: `10.18429/JACoW-HB2016-MOPR025`.

[158] A. Adelmann *et al.* "OPAL a versatile tool for charged particle accelerator simulations". *arXiv preprint arXiv:1905.06654* (2019). doi: `10.48550/arXiv.1905.06654`.

[159] M. SCHWINZERL *et al.* "Optimising and Extending a Single-Particle Tracking Library for High Parallel Performance". *Proc. IPAC'21* (Campinas, Brazil, May 2021). JACoW Publishing, Geneva, Switzerland, pp. 4146–4149. DOI: `10.18429/JACoW-IPAC2021-THPAB190`.

[160] P. HERMES *et al.* "A Novel Tool for Beam Dynamics Studies with Hollow Electron Lenses". *Proc. IPAC'22* (Bangkok, Thailand). International Particle Accelerator Conference 13. JACoW Publishing, Geneva, Switzerland, July 2022, MOPOST045, pp. 176–179. ISBN: 978-3-95450-227-1. DOI: `10.18429/JACoW-IPAC2022-MOPOST045`.

[161] K. ILIAKIS *et al.* "Enabling Large Scale Simulations for Particle Accelerators". *IEEE Transactions on Parallel and Distributed Systems* 33(12) (2022), pp. 4425–4439. DOI: `10.1109/TPDS.2022.3192707`.

[162] C. SKOKOS. "The Lyapunov Characteristic Exponents and Their Computation". *Dynamics of Small Solar System Bodies and Exoplanets*. Ed. by J. J. SOUCHAY and R. DVORAK. Berlin, Heidelberg: Springer Berlin Heidelberg, 2010, pp. 63–135. ISBN: 978-3-642-04458-8. DOI: `10.1007/978-3-642-04458-8_2`.

[163] G. TANCREDI, A. SÁNCHEZ, and F. ROIG. "A Comparison between Methods to Compute Lyapunov Exponents". *The Astronomical Journal* 121(2) (Feb. 2001), p. 1171. DOI: `10.1086/318732`.

[164] G. IADAROLA. *Xsuite documentation pages*. 2022. URL: `https://xsuite.readthedocs.io` (visited on 01/31/2023).

[165] R. D. MARIA *et al.* "SixTrack Version 5: Status and New Developments". *Journal of Physics: Conference Series* 1350(1) (Nov. 2019), p. 012129. DOI: `10.1088/1742-6596/1350/1/012129`.

[166] R. D. MARIA *et al.* "High Luminosity LHC Optics and Layout HLLHCV1.4". *Journal of Physics: Conference Series* 1350(1) (Nov. 2019), p. 012001. DOI: `10.1088/1742-6596/1350/1/012001`.

[167] *MAD - Methodical Accelerator Design*. `https://mad.web.cern.ch/mad/`.

[168] *Pymask - A Python package for beam optics calculations*. `https://github.com/lhcopt/lhcmask`.

[169] E. TODESCO and M. GIOVANNOZZI. "Dynamic aperture estimates and phase-space distortions in nonlinear betatron motion". *Phys. Rev. E* 53 (1996), pp. 4067–4076.

[170] A. Morbidelli and C. Froeschlé. “On the relationship between Lyapunov times and macroscopic instability times”. *Celestial Mechanics and Dynamical Astronomy* 63(2) (June 1995), pp. 227–239. issn: 1572-9478. doi: `10.1007/BF00693416`.

[171] C. Skokos, T. Bountis, and C. Antonopoulos. “Geometrical properties of local dynamics in Hamiltonian systems: The Generalized Alignment Index (GALI) method”. *Physica D: Nonlinear Phenomena* 231(1) (2007), pp. 30–54. issn: 0167-2789. doi: `https://doi.org/10.1016/j.physd.2007.04.004`.

Acknowledgements

The research and findings presented in this thesis would not have been possible without the support, guidance, and mentoring of many individuals. I am first and foremost grateful to my supervisors, Prof. Armando Bazzani at Bologna University and Dr. Massimo Giovannozzi at CERN. Their consistent support, willingness to assist, and unflagging patience have been invaluable to me since my introduction to the field of Accelerator Physics as a Summer Student in 2018. Their guidance has been a constant throughout the entire journey.

I then express my gratitude to the entire BE-ABP-NDC section at CERN for the warm welcome and constant support, offered along the various stages of this research work and, especially, during the very narrow data gathering opportunities which occurred in the last months of 2022 LHC operation. For this last part, a dedicated thanks is due to Dr. Stefano Redaelli and Dr. Pascal Dominik Hermes, for assisting and guiding me through the various crucial stages of data gathering. A sincere thank also goes to Dr. Frederik Van der Veken for both the multiple moments of mentoring and for the inclusion in engaging side projects.

I also want to thank Dr. Axel Poyet and Dr. Guido Sterbini, for enabling the entire application of our diffusive framework on wire compensator losses, and giving us the opportunity of performing dedicated data gathering during the latest wire compensator MD session.

A dedicated thanks goes to Prof. Giorgio Turchetti, for the engaging teaching, the dedicated mentoring, and the research opportunity offered on the vast topic of dynamic indicators.

Prior to submitting the final version of this thesis, I would like to express my gratitude to Prof. Roberto Artuso and Dr. Stefano Redaelli. Their review of the preliminary edition of this work was greatly appreciated, and I am thankful for their thorough reading and motivating comments.

Contemporary research, and, arguably, research in general, cannot be carried forward by lonely individuals, but rather by a dynamic and motivated community of collaborating scientists. The scourging isolation brought on by the Covid pandemic has also highlighted the importance of maintaining these international communities active. I am grateful and honoured to have been included in such a community during this years, and to have had the opportunity to personally meet the wonderful and unique people that constitute it.